MAGNETOM Flash

The Magazine of MR

Issue Number 1/2010
ISMRM Edition
Not for distribution in the US.

SIEMENS

Technology

Clinical

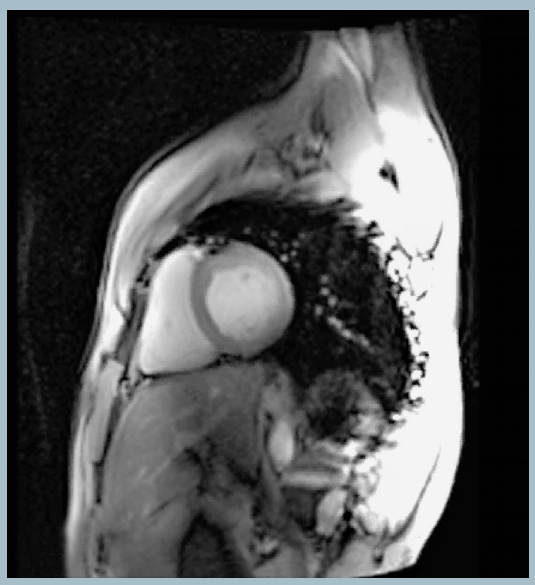

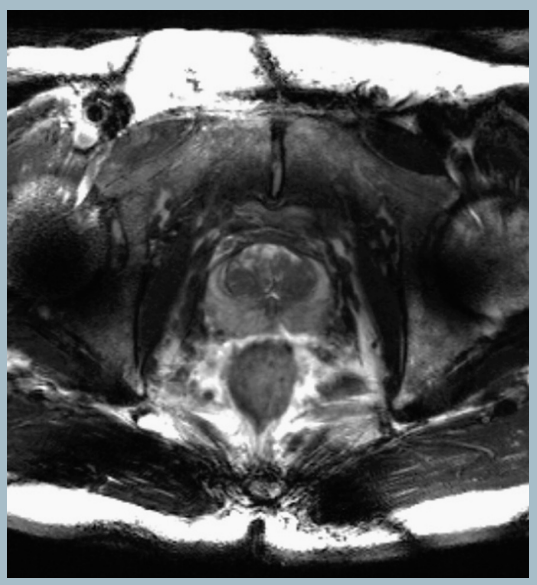

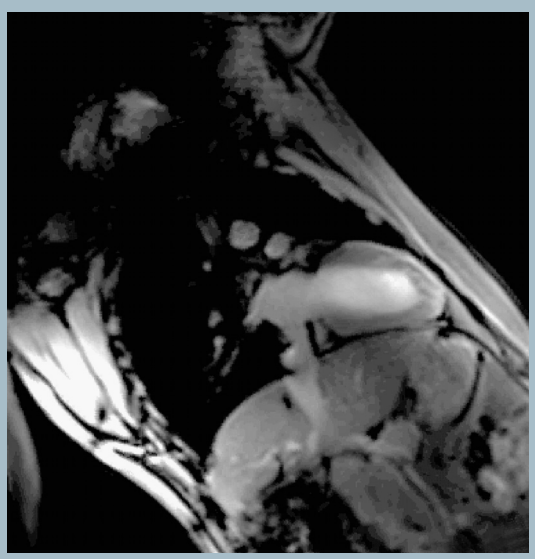

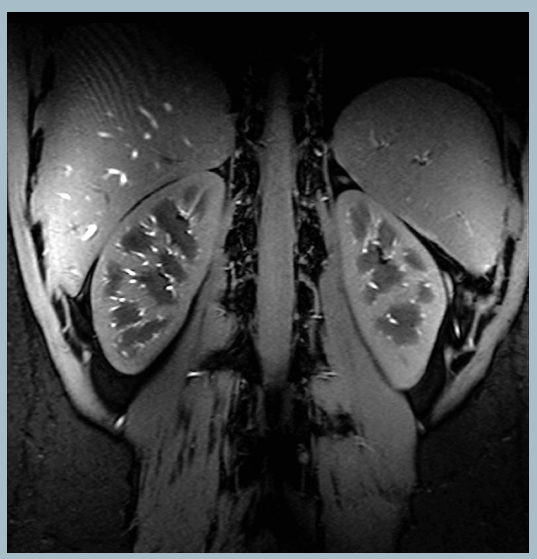

43

Body imaging at 7T

Matthias Lichy, M.D.

Dear MAGNETOM user,

With now more than 20 ultra-high field (UHF) systems with field-strengths of 7 Tesla and above worldwide, the Siemens MAGNETOM UHF community makes a major contribution to further technical and clinical development of MRI.

Whilst new technology often creates new challenges for researchers and clinicians to optimally benefit from this new technology, Siemens is already discovering solutions to these topics. To take just one example: dielectric shading is one of the major challenges for UHF imaging. It has a direct impact on image quality and therefore on diagnostic reliability. With the introduction of the TrueForm technology in 2005, however, the problem of dielectric shading will be overcome for imaging at 3 Tesla in all body regions for the first time in our daily clinical routine.

Improved use of higher field-strength (3T) is now a clinical reality, even for the imaging of body-regions like the left liver lobe. Combined with dedicated (high-density) coils and parallel-imaging technologies, full advantage can be taken of the increased signal-to-noise ratio at 3T, translated into high image quality. This is a direct benefit to patient care. However, the MAGNETOM TX array community not only contributes to overcoming the major challenges of UHF imaging. It also – and more importantly – demonstrates how this technology can be used to enhance existing, and enable new applications, such as restricted FOV "zoomed" imaging and vessel-selective angiography.

Each new issue of MAGNETOM Flash provides, time and again, detailed proof of the clinical advantage achieved by new technologies. In this latest issue, for example, we show how non-contrast enhanced MRI at 7T can display tumor vessels in detail, how diffusion-weighted imaging is used for liver imaging work-up and how motion-insensitive imaging helps to diagnose brain lesions of the posterior fossa in children.

We hope that you will enjoy reading this latest issue of Flash!

Matthias Lichy, M.D.

Not for distribution in the US.

The Editorial Team

We appreciate your comments.
Please contact us at magnetomworld.med@siemens.com

Antje Hellwich
Associate Editor

Dagmar Thomsik-Schröpfer,
Ph.D., MR Marketing-Products,
Erlangen, Germany

Okan Ekinci, M.D.
Center of Clinical Competence –
Cardiology, Erlangen, Germany

Peter Kreisler, Ph.D.
Collaborations & Applications,
Erlangen, Germany

Heike Weh,
Clinical Data Manager,
Erlangen, Germany

Bernhard Baden,
Clinical Data Manager,
Erlangen, Germany

Ignacio Vallines, Ph.D.,
Applications Manager,
Erlangen, Germany

Wellesley Were
MR Business Development
Manager
Australia and New Zealand

Milind Dhamankar, M.D.
Sr. Director, MR Product
Marketing, Malvern, USA

Michelle Kessler, US
Installed Base Manager,
Malvern, PA, USA

Gary R. McNeal, MS (BME)
Advanced Application Specialist,
Cardiovascular MR Imaging
Hoffman Estates, USA

Dr. Sunil Kumar S.L.
Senior Manager Applications,
Canada

Content

Content

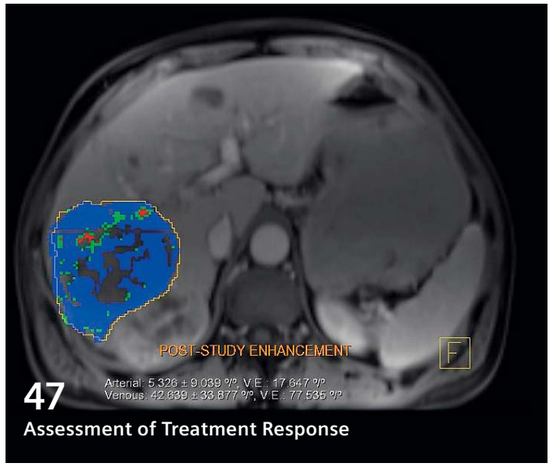

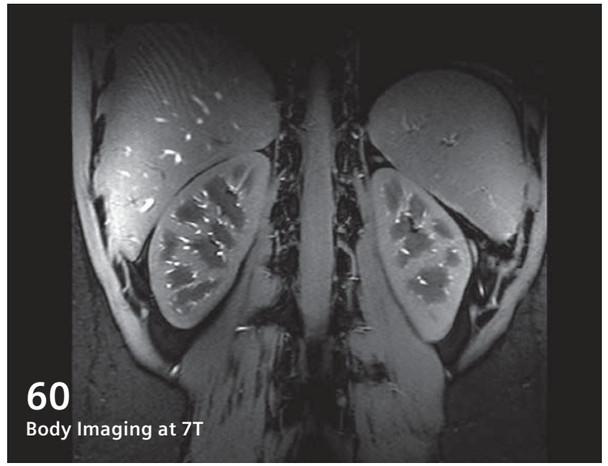

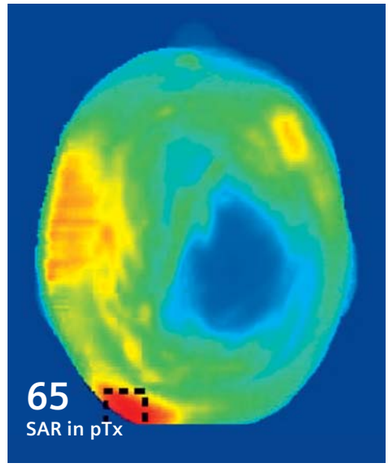

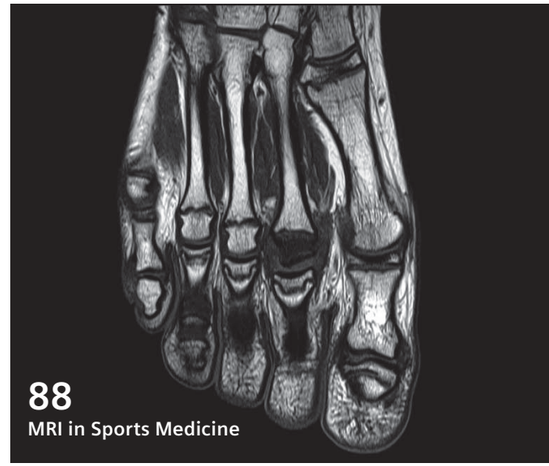

Further clinical information

Visit the MAGNETOM World Internet pages at **www.siemens.com/magnetom-world** for further clinical information and talks by international experts.

Not for distribution in the US.

Not for distribution in the US.

Diagnostic Relevant Reduction of Motion Artifacts in the Posterior Fossa by *syngo* BLADE Imaging

T. von Kalle[1]; B. Blank[2]; C. Fabig-Moritz[1]; P. Müller-Abt[1]; M. Zieger[1]; K. Wohlfarth[3]; P. Winkler[1]

[1]*Department of Pediatric Radiology, Olgahospital Klinikum Stuttgart, Germany*
[2]*Department of Pediatric Oncology, Hematology and Immunology, Olgahospital Klinikum Stuttgart, Germany*
[3]*Siemens Healthcare, Erlangen, Germany*

1

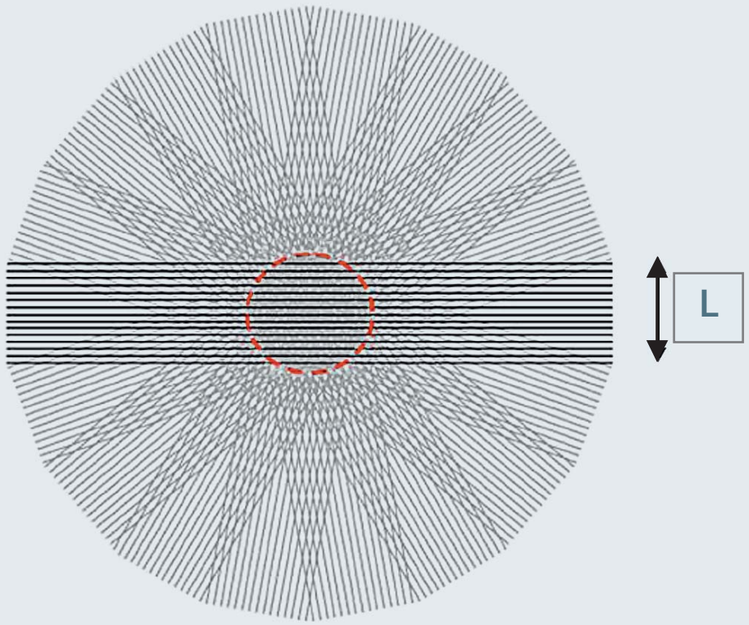

1 k-space trajectory in BLADE imaging. The k-space is covered by a series of blades each of which consists of the lowest phase encoding lines. The centre of the k-space (red circle) with diameter L is resampled for every blade. Data are then combined to a high resolution image.

Although movement and pulsation artifacts are a frequent problem in daily routine [1–4] especially in the diagnostics of pediatric patients, only few articles on this topic can be found in the literature. According to our experience mainly MR images of the posterior fossa, the cerebellum and the brain stem, may be significantly impaired by artifacts from pulsatile flow of blood or cerebrospinal fluid even without patient head movement [5, 6]. Sedation or general anesthesia rarely influence these pulsation or flow artifacts. However, accurate assessment of small brain lesions is essential in many pediatric patients, especially in those with malignant brain tumors.
MR imaging with "rotating blade-like k-space covering" (BLADE) and "Periodically Rotated Overlapping Parallel Lines with Enhanced Reconstruction" (PROPELLER) have been shown to effectively reduce artifacts in healthy volunteers and adult patients [7, 8, 9], as well as in pediatric patients [4, 10] and therefore have the potential to reduce the frequency of anesthesia in children. As these MR techniques reduce motion artifacts by fast segmental image acquisition combined with mathematical algorithms, we assumed that it might at the same time reduce the visibility of small brain lesions. We therefore compared the image quality of two T2-weighted fluid attenuated inversion recovery (T2w FLAIR) sequences with different k-space trajectories (conventional Cartesian and BLADE) with respect to artifacts and depiction of small hyperintense brain lesions [5].

Imaging techniques

We used a 1.5T scanner (MAGNETOM Avanto, Siemens Healthcare, Erlangen, Germany) and the Siemens 12-channel head matrix coil.
For each patient we compared two sequences with transverse 4 mm sections (gap 10%) that were applied in identical slice positions:
1. The T2w FLAIR standard sequence, a spin-echo sequence with conventional rectilinear Cartesian k-space trajectories (image parameters: TI 2500 ms, TR 9000 ms, TE 100 ms, BW 150 Hz/pixel, turbo factor 19, TA160 s, FOV 230 x 230 mm, matrix 256 x 256).
2. The BLADE FLAIR sequence with rotating blade-like k-space trajectories (image parameters: TI 2500 ms, TR 9000 ms, TE 107 ms, BW 250 Hz/pixel, turbo factor 29, TA 260 s, BLADE-Coverage 130 %, FOV 230 x 230 mm, matrix 256 x 256).
During the acquisition of both sequences children were encouraged not to move their head. They were offered video films or audio programs during the examination.

BLADE technique

syngo BLADE is the product name of the motion insensitive Siemens turbo-spin-echo sequence which utilizes the PROPELLER k-space trajectory [11].
The technique is approved for diagnostic MR examinations of patients. It consists of blade-like rotating k-space coverage. During each echo train of a BLADE sequence the lowest phase encoding lines of a conventional rectilinear k-space are acquired. The number of lines, which depends on the length of the echo train, determines the resolution of the image. During the acquisition process the direction of this "blade" is rotated around the k-space centre such that the complete series covers the whole k-space (Fig. 1). Images can be displayed with or without an additional motion correction algorithm.

2

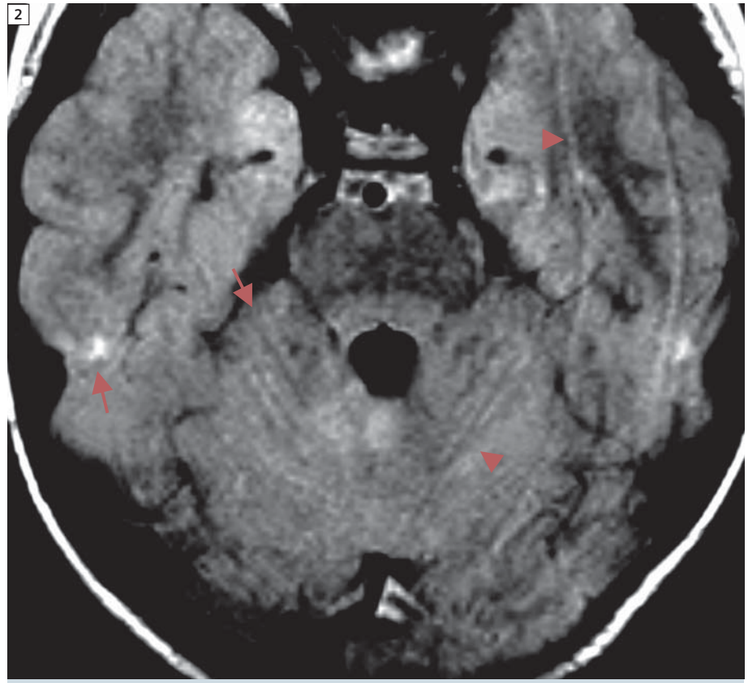

2 Movement artifacts caused by head movements (arrowheads) and pulsation artifacts caused by pulsatile flow (arrows). T2w FLAIR sequence with conventional rectilinear k-space trajectories.

Patients

The typical hyperintense white matter abnormalities in the cerebellum of patients with neurofibromatosis type 1 (NF 1) [12] served the purpose of our study to assess and compare the visibility of small and low contrast lesions.
We re-evaluated images of children with NF 1, who had been routinely scanned for optic pathway gliomas and who had been examined with T2w FLAIR sequences of both techniques. 26 patients, 10 girls and 16 boys from 2 years 7 months to 17 years (median age 8 years 5 months) were included in the study.

Image evaluation

Four experienced pediatric radiologists independently assessed unlabeled images of both FLAIR sequences of each patient. Structures of the posterior fossa, cerebellum and brain stem, were evaluated according to the presence of movement artifacts (caused by head movements) or pulsation artifacts (caused by pulsatile flow of blood and/or cerebrospinal fluid) (Fig. 2), their differentiation from lesions, and their delineation from the surrounding tissue by contrast (difference in signal intensities) and edge definition (clearly or poorly defined margins) as has been described elsewhere

Not for distribution in the US.

Not for distribution in the US.

Table 1: Scores for movement and pulsation artifacts, and the differentiation of artifacts and lesions in the posterior fossa.

	Conventional		*syngo* BLADE	
	yes	**no**	**yes**	**no**
Movement	29	75	4	100
Pulsation	99	5	25	79
Differentiation lesion/artefacts	53	30	81	2

Yes = artifacts present, lesions and artifacts distinguishable. No = artifacts not present, lesions and artifact not distinguishable. Maximum score for each sequence = 104. Last line. Patients with neither artifacts nor lesions were excluded. Results of statistical tests cf Table 2.

[5] The transverse diameters of the largest and smallest lesions were measured in both sequences of each patient. Signal intensities of a representative lesion and the adjacent normal brain tissue were measured. [5]

Discussion

Techniques with rotating blade-like k-space covering (BLADE) [9], with periodically rotated overlapping parallel lines with enhanced reconstruction (PROPELLER) [8,10], and with k-space alignment similar to a trellis [13] have been shown to effectively reduce artifacts in T1- and T2-weighted images. Studies on pediatric [4] and adult patients [7] found a comparable detectability of lesions in contrast-enhanced T1-weighted images of FLAIR BLADE sequences and conventional spin-echo sequences. However, image quality and delineation of small or poorly delineated lesions in MR images in T2-weighted FLAIR acquired with these techniques have not been systematically studied.

In our study, all observers found more pulsation artifacts than movement artifacts in images of both the conventional and the *syngo* BLADE sequence (Table 1). Artifacts were reported significantly less often in images acquired with BLADE technique than in images with rectilinear k-space trajectory (Table 1 and 2). These results confirm that artifacts caused by pulsation, flow and motion are significantly reduced by the BLADE technique in comparison to the standard sequence with conventional

Table 2: Posterior fossa. Comparison of conventional vs. BLADE images. McNemar's test. p-values for each observer. Cohen's kappa for interobserver agreement.

	Presence of movement artifacts	Presence of pulsation artifacts	Differentiation of lesions and artifacts	Delineation of lesions	
				Edge definition	Contrast
Observer 1	0.03	0.02	0.04	> 0.05	> 0.05
Observer 2	0.02	0.00002	0.002	0.0027	0.0009
Observer 3	0.041	0.000007	0.001	> 0.05	> 0.05
Observer 4	0.013	0.00002	0.013	> 0.05	> 0.05
Cohen's kappa	0.34	0.37	0.72	0.11	0.01

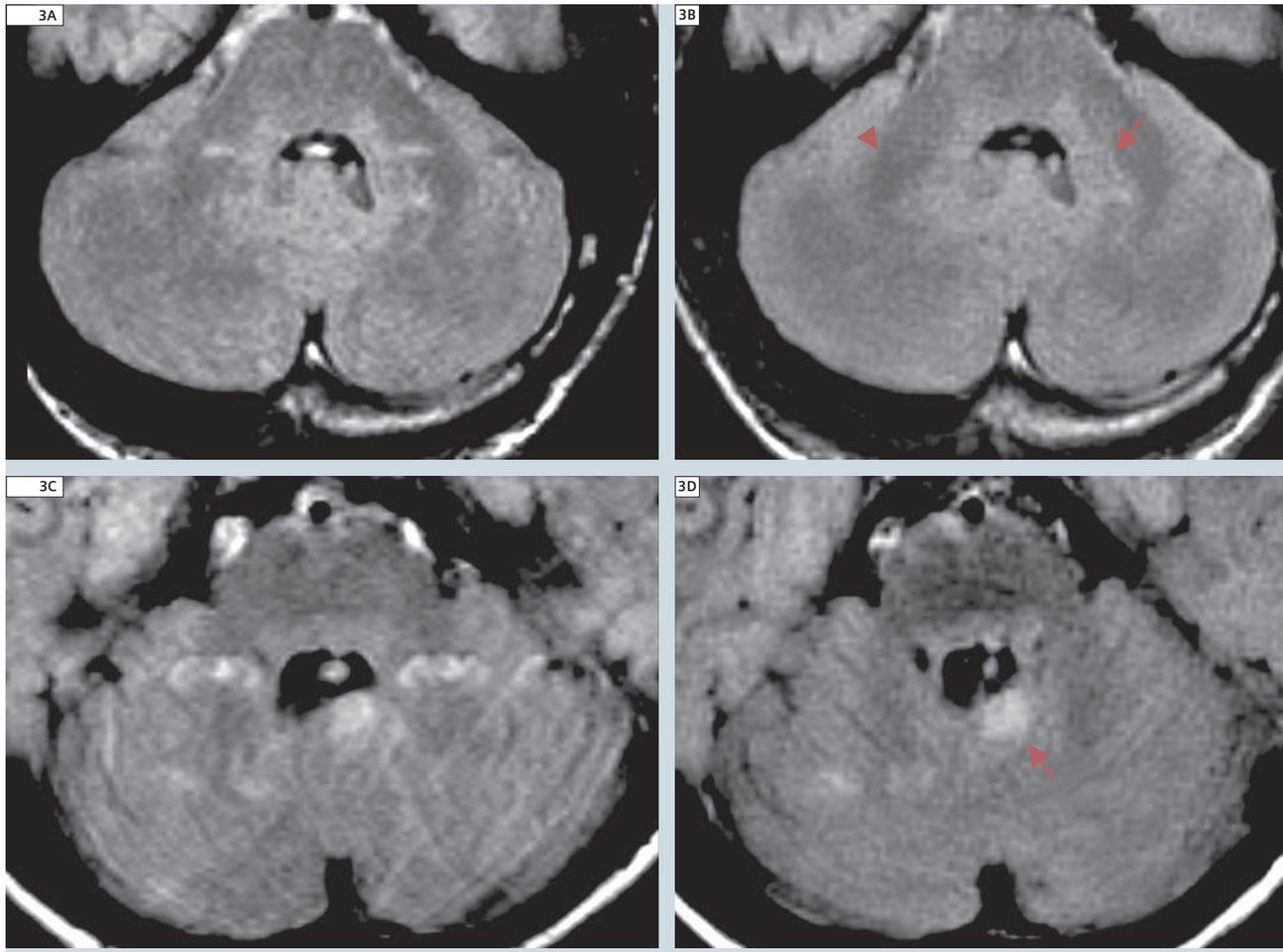

3 T2w FLAIR images of the posterior fossa of two different patients. Rectilinear k-space coverage (left), BLADE (right). Lesions typical of neurofibromatosis type 1: low contrast confluent (arrowhead), high contrast round (arrow). Artifacts and lesions not reliably distinguishable in conventional images (left).

rectilinear k-space covering. As the children were encouraged not to move during the examination, there were only moderate to minor movement artifacts even in conventional T2w FLAIR images. Pulsation artifacts were more frequent and more severe in conventional images and sometimes also present in BLADE images. Ratings of subtle movement artifacts in conventional images and subtle pulsation artifacts in BLADE images led to an only fair interobserver agreement (Cohen's kappa < 0.4, Table 2). These artifacts did not disturb the depiction of lesions.

There was good observer agreement (Cohen's kappa 0.74, Table 2) that artifacts compromised the assessment of lesions more often and more severely in conventional T2w FLAIR images than in BLADE images. In 6 of all 26 patients (23%) observers agreed that in conventional T2w FLAIR images they could not differentiate lesions from artifacts in the posterior fossa, rendering nearly a fourth of the examinations with conventional k-space trajectory inadequate for a reliable diagnosis. In none of the BLADE sequences more than one observer considered artifacts and lesions to be indistinguishable (Fig. 3).

Not for distribution in the US.

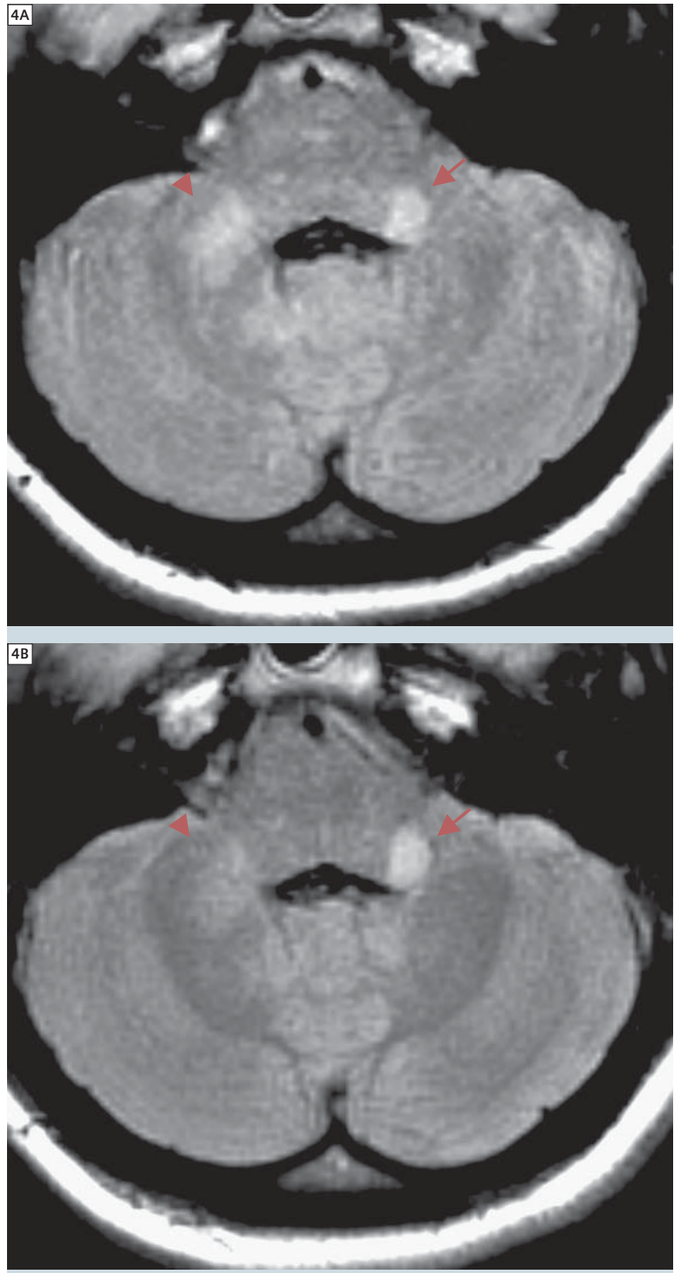

4 Absence of major artifacts and comparable visibility of lesions in images of both techniques (T2w FLAIR: rectilinear k-space top, BLADE bottom), low contrast confluent (arrowhead), high contrast round (arrow).

As Gill et al. reported for their sample [12], most hyperintense lesions in the thalami, brain stem and cerebellum were confluent or diffuse with poorly defined edges. A smaller number of lesions were well circumscribed with edges that were distinct from the adjacent normal tissue. Mean ratios of signal intensities were only slightly lower in the posterior fossa than in cerebrum and midbrain.

If lesions were not obscured by artifacts, visibility of lesions with both clearly and poorly defined edges appeared to be comparable in images of both techniques (Fig. 4). Observers' comparisons of both imaging techniques according to contrast and edge definition did not reveal consistently significant differences for lesions of the posterior fossa (Table 2). There only was a tendency to better edge definition in BLADE images. Visibility of lesions also was independent of size. Even the smallest lesions of our sample (2–3 mm) were equally depicted by both techniques.

BLADE technique is based on standard image acquisition techniques and therefore has the advantage of providing image characteristics equal to standard sequences. As an alternative to *syngo* BLADE imaging, pulsation artifacts may be identified by a second data acquisition after changing the phase encoding direction [1] or the slice orientation, with the disadvantage of a longer examination time and the higher risk of movement artifacts. Reduction of motion artifacts in non-sedated children can also be achieved by rapid sequences (e.g. single shot techniques) which, in neuroimaging, have the disadvantages of a poorer differentiation of gray and white matter [3, 10,14] and a lower spatial resolution [15].

Not for distribution in the US.

Observers of our study had the subjective impression that the appearance of FLAIR BLADE images differed slightly from that of conventional images which did not impair image quality and lesion detectability (Figs. 3 and 4). These subtle differences have already been reported for PROPELLER technique [2]. BLADE images might therefore be identified by experienced radiologists despite "blinding". We have, however, not identified bias due to this fact in our study.

In our study, data acquisition time and image reconstruction time together were approximately 2–3 minutes longer for *syngo* BLADE sequences than for conventional FLAIR sequences. The advantage of artifact reduction by the BLADE technique clearly outweighed the prolonged duration.

There are limitations of our retrospective study: We were not able to measure the degree of patients' movements. Therefore, like other investigators [2, 4, 9], we can only assume that these parameters were similar in statistical mean throughout the examination. As both sequences were performed successively, pulsation and flow artifacts were also assumed as unchanged for both acquisitions. For our retrospective analysis we had to accept that in addition to the k-space trajectory some of the parameters of both sequences were not identical. As the BLADE technique benefits from long echo trains, a turbo factor had been chosen that was larger than that of our routine T2w FLAIR sequence. However, a change of these parameters would have had only minor influence on motion artefacts, and presumably would not have changed the quality of results. Prospective studies of a larger patient group could avoid these shortcomings.

Conclusion

BLADE technique reduces movement and pulsation artifacts in T2w FLAIR images without relevant loss of image quality. It therefore markedly improves depiction of small and low contrast brain lesions in children in the posterior fossa of pediatric patients. This can be crucial especially in patients after surgery of malignant brain tumors. In the absence of major artifacts lesions of all sizes were depicted in comparable quality by both techniques.

References

1 Böck JC, Neumann K, Sander B, Schmidt D, Schörner W (1991) Prepontine artifacts due to pulsation of cerebrospinal fluid in T_2-weighted coronal MRI. Clinical relevance, incidence and a technique for efficient artefact suppression. RoeFo 154: 202-205.

2 Forbes KP, Pipe JG, Bird CR, Heiserman JE (2001) PROPELLER MRI: Clinical testing of a novel technique for quantification and compensation of head motion. J Magn Reson Imaging 14: 215-222.

3 Penzkofer AK, Pfluger T, Pochmann Y, Meissner O, Leisinger G (2002) MR imaging of the brain in pediatric patients: Diagnostic value of HASTE sequences. AJR 179: 509-514.

4 Alibek S, Adamietz B, Cavallaro A, Stemmer A, Anders K, Kramer M, Bautz W, Staatz G (2008) Contrast-enhanced T1-weighted fluid-attenuated inversion-recovery BLADE Magnetic Resonance Imaging of the brain: An alternative to spin-echo technique for detection of brain lesions in the unsedated pediatric patient? Acad Radiol 15: 986-995.

5 Von Kalle T, Blank B, Fabig-Moritz C, Müller-Abt P, Zieger M, Wohlfarth K, Winkler P (2009) reduced artefacts and improved assessment of hyperintense brain lesions with BLADE MR imaging in patients with neurofibromatosis type 1. Pediatr Radiol 39: 1216-1222.
Kallmes DF, Hui FK, Mugler JP III (2001) Suppression of cerebrospinal fluid and blood flow artifacts in FLAIR MR imaging with a single-slab three-dimensional pulse sequence: Initial experience. Radiographics 221: 251-255.

6 Naganawa S, Satake H, Iwano S, Kawai H, Kubota S, Komada T, Kawamura M, Sakurai Y, Fukatsu H (2008) Contrast-enhanced MR imaging of the brain using T1-weighted FLAIR with BLADE compared with a conventional spin-echo sequence. Eur Radiol 18: 337-342.

7 Forbes KP, Pipe JG, Karis JP, Heiserman JE (2002) Improved image quality and detection of acute cerebral infarction with PROPELLER diffusion-weighted MR imaging. Radiology 225:551-555.

8 Wintersperger BJ, Runge VM, Biswas J, Nelson CB, Stemmer A, Simonetta AB, Reiser MF, Naul LG, Schoenberg SO (2006) Brain magnetic resonance imaging at 3 Tesla using BLADE compared with standard rectilinear data sampling. Invest Radio 41: 586-592.

9 Forbes KP, Pipe JG, Karis JP, Farthing V, Heiserman JE (2003) Brain imaging in the unsedated pediatric patient: Comparison of periodically rotated overlapping parallel lines with enhanced reconstruction and single-shot fast spin-echo sequences. AJNR 24: 794-798.

10 Pipe JG (1999) Motion correction with PROPELLER MRI: Application to head motion and free-breathing cardiac imaging. Magn Reson Med 42: 963-969.

11 Gill DS, Hyman SL, Steinberg A, North KN (2006): Age-related findings on MRI in neurofibromatosis type 1. Pediatr Radiol 36: 1048-1056.

12 Maclaren JR, Bones PJ, Millane RP, Watts R (2008) MRI with TRELLIS: a novel approach to motion correction. Magn Res Imaging 26: 474-483.

13 Iskandar BJ, Sansone JM, Medow J, Rowley HA (2004) The use of quick-brain magnetic resonance imaging in the evaluation of shunt-treated hydrocephalus. J Neurosurg (Pediatrics 2) 101: 147-151.

14 Ba-Ssalamah A, Schick S, Heimberger K, Linnau KF, Schibany N, Prokesch R, Trattnig S (2000) Ultrafast magnetic resonance imaging of the brain. Magn Reson Imaging 18: 237-43.

Contact
Thekla v. Kalle, M.D.
Department of Pediatric Radiology
Olgahospital Klinikum Stuttgart
Bismarckstr. 8
70176 Stuttgart
Germany
Phone: +49 (0) 711/ 278-04
t.vonkalle@klinikum-stuttgart.de
www.klinikum-stuttgart.de

Multimodal MRI of the Brain for Improved Diagnosis and Therapy Planning in a Case of Glioblastoma Multiforme

Elna-Marie Larsson, M.D., MSc

Uppsala University Hospital, Uppsala, Sweden

Patient history

A 60-year-old man with approximately one month history of depression, impaired working capacity and personality changes was consulting a psychiatrist due to increasing confusion. Computed Tomography (CT) of the brain was performed and showed a right-sided frontal tumor. The patient was referred to the department of Neurosurgery at the University Hospital. MRI of the brain including Perfusion MRI and MR spectroscopic imaging (MRSI) was performed for preoperative evaluation and guidance.

Sequence details

MRI of the brain with diffusion-weighted imaging (DWI), perfusion MRI and MRS was performed at 1.5 Tesla (MAGNETOM Avanto), using the standard Head Matrix coil.

The imaging protocol included:

- transversal T1w SE: TR/TE 593/9 ms, SL 5 mm
- transversal T2w TSE: TR/TE 4000/98 ms, turbo factor 13, SL 5 mm
- transversal DWI: ADC mapping with high b-value = 1000 s/mm^2, TE 89 ms, SL 5 mm.
- coronal T2w FLAIR: TR/TE 8000/90 ms, turbo factor 17, SL 5 mm
- Perfusion MRI: GRE EPI, TR/TE 1410/30 ms, SL 5 mm. Perfusion maps calculated using Nordic ICE software (NordicNeuroLab, Bergen, Norway, www.nordicneurolab.com)
- contrast-enhanced (Gadovist) transversal 3D T1w MPRAGE: TR/TE 1170/4 ms, SL 0,8 mm (MPR SL 5 mm)
- transversal 2D MRSI: PRESS, TR/TE = 1690/135 ms, 4 averages, matrix 16 x 16, nominal voxel size 10 x 10 x 15 mm^3

Imaging findings

In the right frontal lobe there is a 5 x 5 x 6 cm tumor with irregular contrast enhancement and necrotic portions. It is surrounded by extensive vasogenic oedema (with increased diffusion). Signal changes on T2-weighted images are also extending into the genu of the corpus callosum (Fig. 1). Perfusion with dynamic susceptibility contrast imaging (DSC) shows high relative cerebral blood volume (rCBV) corresponding to contrast enhancement, especially in the lateral portion of the tumor (Fig. 2). DWI with ADC map (Fig. 3) shows restricted diffusion in regions with high rCBV. 2D MRSI (Fig. 4A) shows a large lipid/lactate peak, low NAA and Cr, and elevated Cho in the tumor. Anteromedial to the enhancing tumor there is no lactate/lipid peak, moderately decreased NAA and elevated choline/creatine. The latter is also seen on the Cho/Cr image (Fig. 4B). The tumor with surrounding oedema has a considerable mass effect on the right lateral ventricle and there is a midline shift towards the left side. No other lesions are seen in the brain.

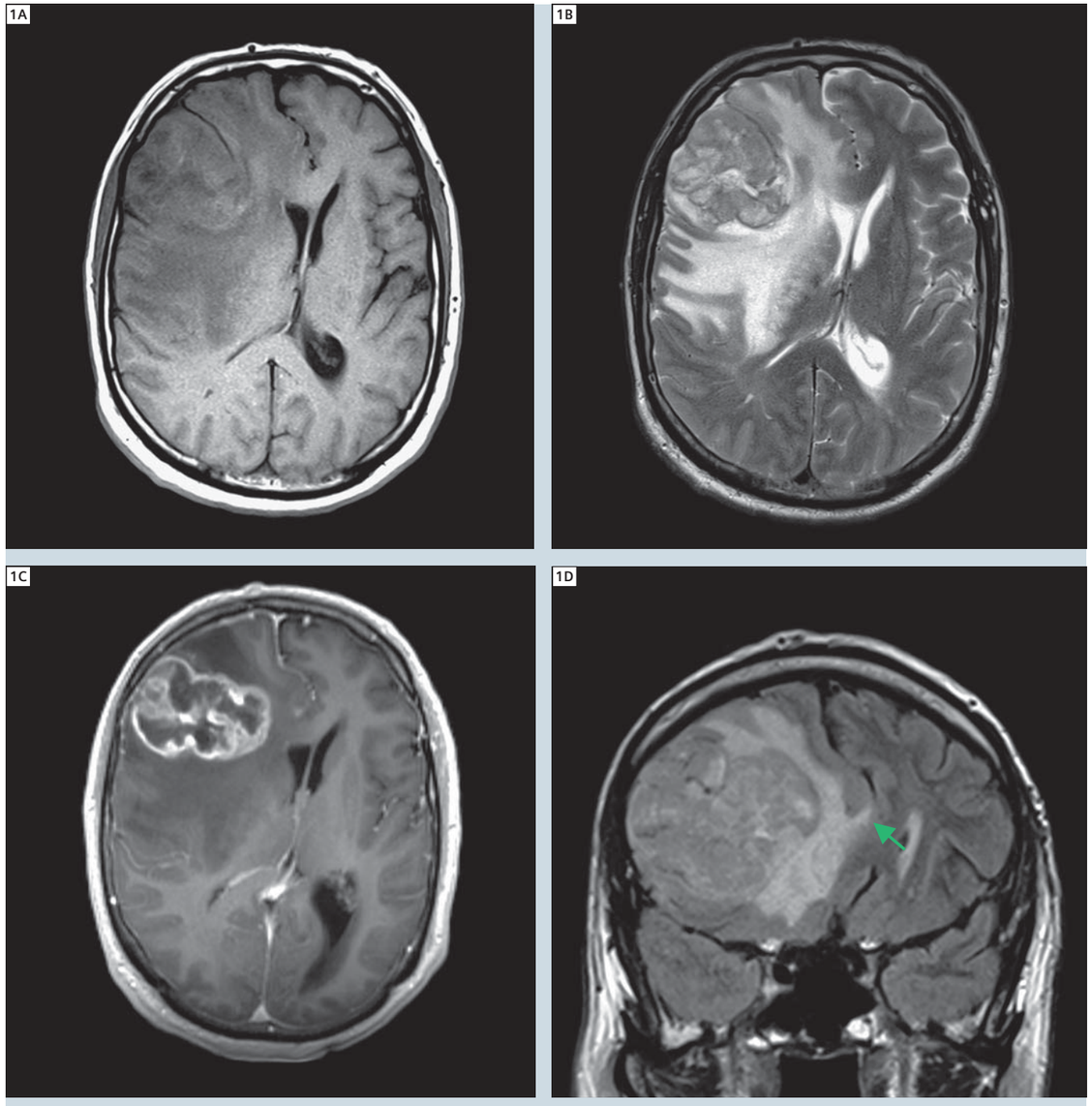

1 Transversal native T1w SE **(A)**, T2w TSE **(B)** and post-contrast T1w MPRAGE images of a tumor with central necroses and mass effect. Coronal T2w FLAIR image **(D)** demonstrating extension of the mass into the genu of the corpus callosum (arrow).

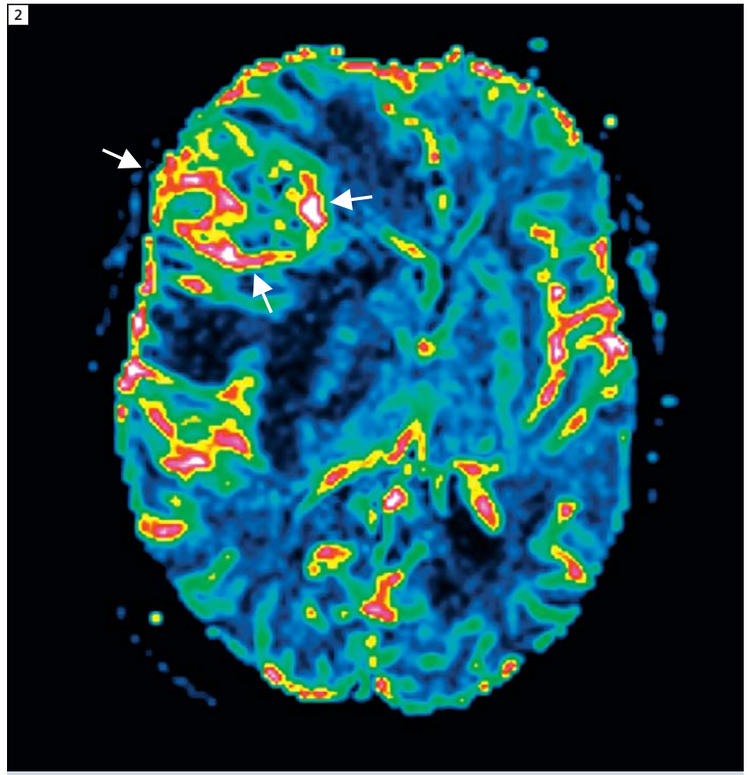

2 Corresponding results of the perfusion measurement is shown and rCBV map of the tumor does visualize high blood volume in areas of contrast-enhancment (arrows).

Discussion

In post-contrast T1w images (Fig. 1C), the contrast-enhancing lesion has the appearance of a malignant tumor with necrotic portions, which could be consistent with glioblastoma multiforme or a solitary metastasis. The signal changes in the genu of the corpus callosum (Figs. 1A, B and D) are most likely due to tumor growth, since oedema is usually not extending into the dense white matter fibres in the corpus callosum. The restricted diffusion (hypointense on ADC map (Fig. 3B) in portions of the tumor is a consequence of high cellularity seen in malignant tissue. The increased perfusion is consistent with malignant tumor and this is supported by the MRSI pattern with increased Cho and low NAA. Elevated superimposed lactate / lipid peaks reveal necrosis. The 2D MRSI imaging shows pathological spectra also outside the enhancing tumor (Fig. 4) speaking in favour of tumor infiltration as seen in malignant glioma but not in metastases. Abscess is not a likely diagnosis although the necrotic portion of an abscess usually has restricted diffusion. In our patient the restricted diffusion is seen in solid enhancing tumor portions and in addition the increased perfusion speaks in favour of malignant tumor (high perfusion is usually not seen in abscesses). The thick irregular contrast enhancement in this patient is not commonly seen in abscesses and the MRSI findings exclude abscess.
Thus the contrast-enhancement appearance, the restricted diffusion in solid tumor portions, the high rCBV and the MRSI pattern including pathological spectra in the tissue adjacent to the tumor strongly supports the diagnosis glioblastoma multiforme. The findings are also helpful for the neurosurgeon in selection of biopsy site in a malignant portion without too extensive necrosis. The MRSI is very helpful for the differentiation between glioma and solitary metastasis.
The patient underwent neurosurgery and the histopathological examination confirmed the suspected diagnosis glioblastoma multiforme.

Conclusion

Multimodality MRI with morphological images, DWI, perfusion and MRSI is thus helpful in the differential diagnosis of brain tumours and for the neurosurgical planning of biopsy locations.

Contact
Elna-Marie Larsson, M.D., D.MSc, Professor
Section of Neuroradiology
Department of Radiology
University Hospital
SE-75185 Uppsala
Sweden
elna-marie.larsson@radiol.uu.se

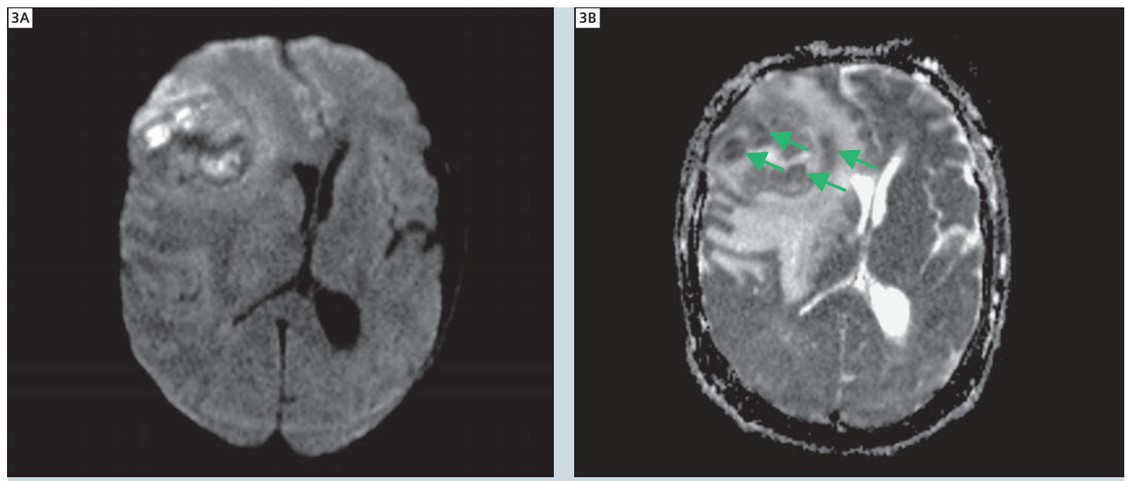

3 High b-value image at b = 1000 s/mm² and ADC map are shown. DWI shows clear restriction of water diffusion in non-necrotic areas of the mass (arrows).

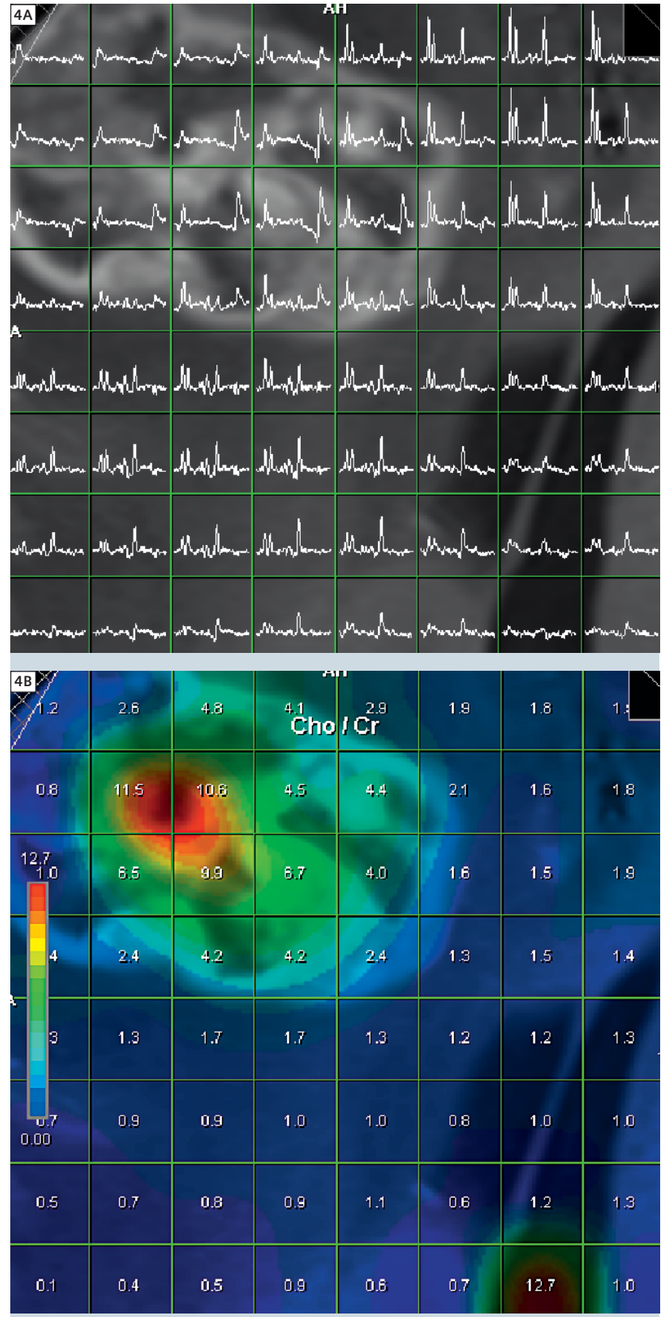

4 Spectra derived from 2D MR spectroscopic imaging are shown in **4A** (range 0.9–3.5 ppm). Choline/Creatine map **(B)** reveals high Cho/Cr ratio in the tumor and also increased ratio outside the contrast enhancing tumor region anteromedially (upper right corner of image, ratio around 1.8).

Case Report: Non-Contrast-Enhanced Evaluation of Perfusion Deficiencies of the Brain

David J. Panasci, M.D.; Steven L. Mendelsohn, M.D.

Zwanger-Pesiri Radiology, Smithtown, NY, USA

Background

Non-invasive and fast evaluation of the arteries and perfusion of the brain are common indications for MRI. Contrast-enhanced T2* perfusion MRI is used for this purpose and is playing an important role in stroke imaging in dedicated centres of care. However, contrast-enhanced perfusion measurements have practical limitations: First, renal function is often limited in elderly patients and may require dedicated preparation e.g. hydration. Second, T2* perfusion measurements require large gauge IVs for high-flow venous injection to achieve perfect bolus shape. Finally, the pressure to reduce costs and optimize the clinical cost-benefit ratio increases the demand for non-contrast enhanced MR methods which allow the evaluation of the vessel and perfusion status of the brain. With the clinical availability of arterial spin labelling techniques (*syngo* ASL), we established a fast, robust and contrast-media free imaging protocol at our imaging centres to meet the demands of a fast, clinical precise, error-robust and cost effective MR examination.

Patient history

The patient had a history of left internal carotid artery occlusion with stenoses of the cavernous segment of the right internal carotid artery and A1 segment of the right anterior cerebral artery. These were treated with angioplasty and stenting and angioplasty alone respectively.

Sequence details

The images have been acquired at 3 Tesla (MAGNETOM Verio) with the standard 12-channel head coil. The imaging protocol comprises 3D T1w FLASH, T2w fat-saturated FLAIR TSE, 3D TOF MRA and *syngo* ASL. For the evaluation of brain tissue perfusion, four different arterial labelling timepoints have been selected: 1.1, 1.5, 1.9 and 2.3 seconds.

Imaging findings

There is white matter microvascular disease involving both cerebral hemispheres with old infarcts in the medial aspect of the left parietal lobe in the watershed area between the middle cerebral and posterior cerebral territories on that side. A second area of infarction is seen in the deep white matter of the left frontal lobe (Fig. 1). The intracranial MRA demonstrates complete occlusion of the left internal carotid artery. Evaluation of the right cavernous carotid artery is limited because of artefact from the patient's stent. The A1 segment of the right anterior cerebral artery is normal in appearance (Fig. 2). No focal stenotic segment can be seen on this examination. The arterial spin labeling perfusion study demonstrates significant reduction in blood flow to the area of infarction in the left parietal lobe and to a lesser extent the left frontal lobe. There is progressively more perfusion seen on the studies performed

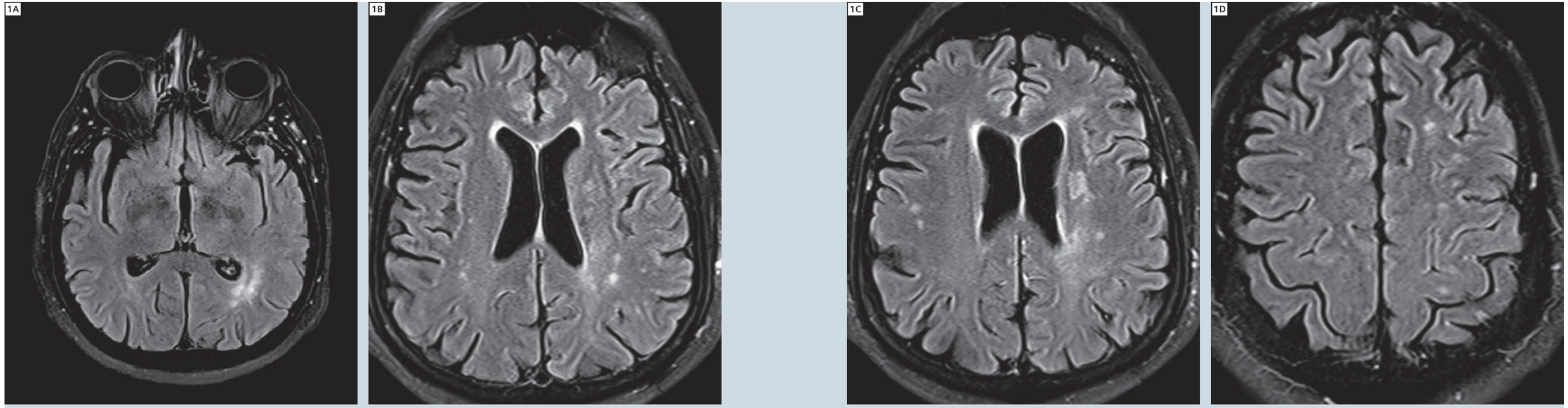

1 Transversal FLAIR images demonstrating multiple microvascular transformations of both cerebral hemispheres and old infarcts.

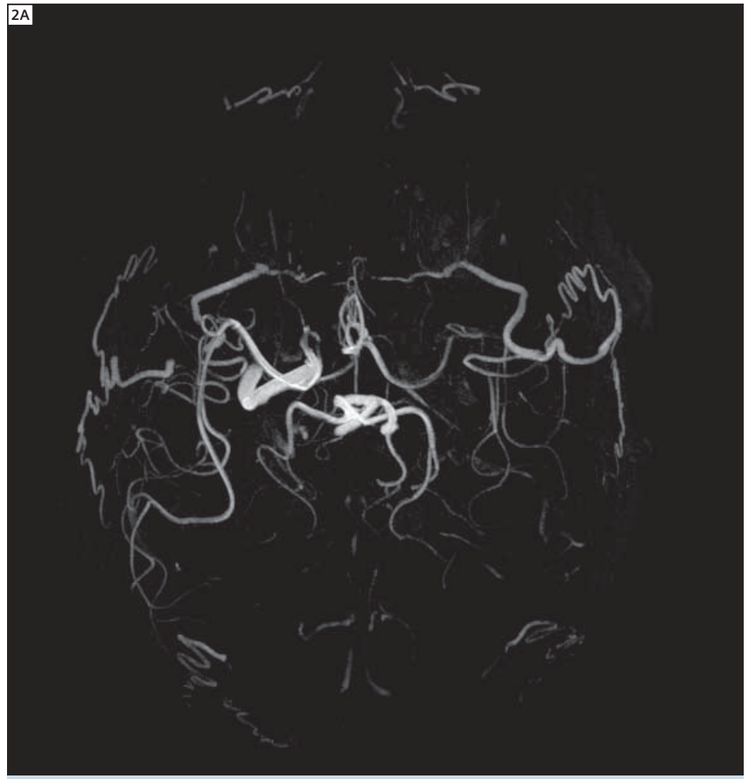

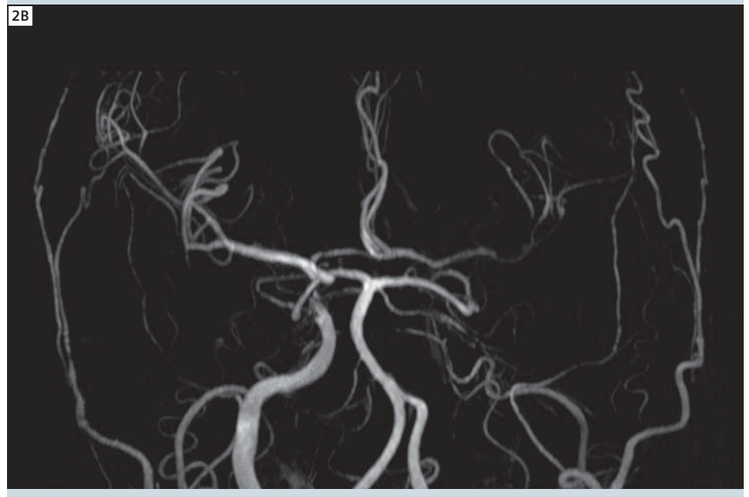

2 Transversal **(A)** and coronal **(B)** maximum intensity projection (MIP) of Time-of-Flight MR Angiography.

at 1.5 and 2 seconds after arterial labelling compared to the perfusion obtained 1 second after arterial labelling (Fig. 3). This would suggest there is delayed transit time into the left hemisphere secondary to the patient's carotid occlusion on that side.

Conclusion

The selected case of a post procedure study following angioplasty and stenting of a high grade right internal carotid artery cavernous segment stenosis and angioplasty of a right A1 segment anterior cerebral artery stenosis demonstrates the potential of this imaging protocol. The TOF MRA demonstrates a normal A1 segment of the right anterior cerebral artery and a patent cavernous segment. With *syngo* ASL, decreased perfusion in the patient's area of infarction in the left hemisphere in the left paretal and frontal lobes could be clearly visualized. In this case there also appears to be a delay in perfusion of the left hemisphere compared to the contralateral right side, another finding expected in this patient with occlusion of the left internal carotid artery.

Contact
David Panasci, M.D.
Zwanger-Pesiri Radiology
80 Maple Avenue
Smithtown, NY 11787
USA
Phone: +1 631-265-5777

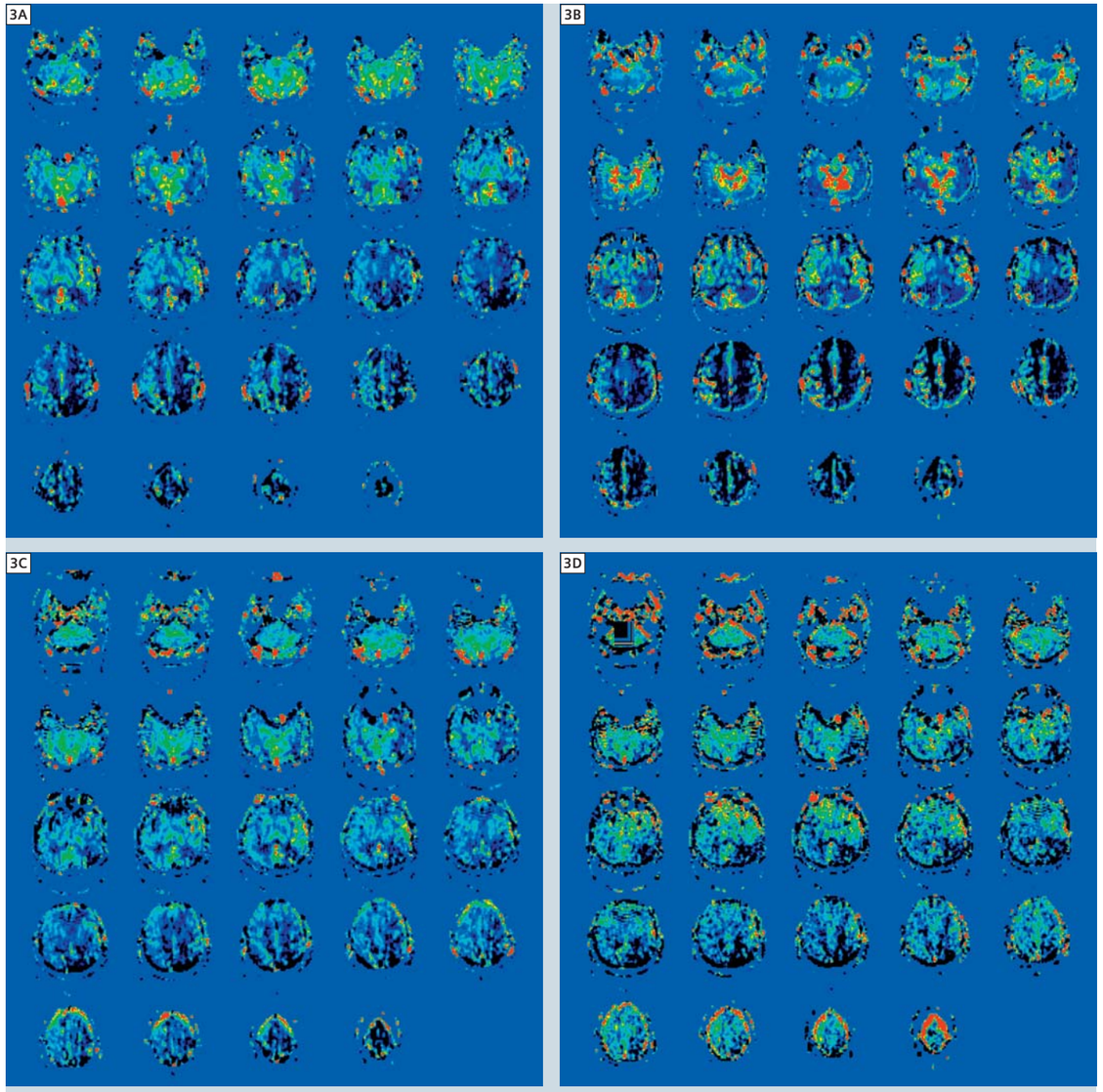

3 *syngo* ASL exam with different delays of blood labelling: 1.1 **(3A),** 1.5 **(3B),** 1.9 **(3C)** and 2.3 **(3D)** seconds. There is progressively more perfusion seen on the studies performed at 1.5 and 2 seconds after arterial labeling compared to the perfusion obtained 1.1 second after arterial labelling, suggesting that there is a delayed transit time into the left hemisphere secondary to the patient's carotid occlusion on that side.

syngo BreVis – Efficient and Standardized Workflow for Breast MRI

Pascal A. T. Baltzer, M.D.; Matthias Dietzel, M.D.; Ramy Zoubi; Tibor Vag, M.D., Ph.D.; Werner A. Kaiser, M.D., M.S.

Institute of Diagnostic and Interventional Radiology, Friedrich-Schiller-University Jena, Jena, Germany

Background

Breast MR imaging is worldwide an important diagnostic tool. It has shown the highest sensitivity for detection of breast cancer by successfully performing in clinical as well as in high-risk screening scenarios [1-3]. To achieve the best possible specificity, a standardized approach on breast MRI analysis applying a variety of descriptors (or signs) using standardized vocabulary should be performed. Furthermore, the implementation of new techniques (e.g. diffusion-weighted imaging (DWI), computer assisted (CAD) evaluation) is promising. Ongoing developments also center on cost reduction and optimizing workflow. This includes the use of open-bore systems for improved patient comfort and also software tools for streamlining the reading process.

Analysis of breast MRI examinations might be divided into 3 tasks:

1. Lesion detection
2. Lesion differentiation
3. Reporting lesion type, size and position

Lesion detection is rather straightforward in breast MRI, as malignant lesions exceeding 2–3 mm in size enhance on post-contrast images based on the paradigm of neoangiogenesis. The truth of this paradigm is underlined by the exceptional high negative predictive value of breast MRI. Even noninvasive cancers (ductal carcinoma in situ, DCIS) can be detected by MRI in the majority of cases [4, 5]. The most complex task in the analysis of breast MRI is lesion differentiation. There is good agreement in the literature on an approach that combines the analysis of dynamic enhancement patterns with the analysis of morphological criteria [6-9]. This is done to account for overlapping dynamic and morphologic features between benign and malignant lesions. In our experience, a standardized layout (or hanging protocol) showing native, early and delayed phase T1-weighted as well as T2-weighted images at standardized window/center settings enables the reader to assess both dynamic and morphologic lesion features at the same time. This approach also increases diagnostic certainty, leading to improved specificity. The last task to be performed in the analysis of breast MRI is to report lesion type, size and position. For breast surgeons, the reporting of a lesion position in a clock face scheme is beneficial as most of them are familiar with ultrasound orientation. In order to identify the exact location of a lesion in relation to the nipple, 3D reconstructions like maximum intensity projections or multiplanary reconstructions are helpful. Finally, reporting should be as short and precise as possible, making use of standardized descriptive vocabulary as proposed in the MRI BI-RADS lexicon of the ACR [6].

syngo BreVis features

syngo BreVis improves reading of breast MRI by means of several features. First, a study is opened by simply double clicking it in the patient browser. A layout is applied, loading imaging series at preset window/center levels into preset segments. A spatially synchronized crosshair marker can be used to identify even the smallest lesions in all segments populated with different contrast series and dynamic time points simultaneously. Furthermore, this marker can be used to measure signal intensity/time (SI/t) curves which are displayed in a separate segment. Spare segments may show multiplanar reconstructions of 3D data sets and/or additional imaging series like DWI images at different b-values or ADC maps. If needed, all segments can be re-specified to accommodate the individual reader's preferences. The dual monitor configuration of the *syngo* BreVis Multi-Modality-Workplace (MMWP) workstation allows the display of various images and data to accommodate most if not all clinical needs for the analysis of breast MRI.

A special feature of *syngo* BreVis is semi-automatic dynamic-enhancement pattern analysis. Based on one unenhanced, one early and one delayed-enhanced image series, enhancement patterns of all pixels are automatically analyzed. Results are given as a color-coded parametric map showing whether early enhancement is slow, intermediate or fast and whether delayed enhancement curve type shows Washout, Plateau or Persistent enhancement [6]. Thresholds and time points for these general classifications can be preset based on empirical experience and default settings, but additionally – unlike other comparable systems – can be adjusted simply by moving a slider. Thus, both navigation through complicated menus and additional postprocessing time are avoided. This feature is especially important in the clinical setting, where biologic conditions may vary (e.g. after neoadjuvant chemotherapy or reduced cardiac output of the patient) and errors (e.g. delayed contrast agent injection by the technologist) do occur. For the scientific setting, preset values provide standardized measurement conditions for dynamic enhancement data. The data displayed on the color-coded map can be analyzed further by semi-automatically identifying the most suspicious enhancing area of a lesion. This is done by simply drawing a volume of interest (VOI) around a color-coded lesion. Volumetric data on voxel percentages of enhancement, curve type distribution and the lesion volume are also obtained. It is important to note in this context that the software offers also image registration for elastic 3D motion artifact correction. Finally, *syngo* BreVis enables the user to save and report findings based on the MRI BI-RADS (Breast Imaging Reporting And Data System) lexicon from the American

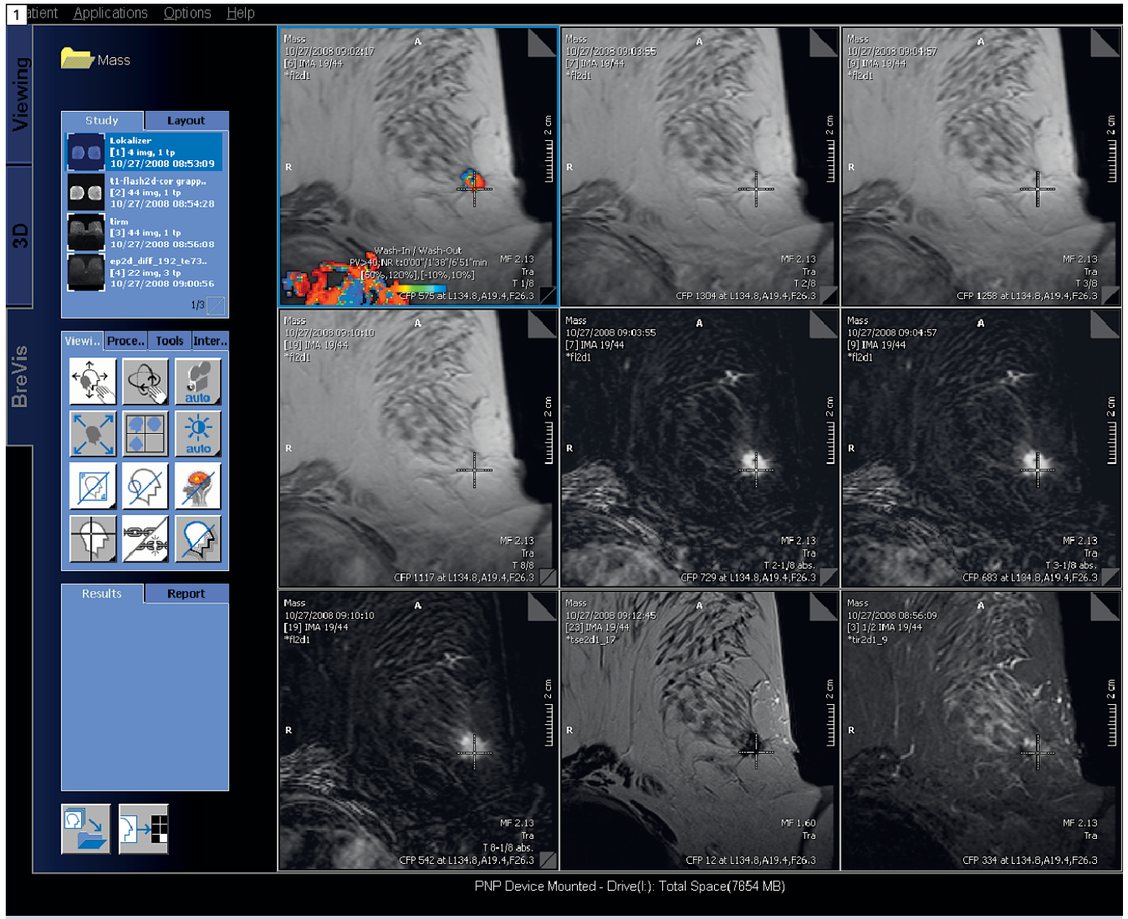

1 *syngo* BreVis workspace with customized layout used at the Institute of Diagnostic and Interventional Radiology, University Hospital of Jena. Segments from upper left to lower right show: pre-contrast T1w (FLASH 2D) with superimposed color-coded enhancement map (can be turned off), 1st, 2nd and 5th dynamic T1w scan, followed by corresponding subtraction images at corresponding time points. Final segments show T2w TSE and TIRM images. Morphologic and enhancement pattern analysis can be performed on one view: mass lesion with spiculated borders, inhomogeneous enhancement pattern, positive blooming phenomenon and dark in T2w. Kinetic analysis (visual and color-coded map) shows initially strong enhancement followed by washout. According to MRI BI-RADS, this lesion is highly suspicious for malignancy (BI-RADS V). Histology revealed invasive ductal cancer G2.

2

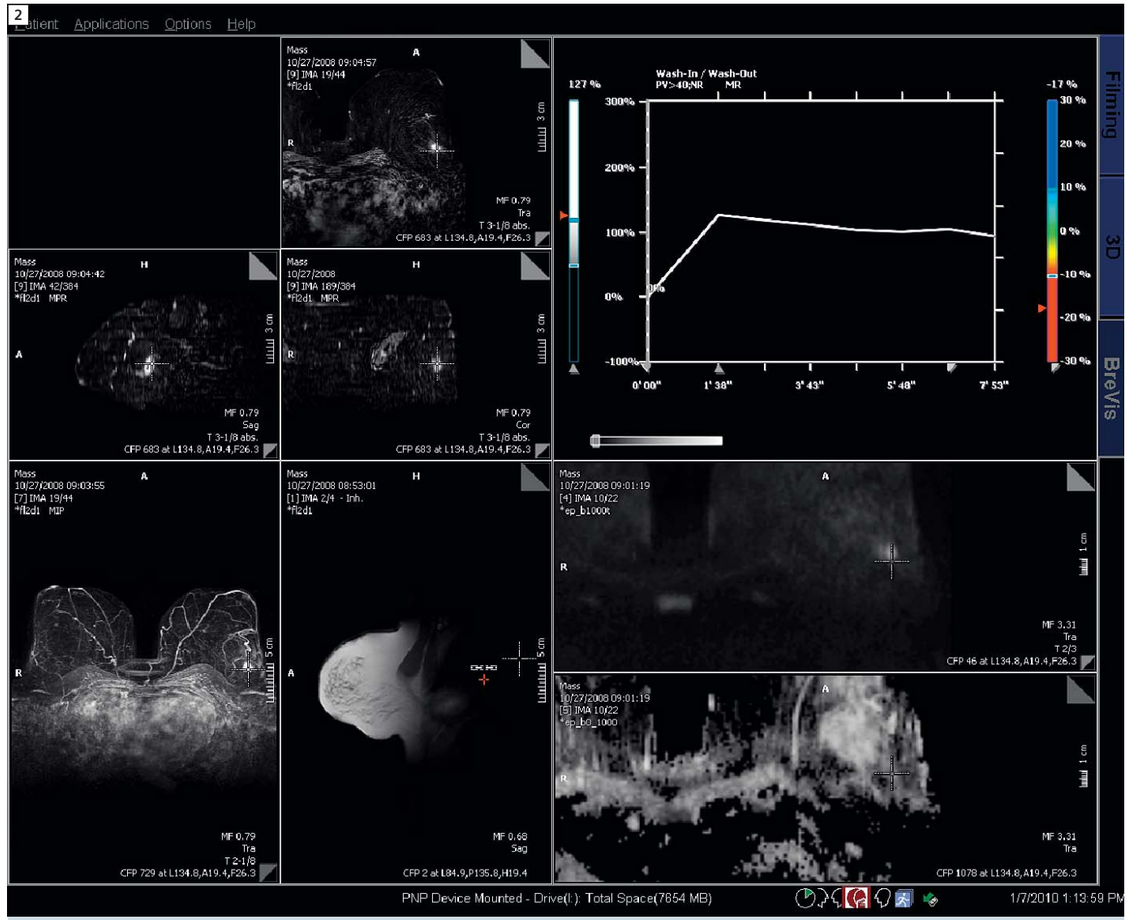

2 *syngo* BreVis workspace showing multiplanar reconstruction (MPR) of T1w subtraction images showing the lesion in the outer lower quadrant at 4 o'clock. Left lower segment with maximum intensity projection of contrast-enhanced subtraction (T1w) reveals a unilateral pathological increase in vasculature besides the enhancing lesion. The upper right segment displays signal intensity/time curve as well threshold controls. Curve type information is given in numbers (127% initial enhancement, 17% Washout). The lower right segments show the DWI image at b = 1000 together with the corresponding ADC map. Diffusivity in the lesion is restricted (1.08 x 10^{-3} mm^2/s), which is typical for invasive cancer.

College of Radiology (ACR). Several opportunities are given to export the results.

Our clinical experience with *syngo* BreVis

At our university hospital, both research as well as pure clinical examination breast MRI protocols are in use (>1500–2000 examinations/year). Clinical examinations are performed on a 1.5T MAGNETOM Avanto and research examinations are conducted on both a 1.5T MAGNETOM Avanto and a 3T MAGNETOM Trio with Tim. The basic clinical protocol at 1.5T includes an axial bilateral dynamic 2D gradient echo sequence. 44 slices with a thickness of 3 mm cover the whole breast without gaps at an in-plane resolution of 1.1 x 0.9 mm (see table 1). Acquisition time is 1 minute and this sequence is repeated to obtain six timepoints (fist scan native). Afterwards, a high spatial resolution (in plane resolution 0.7 x 0.9 mm) T2w sequence (see table 1) as well as a Turbo Spin Echo Inversion Recovery sequence (TIRM, see table 1) with identical slice positions are acquired. The advantage of this protocol is high and stable image quality with reasonable data size to be read and post process in clinical routine. As all important series are acquired in the same slice positions, linked segment reading of different contrasts and dynamic time points is possible even without *syngo* BreVis. Another advantage is the short effective magnet time of 12–14 minutes. This imaging protocol enables examination of 4 patients per hour and thus 40–50 patients per day and per scanner. This is routinely performed at our institution with one radiologist supervising, reading and reporting all examinations. However, this workflow is challenging as one examination has to be read and reported while the next examination is acquired in order to avoid serious delays or the need for further workforce.

Given the described protocol, *syngo* BreVis is able to handle these amounts of data at transfer and preprocessing times acceptable in the clinical setting. Before *syngo* BreVis, our layout, consisting of 9 segments showing dynamic images (time point 0, 1, 2 and 5 together with corresponding subtractions), T2w-TSE and TIRM images required loading as well as windowing/centering of all single series, a task which is now performed simply by double clicking the examination. Although the color-coded map is not necessary for differential diagnosis, it can help in cases with multiple lesions or background enhancement. The same can be said for motion correction, which is not needed regularly, but can be helpful in single cases. The research scenario differs from the one described above in several ways. Here, a variety of dynamic protocols, including high temporal and/or spatial resolution dynamic sequences in 2D or 3D techniques, in part with fat saturation, are performed. As a result, fewer patients are examined, but much more data is acquired per patient. *syngo* BreVis is able to handle these amounts of data and even automatically detects double dynamic imaging (split dynamics) protocols. Volumetric data measurements are useful for a wide variety of purposes and analysis methods can be systematically performed and varied. The additional display segments easily allow the review of supplemental (e.g. DWI) data together with dynamic as well as morphologic analysis.

3

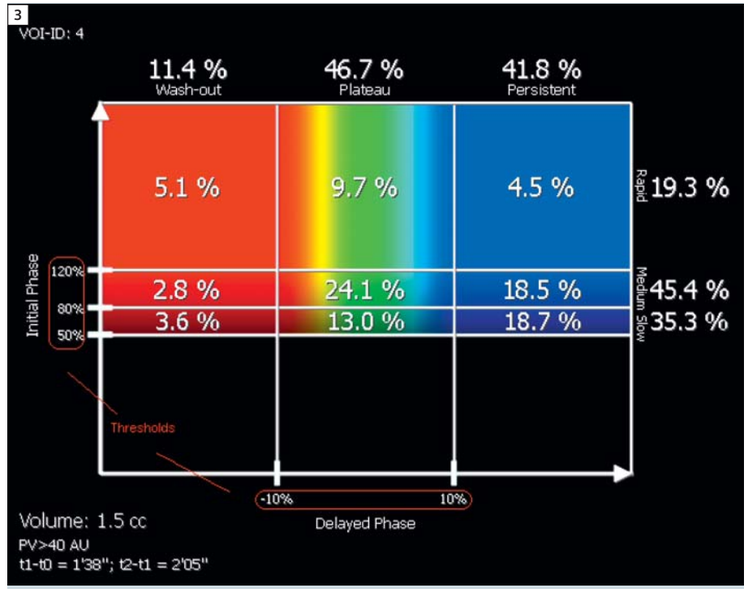

3 Volume of Interest (VOI) statistics: besides the color-coded volume (lower left), percentages for all curve types applying given thresholds are displayed. Note that all thresholds can be varied without additional calculation time.

4

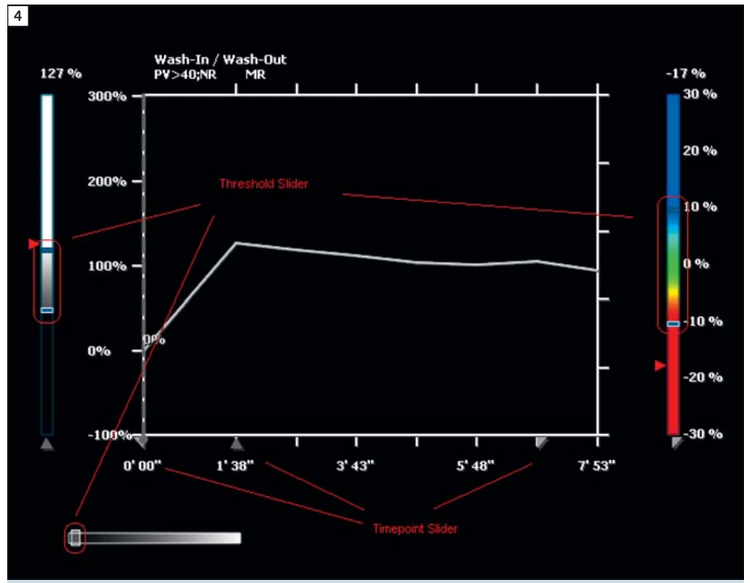

4 Signal intensity/time curve segment from region-of-interest (ROI) analysis: time point markers (x-axis), thresholds for initial (left) and delayed (right) enhancement phase are shown and can be varied without additional computational time. The AU threshold regulator in the lower left corner can be adjusted to reduce noise in the color-coded map (c.f. recommendations table 1 and table 2).

Table 1: Basic FLASH 2D 1.5 Tesla (MAGNETOM Avanto) protocol with suggested *syngo* BreVis thresholds.

	TR	TE	Flip angle	*syngo* GRAPPA	fatsat	TA (min.)	Repet.	Slices	voxel size (mm)	*syngo* BreVis thresholds
T1w FLASH 2D	106	4.56	80	2	None	01:03	6	44	1.1 x 0,9 x 3	40%/80%/120%*
T2w TSE	8900	193	150	2	None	2:15	1	44	0.8 x 0.7 x 3	n.a.
TIRM	2770	73	150	2	TI 150 ms	1:58	1	44	1.1 x 0.9 x 3	n.a.

*AU threshold of 300 recommended; delayed enhancement threshold for Washout/Plateau/Persistent: +/-10%

Table 2: Basic 3D VIBE 3Tesla (MAGNETOM Trio, A Tim System) protocol with suggested *syngo* BreVis thresholds.

	TR	TE	Flip angle	*syngo* GRAPPA	fatsat	TA (min.)	Repet.	Slices	voxel size (mm)	*syngo* BreVis thresholds
T1w VIBE	4,09	1,54	6	2	SPAIR	01:00	6	88	0,8 x 0,7 x 2	50%/100%/150%*
T2w TSE	15740	196	90	3	none	03:10	1	88	0,9 x 0,7 x 2	n.a.
TIRM	4460	81	90	2	TI 230 ms	03:36	1	88	1.4 x 1.1 x 2	n.a.

*AU threshold of 200 recommended; delayed enhancement threshold for Washout/Plateau/Persistent: +/-10%

Conclusion

syngo BreVis is a helpful software tool for improved workflow in both the clinical and research setting. Its advantages are robust performance, simple operation and the possibility for individual adjustments. The latter allows for compensation of unexpected clinical and technical variations which are encountered in daily clinical routine.

Acknowledgement

This article was written in collaboration with Dr. Christian Geppert; Karoly Kiss from Siemens Healthcare and Dr. Markus Michelbrink from MeVis BreastCare GmbH & Co. KG.

References

1 Houssami, N., et al., Accuracy and surgical impact of magnetic resonance imaging in breast cancer staging: systematic review and meta-analysis in detection of multifocal and multicentric cancer. J Clin Oncol, 2008. 26(19): p. 3248-58.
2 Peters, N.H., et al., Meta-analysis of MR imaging in the diagnosis of breast lesions. Radiology, 2008. 246(1): p. 116-24.
3 Warner, E., et al., Surveillance of BRCA1 and BRCA2 mutation carriers with magnetic resonance imaging, ultrasound, mammography, and clinical breast examination. Jama, 2004. 292(11): p. 1317-25.
4 Kuhl, C.K., et al., MRI for diagnosis of pure ductal carcinoma in situ: a prospective observational study. Lancet, 2007. 370(9586): p. 485-92.
5 Vag, T., et al., Diagnosis of ductal carcinoma in situ using contrast-enhanced magnetic resonance mammography compared with conventional mammography. Clin Imaging, 2008. 32(6): p. 438-42.
6 Ikeda, D.M., et al., MRI Breast Imaging Reporting And Data System Atlas. 2003: 1 ed. Reston: American College of Radiology.
7 Kaiser, W., Signs in MR-Mammography. Vol. Auflage: 1. 2007, Berlin: Springer.
8 Malich, A., et al., Potential MRI interpretation model: differentiation of benign from malignant breast masses. AJR Am J Roentgenol, 2005. 185(4): p. 964-70.
9 Schnall, M.D., et al., Diagnostic architectural and dynamic features at breast MR imaging: multicenter study. Radiology, 2006. 238(1): p. 42-53.

Contact
Dr. med. Pascal A. T. Baltzer
Institute of Diagnostic and Interventional Radiology
Friedrich-Schiller-University Jena
Erlanger Allee 101
D-07740 Jena
Phone: +49-3641-935661
Fax: +49-3641-9324832
pascal.baltzer@med.uni-jena.de

Relevant clinical information at your fingertips

From technology to clinical applications, you will find all the latest news about Women's Health at Siemens MR at

www.siemens.com/magnetom-world

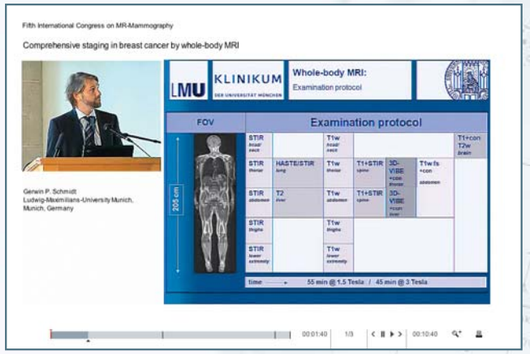

Don't miss the talks of international experts on Magnetic Resonance Mammography (MRM) that Professor Kaiser brought together in Jena to discuss all aspects of this novel imaging modality:

Go to International Version > Education > e-trainings & Presentations

The centerpiece of the MAGNETOM World Internet platform consists of our users' clinical results. Here you will find case reports, application tips and clinical methods:

Go to International Version > Clinical Corner

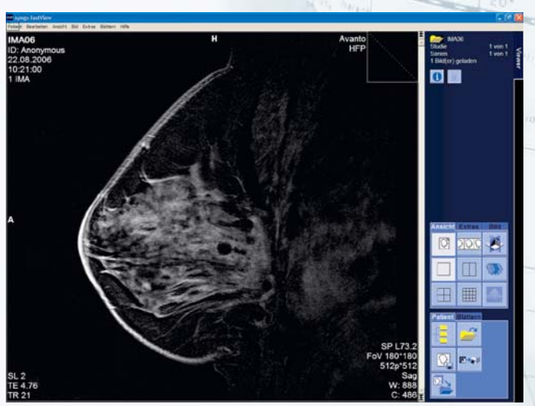

Just a mouse click away you will find protocols and useful tips allowing you to optimize your daily MR examinations:

Go to International Version > Phoenix Gallery

For the whole range of clinical MR information visit us at
www.siemens.com/magnetom-world
Go to
International Version

Not for distribution in the US.

Not for distribution in the US.

Preoperative Diagnosis of Ovarian Disease by In Vivo MR Spectroscopy

Peter Stanwell, Ph.D.; Carolyn E. Mountford, D.Phil.

Centre for Clinical Spectroscopy, Department of Radiology, Brigham & Women's Hospital, Harvard Medical School, Boston, USA

Background

Ovarian cancer is the most frequent cause of death from gynaecologic malignancy in the Western world with one in 55 women developing ovarian cancer in their lifetime [1]. Up to 50% of women diagnosed with ovarian malignancy will not survive their disease [2]. This high mortality is due to the high proportion of women who are diagnosed with advanced stage disease [3, 4]. Disease stage at diagnosis is a key factor in predicting patient prognosis [2, 4]. Patients with early stage ovarian cancer (FIGO stage I-II) have 5-year survival rates of 84% and may not require adjuvant chemotherapy [5, 6]; however patients with advanced disease (FIGO stage III–IV) have a 5-year survival rate of only 29% [2].
Ovarian cancer is staged surgically, based on the International Federation of Obstetrics and Gynaecology (FIGO) system [5] and takes into account the primary mechanisms of spread of ovarian cancer (i.e. local extension, intraperitoneal seeding, lymphatic invasion and haematogenous dissemination [7]. However there is substantial evidence that the recommended surgery for ovarian cancer is often not performed [8, 9], especially when the preoperative diagnosis is that of a benign process [7] or performed by either a general surgeon or gynecologist [8, 9]. Accordingly, it has been shown that patients managed in a specialist gynecologic oncology unit have better outcomes [10].
Presently women with a clinical suspicion of ovarian malignancy are assessed with a pelvic examination, analysis of serum tumor markers and pelvic ultrasonography (transvaginal and/or tansabdominal) [4, 7]. However all these techniques suffer from limitations [4, 11, 12] that ultimately result in only about 25% of ovarian cancers being early stage (FIGO stage I) when diagnosed [2].
Radiologic imaging plays a significant role in the detection and characterisation of ovarian masses. Ultrasound remains the primary modality for initial evaluation of adnexal masses [13, 14] with CT being the standard for staging, monitoring response to treatment, and assessing for resectability and detecting recurrence [15]. Contrast-enhanced MRI may be helpful in cases of complex ultrasound findings [16, 17]; especially in pre-menopausal women or when serum markers are not raised [17]. PET is currently not recommended for routine diagnostic procedures but may have a role in assessing recurrent disease [18, 19]. However, no imaging modality currently allows for the detection of microscopic spread of ovarian cancer and a full staging laparotomy is required for accurate cancer staging [20].
Proton (1H) magnetic resonance spectroscopy (MRS) reports on tumor biochemistry and metabolism [21, 22] and can be undertaken in vivo using the same hardware used in MR imaging. It has been shown that ex vivo 1H MRS of biopsied ovarian tissue can distinguish between malignant and benign tissues [23–25]. Several recent studies have shown the utility of MRS undertaken on pelvic lesions including MRS of the ovary and cervix [26–28]. We have demonstrated that it is possible to acquire in vivo 1H MRS data at 3T and that this data may be used to preoperatively characterize ovarian tumors thus allowing for the triaging of patients to appropriate medical specialists [29].

Methods

Pelvic imaging for lesion localization was performed on a whole-body 3T clinical scanner (MAGNETOM Trio, Siemens Healthcare, Erlangen, Germany) in conjunction with an eight-element phased-array surface coil (USA Instruments, Aurora, USA). Patients were examined in the supine position and MR imaging consisted of orthogonal imaging to identify and define the ovarian mass which in turn allowed for the accurate placement of each individual spectroscopy voxel. T2-weighted (T2w) turbo-spin echo images were obtained in the axial, sagittal, and coronal planes (TE 98 ms, TR 4000 ms, FOV 22 cm, matrix 266 x 512, slice thickness 3 mm) while T1w spin echo (SE) images were also obtained in the axial plane in the same slice locations as the T2w acquisition (TE 25 ms, TR 450 ms, FOV 22 cm, matrix 224 x 448, slice thickness 3 mm).
Single voxel spectroscopy (SVS) measurements of ovarian tumors were undertaken following identification of lesions on orthogonal imaging. Spectroscopy was performed in the axial plane with each voxel carefully placed to sample the ovarian mass without contamination from surrounding tissues as assessed from orthogonal imaging. Any areas of haemorrhage were avoided.
All spectra were acquired using a double spin-echo, slice-selective technique (PRESS) [30], an echo time of 135 ms, a repetition time of 2000 ms, and 192 signal averages. This echo time of 135 ms was chosen to reduce the amplitude of the lipid and water signals through natural T2 relaxation effects as well as to facilitate the identification of lactate that has previously been suggested as a diagnostically important metabolite from previous in vivo studies of ovarian neoplasms [26, 27].
Magnetic field homogeneity adjustment was initially undertaken using the automated shimming program provided by the manufacturer. Following successful completion of prescan parameters the quality of the localized shim was checked and manually improved where possible with the results recorded for assessment of final MRS quality.
Spectral processing and spectral reconstruction was performed using software provided by the manufacturer (*syngo*, Siemens Healthcare, Erlangen, Germany) and consisted of: water referencing (frequency shift correction) and Gaussian lineshape fitting (8 Hz) of the time domain signal followed by fast Fourier transformation and then phase correction (automatic zero-order phase correction and manual first-order phase correction) where necessary.
Semi-quantitative spectroscopic analysis of tumors was performed after assessing the signals from lactate (1.31 ppm),

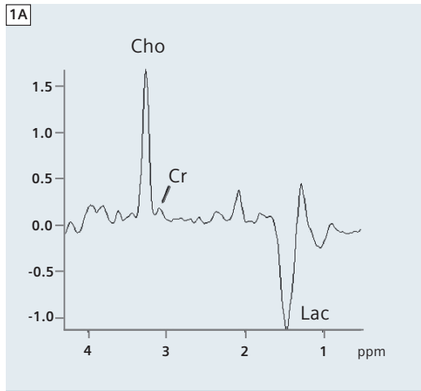

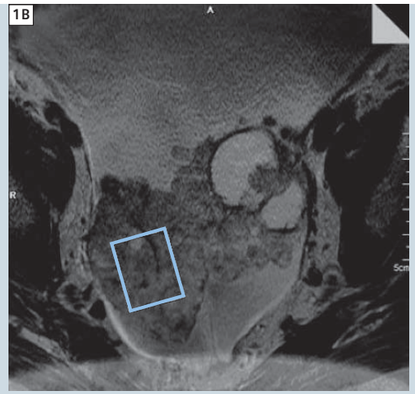

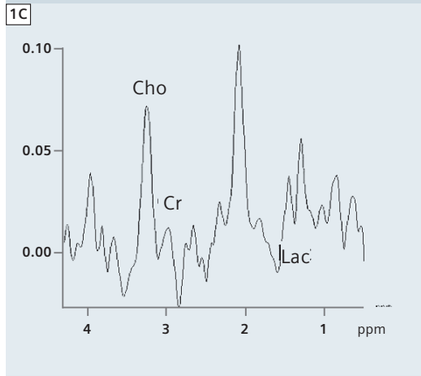

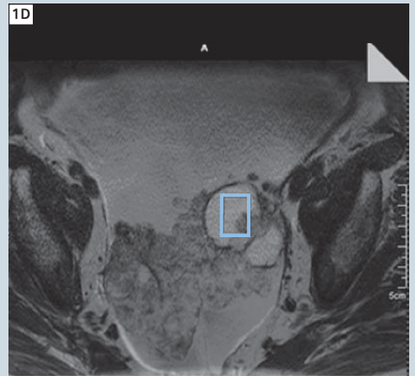

1 High grade serous carcinoma with metastatic spread. **A:** TE 135 ms, TR 2000 ms, 192 scans. Prominent resonances corresponding to choline-containing compounds (3.23 ppm), creatine (3.04 ppm) and an inverted resonance at 1.31 ppm corresponding to lactate. **B:** Axial T2w (TE 98 ms, TR 4000 ms) image with voxel location shown. **C:** TE 135 ms, TR 2000 ms, 192 scans. Resonances corresponding to choline-containing compounds (3.23 ppm), creatine (3.04 ppm) and an inverted resonance at 1.31 ppm corresponding to lactate. **D:** Axial T2w (TE 98 ms, TR 4000 ms) image with voxel location shown.

Not for distribution in the US.

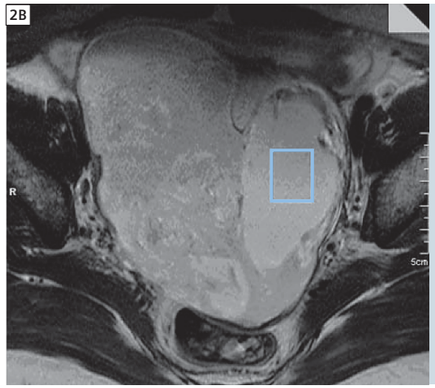

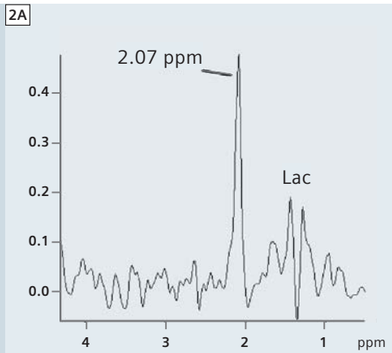

2 Mature cystic teratoma (cystic portion).
A: TE 135 ms, TR 2000 ms, 192 scans. Prominent resonances at 2.07 ppm (consistent with N-acetylasparate or sialic acid [29]) and an inverted resonance at 1.31 ppm corresponding to lactate.
B: Axial T2w (TE 98 ms, TR 4000 ms) image with voxel location shown.
Taken from Stanwell et al. [29] with permission.

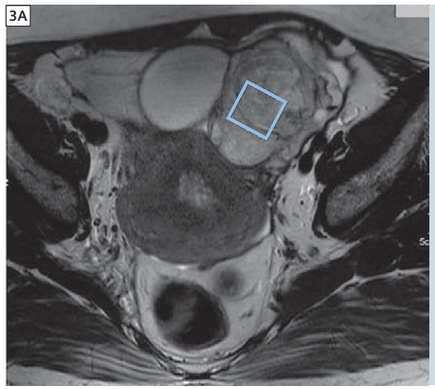

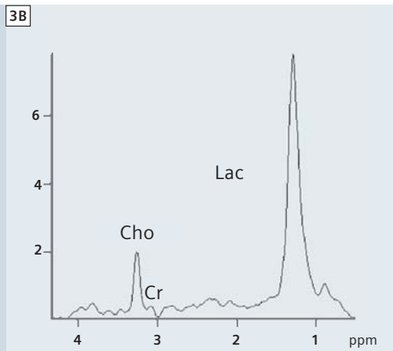

3 Clear cell carcinoma.
A: Axial T2w (TE 98 ms, TR 4000 ms) image with voxel location shown.
B: TE 135 ms, TR 2000 ms, 192 scans. Prominent resonances corresponding to choline-containing compounds (3.23 ppm) and creatine (3.04 ppm).

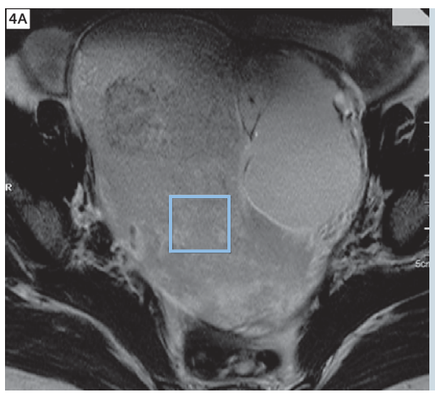

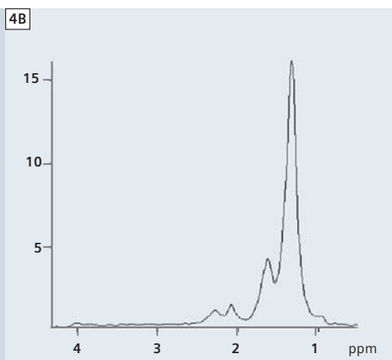

4 Mature cystic teratoma (solid portion).
A: Axial T2w (TE 98 ms, TR 4000 ms) image with voxel location shown.
B: TE 135 ms, TR 2000 ms, 192 scans. Prominent resonances corresponding lipid and an unknown resonance at 2.07 ppm.
Taken from Stanwell et al. [29] with permission.

Not for distribution in the US.

lipid (1.33 ppm), creatine (3.04 ppm), choline containing compounds (3.23 ppm) and other prominent metabolite signals. The area under specific resonances (integrals) were determined assuming Gaussian fits for lipid (Lip), creatine (Cr), and choline-containing compounds (Cho), and j-coupled fit for lactate (Lac). The ratio of Cho/Cr was calculated for each voxel studied. Elevation of this ratio has previously been reported in studies of many human cancers including breast [31]; thyroid [32]; prostate [33]. The presence of lactate, lipid and other prominent metabolites were also examined for their significance [29].

Histopathology

Each excised tumor was fixed in 10% buffered formalin, paraffin embedded, sectioned at 5 µm and stained with haematoxylin and eosin according to a standard protocol. Correlation was then made with the detailed pathology reports of the tertiary referral hospital from which the patients were recruited. Tumor sub-types were identified according to the WHO Histological Classification of Ovarian Tumors [34].
We have now completed two studies of which one is reported and the other an honors thesis where a further 7 cases were examined (unpublished data). In both these studies the presence of a Cho/Cr ratio greater than, or equal to

Table 1: Summary of patient age, histologic findings, lesion size, and clinical presentation in 14 ovarian tumors.

Patient No.	Age (yrs)	Pathology	Size (mm)	Clinical
1.	81	High-grade poorly differentiated serous carcinoma	60 x 40 x 25	Rectal bleeding; ↑CA-125 (197)
2.	47	High-grade serous carcinoma	80 x 50 x 35	↑CA-125; vaginal discharge; mass on US
3.	45	Ovarian endometrioma	50 x 20 x 15	↑CA-125 (208); complex mass on US
4.	47	Moderately differentiated clear cell carcinoma	105 x 90 x 100	Mass on US
5.	45	Serous adenocarcinoma with pelvic metastases (pouch of Douglas)	80 x 55 x 45	↑CA-125; solid mass on US
6.	57	High grade serous carcinoma with pelvic (small bowel mesentery) metastases	40 x 35 x 20	↑CA-125 (365); abdominal bloating
7.	45	Mature cystic teratoma	140 x 120 x 60	Cystic mass on US
8.	56	High grade serous carcinoma with pelvic (omentum) and abdominal (spleen) metastases	80 x 80 x 55	↑CA-125 (>700); complex mass on US
9.	53	Mature teratoma (struma ovarii)	110 x 110 x 70	Mass on US
10.	43	Benign serous cystadenoma	95 x 80 x 70	Bilateral complex masses on US
11.	69	Benign serous cystadenofibroma	65 x 30 x 25	Menorrhagia; bilateral ovarian masses
12.	71	Benign serous cystadenofibroma	130 x 120 x 80	CA-125 (350); large ovarian mass
13.	43	High-grade mucinous adenocarcinoma with focal involvement of ovarian surface	150 x 110 x 90	↑CA-125 (440); complex ovarian mass on US
14.	38	Mature cystic teratoma	65 x 60 x 30	CA-125 (25); bowel symptoms

Taken from Stanwell et al. [29] with permission.

Not for distribution in the US.

Not for distribution in the US.

Table 2: Summary of histologic and MR spectroscopic findings in 14 ovarian tumors

Patient No.	Pathology	Solid / cystic	Water FWHM	Choline (Cho)	Cho/ Cr ratio	Lactate
1.	High-grade poorly differentiated serous carcinoma	Solid	9 Hz	+	4.99	–
2.	High grade serous carcinoma	Solid	13 Hz	+	7.87	+
3.	Ovarian endometrioma	Cystic	18 Hz	–	*	–
4.	Moderately differentiated clear cell carcinoma	Solid	11 Hz	+	18.46	–
5.	Serous adenocarcinoma with pelvic metastases (pouch of Douglas)	Solid	10 Hz	+	15.98	–
6.	High grade serous carcinoma with pelvic (small bowel mesentery) metastases	Solid	12 Hz	+	7.68	–
7.	Mature cystic teratoma	Solid Cystic	5 Hz 4 Hz	– –	* *	– +
8.	High grade serous carcinoma with pelvic (omentum) and abdominal (spleen) metastases	Solid Cystic	7 Hz 5 Hz	+ +	9.10 5.05	+ +
9.	Mature teratoma (struma ovarii)	Cystic	7 Hz	+	1.15	–
10.	Benign serous cystadenoma	Cystic	7 Hz	+	1.04	+
11.	Benign serous cystadenofibroma	Cystic	6 Hz	–	*	–
12.	Benign serous cystadenofibroma	Cystic	17 Hz	+	3.13	–
13.	High-grade mucinous adenocarcinoma with focal involvement of ovarian surface	Solid	9 Hz	+	3.09	–
14.	Mature cystic teratoma	Cystic	7 Hz	+	1.09	–

Taken from Stanwell et al. [29] with permission.
– signal not detected above baseline noise level;
+ signal detected above baseline noise level;
* ratio not calculated due to non-detection of choline-containing metabolites.

3.09 was found to indicate that the tumor was likely malignant in nature. In contrast the complete absence of a choline signal, or a Cho/Cr ratio less than, or equal to 1.15 was found to indicate that the tumor was benign in character. Elevation of this ratio is probably due to an increase in choline-containing metabolites though creatine may also increase with malignancy [28, 31, 35]. Choline-containing metabolites are needed for the synthesis of phospholipids in cell membranes, methyl metabolism, transmembrane signaling, and lipid-cholesterol transport and metabolism. These results are consistent with others where elevated levels of choline-containing compounds have been reported in cancer cells [31, 35].

This in vivo MR spectroscopy method offers the possibility of reducing unnecessary radical surgery for younger women with genuinely benign disease who wish to conserve fertility. Further experience, with a larger number and variety of ovarian tumors, should yield an effective tool for pre-operative assessment of ovarian neoplasms that may ultimately lead to more appropriate triaging of patients and better outcomes for sufferers.

References

1 Boyle, P., P. Maisonneuve, and P. Autier, *Update on cancer control in women.* International Journal of Gynecology & Obstetrics, 2000. 70(2): p. 263-303.
2 Chan, J.K., et al., *Patterns and progress in ovarian cancer over 14 years.* Obstetrics & Gynecology, 2006. 108(3): p. 521-528.
3 Tropé, C. and J. Kaern, *Primary surgery for ovarian cancer* European Journal of Surgical Oncology 2006. 32(8): p. 844-852.
4 Bhoola, S. and W.J. Hoskins, *Diagnosis and management of epithelial ovarian cancer.* Obstetrics & Gynecology, 2006. 107(6): p. 1399-1410.
5 Friedlander, M.L., *Prognostic factors in ovarian cancer.* Seminars in Oncology, 1998. 25(3): p. 305-314.
6 Chan, J.K., et al., *Patterns and progress in ovarian cancer over 14 years.* Obstetrics & Gynecology, 2006. 108(3, Part 1): p. 521-528.
7 Ozols, R.F., P.E. Schwartz, and P.J. Eifel, *Ovarian cancer, fallopian tube carcinoma, peritoneal carcinoma,* in *Cancer: principles and practice of oncology,* V.T. De Vita, S. Hellman, and S.A. Rosenberg, Editors. 2001, Lippincott Williams and Wilkins: Philadelphia. p. 1597-1632.
8 Munoz, K.A., L. Harlan, C. , and E.L. Trimble, *Patterns of care for women with ovarian cancer in the United States.* Journal of Clinical Oncology, 1997. 15(11): p. 3408-3415.
9 Earle, C.C., et al., *Effect of surgeon specialty on processes of care and outcomes for ovarian cancer patients*. Journal of the National Cancer Institute, 2006. 98(3): p. 172-180.
10 Engelen MJA, K.H., Willemse PHB, et al., *Surgery by consultant gynecologic oncologists improves survival in patients with ovarian carcinoma.* Cancer, 2006. 106: p. 589-59.
11 Oei, A.L., et al., *Surveillance of women at high risk for hereditary ovarian cancer is inefficient.* British Journal of Cancer, 2006. 94(6): p. 814-819.
12 Partridge, E.E. and M.N. Barnes, *Epithelial ovarian cancer: prevention, diagnosis, and treatment.* CA: Cancer Journal for Clinicians, 1999. 49(5): p. 297-320.
13 Kinkel, K., et al., *US characterization of ovarian masses: a meta-analysis.* Radiology, 2000. 217(3): p. 803-811.
14 Funt, S.A. and L.E. Hann, *Detection and characterization of adnexal masses.* Radiologic Clinics of North America, 2002. 40(3): p. 591-608.
15 Coakley, F.V., *Staging ovarian cancer: role of imaging.* Radiologic Clinics of North America, 2002. 40(3): p. 609-636.
16 Kinkel, K., et al., *Indeterminate ovarian mass at US: incremental value of second imaging test for characterization-meta-analysis and Bayesian analysis.* Radiology, 2005. 236(1): p. 85-94.
17 Sohaib, S.A., et al., *The role of magnetic resonance imaging and ultrasound in patients with adnexal masses* Clinical Radiology, 2005. 60(3): p. 340-348.
18 Rieber, A., et al., *Preoperative diagnosis of ovarian tumors with MR imaging: comparison with transvaginal sonography, positron emission tomography, and histologic findings.* American Journal of Roentgenology, 2001. 177(1): p. 123-129.
19 Nakamoto, Y., et al., *Clinical value of positron emission tomography with FDG for recurrent ovarian cancer.* American Journal of Roentgenology, 2001. 176(6): p. 1449-1454.
20 Woodward, P.J., K. Hosseinzadeh, and J.S. Saenger, *From the archives of the AFIP: radiologic staging of ovarian carcinoma with pathologic correlation.* Radiographics, 2004. 24(1): p. 225-246.
21 Mountford, C., et al., *Proton spectroscopy provides accurate pathology on biopsy and in vivo.* Journal of Magnetic Resonance Imaging, 2006. 24(3): p. 459-477.
22 Mountford, C., et al., *Proton MRS Can Determine the Pathology of Human Cancers With A High Level of Accuracy.* Chemical Reviews, 2004. 104: p. 3677-3704
22 Mountford, C., et al., *Proton MRS Can Determine the Pathology of Human Cancers With A High Level of Accuracy.* Chemical Reviews, 2004. 104: p. 3677-3704
22 Mountford, C., et al., *Proton MRS Can Determine the Pathology of Human Cancers With A High Level of Accuracy.* Chemical Reviews, 2004. 104: p. 3677-3704
23 Mackinnon, W.B., et al., *Characterization of human ovarian epithelial tumors (ex vivo) by proton magnetic resonance spectroscopy.* International Journal of Gynecological Cancer, 1995. 5(3): p. 211-221.
24 Massuger, L.F.A.G., et al., *1H-magnetic resonance spectroscopy: a new technique to discriminate benign from malignant ovarian tumors.* Cancer, 1998. 82(9): p. 1726-1730.
25 Kolwijck, E., et al., *N-acetyl resonances in in vivo and in vitro NMR spectroscopy of cystic ovarian tumors.* NMR in Biomedicine, 2009. 9999(9999): p. n/a.
26 Okada, T., et al., *Evaluation of female intrapelvic tumors by clinical proton MR spectroscopy.* Journal of Magnetic Resonance Imaging, 2001. 13(6): p. 912-917.
27 Hascalik, S., et al., *Metabolic changes in pelvic lesions: findings at proton MR spectroscopic imaging.* Gynecologic and Obstetric Investigation, 2005. 60(3): p. 121-127.
28 Mahon, M.M., et al., *1H magnetic resonance spectroscopy of invasive cervical cancer: an in vivo study with ex vivo corroboration.* NMR in Biomedicine, 2004. 17(1): p. 1-9.
29 Stanwell, P., et al., *Evaluation of ovarian tumors by proton magnetic resonance spectroscopy at three Tesla.* Investigative Radiology, 2008. 43(10): p. 745-751.
30 Bottomley, P.A., *Spatial localization in NMR spectroscopy in vivo.* Annals of the New York Academy of Sciences, 1987. 508: p. 333-348.
31 Glunde, K., C. Jie, and Z.M. Bhujwalla, *Molecular causes of the aberrant choline phospholipid metabolism in breast cancer.* Cancer Research, 2004. 64(12): p. 4270-4276.
32 King, A.D., et al., *In vivo 1H MR spectroscopy of thyroid carcinoma* European Journal of Radiology, 2005. 54(1): p. 112-117.
33 Kurhanewicz, J., et al., *Prostate cancer: metabolic response to cryosurgery as detected with 3D H-1 MR spectroscopic imaging.* Radiology, 1996. 200(2): p. 489-96.
34 Russell, P., S. Robboy, and M. Anderson, *Epithelial/Stromal Ovarian Tumors, in Pathology of the female reproductive tract,* S. Robboy, M. Anderson, and P. Russell, Editors. 2002, Churchill Livingstone: London. p. 539-601.
35 Katz-Brull, R., et al., *Metabolic markers of breast cancer: enhanced choline metabolism and reduced choline-ether-phospholipid synthesis.* Cancer Research, 2002. 62: p. 1966-1970.

Contact
Professor Carolyn Mountford
Centre for Clinical Spectroscopy
Department of Radiology
Brigham & Women's Hospital
Harvard Medical School
4 Blackfan St., HIM-817
Boston, MA 02115
USA
Phone: +1 617 525 5081
cemountford@bics.bwh.harvard.edu

Not for distribution in the US.

Not for distribution in the US.

Proton Magnetic Resonance Spectroscopy of the Breast

Peter Stanwell, RT, Ph.D.[1]; Carolyn Mountford, D.Phil.(Oxon)[1]; Pascal Baltzer, M.D.[2]; Matthias Dietzel, M.D.[2]; Peter Malycha, FRACS[3]; Werner Kaiser, M.D., M.S.[2]

[1]Centre for Clinical Spectroscopy, Department of Radiology, Brigham & Women's Hospital, Harvard Medical School, Boston, USA
[2]Institute of Diagnostic and Interventional Radiology, Friedrich Schiller University Jena, Jena, Germany
[3]Endocrine Surgery, Royal Adelaide Hospital, Adelaide, Australia

Introduction

Contrast-enhanced magnetic resonance imaging has gained acceptance as an important breast imaging modality [11]. However it does not always provide a definitive pathology. In 2007 Lehman [8] reported that magnetic resonance imaging (MRI) could improve on clinical breast examination and mammography by detecting contralateral breast cancer soon after the initial diagnosis of unilateral breast cancer. The study found that the specificity of MRI in this cohort of patients was 88%. Subsequent guidelines from the American Cancer Society for breast screening, with MRI as an adjunct to mammography, reported that, "MRI scans are more sensitive than mammograms, but they are also more likely to show spots in the breast that may or may not be cancer. Often there is no way of knowing whether or not these spots are cancerous short of a follow-up biopsy or some other invasive procedure" [11]. The question now to be addressed is "can the diagnostic accuracy of MRI be improved by adding proton magnetic resonance spectroscopy (MRS)?".

In vivo MRS can be performed along with a conventional MRI study and produces information about the chemical content of the breast, or a distinct breast lesion. Initial studies where in vivo proton MR spectroscopy has been added as an adjunct to dynamic contrast-enhanced MR imaging of the breast have shown promising results and a growing number of research groups are incorporating the technique into their breast MR protocols. The aim of this article is to illustrate the expected examination results and outline some of the pitfalls associated with undertaking a breast MRS examination.
Initially and at 1.5T the diagnosis of breast cancer using MRS, was based on the observation of the choline-containing metabolite (tCho) signal at 3.2 ppm. The resonant frequency of the observed tCho signal has been suggested as having diagnostic potential for discriminating between normal glandular tissue and malignancy [12]. Likewise, quantification of the observed tCho signal has been suggested as means of discriminating between benign and malignant lesions [5] and also for monitoring response to chemotherapy [10].

tChol vs the resolved resonances at 3.23 and 3.28 ppm
Historically the tChol signal was measured because it was not possible to achieve the necessary spectral resolution to separate the resonances. However, recognition of the exact resonant frequency of the tCho signal may be helpful to further distinguish malignant from benign with higher accuracy. In addition, it may help to monitor chemotherapy where the biology is such that some of the component resonances alter while others do not [2, 19]. On current hardware it is possible to process the data such that the tChol signal as well as the choline resonant frequency can be inspected and compared (Fig. 1) [12, 13]. In order to undertake such a comparison there are many experimental aspects to be taken into account.

1

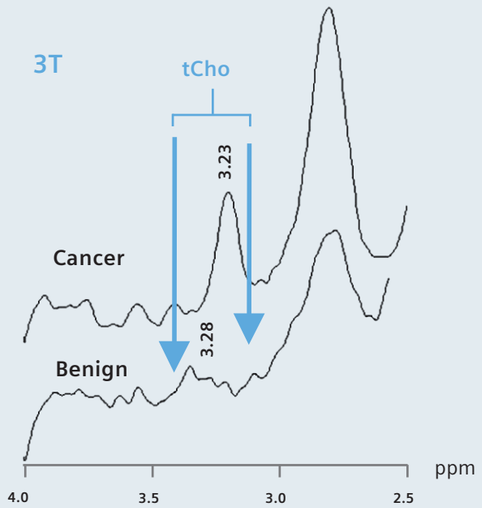

1 In vivo breast single voxel spectra (3T, PRESS, TE = 135 ms / TR = 2000 ms, 192 signal averages). Spectra are processed as described [12, 13] were referenced to the methylene resonance of lipid at 1.33 ppm and water at 4.74 ppm. In the spectrum from the cancer bearing patient (top) the resonance is at 3.23 ppm and consistent with phosphocholine. For comparison, a spectrum derived from a fibroadenoma (bottom) is shown. The total choline "tChol" region is shown in blue.

2

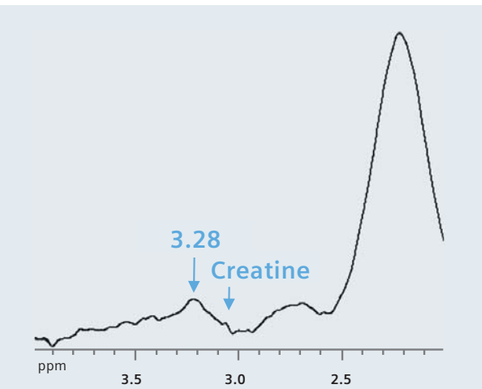

2 In vivo breast single voxel spectrum (1.5T; TR = 135 ms; TE = 2000 ms; 256 averages) of a lesion identified intraoperatively as DCIS with no micro-invasion. Data was processed and referenced as shown in figure 1.

DCIS without micro-invasion

In our experience, there are a small number of cases where the pathology was DCIS with no micro-invasion where the resonance present in this region was at 3.28 ppm.

Size of detectable lesion

With the new MR technologies and coils we are in a better position to interrogate lesion sizes 8 mm and above that need pathological discrimination. Thus an understanding of the significance of the choline resonance detected in vivo is even greater, especially seeing that any detected resonances in this spectral region may have arisen from surrounding "normal" or preinvasive breast tissue and maybe involve processes other than a malignant process (e.g. hormonal).
We and others have demonstrated that 1D MRS can be successfully applied to the breast in vivo, preoperatively and non invasively, giving a diagnosis of breast pathology that distinguishes the categories of malignant, benign, and healthy with a high level of accuracy but these reports were on tumors 1 cm or larger.

Not for distribution in the US.

Experimental concerns

This technology is routinely operational at the sites of the authors. However it should be recognized that the operators of the scanners at both sites are highly trained. Many technical difficulties can and do occur and this requires expertise at the scanner. Below we summarize some of the issues that can be faced in order to produce high quality spectral data.

What you might expect with standard software on the scanner

3A

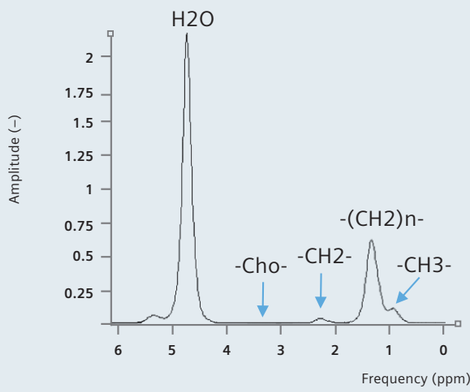

3B

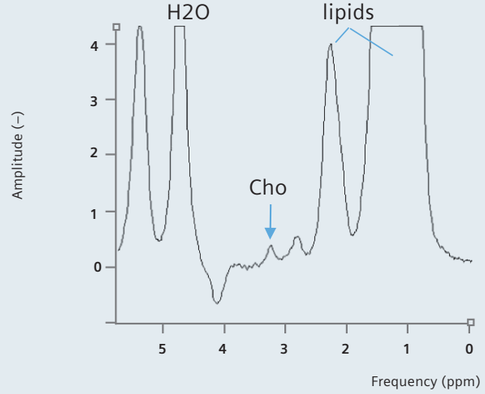

3 Proton single-voxel spectrum acquired with the PRESS sequence (repetition time (TR) 2000 ms, echo time (TE) 135 ms) from glandular tissue in a breast volunteer. **A)** Non-water suppressed spectrum shows strong water and lipid signals and a barely visible choline resonance (arrow). **B)** The vertical display is increased with the choline signal becoming more apparent.

4A

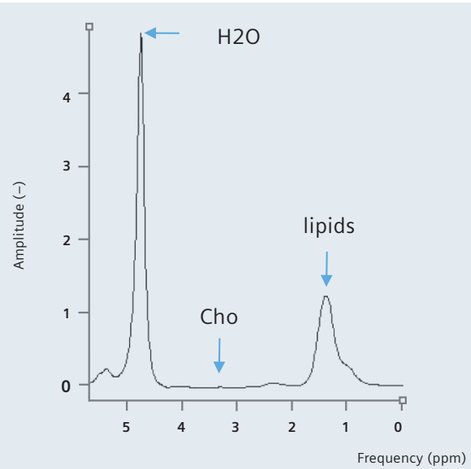

4B

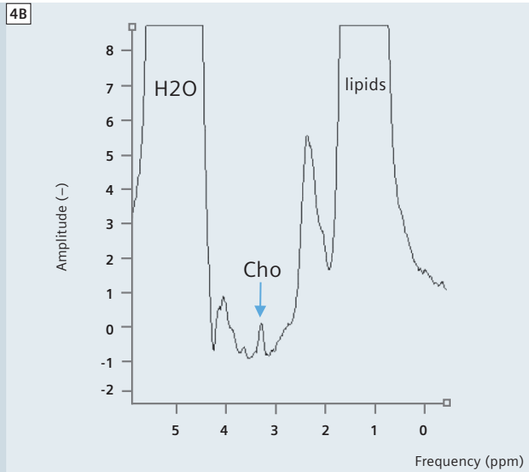

4 Proton single-voxel spectrum acquired with the PRESS sequence (repetition time (TR) 2000 ms, echo time (TE) 135 ms) from a biopsy-proven breast cancer. **A)** Non-water suppressed spectrum shows strong water and lipid signals and a barely visible choline resonance (arrow). **B)** The vertical display is increased with the choline signal becoming more apparent.

Not for distribution in the US.

Shimming

5A

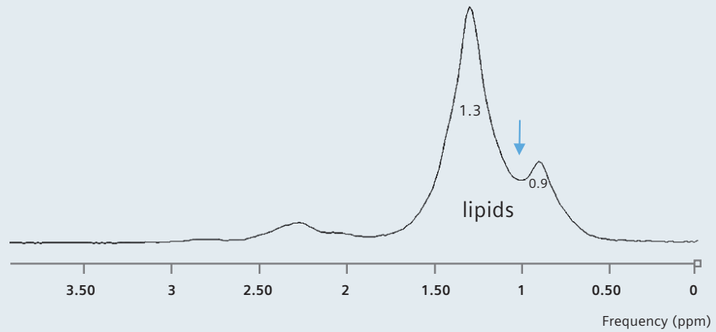

5B

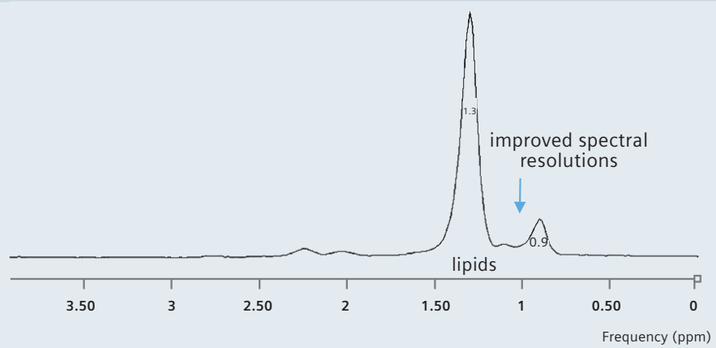

5 Voxel shimming. Proton single-voxel spectrum acquired with the PRESS sequence (repetition time (TR) 2000 ms, echo time (TE) 135 ms) in a breast volunteer.
A) Spectrum was acquired using the automatic shimming program only. Prominent signals are visible from lipids at 0.9 and 1.3 ppm.

B) Spectrum was acquired with the addition of manual shimming. Prominent signals from lipids are again noted (0.9 & 1.3 ppm) but with enhanced spectral resolution with these two peaks now resolved to their baselines.

Referencing

6

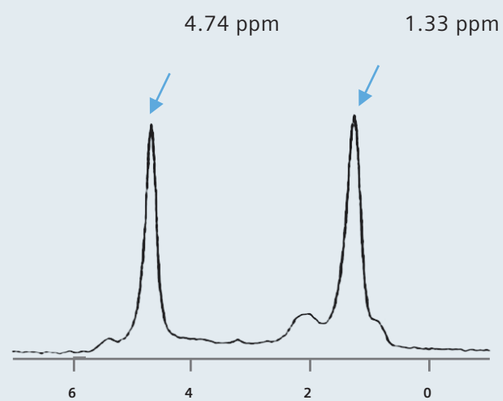

6 Correct referencing is undertaken on the non suppressed water spectrum and provides necessary accuracy which is required to distinguish the 3.23 ppm from 3.28 ppm resonances seen in figures 1 and 2.

Not for distribution in the US.

Not for distribution in the US.

Quantification

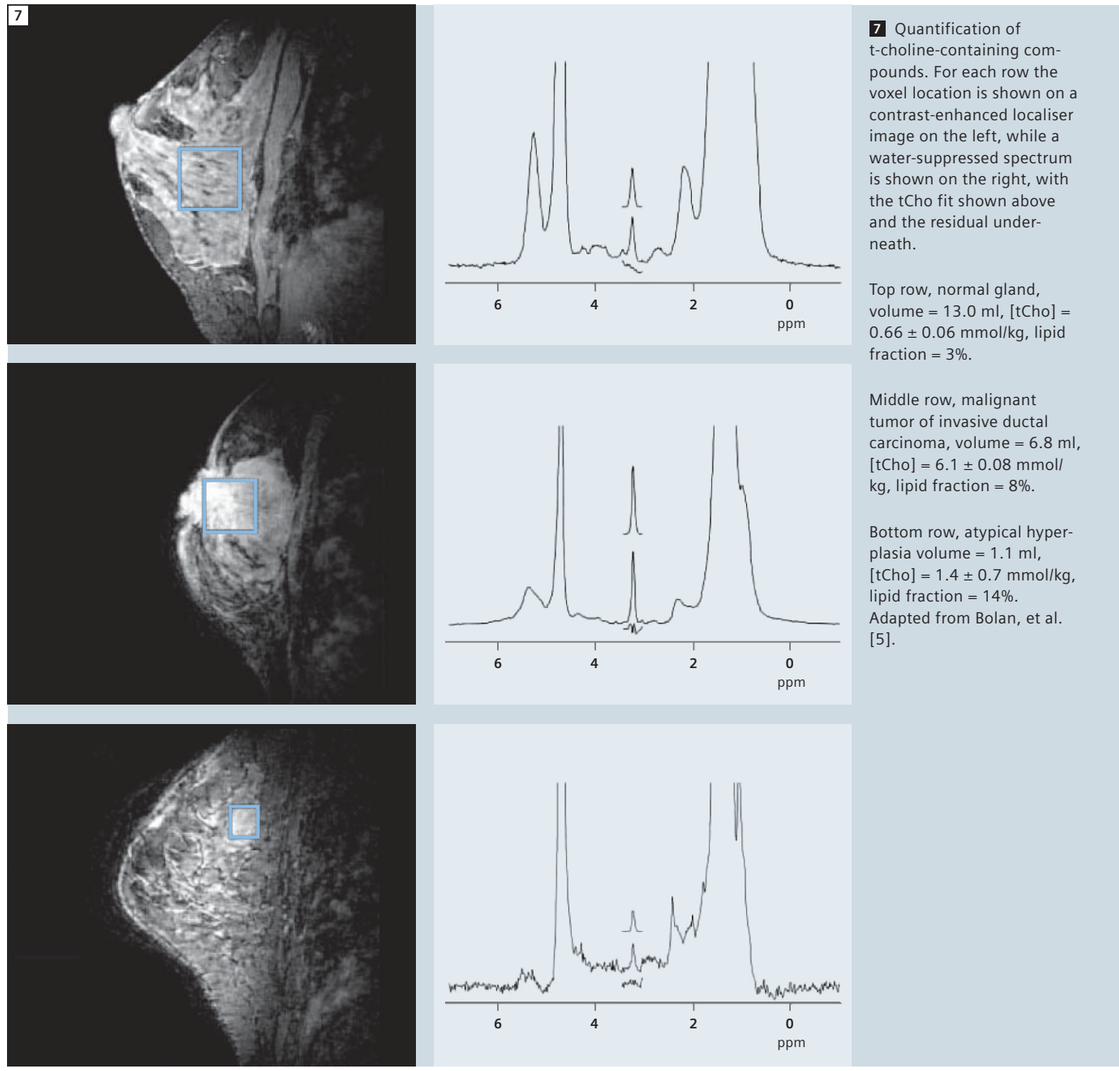

7 Quantification of t-choline-containing compounds. For each row the voxel location is shown on a contrast-enhanced localiser image on the left, while a water-suppressed spectrum is shown on the right, with the tCho fit shown above and the residual underneath.

Top row, normal gland, volume = 13.0 ml, [tCho] = 0.66 ± 0.06 mmol/kg, lipid fraction = 3%.

Middle row, malignant tumor of invasive ductal carcinoma, volume = 6.8 ml, [tCho] = 6.1 ± 0.08 mmol/kg, lipid fraction = 8%.

Bottom row, atypical hyperplasia volume = 1.1 ml, [tCho] = 1.4 ± 0.7 mmol/kg, lipid fraction = 14%. Adapted from Bolan, et al. [5].

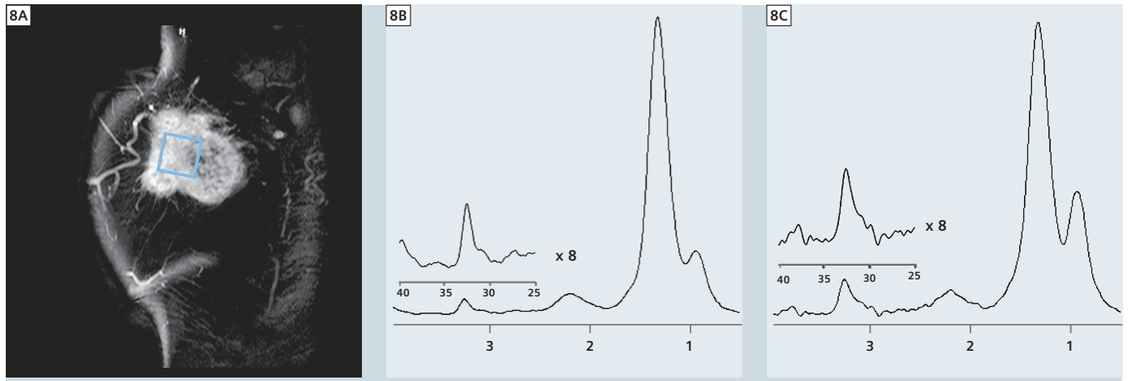

8 Effect of echo time (TE) in breast spectroscopy. Proton single-voxel spectrum acquired with the PRESS sequence from a biopsy-proven breast cancer. **A)** Indicates the voxel placement within the breast cancer. **B)** Single-voxel spectrum acquired with TR of 2000 ms, TE of 135 ms. **C)** Single-voxel spectrum acquired with TR of 2000 ms, TE of 270 ms. Increasing the TE from 135 to 270 ms reduces the amplitude of lipid (at 0.90 and 1.33 ppm) due to increased T2 relaxation [13].

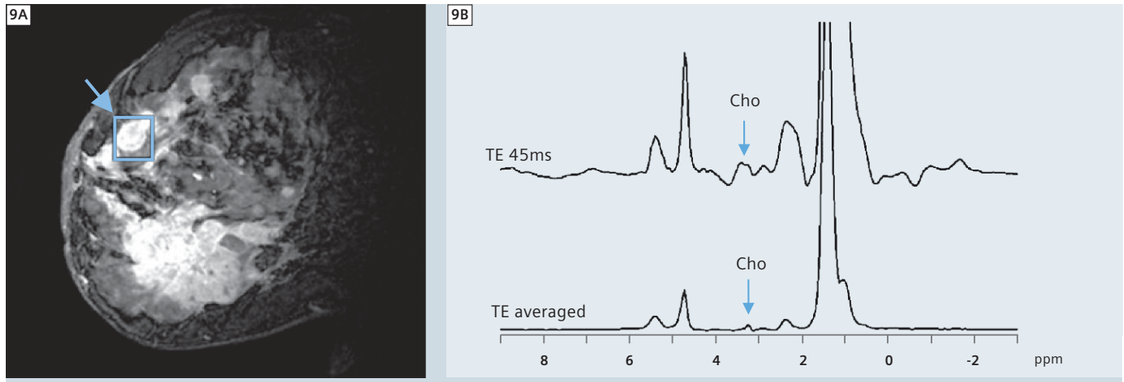

9 Lipid-induced sidebands. Proton single-voxel spectrum collected in a breast cancer patient. **A)** Contrast-enhanced image demonstrates a 15 x 16 x 15 mm^3 voxel surrounding a biopsy-proven case of inflammatory breast cancer with included surrounding adipose tissue. **B)** Water-suppressed spectra, top spectrum collected with a single echo time (45 ms), bottom spectrum collected with TE-averaged acquisition (TE 45-196 ms). The Cho signal (vertical arrows) is more distinct in the TE-averaged acquisition due to reduction in gradient-induced artifacts compared with the single TE acquisition. (Adapted from Bolan, et al. [3]).

Lipids

The in vivo spectra from the breast are often dominated by lipid resonances. When adipose tissue that is not part of the pathologic process is included in the voxel this inclusion can cause several problems [3, 13]. The impact of lipids can be reduced by increasing the echo time [7] or by employing a TE-averaging acquisition [3].

Not for distribution in the US.

Pre-scan set-up

In MR spectroscopy the line width of a peak is dependent both on the intrinsic T2 relaxation time of that metabolite and the homogeneity of the magnetic field in the region. The line width of a peak due to its intrinsic T2 relaxation time is typically less than 1 Hz, whereas the line width from field inhomogeneity (i.e. poor localized shim) may be from 5 to 10 Hz. In any MRS experiment the MR acquisition parameters are adjusted on a patient-by-patient basis in order to obtain optimum spectral resolution and signal-to-noise ratio (SNR) ratio. Two important parameters in the acquisition of high quality in vivo breast MRS data are pre-scan adjustment and shimming and thus it is crucial to spend the necessary time to achieve a well-shimmed region-of interest (ROI) and to ensure all pre-scan conditions have been successfully completed.

Shimming

Shimming is the process by which the local B0 field is made as homogeneous as possible. Obtaining a good localized shim is critical for the identification and characterization of any observable peaks. The quality of localized shim also directly affects the accuracy of referencing, and hence chemical assignment, of any observed choline signal in breast MRS. Due to inherent adjacent susceptibility differences encountered in breast MRS examinations (e.g. air-filled thorax, respiratory-motion) manual shimming is often required to optimize the final MRS result.

Prescan frequency adjustment

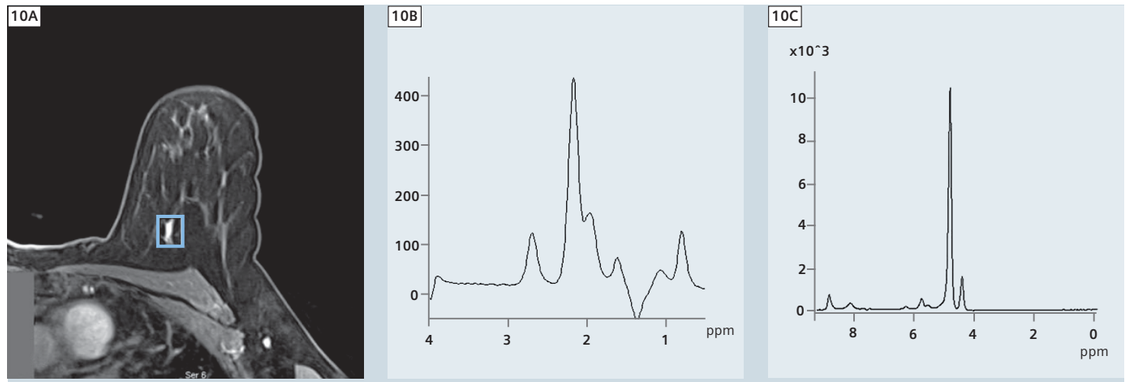

10 Prescan frequency adjustment. Proton single-voxel spectrum acquired with the PRESS sequence (repetition time (TR) 2000 ms, echo time (TE) 135ms) in a breast cancer patient. **A)** Contrast-enhanced image demonstrates a 15 x 12 x 14 mm^3 voxel surrounding a small ductal cancer with included surrounding adipose tissue. **B)** Water suppressed spectrum with unusual appearance of resonances. **C)** Non-water suppressed reference spectrum demonstrates lipid-water ratio of approximately 11 which resulted in the prescan adjustment wrongly assigning the lipid resonance at 1.3 ppm (the highest amplitude peak) as the water and thus applying water suppression at the wrong frequency. The result was the abnormal appearing spectrum in B).

Frequency confirmation:
During the pre-scan set-up it is routine for the MR system to assign the highest peak in the pre-acquisition phase as the water resonance. This is not always the case in breast MRS. If this situation is not recognized, and corrected, before the acquisition it is possible that the erroneous application of water suppression can lead to spectral artifacts in the final spectrum. This can be avoided by selecting the "frequency confirmation" box that allows the user to confirm that the MR system has selected the correct peak for water suppression.

Not for distribution in the US.

Contrast agents

Some gadolinium-based MR contrast agents have been shown to affect the spectra from breast tumors [6]. Other agents have been suggested as acceptable for MRS studies [9].

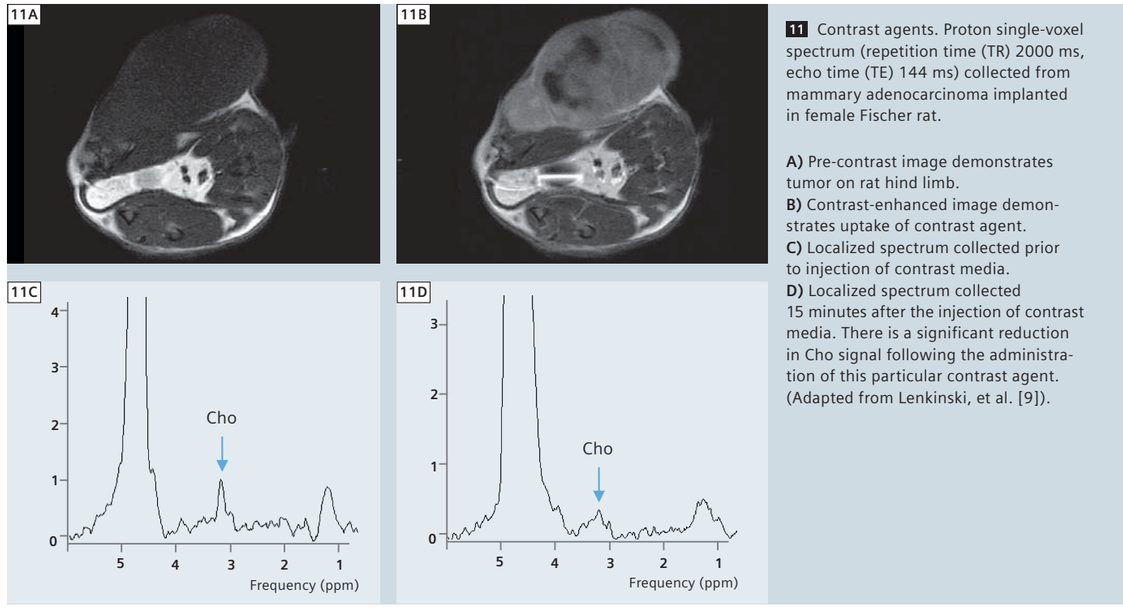

11 Contrast agents. Proton single-voxel spectrum (repetition time (TR) 2000 ms, echo time (TE) 144 ms) collected from mammary adenocarcinoma implanted in female Fischer rat.

A) Pre-contrast image demonstrates tumor on rat hind limb.
B) Contrast-enhanced image demonstrates uptake of contrast agent.
C) Localized spectrum collected prior to injection of contrast media.
D) Localized spectrum collected 15 minutes after the injection of contrast media. There is a significant reduction in Cho signal following the administration of this particular contrast agent. (Adapted from Lenkinski, et al. [9]).

Respiratory motion

Respiratory motion during the acquisition of breast MRS produces B_0 magnetic field distortions resulting in shot-to-shot frequency shifts [4]. These variations can be corrected by frequency shifting each individual measurement prior to summing the total number of averages resulting in an improvement in spectral resolution.

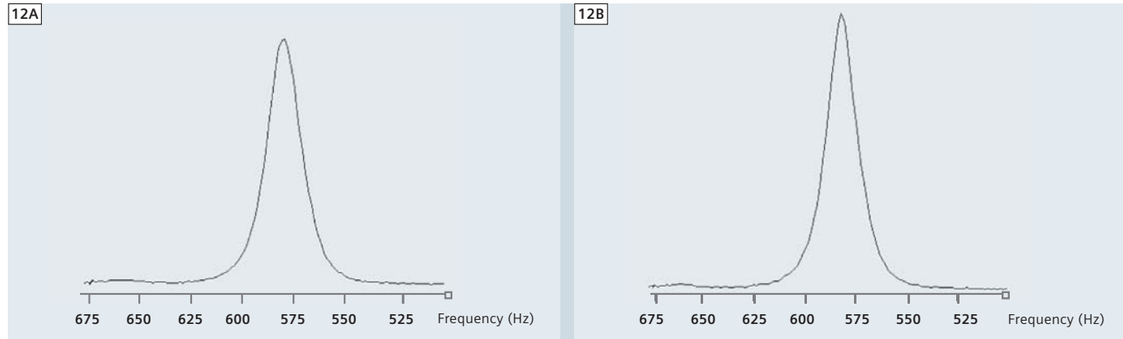

12 Compensation for respiratory induced artifact. Proton single-voxel spectrum acquired with the PRESS sequence (repetition time (TR) 2000 ms, echo time (TE) 135 ms) in a breast cancer patient. **A)** Non-water suppressed spectrum with FWHM of the water peak = 20 Hz without correction of frequency shifts due to respiration. **B)** Non-water suppressed spectrum with FWHM of the water peak = 16 Hz following correction of frequency shifts.

Not for distribution in the US.

Signal-to-noise ratio (SNR)

In MRS, adequate SNR is needed to detect and characterize any detected MRS signal. In breast MRS the signal from choline-containing metabolites is often small necessitating the collection of spectra with high SNR to allow for the accurate depiction of the choline signal, and determination of its MRS characteristics (e.g. chemical shift, signal integral).

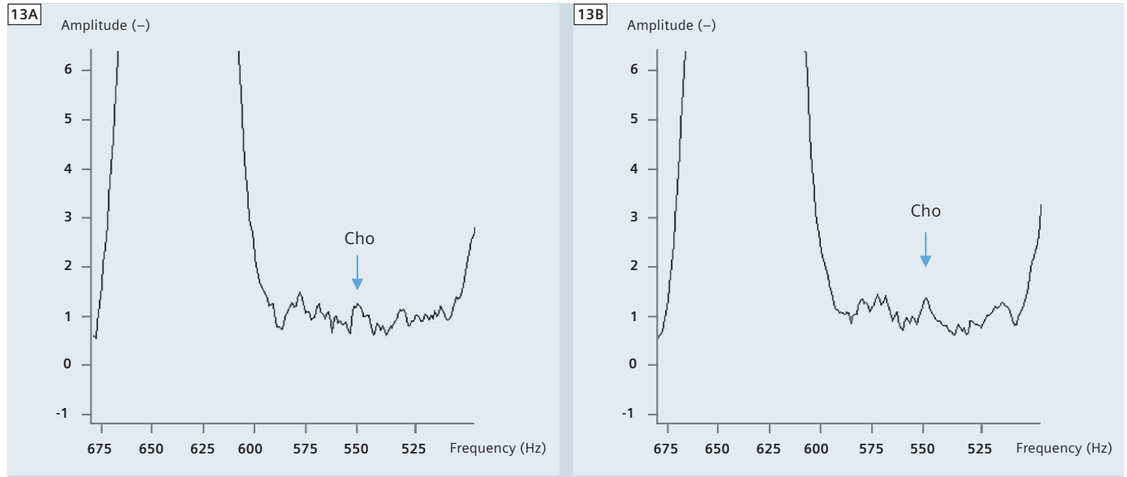

13 Signal-to-noise ratio, effect of acquisition time. Proton single-voxel spectrum acquired with the PRESS sequence (repetition time (TR) 2000 msec, echo time (TE) 135msec) in a breast cancer patient. **A)** Spectrum acquired from a 7 x 15 x 10 mm^3 voxel with 128 signal averages. A choline resonance is visible but barely above the background noise level. **B)** Spectrum acquired from the same location with the same voxel dimensions but with 256 signal averages. Choline signal is now clearly discernible above the background noise level.

Gross patient movement

As in all MR techniques patient movement can degrade the diagnostic utility of an examination. In MRS gross motion artifact can be identified by distortion of the resonant peaks, often with a double appearance of each peak.

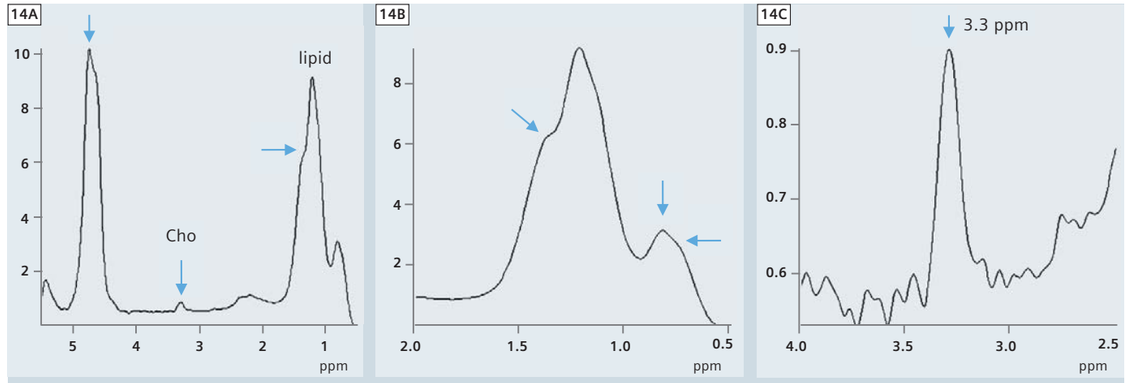

14 Proton single-voxel spectrum acquired with the PRESS sequence (repetition time (TR) 2000 ms, echo time (TE) 135 ms) in a breast cancer patient. **A)** Non-water suppressed spectrum demonstrating distortion (double peaks) of water and lipid resonances consistent with gross patient movement. **B)** Same spectrum as in A), displayed from 0.5 to 2.0 ppm demonstrating distortion of the lipid resonances at 0.9 and 1.3 ppm. **C)** Same spectrum as in A) & B), displayed from 2.5 to 4.0 ppm demonstrating distortion and frequency shifting of the choline resonance at 3.2 ppm.

Not for distribution in the US.

Undertaking MRS after:

A. Core biopsy
Core biopsies cause tissue damage and bleeding. The effect of this on the tumor is seen below. The effect on the MR spectrum is a broad series of resonances at 1.2 ppm from blood and bruising. This makes referencing of the spectrum difficult to impossible.
B. Placement of magnetic clip
Undertaking MRS in vivo on a breast lesion marked by a magnetic clip, for the surgeon to locate the tumor, results in a broad spectrum. The presence of a clip makes shimming very difficult to impossible. There are now non-magnetic clips available.

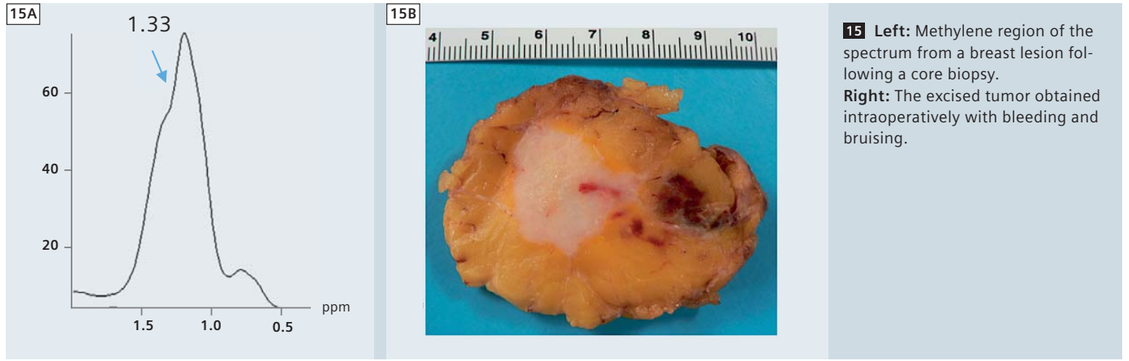

15 **Left:** Methylene region of the spectrum from a breast lesion following a core biopsy.
Right: The excised tumor obtained intraoperatively with bleeding and bruising.

Monitoring therapy

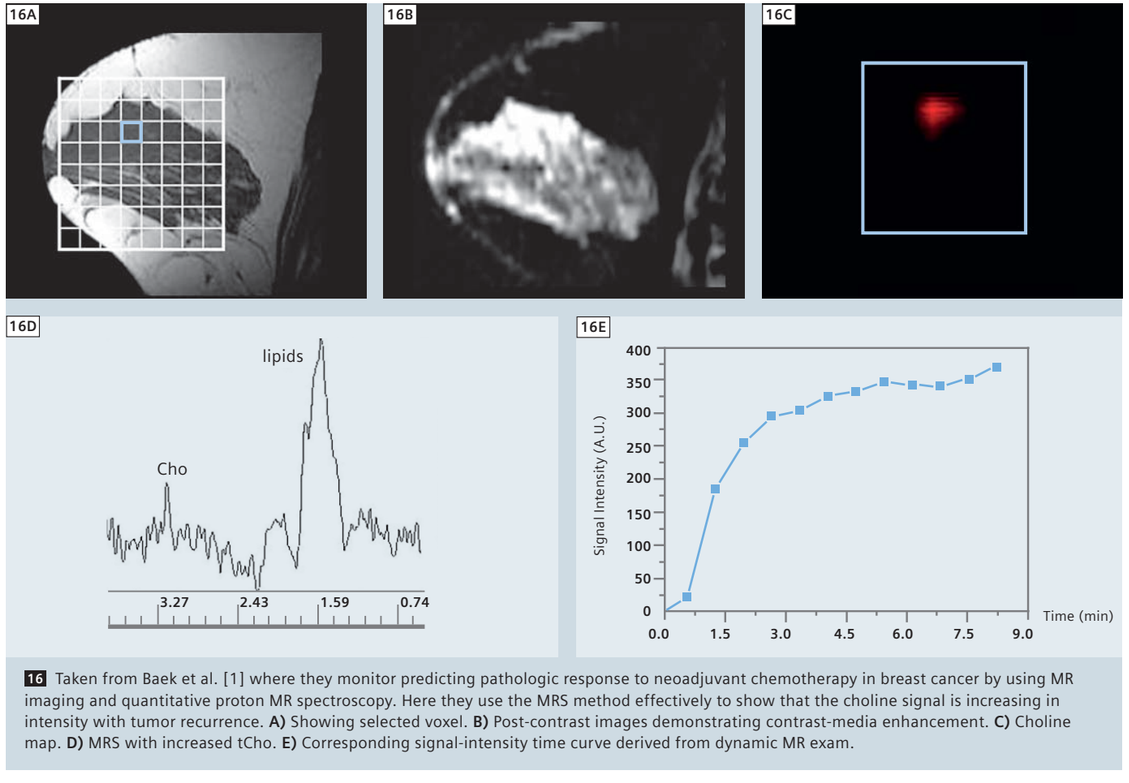

16 Taken from Baek et al. [1] where they monitor predicting pathologic response to neoadjuvant chemotherapy in breast cancer by using MR imaging and quantitative proton MR spectroscopy. Here they use the MRS method effectively to show that the choline signal is increasing in intensity with tumor recurrence. **A)** Showing selected voxel. **B)** Post-contrast images demonstrating contrast-media enhancement. **C)** Choline map. **D)** MRS with increased tCho. **E)** Corresponding signal-intensity time curve derived from dynamic MR exam.

Summary

First MRS reports on breast interrogated large tumors of 1.5 x 1.5 x 1.5 cm^3 or above. However, very often lesions detected by MRI are smaller (3–15 mm in size) and the following issues need to be addressed in order to make in vivo MRS robust and diagnostically useful. If successful this should increase the accuracy afforded by dynamic T1w MRI combined with breast MRS.

The issues to be considered include:

- The MRS exam needs to be undertaken prior to the placement of a clip and prior to a core biopsy being taken.
- Tumor size needs to be 8 mm or above for robust measurement of the chemical species responsible for appearance of diagnostic signals.
- Shimming is integral to a successful exam.
- Relative quantities of the diagnostic resonances can be measured as well as tCho using either 4, 7 or 16-channel coils.
- When using the method for definitive diagnosis or monitoring therapy the spectra need to be accurately referenced.
- Some tumors will have a mixture of pathology.

→ Visit **www.siemens.com/magnetom-world** for case reports, protocols, application tips, talks and much more clinical MR information

References

1 Baek, H.-M., J.-H. Chen, et al. (2009). "Predicting Pathologic Response to Neoadjuvant Chemotherapy in Breast Cancer by Using MR Imaging and Quantitative 1H MR Spectroscopy." Radiology 251(3): 653-662.

2 Baek, H.-M., J.-H. Chen, et al. (2008). "Detection of choline signal in human breast lesions with chemical-shift imaging." Journal of Magnetic Resonance Imaging 27: 1114-1121.

3 Bolan, P. J., L. DelaBarre, et al. (2002). "Eliminating spurious lipid sidebands in 1H MRS of breast lesions." Magnetic Resonance in Medicine 48(2): 215-222.

4 Bolan, P. J., P.-G. Henry, et al. (2004). "Measurement and correction of respiration-induced B0 variations in breast 1H MRS at 4 Tesla." Magnetic Resonance in Medicine 52(6): 1239-1245.

5 Bolan, P. J., S. Meisamy, et al. (2003). "In vivo quantification of choline compounds in the breast with 1H MR spectroscopy." Magnetic Resonance in Medicine 50(6): 1134-1143.

6 Joe, B. N., V. Y. Chen, et al. (2005). "Evaluation of 1H-magnetic resonance spectroscopy of breast cancer pre- and postgadolinium administration." Investigative Radiology 40(7): 405-411.

7 Kvistad, K. A., I. J. Bakken, et al. (1999). "Characterization of neoplastic and normal human breast tissues with in vivo 1H MR spectroscopy." Journal of Magnetic Resonance Imaging 10(2): 159-164.

8 Lehman, C. D., C. Gatsonis, et al. (2007). "MRI evaluation of the contralateral breast in women with recently diagnosed breast cancer." New England Journal of Medicine 356(13): 1295-1303.

9 Lenkinski, R. E., X. Wang, et al. (2009). "Interaction of gadolinium-based MR contrast agents with choline: Implications for MR spectroscopy (MRS) of the breast." Magnetic Resonance in Medicine 61(6): 1286-1292.

10 Meisamy, S., P. J. Bolan, et al. (2004). "Neoadjuvant chemotherapy of locally advanced breast cancer: predicting response with in vivo 1H MR spectroscopy – A pilot study at 4 T." Radiology 233(2): 424-431.

11 Saslow, D., C. Boetes, et al. (2007). "American Cancer Society guidelines for breast screening with MRI as an adjunct to mammography." CA Cancer Journal for Clinicians 57(2): 75-89.

12 Stanwell, P., L. Gluch, et al. (2005). "Specificity of choline metabolites for in vivo diagnosis of breast cancer using 1H MRS at 1.5T." European Radiology 15(5): 1037-1043.

13 Stanwell, P. and C. Mountford (2007). "Proton magnetic resonance spectroscopy of the breast in vivo " RadioGraphics 27(Supplement 1): S253-S266.

Contact
Professor Carolyn Mountford
Centre for Clinical Spectroscopy
Department of Radiology
Brigham & Women's Hospital
Harvard Medical School
4 Blackfan St.
HIM-817
Boston MA 02115
USA
Phone: +1 617 525 5801
cemountford@bics.bwh.harvard.edu

Try them on your system

Trial licenses for most of the applications featured in this issue of MAGNETOM Flash are available free of charge for a period of 90 days: Please contact your local Siemens representative for system requirements and ordering details or visit us online* at **www.siemens.com/discoverMR** for further details, product overviews, image galleries, step-by-step demos, case studies and general requirement information.

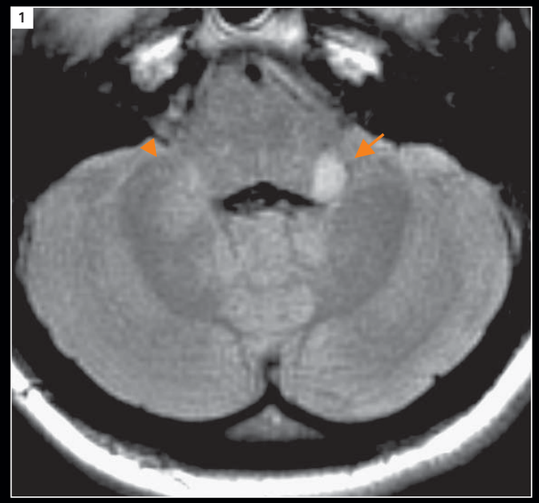

1 Reduced motion artifacts with *syngo* BLADE (page 10).

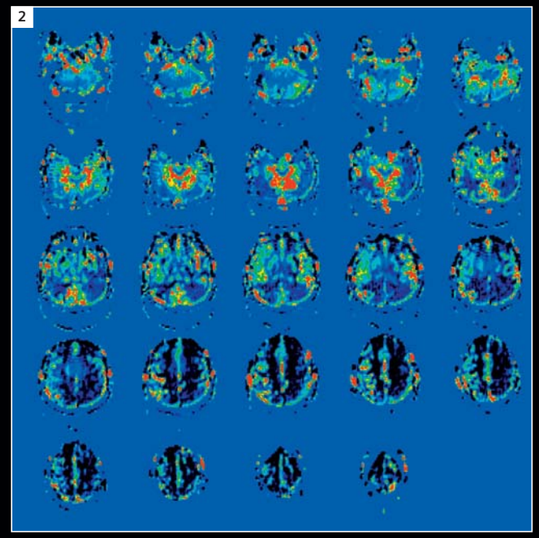

2 Non-contrast perfusion evaluation with *syngo* ASL (page 19).

*Direct link for US customers: **www.siemens.com/WebShop**
Direct link for UK customers: **www.siemens.co.uk/mrwebshop**

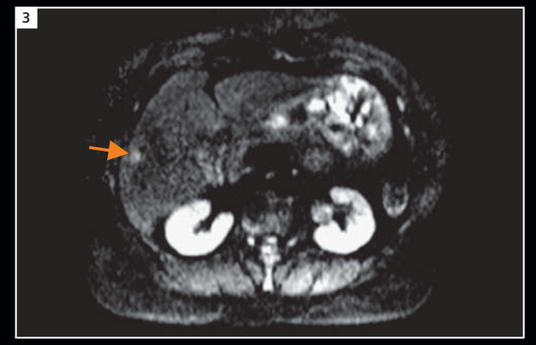

3 Diffusion-weighted imaging with *syngo* REVEAL (page 44).

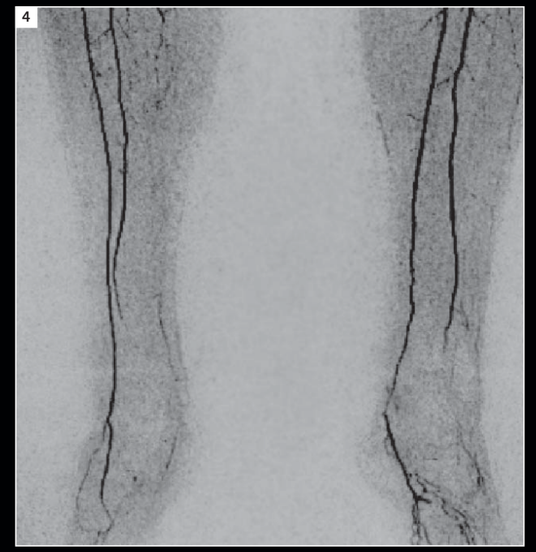

4 Dynamic imaging of the calf vessels with low-dose *syngo* TWIST angiography (page 82).

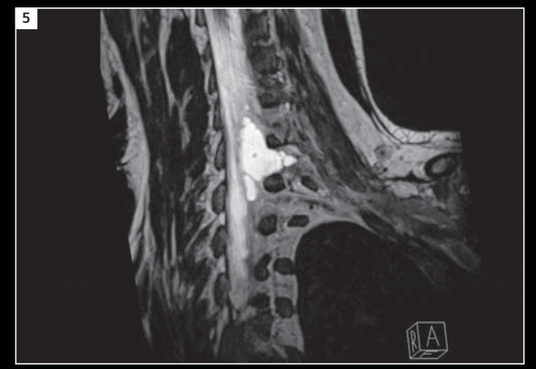

5 *syngo* SPACE for detailed visualisation of the nerve roots (page 105).

Case Report:
Metastases from Neuroendocrine Carcinoma: Value of Diffusion-Weighted MR Imaging Compared to ^{68}Ga-DOTATOC PET-CT

Bernhard Klumpp, M.D.; Philip Aschoff, M.D.; Mehmet Oeksuez, M.D.; Christiane Pfannenberg, M.D.; Heinz-Peter Schlemmer, M.D.

Department for Diagnostic and Interventional Radiology, University of Tuebingen, Germany

Introduction

Neuroendocrine tumors occur most frequently in the gastrointestinal tract [1]. Cells of neuroendocrine tumors characteristically express somatostatin receptors [2]. Due to small size and often slow progression of tumor manifestations the diagnostic work up is challenging.
Staging usually includes morphological imaging such as ultrasound, computed tomography (CT), MRI and somatostatin receptor scintigraphy (SRS) for functional imaging [3–5]. However, the diagnostic yield is limited, as some liver metastases remain unapparent in MRI and CT and spatial resolution of SRS is restricted.
Recent promising technical developments for the detection of neuroendocrine tumors include diffusion-weighted MR imaging (DWI) and ^{68}Ga-DOTATOC PET-CT [6, 7]. Relying on the measurement of the apparent diffusion coefficient (ADC) which is reduced in neoplastic tissue [8], DWI provides high lesion to liver contrast reflected by high sensitivity of DWI for liver metastases [9].
Due to the overexpression of somatostatin receptors, neuroendocrine tumors can be detected by ^{68}Ga-DOTATOC PET (-CT). The degree of receptor expression reflected by the amount of tracer uptake is crucial when considering therapy with radiolabel somatostatin analoga. In patients eligible for radio peptide therapy, this imaging technique also allows evaluation and monitoring of therapy [10, 11].

Methods

In a 70-year-old female patient with a history of neuroendocrine carcinoma at the ileocoecal valve resected five months ago, a solitary hepatic mass was detected by ultrasound. For further differentiation and evaluation of potential metatstatic spread of the neuroendocrine carcinoma, ^{68}Ga-DOTATOC PET-CT and MRI of the abdomen were performed. MR examination was performed as a multi-step exam covering the whole abdomen. The protocol included coronal T2w HASTE, transversal T1w FLASH 2D with spectral fat-suppression, transversal T1w in- and opposed-phase FLASH 2D, transversal fat-suppressed T2w TSE with respiratory gating (PACE), transversal repiratory gated diffusion-weighted MRI

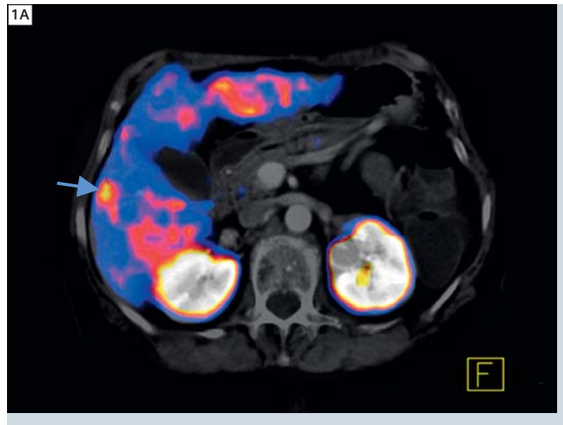

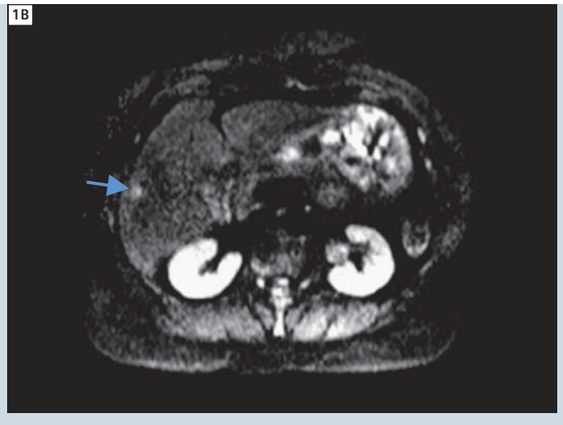

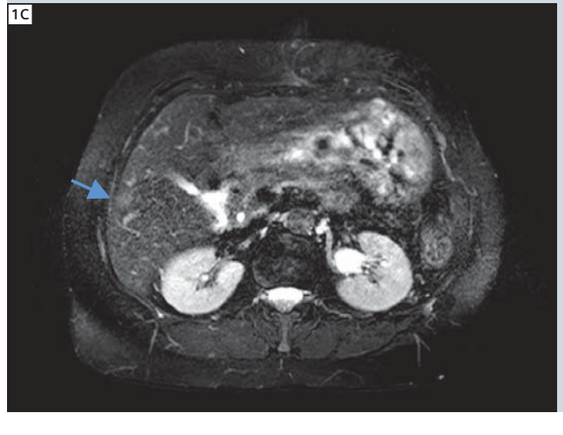

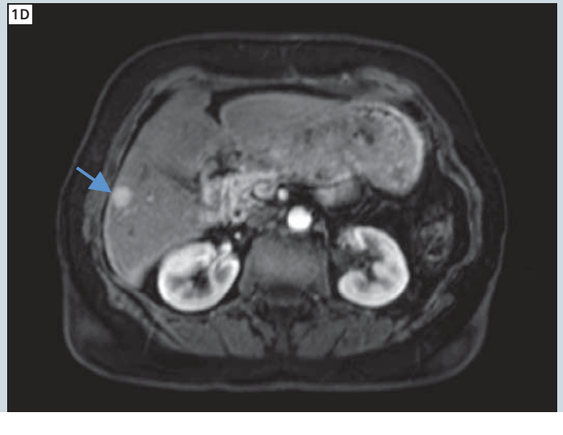

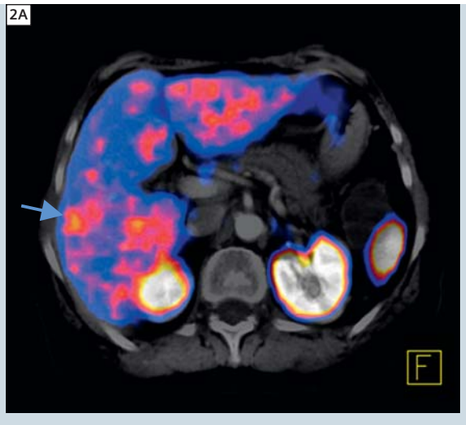

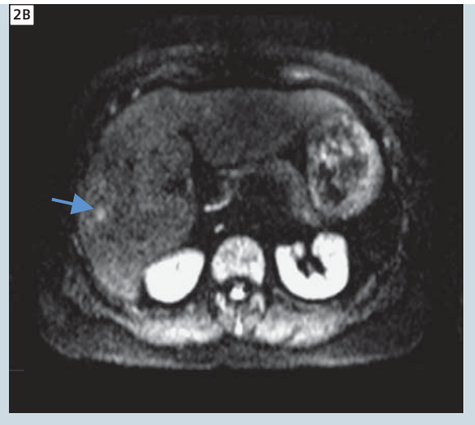

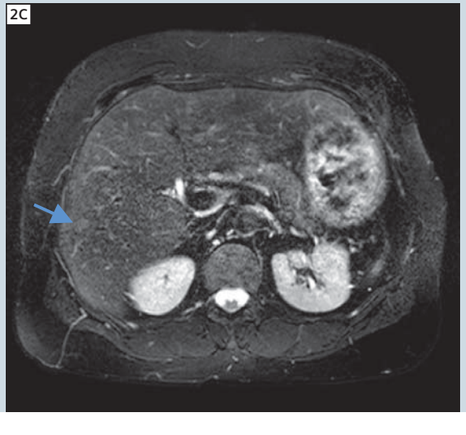

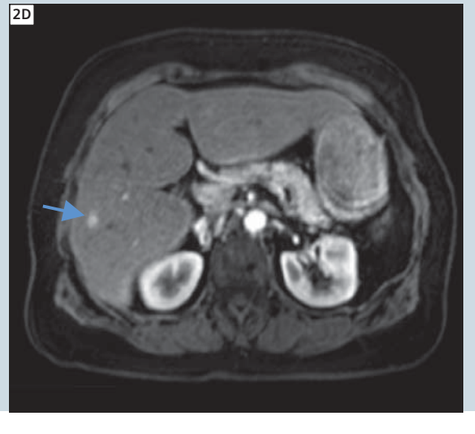

1,2 1A and 2A: (left upper row) PET-CT fusion, **1B and 2B:** (right upper row) DWI, **1C and 2C:** (left lower row), T2w TSE, **1D and 2D:** (right lower row) contrast enhanced T1w images of the liver in corresponding slice position depicting subcapsular liver metastases in the right lobe. In **Fig. 2B**, DWI indicates a small metastasis neighbouring the larger one, which could not be detected by conventional MRI or PET-CT.

(*syngo* REVEAL) with spectral fat suppression (TE 71 ms, TR 5265 ms, baseline matrix 192, voxel size 2.1 x 2.1 x 6 mm, receiver bandwidth 1735 Hz / pixel), multi-phase dynamic T1w 3D FLASH (TE 2.4 ms, TR 4.5 ms, baseline matrix 256, voxel size 2.2 x 1.5 x 2.7 mm, receiver bandwidth 455 Hz / pixel, flip angle 10°) including arterial phase and finally transversal contrast enhanced T1w FLASH 2D sequences (TE 4.1 ms, TR 186 ms, baseline matrix 256, voxel size 2.0 x 1.4 x 6 mm, receiver bandwidth 140 Hz / pixel, flip angle 70°). All images were acquired at 1.5 Tesla (MAGNETOM Avanto).
PET-CT: Imaging included multiphasic contrast enhanced whole body CT after intravenous injection of contrast media and PET 20 minutes after intravenous injection of 187 MBq ^{68}Ga-DOTATOC with 4 minutes acquisition time for each bed position (Biograph 16). The indication for a ^{68}Ga-DOTATOC PET was based on an individualized therapy decision.

Imaging findings

MRI: Three T2 hyperintense lesions suspicious of being metastasis could be identified. In early phase contrast enhancement was found in these lesions. On later phase contrast enhanced images these lesions were isointense to adjacent normal hepatic tissue. Diffusion-weighted images revealed seven lesions with decreased water diffusion capacity suspicious of being metastases. Only three of those were also depicted by T2-weighted and contrast enhanced images. DWI enabled the additional detection of smaller metastases compared to T2-weighted and contrast enhanced MR imaging, reflected by a significantly smaller average lesion size on DWI (DWI: 8.3 ± 2.4 mm, T2 TSE: 12.3 ± 3.5 mm, ceMRI: 13 ± 2.7 mm; $p < 0.05$).
PET-CT: Contrast enhanced CT revealed three discretely hypodense hepatic lesions correlating in size and location with those identified by T2-weighted and contrast enhanced T1-weighted MR images. Yet, increased focal ^{68}Ga-DOTATOC uptake could be found in eight lesions. Thereof, five correlated with the finding on diffusion-weighted MR images, whereas three small areas of focal tracer uptake could not be identified on DWI and two small lesions on DWI did not appear to have focal tracer uptake in PET-CT respectively.

Conclusion

DWI plays an important role in the accurate detection of additional liver lesions, which may be occult in conventional MRI and especially in CT. In our case, the suspicion of diffuse hepatic spread is also supported by the additionally performed ^{68}Ga-DOTATOC PET. Also in concordance with our clinical experience with different tumor entities, DWI of the liver is a valuable tool for the exact estimation of hepatic tumor load. Compared to T2-weighted and contrast enhanced MR-imaging, DWI is more accurate, faster to perform, easy to interpret and provides also the potential for therapy monitoring. Moreover it is less expensive as it does not rely on the application of contrast media.

Contact
Bernhard Klumpp, M.D.
Department for Diagnostic and Interventional Radiology
Eberhard-Karls-University Tuebingen
Hoppe-Seyler-Str. 3
72076 Tuebingen
Germany
Bernhard.klumpp@med.uni-tuebingen.de

References

1 Modlin I, Lye K, Kidd M. A 5-Decade Analysis of 13,715 Carcinoid Tumors. Cancer 2003 Feb; 97 (4): 934–959.
2 Papotti M, Bongiovanni m, Volante M, Allia E, Landolfi S, Helboe L, Schindler M, Cole SL, Bussolati G. Expression of somatostatin receptor types 1-5 in 81 cases of gastrointestinal and pancraetic endocrine tumors. A correlative immunohistochemical and reverse-transcriptase polymerase chain reaction analysis. Virchows Arch 2002 Mar; (440): 461–475.
3 Sundin A, Garske U, Orlefors H. Nuclear imaging of neuroendocrine tumors. Best Pract Res Clin Endocrinol Metab 2007 Mar; 21 (1): 69–85.
4 Ramage JK, Davies AHG, Ardill J, Bax N, Caplin M, Grossman A, Hawkins R, McNicol AM, Reed N, Sutton R, Thakker R, Aylwin A, Breen D, Britton K, Buchanan K, Corrie P, Gillams A, Lewington V, McCane D, Meeran K, Watkinson A. Guidelines for the management of gastroenteropancreatic neuroendocrine (including carcinoid) tumours. UKNETwork for neuroendocrine tumours. Gut 2005; 54 (Suppl IV): iv1-iv16.
5 Kumbasar B, Kamel IR, Tekes A, Eng J, Fishman EK, Wahl RL. Imaging of neuroendocrine tumors: accuracy of helical CT versus SRS. Abdom Imaging 2004 (29): 696–702.
6 Bruegel M, Gaa J, Waldt S, Woertler K, Holzapfel K, Kiefer B, Rummeny EJ. Diagnosis of Hepatic Metastasis: COmparison of Respiration-Triggered Diffusion-Weighted Echo-Planar MRI and Five T2-Weighted Turbo Spin-Echo Sequences. AJR 2008 Nov; (191): 1421–1429.
7 Gabriel M, Decristoforo C, Kendler D, Dobrozemsky G, Heute D, Uprimny C, Kovacs P, Von Guggenberg E, Bale R, Virgolini IJ. ^{68}Ga-DOTA-Tyr3-octreotide PET in neuroendocrine tumors: comparison with somatostatin receptor scintigraphy and CT. J Nucl Med. 2007 Apr;48(4):508–18.
8 Herneth A, Guccione S, Bednarski M. Apparent Diffison Coefficient: a quantitative parameter for in vivo tumor characterization. Eur Journ Rad 2003; (45): 208–213.
9 Nasu K, Kuroku Y, Nawano S, Kuroki s, Tsukamoto T, Yamamoto S, Motoori K, Ueda T. Hepatic Metastases: Diffusion-weighted Sensitivity-encoding versus SPIO-enhanced MR Imaging. Radiology 2006 Apr; 239(1): 122–130.
10 Waldherr C, Pless M, Maecke HR, Schumacher T, Crazzolara A, Nitzsche EU, Haldemann A, Mueller-Brand J. Tumor response and clinical benefit in neuroendocrine tumors after 7.4 GBq (90) Y-DOTATOC. J Nucl Med. 2002 May;43(5):610–6.
11 Koukouraki S, Strauss LG, Georgoulias V, Eisenhut M, Haberkorn U, Dimitrakopoulou-Strauss A. Comparison of the pharmacokinetics of 68Ga-DOTATOC and [18F]FDG in patients with metastatic neuroendocrine tumours scheduled for 90Y-DOTATOC therapy. Eur J Nucl Med Mol Imaging. 2006 Oct;33(10):1115–22. Epub 2006 Jun 9.

Not for distribution in the US.

First Experiences with a Novel Software Prototype for Assessment of Treatment Response of Liver Tumors to Transarterial Chemoembolization

Susanne Bonekamp[1]; Atilla Peter Kiraly[2]; Mehmet Akif Gulsun[2]; Prashant Jolepalem[1]; Ihab R. Kamel[1].

[1]Russell H. Morgan Department of Radiology and Radiological Science, The Johns Hopkins Hospital, Baltimore, MD, USA
[2]Siemens Corporate Research, Princeton, NJ, USA

Introduction

Liver cancer (hepatocellular cancer, HCC) is the most common solid organ tumor and one of the most fatal cancers in the world [1, 2]. Treatment options are limited and clinical outcome is generally poor with median survival rates of less than 1 year. Surgical resection and transplantation, which can only be performed in about 15% to 20% of patients, continue to be plagued by significant morbidity, mortality and high recurrence rates, whereas systemic chemotherapy and radiation therapy are ineffective [3, 4]. Loco-regional therapies, for example transcatheter arterial chemoembolization or Yttrium-90 microsphere radioembolization, have become the mainstay of therapy against most unresectable primary and secondary hepatic malignancies [5–10].
Following regional therapy, cross-sectional imaging is necessary to assess tumor response. The Response Evaluation Criteria in Solid Tumors (RECIST) are generally accepted as the standard for evaluation of treatment response in solid tumors [11–13]. A decrease in tumor size measured by a highly reproducible and objective imaging modality such as CT or MR imaging is taken as a measure of treatment effect. Recent data suggest that RECIST is not the optimal criteria to evaluate response to trans-arterial therapy because those criteria evaluate only unidimensional tumor measurements and disregard the extent of necrosis, which is the target of all effective locoregional therapies [14–17]. However, change in tumor diameter after transarterial chemoembolization (TACE) is a late finding, and residual enhancement assessed by contrast-enhanced MRI or CT can be difficult to evaluate owing to the presence of changes in signal intensity (hyperintensity on unenhanced T1-weighted images) related to a combination of iodized oil injection and hemorrhagic necrosis. In contrast functional MRI, including diffusion-weighted imaging (DWI) and dynamic contrast enhancement (DCE), has been shown to be a sensitive indicator of tumor response [18–20]. Recent studies have shown that contrast-enhanced MRI with subtraction technique and DWI correlate highly with the histopathologic findings in the evaluation of necrosis of HCC after TACE [21–23].
Measurements of tumor size, DWI characteristics (apparent diffusion coefficient, ADC) and perfusion are usually performed manually. This process is inherently subjective and time consuming. The standardization, respectively (semi-) automation of this task would allow for objective evaluation of tumor response to therapy, decrease interobserver variability and increase accuracy. Furthermore, the analysis of DWI and DCE imaging is usually based on a region of interest (ROI) approach and the average ADC or enhancement value of a single ROI or several ROIs is used as a measure of diffusion or enhancement of the liver lesion. However, a volumetric, pixel by pixel analysis has been suggested as more accurate measure of tumor response [13, 17, 24, 25]. The idea for the development of a novel software tool (MR Oncotreat) for the registration, segmentation and analysis of MR images both within a single study and between serial studies and its first practical realization was based on a close co-operation between Dr. Kamel and Siemens Healthcare.

Not for distribution in the US.

Not for distribution in the US.

1.1

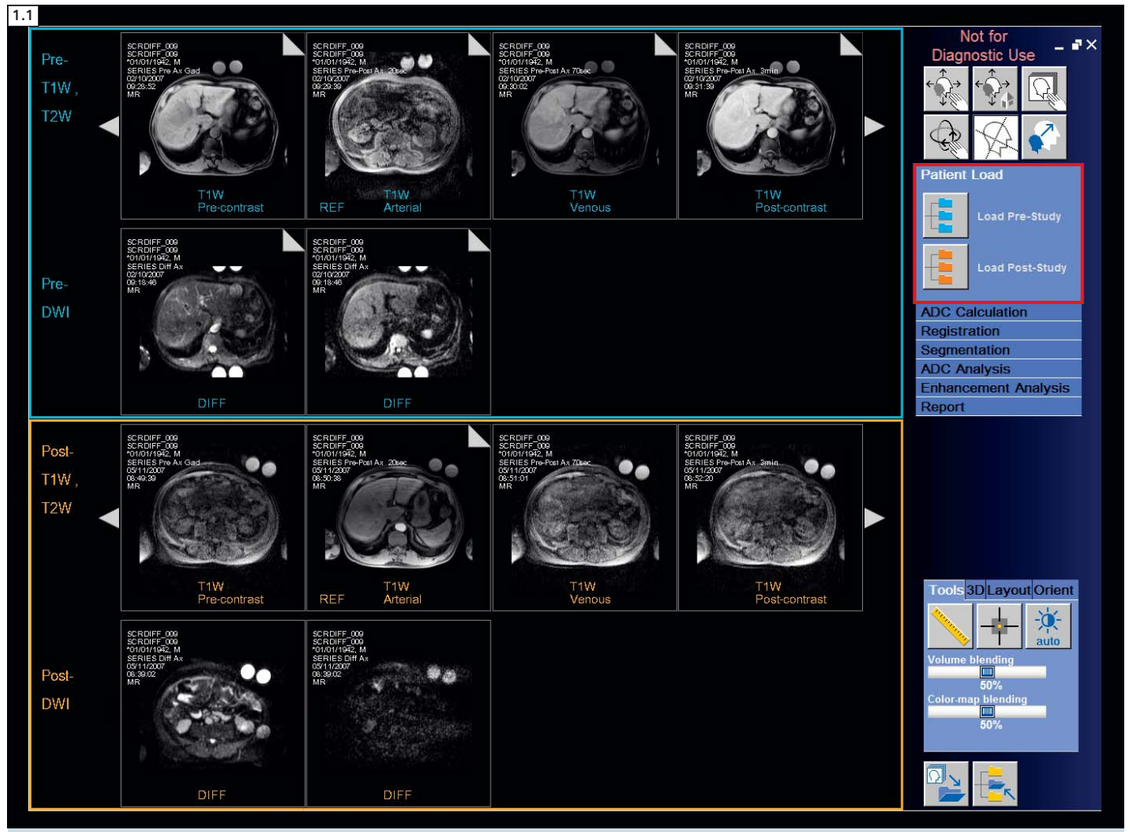

1.1 Loaded and classified pre- and post-treatment studies. Blue color indicates pre-treatment and orange indicates post-treatment images.

1.2

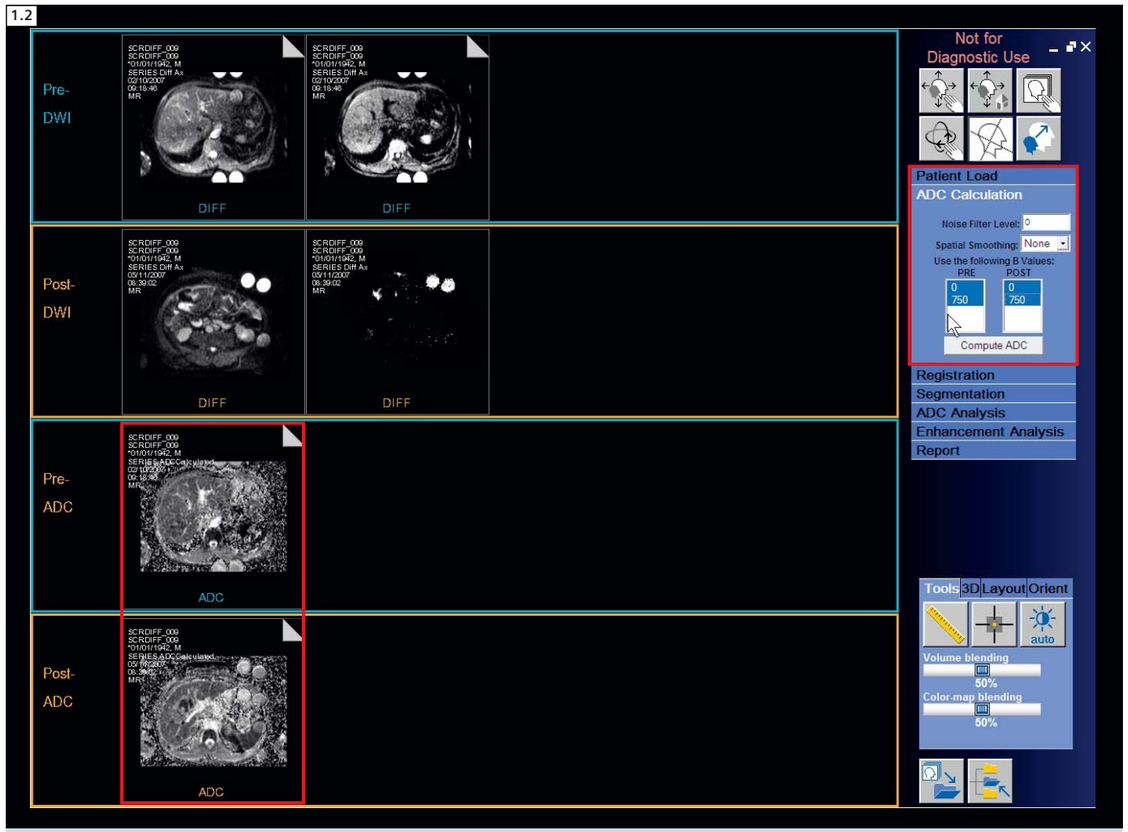

1.2 Computation of ADC maps can be performed if diffusion images when at least two b-values are loaded.

The prototype – workflow

The prototype of the MR Oncotreat software is a semi-automatic software package for three-dimensional *intra* and *inter*-study registration, segmentation, and volume and functional analysis [26]. Images within and between two treatment studies are aligned with a deformable registration [27] and tumor borders are defined with an interactive segmentation technique [28]. The prototype then assists the radiologists in the evaluation of volumetric data including tumor volume, surface, RECIST diameter, 3D longest diameter, and functional data including ADC values and DCE in multiple vascular phases. The prototype offers comparison of two studies based on either using a percent volume or on a voxel-by-voxel basis. Data presentation with this tool includes scatter plots, histograms as well as more conventional mean and median values for each parameter measured. Color maps produced in ADC and DCE analysis can be overlaid on images from both studies, and direct comparison can be made between the results obtained from ADC and DCE analysis. Beside the main functionality, the application also includes tools for 3D visualization, including Maximum Intensity Projection (MIP), Volume Rendering Technique (VRT) and 3D Multi-Planar Reformat (MPR) rendering modes, and tools for measurement, including distance and pixel lens tools.

The general workflow using the MR Oncotreat prototype is as follows:

1) Patient DICOM data is imported into the MR Oncotreat database

2) After loading patient data a data classification is done which classifies data into several categories based on the protocol settings stored in the DICOM headers (Figure 1.1).

3) Computation of ADC images is possible when at least two diffusion images of different b-values are loaded (Figure 1.2).

4) A non-linear registration is performed to correct motion in T1w images as well as to register between T1w, T2w and DWI image series for each pre- and post-treatment studies. Following this *intra*-study registration, two studies are also registered by either a non-linear or a linear registration. A screenshot from the registration workflow is shown in figure 1.3.

5) "Random Walker", a semi-automatic 3D segmentation technique is used to segment the tumor. The user is able to make multiple segmentations which can be analyzed and visualized together (Figure 1.4).

6) Once the images are registered and segmented, ADC maps of pre- and post-treatment studies can be compared either on a global or voxel-by-voxel basis where intersection occurs. Histogram of ADC values are generated for both studies from the segmented tumor volume, and their mean and standard deviation values are calculated and displayed (Figure 1.5).

7) Arterial and venous enhancement of pre- and post-treatment studies are calculated for the segmented tumor volume and displayed as a color map overlaid on user selected images. Histogram of enhancement values are generated for both studies from the segmented tumor volume, and their

Not for distribution in the US.

Not for distribution in the US.

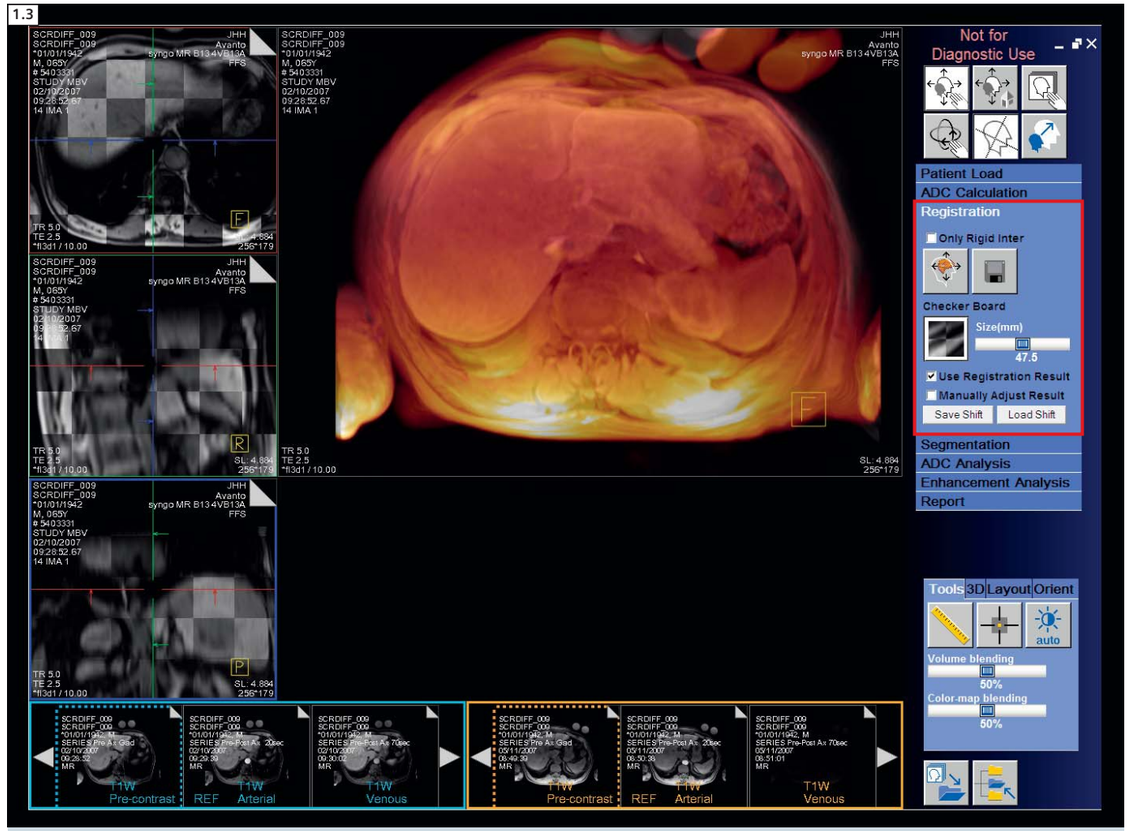

1.3 Registration of pre- and post-treatment T1-weighted images shown as color blended (right) and checker board (smaller images on the right).

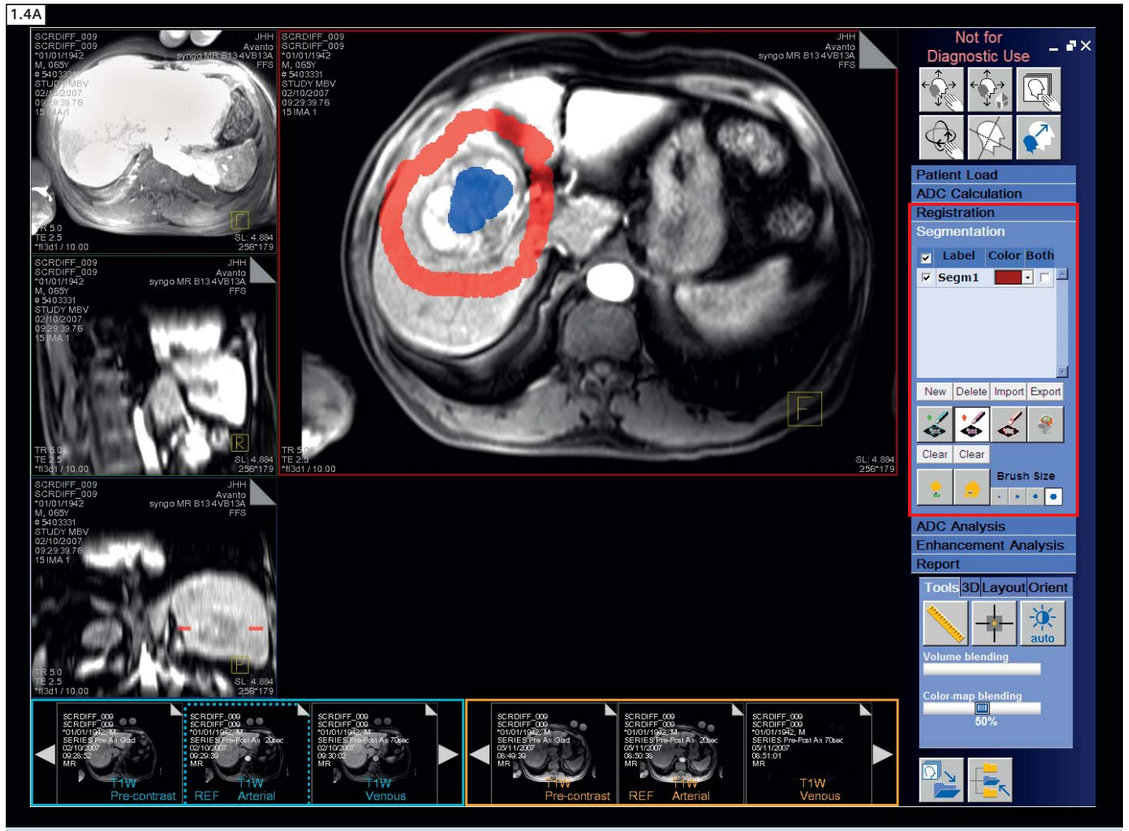

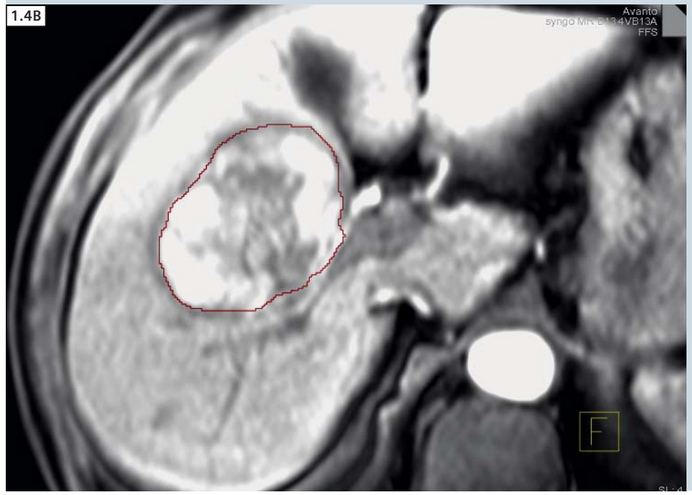

1.4 **A:** Lesion segmentation involves simply brushing the inside (blue) and surrounding tissue (red).
B: The resulting segmentation.

mean and standard deviation values are calculated and displayed to user (Figure 1.6).

8) The results of functional analysis are displayed in an overview (figure 1.7), but can also be saved to an ASCII file for further data analysis and a summary report can be generated (PDF file).

9) For advanced data presentation, the MRI data sets can be visualized in 3D by MIP, VRT or 3D MPR. It can be also visualized in 2D with three MPR views in any orientation.

Liver imaging protocol

At Johns Hopkins Hospital, until recently, our MRI protocol uses a 1.5T MRI scanner (MAGNETOM Avanto, Siemens Healthcare), and a combination of the spine and body matrix coil. The technique consists of T2w turbo spin echo images (matrix size 256 x 256 px; slice thickness 8 mm; interslice gap 2 mm; TR 4500 ms, TE 92 ms) and breath-hold DWI (*syngo* REVEAL) (matrix 128 x 128 px; slice thickness 8 mm; interslice gap 2 mm; b–values 0 s/mm^2, 750 s/mm^2; TR 3000 ms, TE 69 ms). Breath-hold native and contrast-enhanced T1-weighted three-dimensional fat suppressed VIBE (FOV 320 – 400 mm; matrix 192 x 160 px; slice thickness 2.5 mm; TR 5.77 ms; TE 2.77 ms; flip angle 10°) in the arterial phase (20 s) and portal venous phase (70 s) are also obtained.

Assessment of response to transarterial chemoembolization

A retrospective review was performed with an exemption granted by our institutional review board, and informed

Not for distribution in the US.

Not for distribution in the US.

1.5

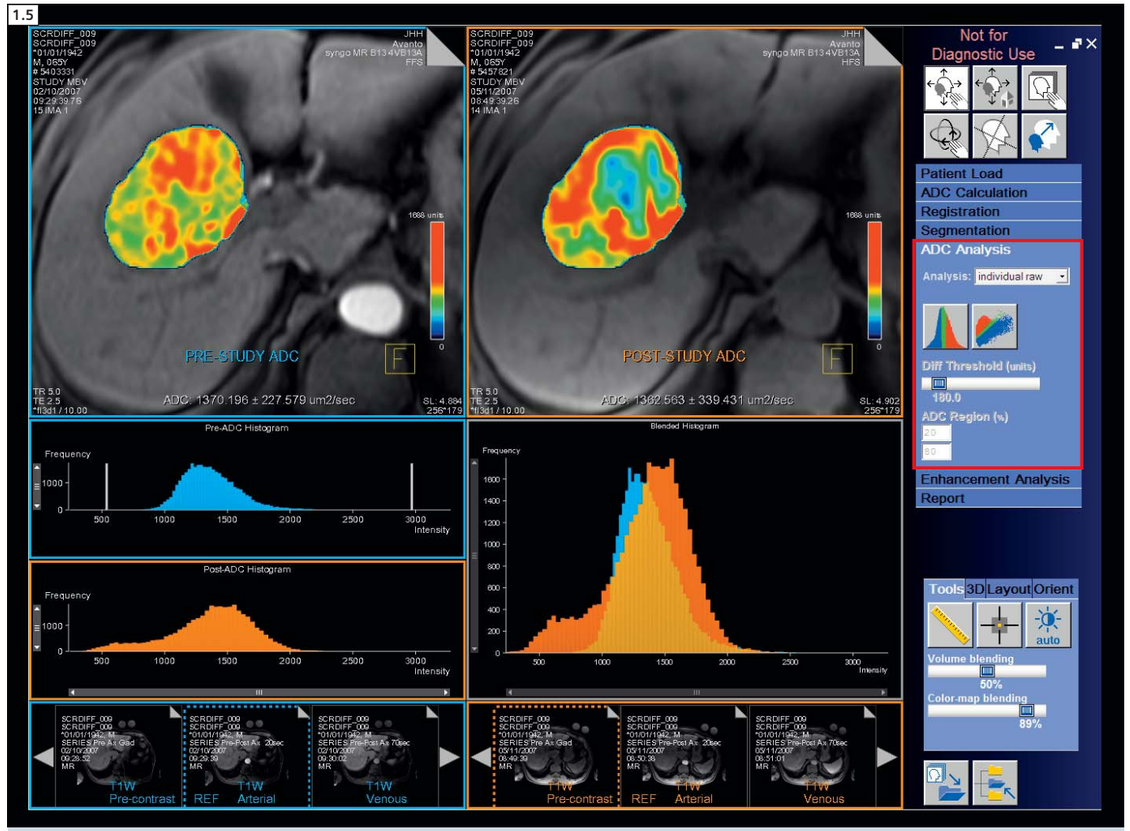

1.5 Individual ADC values of the pre-treatment (shown on the left) and post-treatment (shown on the right) study shown as an overlay on the arterial phase T1-weighted images. The corresponding histograms are shown below (blue = pre-treatment, orange = post-treatment).

1.6

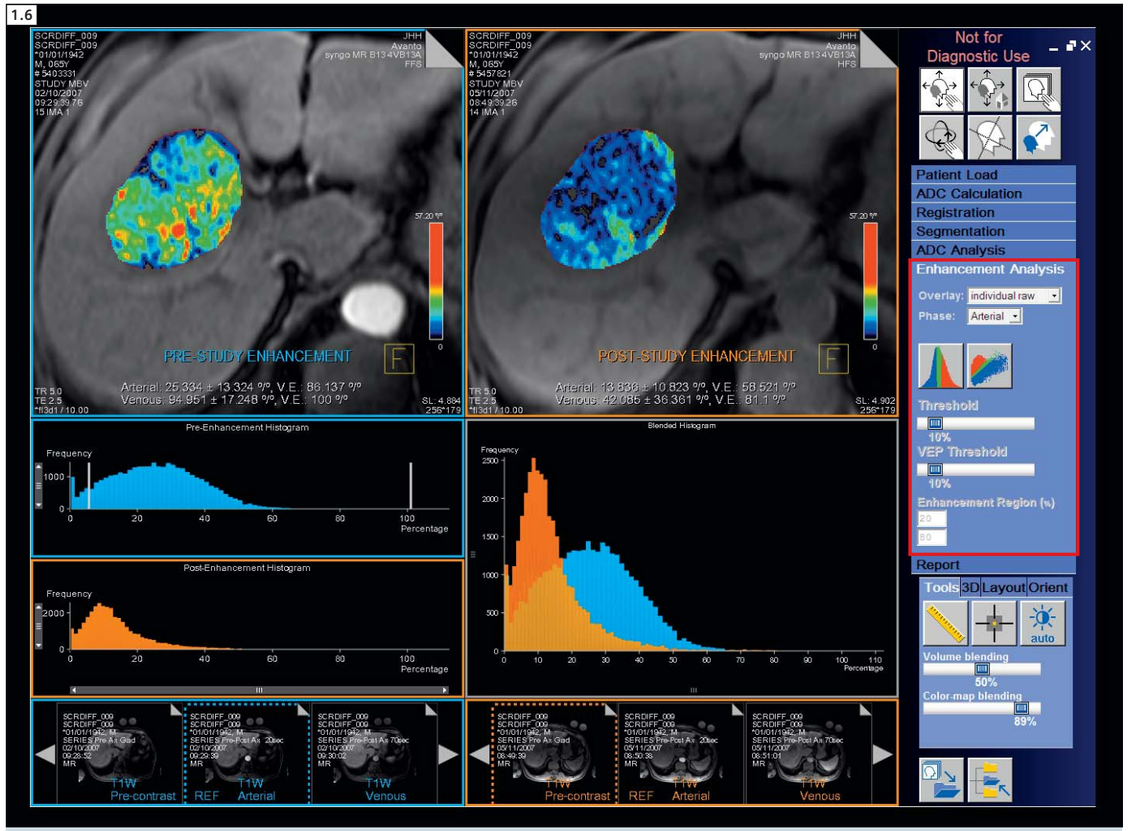

1.6 Individual arterial enhancement values of the pre-treatment (shown on the left) and post-treatment (shown on the right) study. The corresponding histograms are shown below (blue = pre-treatment, orange = post-treatment).

consent was waived. The study was HIPAA compliant with all patient identifiers removed before data interpretation. To be included in the study, patients with known HCC treated primarily by TACE had to undergo a pre-treatment MRI, followed by MRI within 6 weeks of treatment, and then a follow-up MRI approximately 6 months after TACE. Patients were excluded if they had received radiation, undergone resection, or received transplant prior to completing the 6 month follow-up MRI. In the process of reviewing cases, we also included several tumors that were not treated or "non-targeted" by TACE. Two observers (P.J. and I.K.) reviewed all MR images and selected index HCC lesions with a diameter greater than 1 cm suitable for evaluation. A maximum of five lesions were selected per patient. Three exemplary chosen cases from this study and how treatment response was evaluated with the MR Oncotreat prototype are shown in figures 2–4:

Patient 1

54-year-old male with a twenty year history of hepatitis B and an infiltrating tumor occupying most of the left lobe of the liver and extending into the right lobe along its margin. Several separate 1–2 cm lesions were also noted posteriorly in the right dome. Figure 2 shows marked decrease of venous enhancement with unchanged ADC in a large section of the tumor after TACE and the corresponding histogram.

Patient 2

59-year-old male with a history of hepatitis C and with multifocal HCC. The largest, conglomerate mass is located in the right hepatic lobe, predominantly located within segments 6 and 7, demonstrating heterogeneous enhancement and lobulated irregular margins. Figure 3 shows significant decrease in venous enhancement and heterogeneous ADC response along with the corresponding histograms.

Patient 3

57-year-old female with a history of hepatitis C, cirrhosis and HCC. MRI demonstrates two heterogenous enhancing masses in the right lobe and a dome lesion in the background of hepatitis C. Figure 4 shows significant decrease of enhancement and increase in ADC within the tumor after TACE and the corresponding histograms.

Not for distribution in the US.

Not for distribution in the US.

1.7

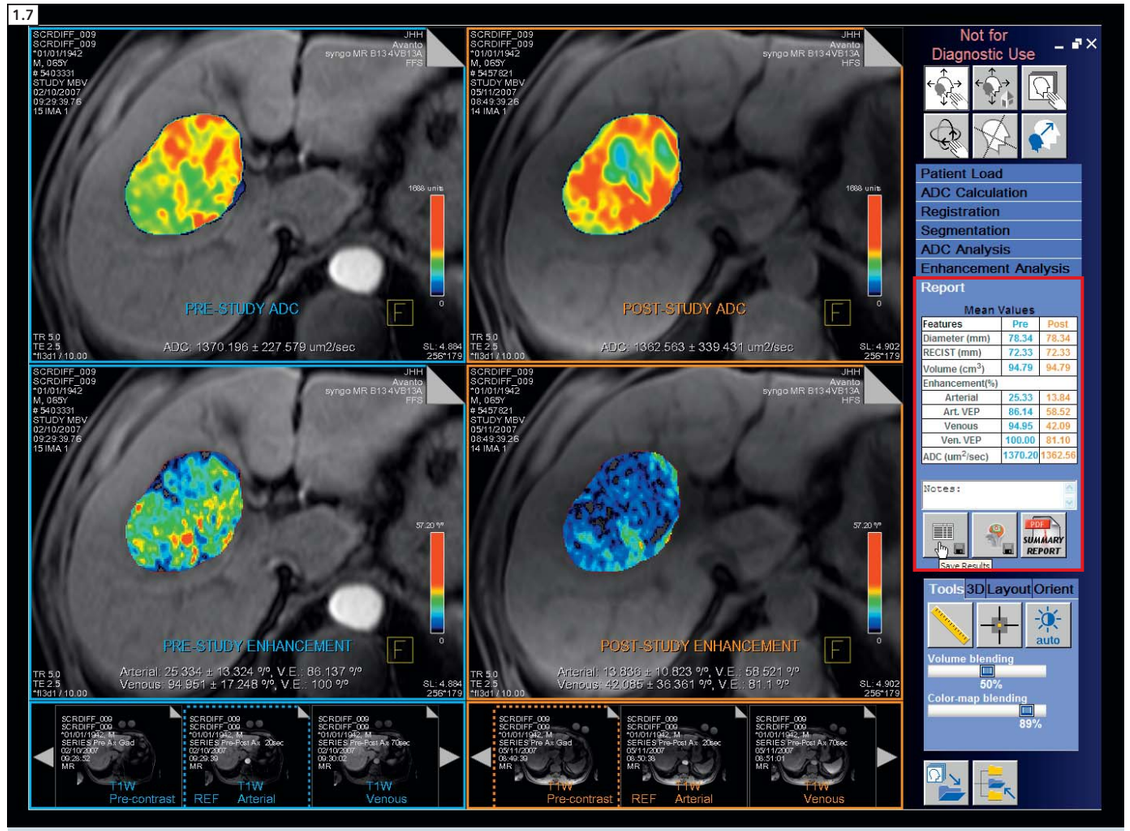

1.7 Report including overlay of ADC and enhancement values (blue = pre-treatment, orange = post-treatment) on the T1-weighted arterial phase image along with the mean values of the lesion including RECIST diameter, volume, arterial and venous enhancement as well as ADC.

Conclusion

As the cases and images above show, with the prototype of the MR Oncotreat software, volumetric MR oncologic evaluation and pixel-by-pixel comparison of pre- and post-treatment MRI is feasible, also in a clinical setting. The usage of such a software tool has the potential to overcome some of the drawbacks of current criteria for the assessment of response to treatment in HCC. We found it to be a robust method to facilitate the co-registration and segmentation of liver lesions and a great tool for assessing changes within the treated tumor. The flexible workflow in the presented prototype of the MR Oncotreat software can also be used for the assessment of liver lesions which underwent large changes in size. In these cases a rigid inter-registration is used and the tumors are segmented individually. Although a voxel-to-voxel comparison is not possible, qualitiative comparisons via histograms and physical features are already fully realized in this prototype. Further development is focusing on different aspects of the prototype including further optimization of the workflow and integration of additional imaging data.

Acknowledgements

We would like to thank Li Pan, Christine Lorentz, and Wesley Gilson from Siemens Healthcare for their assistance during this project.

2A

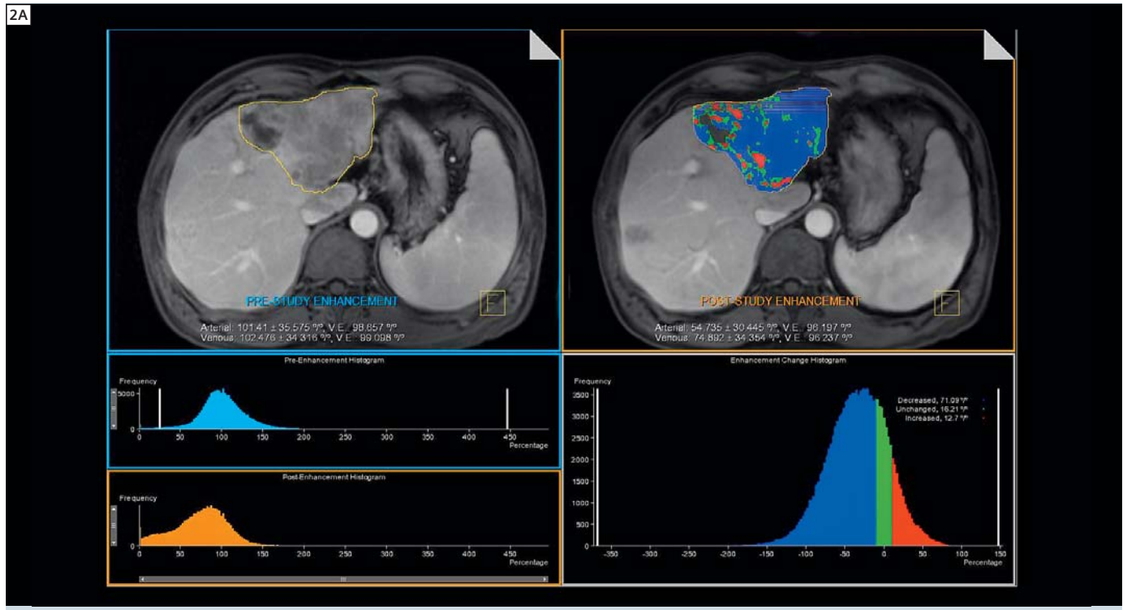

2B

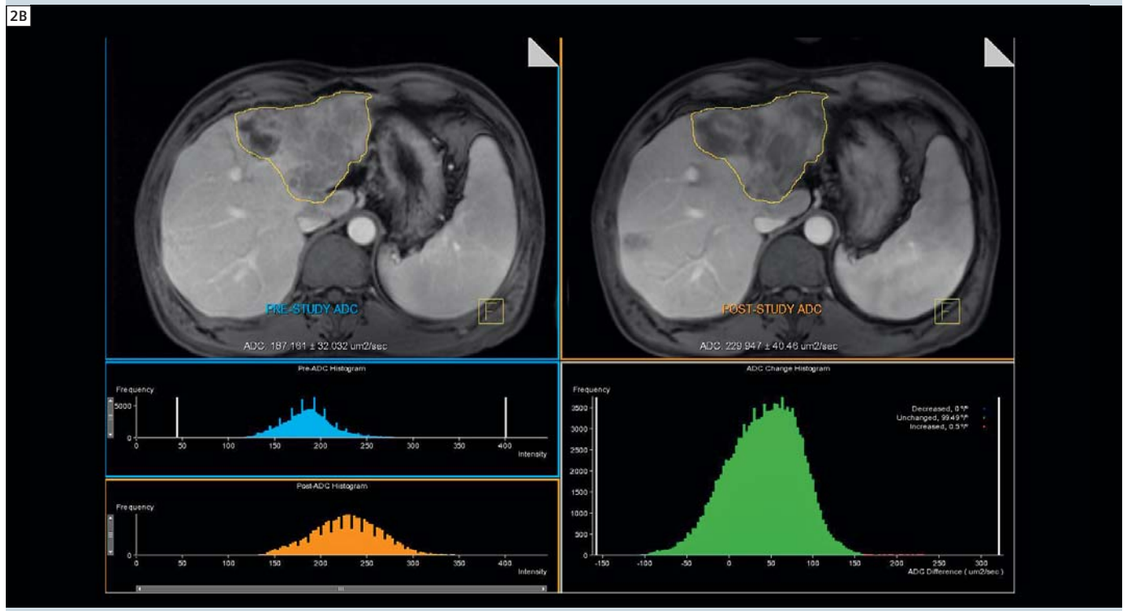

2 **A:** Venous enhancement before and after TACE in a 54-year-old male with HCC. The overlaying color map and the histograms show the change in enhancement between pre- and post-treatment (blue = decrease, green = no change, red = increase). Venous enhancement decrease in 71% of the tumor.
B: ADC histograms showing the change in ADC between pre- and post-treatment (blue = decrease, green = no change, red = increase). ADC is unchanged in 99% of the tumor. Pre- and post-treatment histograms show discrepant average ADC, however the values are below a preset threshold for significant change in diffusion. The thresholds for determining whether there was a significant change in diffusion within a voxel were determined empirically from 25 co-registered data sets.

Not for distribution in the US.

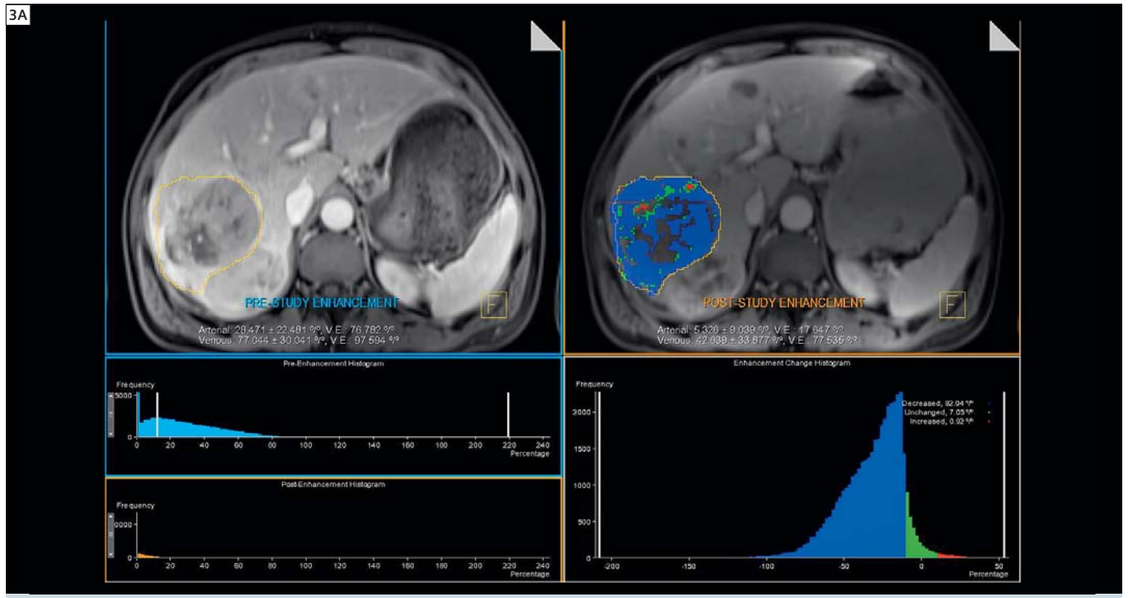

3 **A:** Venous enhancement before and after TACE in a 59-year-old male with multifocal HCC. The overlaying color map and the histograms show the change in enhancement between pre- and post-treatment (blue = decrease, green = no change, red = increase). Venous enhancement decrease in 92% of the tumor.
B: ADC color map and histograms showing the change in ADC between pre- and post-treatment (blue = decrease, green = no change, red = increase). ADC increased in 35% and decreased in 25% of the tumor.

Not for distribution in the US.

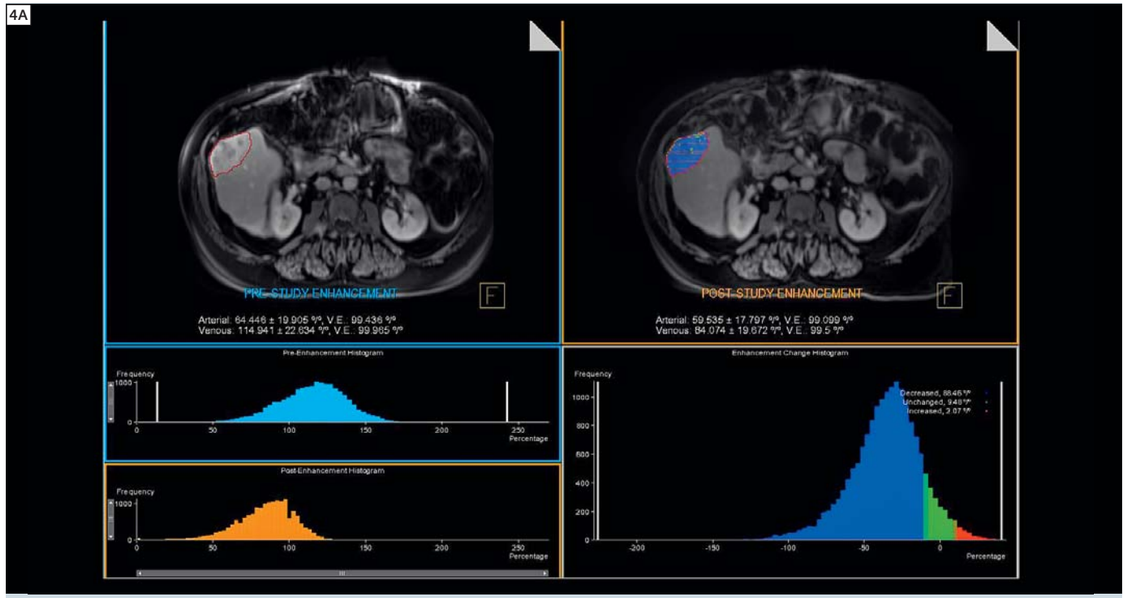

4 **A:** Venous enhancement before and after TACE in a 57-year-old female with HCC. The overlaying color map and the histograms show the change in enhancement between pre- and post-treatment (blue = decrease, green = no change, red = increase). Venous enhancement decrease in 88% of the tumor.
B: ADC color map and histograms showing the change in ADC between pre- and post-treatment (blue = decrease, green = no change, red = increase). ADC increased in ~50% of the tumor.

Not for distribution in the US.

References

1 http://seer.cancer.gov/csr/1975_2005/.
2 Espey, D. K. et al. Annual report to the nation on the status of cancer, 1975–2004, featuring cancer in American Indians and Alaska Natives. *Cancer* 110, 2119–2152 (2007).
3 Okuda, K. *et al.* Natural history of hepatocellular carcinoma and prognosis in relation to treatment. Study of 850 patients. *Cancer* 56, 918–928 (1985).
4 Proye, C. Natural history of liver metastasis of gastroenteropancreatic neuroendocrine tumors: place for chemoembolization. *World J. Surg.* 25, 685–688 (2001).
5 Choi, B. I. *et al.* Therapeutic effect of transcatheter oily chemoembolization therapy for encapsulated nodular hepatocellular carcinoma: CT and pathologic findings. *Radiology* 182, 709–713 (1992).
6 Higuchi, T., Kikuchi, M. & Okazaki, M. Hepatocellular carcinoma after transcatheter hepatic arterial embolization. A histopathologic study of 84 resected cases. *Cancer* 73, 2259–2267 (1994).
7 Khodjibekova, M. et al. Selective internal radiation therapy with Yttrium-90 for unresectable liver tumours. *Rev. Recent. Clin.* Trials 2, 212–216 (2007).
8 Khodjibekova, M. *et al.* Treatment of primary and secondary liver tumours with selective internal radiation therapy. *J. Exp. Clin. Cancer Res.* 26, 561–570 (2007).
9 Ibrahim, S. M. *et al.* Radioembolization for the treatment of unresectable hepatocellular carcinoma: a clinical review. *World J. Gastroenterol.* 14, 1664–1669 (2008)
10 Vogl, T. J. *et al.* Review on transarterial chemoembolization in hepatocellular carcinoma: palliative, combined, neoadjuvant, bridging, and symptomatic indications. *Eur. J. Radiol.* 72, 505–516 (2009).
11 Therasse, P. *et al.* New guidelines to evaluate the response to treatment in solid tumors. European Organization for Research and Treatment of Cancer, National Cancer Institute of the United States, National Cancer Institute of Canada. *J. Natl. Cancer Inst.* 92, 205–216 (2000).
12 Therasse, P., Eisenhauer, E. A. & Verweij, J. RECIST revisited: a review of validation studies on tumour assessment. *Eur. J. Cancer* 42, 1031–1039 (2006).
13 Eisenhauer, E. A. *et al.* New response evaluation criteria in solid tumours: revised RECIST guideline (version 1.1). *Eur. J. Cancer* 45, 228–247 (2009).
14 Forner, A. *et al.* Evaluation of tumor response after locoregional therapies in hepatocellular carcinoma: are response evaluation criteria in solid tumors reliable? *Cancer* 115, 616–623 (2009).
15 Wahl, R. L., Jacene, H., Kasamon, Y. & Lodge, M. A. From RECIST to PERCIST: Evolving Considerations for PET response criteria in solid tumors. *J. Nucl. Med.* 50 Suppl 1, 122S–50S (2009).
16 Kamel, I. R. & Bluemke, D. A. Magnetic resonance imaging of the liver: assessing response to treatment. *Top. Magn. Reson. Imaging* 13, 191–200 (2002).
17 Mantatzis, M., Kakolyris, S., Amarantidis, K., Karayiannakis, A. & Prassopoulos, P. Treatment response classification of liver metastatic disease evaluated on imaging. Are RECIST unidimensional measurements accurate? *Eur. Radiol.* 19, 1809–1816 (2009).
18 Assumpcao, L., Choti, M., Pawlik, T. M., Gecshwind, J. F. & Kamel, I. R. Functional MR imaging as a new paradigm for image guidance. *Abdom. Imaging* 34, 675–685 (2009).
19 Kamel, I. R. *et al.* Unresectable hepatocellular carcinoma: serial early vascular and cellular changes after transarterial chemoembolization as detected with MR imaging. *Radiology* 250, 466–473 (2009).
20 Vossen, J. A. *et al.* Diffusion-weighted and Gd-EOB-DTPA-contrast-enhanced magnetic resonance imaging for characterization of tumor necrosis in an animal model. *J. Comput. Assist. Tomogr.* 33, 626–630 (2009).
21 Mannelli, L. *et al.* Assessment of tumor necrosis of hepatocellular carcinoma after chemoembolization: diffusion-weighted and contrast-enhanced MRI with histopathologic correlation of the explanted liver. *AJR Am. J. Roentgenol.* 193, 1044–1052 (2009).
22 Kim, S. *et al.* Hepatocellular carcinoma: assessment of response to transarterial chemoembolization with image subtraction. *J. Magn. Reson. Imaging* 31, 348–355 (2010).
23 Yu, J. S., Kim, J. H., Chung, J. J. & Kim, K. W. Added value of diffusion-weighted imaging in the MRI assessment of perilesional tumor recurrence after chemoembolization of hepatocellular carcinomas. *J. Magn. Reson. Imaging* 30, 153–160 (2009).
24 Moffat, B. A. *et al.* Functional diffusion map: a noninvasive MRI biomarker for early stratification of clinical brain tumor response. *Proc. Natl. Acad. Sci. U. S. A.* 102, 5524–5529 (2005).
25 Chenevert, T. L. *et al.* Diffusion MRI: a new strategy for assessment of cancer therapeutic efficacy. *Mol. Imaging* 1, 336–343 (2002).
26 Gulsun, M., Weiss, C., Strecker, R., Meredith, G. & Kamel, I. *A new tool for volumetric and functional analysis of hepatic tumors monitored with multi-modal MRI,* 2009).
27 CHEFD'HOTEL Christophe, Hermosillo, G. & Faugeras, O. Flows of diffeomorphisms for multimodal image registration. *Proceedings of the IEEE Symposium on Biomedical Imaging* (2002).
28 Grady, L. Random walks for image segmentation. *IEEE Trans. Pattern Anal. Mach. Intell.* 28, 1768–1783 (2006).

Contact
Dr. Susanne Bonekamp
The Russell H. Morgan Department of Radiology and Radiological Science
Johns Hopkins Medical Institutions
601 North Caroline Street
JHOC 4240
Baltimore, Maryland 21287
USA
Phone: + (410) 614 5524
shemker2@jhmi.edu

Missing information?

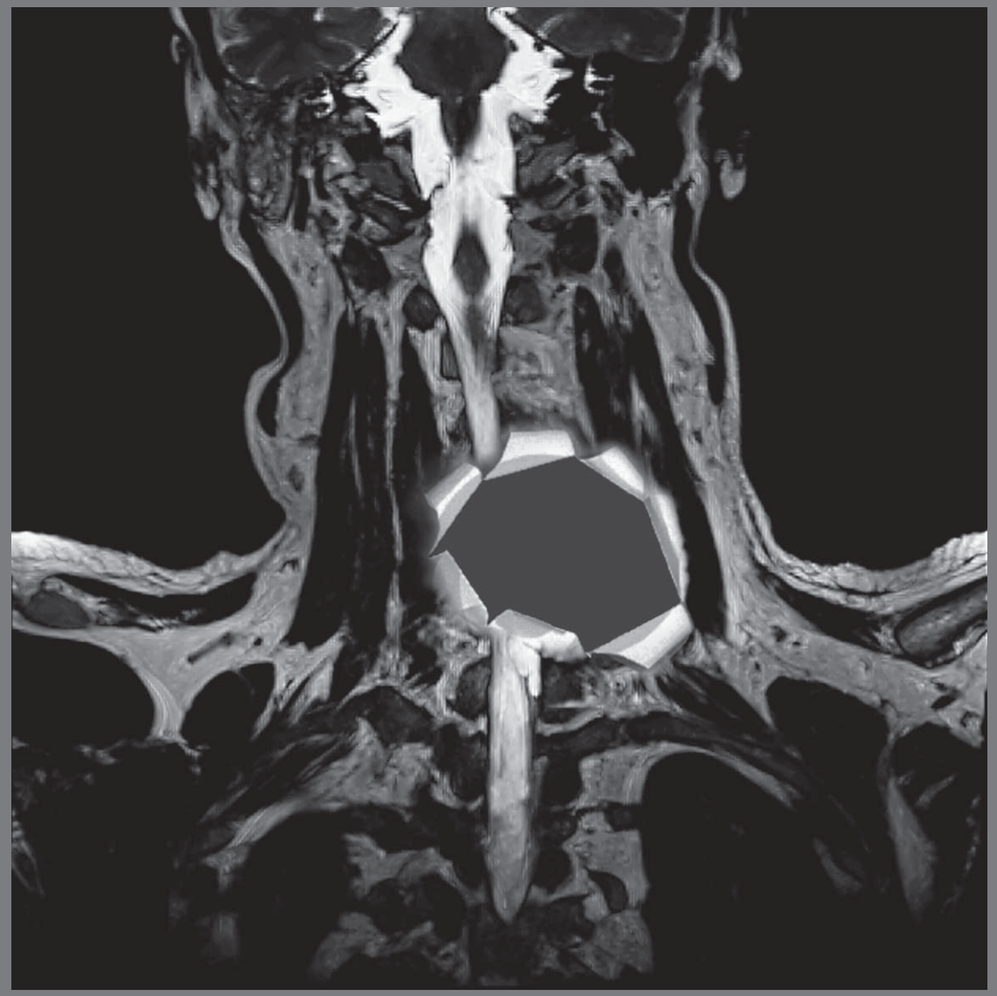

To make sure you have all the information you need, register for our free monthly newsletter on clinical MRI information.
Check out case reports from MAGNETOM users around the world and stay up-to-date with Siemens software applications.

Register at
www.siemens.com/magnetom-world
Go to
Publications > Subscriptions

Not for distribution in the US.

Not for distribution in the US.

Body Imaging at 7 Tesla with Multichannel Transmit Capability

K. Ugurbil[1]; J.T. Vaughan[1]; G.J. Metzger[1]; P.-F. van de Moortele[1]; C.J. Snyder[1]; L. DelaBarre[1]; P. Bolan[1]; E Auerbach[1]; P. Weale[2]; S. Zuehlsdorff[2]; S. Nielles-Vallespin[2,3]; R. Jerecic[2]

[1]*Center for Magnetic Resonance Research (CMRR), Dept. of Radiology, University of Minnesota, Minneapolis, USA*
[2]*Siemens Healthcare*
[3]*Current address: Royal Brompton Hospital, London, UK*

In the last two decades, a plethora of magnetic resonance (MR) techniques, such as functional magnetic resonance imaging (fMRI), have come to play an indispensable role in the neurosciences. In our laboratory, the Center for Magnetic Resonance Research (CMRR) at the University of Minnesota, the evolution of such methods has been intricately tied with the development of high field MR, starting with the installation of one of the first three 4 Tesla (T) scanners in approximately 1990, followed by the establishment of the very first 7 Tesla system in 1999 (e.g. reviews [1–5]).
The development of this 7T scanner for human imaging was justified based on the results of numerous human and animal model studies conducted at 4 and 9.4T, respectively, in our lab through the mid-nineties. These studies demonstrated that despite many contravening notions of the time, high magnetic fields could provide significant advantages.
Using this first ultra-high[1] field 7T system, we were able to demonstrate that challenges faced at such field strengths in human imaging could be overcome. Although it is taken for granted today, at the time we started working with 7T, even field-dependent signal-to-noise ratio (SNR) gains in the human head were questioned. In one of first 7T studies, however, we were able to experimentally demonstrate for the first time that SNR does increase with magnetic field in the human head, though this increase was complex and spatially non-uniform [6]. More importantly, over the years, 7T has been shown to provide unique anatomical, functional and physiologic information beyond just gains in SNR (e.g. [7–11]). With the rapidly increasing number of recent 7T installations, demonstration of such unique uses of ultra-high fields is also rapidly blooming.
For approximately a decade, 7T studies were restricted to the human head. Ever since the discouraging early 4T results from manufacturers' laboratories [12], the human torso has been considered too difficult to tackle at ultra-high fields. The large B_1 and signal intensity inhomogeneities noted in these early 4T head and body images were ascribed to "dielectric resonances". However, some of the first experiments we conducted at 7T to understand the RF behavior in the human body at the proton Larmor frequency at this field strength (300 MHz) indicated that we are not dealing with a "resonance" phenomenon. Rather, in a paper we and our collaborators from Penn State University published in 2001 [13], we concluded that 300 MHz RF behaves as a damped traveling wave in the human body and that (to quote from our original paper) "the characteristic image intensity distribution in the human head is the result of spatial phase distribution and amplitude modulation by the interference of the RF traveling waves determined by a given sample-coil configuration". Later studies further confirmed that when the object size exceeds the wavelength of the RF used, we operate in the damped traveling wave regime, leading to large and spatially rapid phase variations over the object, resulting in destructive interferences [14] and these destructive interferences are responsible for the spatially non-uniform SNR gains that was noted in our earlier study [6]. This was in fact good news: Resonance phenomena are difficult to deal with for recovering signal where there is virtually none; but destructive interferences due to traveling waves can be managed to extract full SNR gains intrinsically provided by increasing magnetic fields.
This complex RF behavior at ultra-high fields in fact turns out to be a major advantage for signal reception, leading to significantly better parallel imaging performance on the receive side at 7T or above. Thus, as the magnetic field increases, spatial encoding information provided by the receive array replaces k-space data to a larger extend due to the complex RF phase and amplitude over the sample [15–17]. However, the consequences of damped traveling wave behavior is a major problem on the transmit side and it is particularly severe in the human body where the object size is 4 to 6 (or more) times larger than the 300 MHz wavelength, which is ~12 cm in human tissues such as muscle and brain.

Figure 1 illustrates electro-dynamic simulations taken from our recent paper [18] for the human body at 7T: The RF field and SAR were modeled by the finite difference time domain (FDTD) method, for a "body" coil at 7T with and without the human body loading the coil.
The circularly polarized transmit B_1 (i.e. B_1^+) field magnitude generated in the unloaded body coil shown in figure 1 was *uniform* in a cylindrical volume with a length slightly less than the length of the resonant elements in this coil (33 cm). The axial plane shown in figure 1 (top row, left) is for a slice in the center of this volume. Despite the uniformity of B_1^+ in the *unloaded* coil, upon loading with a human body, the magnetic field and consequently power deposition becomes extremely non-uniform (Fig. 1, lower part). There are regions in the center of the body where there is virtually no RF (light blue color). Note that highest intensity of the B_1^+ and the largest SAR is in the human head, even though the head is significantly outside the coil and that when unloaded the coil does not have any significant B_1^+ in the region where the head is.
Our solution to the destructive interferences induced by traveling waves has been the use of multichannel parallel transmit (pTx) with channel-specific independent control [19–22, 18]. With this approach, the B_1^+ fields can be targeted and homogenized over a predefined region, enabling body imaging for the first time in the human torso at 7T [23, 24, 18]. The strategy is not to aim for a homogeneous image over the entire slice but rather over the targeted organ. Figure 2 illustrates the cardiac set-up, the B_1^+ distribution before and after B_1^+ optimization over the heart (images in color) and the resultant cardiac image at 7T. In this approach, we employ a dual 8-channel transmit and receive array placed one above and one below the human torso for a total of 16 transmit and receive elements (Fig. 2). Excellent quality cardiac images were also obtained using a more traditional circumscribing TEM body coil but driven as a 16-channel transmit and receive array [18]. Two cardiac imaging examples from such a body coil are illustrated in figure 3. Functional cardiac cines of these and other cardiac images can be found at http://www.cmrr.umn.edu/research/videos/. We have had similar success with imaging the prostate [23] and the kidney (unpublished results), demonstrating the feasibility of excellent high resolution torso imaging at 7T (Fig. 3).
So far, we have employed multichannel transmit only for "B_1^+shimming" but not for generating spatially targeted pulses (e.g. [25–28]) using transmit SENSE principles [29, 30]. In the B_1^+shimming approach, all pTx channels transmit the same RF pulse waveform but with differing phases and/or amplitudes. This approach is particularly suitable in body imaging where the targeted organ is often much smaller then the dimensions of the torso, which dictates the dimensions of the RF transmit array to be used. When the target covers a small portion of the entire field of view, optimizing the B_1^+ over this target in fact results in decreases in power deposition (SAR) [23], which is a major confound at ultra-high field applications. Spatially tailored pulses, on the other hand rely on different modulation patterns on each channel, which can be generated on the Siemens pTx system. Such pulses have been known

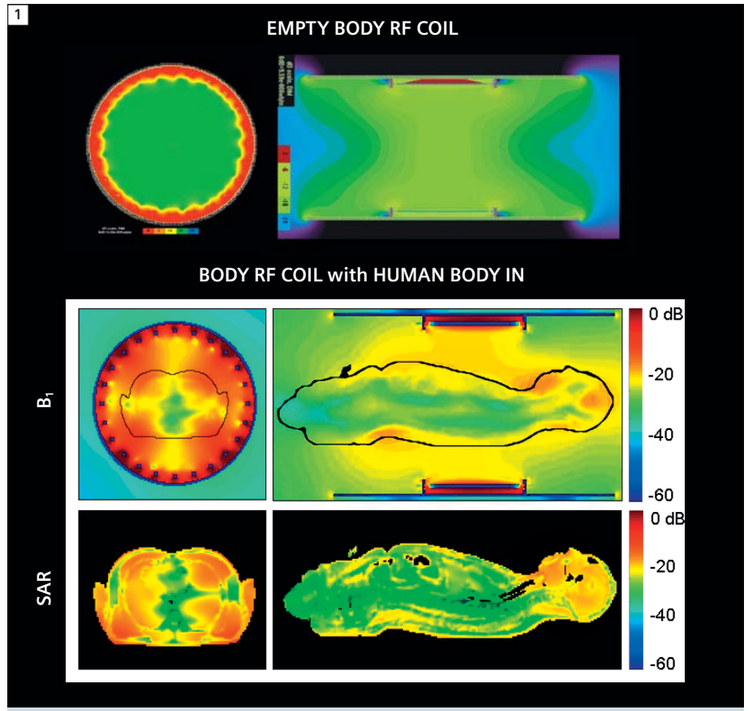

1 B_1 and SAR calculations for a TEM Body RF coil tuned to 300 MHz with and without the human body in the coil. The body model used was derived from the National Library of Medicine (NLM) Visual Human digital atlas whose segmented anatomy was adjusted to match the conductivity and permittivity of tissues at 300 MHz. The coil was driven at four ports (45°, 135°, 225°, and 315°).

[1] The radiofrequency band 300 MHz to 3 GHz is defined as Ultra high frequency (UHF) (see http://en.wikipedia.org/wiki/Ultra_high_frequency). The hydrogen nucleus resonance frequency at 7T is 300 MHz i.e. in UHF band. Therefore, 7T to 70T can be defined as Ultra High Field (UHF).

Not for distribution in the US.

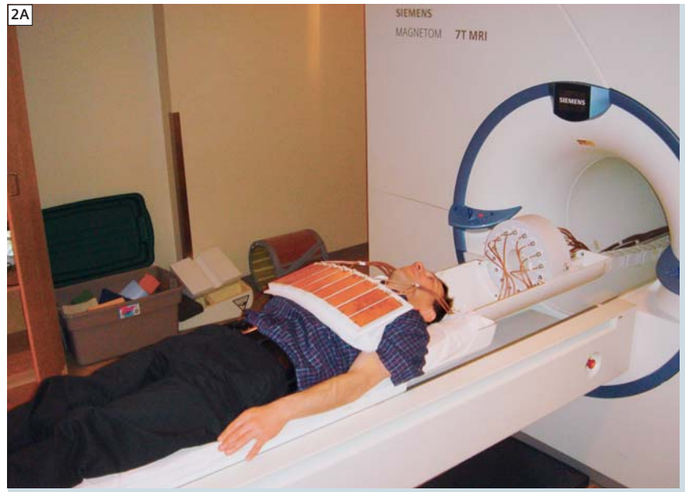

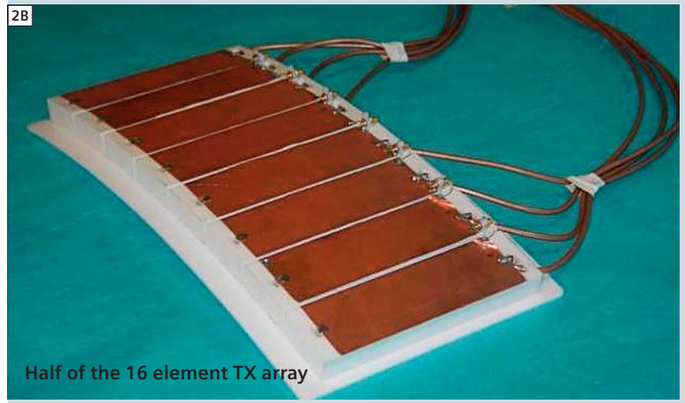

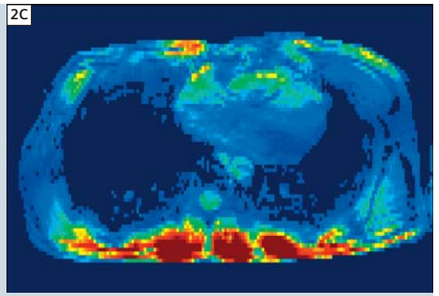

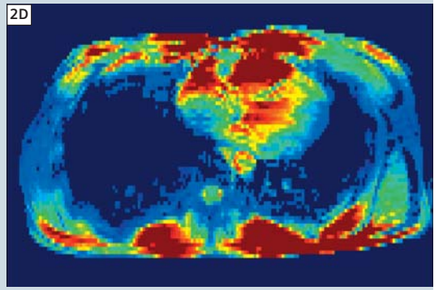

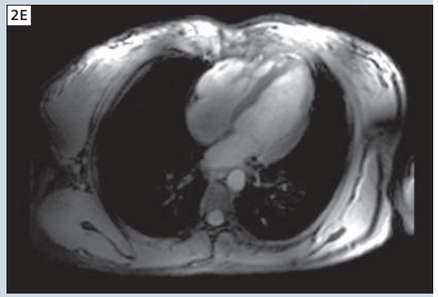

2 The multichannel transmit and receive array coil that is used for body imaging at 7T. Only the 8 elements positioned superior to the subject are shown. An identical unit is placed below the subject. The images in color display the B_1^+ map before and after optimization over the heart. Lower right shows the resulting cardiac image at 7T. TR/TE=45/3.06 ms; 2.0 x 2.0 x 5.5 mm resolution; Matrix size 144 x 192; Breath held and ECG retrogated; Snyder, et. al. MRM 61, 517 (2009); Vaughan, et. al. MRM 61, 244 (2009)

for some time; however, they are typically very long when applied with a single transmit channel and as such not practical in most human applications. The use of pTx capability, however, enables the spatial encoding to be performed in part by the coil transmit sensitivity profiles, leading to a significant shortening of the pulse. This shortening, however, results in substantial increases in peak voltage that must be used, and hence SAR. Strategies to control this SAR amplification are pursued in several laboratories and will be critical in successfully using this approach. The number of channels employed likely plays an important role in SAR deposition with pTx applications. Just as in spatial encoding with multichannel receive to replace k-space encoding [15–17], spatial encoding to shorten the k-space trajectory in spatially targeted RF pulses works much more efficiently as the relative object size gets larger. Thus, the acceleration factors that can be achieved to shorten otherwise extremely long, and, as such, impractical pulses also improve with higher magnetic fields and with a larger object size. Thus, one solution to the ultra-high field transmit RF non-uniformity problem is actually a strategy that works particularly well in ultra-high fields. Provided that SAR limitations can be overcome, spatially targeted pulses applied using pTx introduces the possibility of applications beyond just B_1 flattening, such as restricted FOV

Not for distribution in the US.

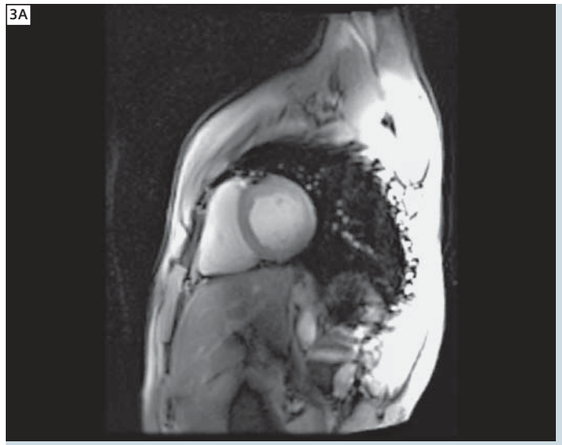

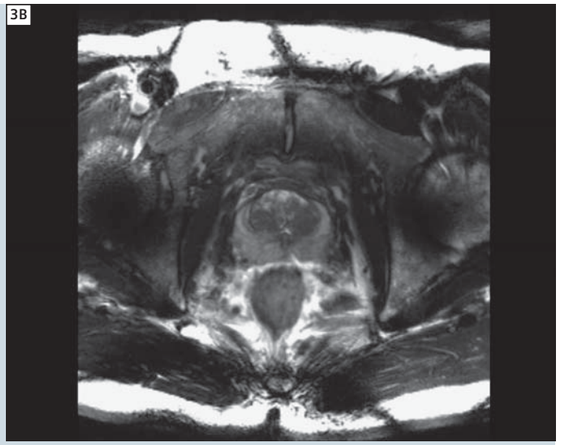

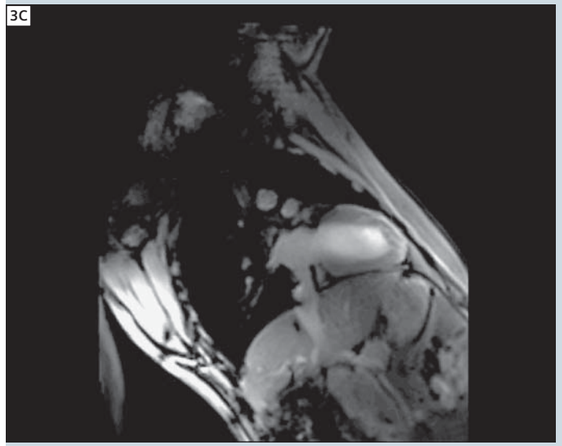

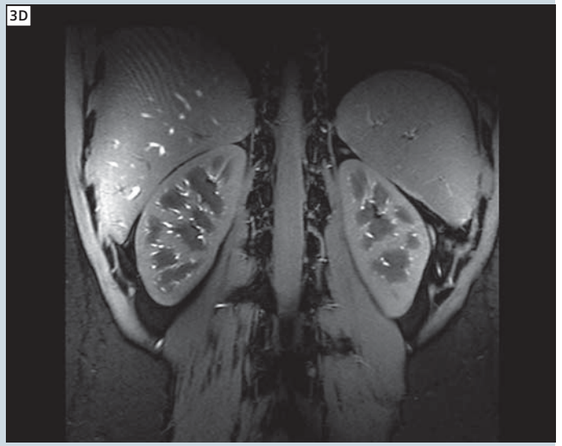

3 7T body images with targeted B_1 shimming using 16-channel pTx capability; cardiac images (on two different planes), a transaxial image through the torso at the level of prostate and a coronal plane through the kidneys obtained using pTx and multichannel receive technology. Note that while there exists strong non-uniformities in the entire image, the image over the targeted organ(s) (heart, prostate and kidneys) is relatively uniform.

"zoomed" imaging, vessel selective angiography etc.
These initial results are a prelude to dramatic improvements that are sure to come in body imaging using pTx methodology and enabling the exploitation of advantages provided by ultrahigh fields, such as improved SNR, improved contrast in many instances, longer T1 times of blood, and improved parallel imaging. In particular, many SNR limited applications in the body, such as angiography and perfusion imaging without using an exogenous contrast agent, vessel wall imaging, high resolution imaging of pathology and of musculoskeletal structures and high resolution spectroscopy, to name a few potential applications, will come to exist and will be further enhanced even at higher magnetic fields. Finally, it is inevitable that these successes will impact, in some fashion, how we do body imaging at the lower magnetic field of 3 or even 1.5T.

Contact
Professor Kamil Ugurbil, Ph.D.
Center for Magnetic Resonance Research
Dept. of Radiology
University of Minnesota
Minneapolis, 55455
USA
kamil@cmrr.umn.edu

Not for distribution in the US.

References

1 Ugurbil, K., G. Adriany, P. Andersen, W. Chen, M. Garwood, R. Gruetter, P.G. Henry, S.G. Kim, H. Lieu, I. Tkac, T. Vaughan, P.F. Van De Moortele, E. Yacoub, and X.H. Zhu, *Ultrahigh field magnetic resonance imaging and spectroscopy. Magn Reson Imaging,* 2003. 21(10): p. 1263–81.

2 Ugurbil, K., L. Toth, and D.S. Kim, *How accurate is magnetic resonance imaging of brain function?* Trends Neurosci, 2003. 26(2): p. 108–14.

3 Harel, N., K. Ugurbil, K. Uludag, and E. Yacoub, *Frontiers of brain mapping using MRI.* J Magn Reson Imaging, 2006. 23(6): p. 945–57.

4 Ugurbil, K., G. Adriany, C. Akgün, P. Andersen, W. Chen, M. Garwood, R. Gruetter, P.-G. Henry, M. Marjanska, S. Moeller, P.-F. Van de Moortele, K. Prüssmann, I. Tkac, J.T. Vaughan, F. Wiesinger, E. Yacoub, and X.-H. Zhu, *High Magnetic Fields for Imaging Cerebral Morphology, Function and Biochemistry, in Biological Magnetic Resonance: Ultra High Field Magnetic Resonance Imaging*, P.M.L. Robitaille, and Berliner, L.J., Editor. 2006, Springer: New York. p. 285–342.

5 Ugurbil, K., W. Chen, N. Harel, P.-F. Van de Moortele, E. Yacoub, X.H. Zhu, and K. Uludag, *Brain Function, Magnetic Resonance Imaging of, in Wiley Encyclopedia of Biomedical Engineering*, M. Akay, Editor. 2006, John Wiley & Sons, Inc: Hoboken. p. 647–668.

6 Vaughan, J.T., M. Garwood, C.M. Collins, W. Liu, L. DelaBarre, G. Adriany, P. Andersen, H. Merkle, R. Goebel, M.B. Smith, and K. Ugurbil, *7T vs. 4T: RF power, homogeneity, and signal-to-noise comparison in head images.* Magn Reson Med, 2001. 46(1): p. 24–30.

7 Duyn, J.H., P. van Gelderen, T.Q. Li, J.A. de Zwart, A.P. Koretsky, and M. Fukunaga, *High-field MRI of brain cortical substructure based on signal phase.* Proc Natl Acad Sci U S A, 2007. 104(28): p. 11796–801.

8 Rooney, W.D., G. Johnson, X. Li, E.R. Cohen, S.G. Kim, K. Ugurbil, and C.S. Springer, Jr., *Magnetic field and tissue dependencies of human brain longitudinal 1H2O relaxation in vivo.* Magn Reson Med, 2007. 57(2): p. 308–18.

9 Yacoub, E., A. Shmuel, N. Logothetis, and K. Ugurbil, *Robust detection of ocular dominance columns in humans using Hahn Spin Echo BOLD functional MRI at 7 Tesla.* Neuroimage, 2007. 37(4): p. 1161–77.

10 Cho, Z.H., C.K. Kang, J.Y. Han, S.H. Kim, K.N. Kim, S.M. Hong, C.W. Park, and Y.B. Kim, *Observation of the lenticulostriate arteries in the human brain in vivo using 7.0T MR angiography.* Stroke, 2008. 39(5): p. 1604–6.

11 Yacoub, E., N. Harel, and K. Ugurbil, *High-field fMRI unveils orientation columns in humans.* Proc Natl Acad Sci U S A, 2008. 105(30): p. 10607–12.

12 Barfuss, H., H. Fischer, D. Hentschel, R. Ladebeck, A. Oppelt, R. Wittig, W. Duerr, and R. Oppelt, *In vivo magnetic resonance imaging and spectroscopy of humans with a 4 T whole-body magnet.* NMR Biomed, 1990. 3(1): p. 31–45.

13 Yang, Q.X., J. Wang, X. Zhang, C.M. Collins, M.B. Smith, H. Liu, X.H. Zhu, J.T. Vaughan, K. Ugurbil, and W. Chen, *Analysis of wave behavior in lossy dielectric samples at high field.* Magn Reson Med, 2002. 47(5): p. 982–989.

14 Van de Moortele, P.F., C. Akgun, G. Adriany, S. Moeller, J. Ritter, C.M. Collins, M.B. Smith, J.T. Vaughan, and K. *Ugurbil, B(1) destructive interferences and spatial phase patterns at 7 T with a head transceiver array coil.* Magn Reson Med, 2005. 54(6): p. 1503–18.

15 Ohliger, M.A., A.K. Grant, and D.K. Sodickson, *Ultimate intrinsic signal-to-noise ratio for parallel MRI: electromagnetic field considerations.* Magn Reson Med, 2003. 50(5): p. 1018–30.

16 Wiesinger, F., P.F. Van de Moortele, G. Adriany, N. De Zanche, K. Ugurbil, and K.P. Pruessmann, *Parallel imaging performance as a function of field strength--an experimental investigation using electrodynamic scaling.* Magn Reson Med, 2004. 52(5): p. 953–64.

17 Wiesinger, F., P.F. Van de Moortele, G. Adriany, N. De Zanche, K. Ugurbil, and K.P. Pruessmann, *Potential and feasibility of parallel MRI at high field.* NMR Biomed, 2006. 19(3): p. 368–78.

18 Vaughan, J.T., C.J. Snyder, L.J. DelaBarre, P.J. Bolan, J. Tian, L. Bolinger, G. Adriany, P. Andersen, J. Strupp, and K. Ugurbil, *Whole-body imaging at 7T: preliminary results.* Magn Reson Med, 2009. 61(1): p. 244–8.

19 Vaughan, J., RF coil for imaging system. 2003: USA patent 6,633,161.

20 Adriany, G., P.F. Van de Moortele, F. Wiesinger, S. Moeller, J.P. Strupp, P. Andersen, C. Snyder, X. Zhang, W. Chen, K.P. Pruessmann, P. Boesiger, T. Vaughan, and K. Ugurbil, *Transmit and receive transmission line arrays for 7 Tesla parallel imaging.* Magn Reson Med, 2005. 53(2): p. 434–445.

21 Vaughan, J., G. Adriany, K. Ugurbil, J. Strupp, and P. Andersen, *University of Minnesota, assignee. Parallel Transceiver for Nuclear Magnetic Resonance System.* 2005, University of Minnesota: USA 6,969,992.

22 Vaughan, T., L. DelaBarre, C. Snyder, J. Tian, C. Akgun, D. Shrivastava, W. Liu, C. Olson, G. Adriany, J. Strupp, P. Andersen, A. Gopinath, P.F. van de Moortele, M. Garwood, and K. Ugurbil, *9.4T human MRI: preliminary results.* Magn Reson Med, 2006. 56(6): p. 1274–82.

23 Metzger, G.J., C. Snyder, C. Akgun, T. Vaughan, K. Ugurbil, and P.F. Van de Moortele, *Local B_1^+ shimming for prostate imaging with transceiver arrays at 7T based on subject-dependent transmit phase measurements.* Magn Reson Med, 2008. 59(2): p. 396–409.

24 Snyder, C.J., L. DelaBarre, G.J. Metzger, P.F. van de Moortele, C. Akgun, K. Ugurbil, and J.T. Vaughan, *Initial results of cardiac imaging at 7 Tesla.* Magn Reson Med, 2009. 61(3): p. 517–24.

25 Setsompop, K., L.L. Wald, V. Alagappan, B. Gagoski, F. Hebrank, U. Fontius, F. Schmitt, and E. Adalsteinsson, *Parallel RF transmission with eight channels at 3 Tesla.* Magn Reson Med, 2006. 56(5): p. 1163–71.

26 Setsompop, K., V. Alagappan, A.C. Zelinski, A. Potthast, U. Fontius, F. Hebrank, F. Schmitt, L.L. Wald, and E. Adalsteinsson, *High-flip-angle slice-selective parallel RF transmission with 8 channels at 7 T.* J Magn Reson, 2008. 195(1): p. 76–84.

27 Zelinski, A.C., L.L. Wald, K. Setsompop, V. Alagappan, B.A. Gagoski, V.K. Goyal, and E. Adalsteinsson, *Fast slice-selective radio-frequency excitation pulses for mitigating B+1 inhomogeneity in the human brain at 7 Tesla.* Magn Reson Med, 2008. 59(6): p. 1355–64.

28 Wu, X., J.T. Vaughan, K. Ugurbil, and P.F. Van de Moortele, *Parallel excitation in the human brain at 9.4 T counteracting k-space errors with RF pulse design.* Magn Reson Med, 2010. 63(2): p. 524–9.

29 Katscher, U., P. Bornert, C. Leussler, and J.S. van den Brink, *Transmit SENSE.* Magn Reson Med, 2003. 49(1): p. 144–50.

30 Grissom, W.A., C.-Y. Yip, and D.C. Noll, *An image domain approach for the design of RF pulses in transmit SENSE.* Proc. Intl. Soc. Mag. Reson. Med., 2005. 13: p. 19.

Not for distribution in the US.

Specific Absorption Rate (SAR) in Parallel Transmission (pTx)

Lawrence L. Wald[1]; Elfar Adalsteinsson[1,2]

[1]*Athinoula A. Martinos Center for Biomedical Imaging, Department of Radiology, Massachusetts General Hospital. Harvard Medical School and Harvard-MIT Division of Health Sciences and Technology, Boston, MA, USA*
[2]*Department of Electrical Engineering and Computer Science, Massachusetts Institute of Technology, Boston, MA, USA*

Introduction

Parallel transmission (pTx) uses multiple excitation coils driven by independent RF pulse waveforms to subdivide the transmit field into multiple spatial regions each controlled by a separate transmit channel. Increasing the number of spatially distinct transmit elements and temporally distinct RF pulse waveforms compared to conventional single-channel RF systems creates spatial degrees of freedom that allow the spatial information in the array to be exploited in the excitation process. Previous pTx work has concentrated on the potential to utilize this additional flexibility in spatial information to move beyond the uniform slice-select excitation to generate spatially tailored RF pulses; excitation pulses with a carefully controlled spatially varying flip angle pattern or excitation phase that can mitigate artifacts or isolate specific anatomy. Operating in analogy to parallel reception, parallel transmission offers the possibility to move beyond the uniform slice-select excitation and create a more anatomy-specific excitation which could mitigate drop-out regions from inhomogeneous excitation fields at 3T or 7T, reduce image encoding needs (e.g. for cardiac or shoulder imaging) by reducing the needed field-of-view, allow selective spin-tagging excitations (potentially allowing vessel territory perfusion imaging), or simply provide clinically useful but non-traditional excitations such as curved saturation bands for the spine or brain.

While the development of these novel RF pulse designs and applications continue to be an area of intense development, the clinical utility of a given RF excitation pulse is characterized by more than just its spatial fidelity. The Specific Absorption Rate (SAR) of an excitation pulse is often the critical limiting factor when applied to a clinical imaging sequence. The need to stay below safe SAR limits often requires unfavorable tradeoffs in acquisition parameters such as increased TR or reduced flip angle. This is especially problematic at 3T, where the power needed for a given flip angle increases as much as 4 fold compared to 1.5T applications, and thus the SAR ceiling is acutely felt.

Fortunately, while the use of parallel transmission creates some SAR problems of its own (such as the need to carefully monitor for local SAR hotspots in a specific RF pulse design), the spatial degrees of freedom that give rise to the wealth of spatial design potential also offers novel opportunities for SAR manipulation. While attempts to minimize SAR during the design of parallel transmit pulses has been ongoing since the first pTx papers, the full potential of our ability to manipulate these degrees of freedom as well as the engineering solutions needed to realize SAR reduction and management via pTx are just appearing.

In this article we review some of the progress which has been made toward strategies for reducing SAR with pTx in a prototype Siemens MAGNETOM Trio, a Tim System, and a MAGNETOM 7T. We review the pTx SAR problem and discuss some of the recent advances in calculating parallel transmit RF pulses for spatially tailored excitation with optimization methods which penalize global and local SAR. Further, we describe some recent advances in real-time SAR monitoring as well as outstanding issues that must be overcome for routine application.

SAR in spatially tailored excitations

To achieve an arbitrary spatial flip angle distribution after excitation, we modulate the RF waveform in amplitude and phase during a time-varying gradient waveform. These "spatially tailored" RF excitations have been pursued for more than two decades [1]. The design procedure is illustrated in figure 1, where the Fourier transform of the desired pattern is sampled on a spiral excitation k-space trajectory to produce the amplitude and phase modulations needed during the gradient waveform.

Although spatially tailored excitation pulses are easily demonstrated, there are serious engineering challenges to their routine and practical use. First and foremost is the lengthy and largely impractical encoding period needed (as long as 50 ms). Parallel excitation directly addresses this problem by allowing the

Not for distribution in the US.

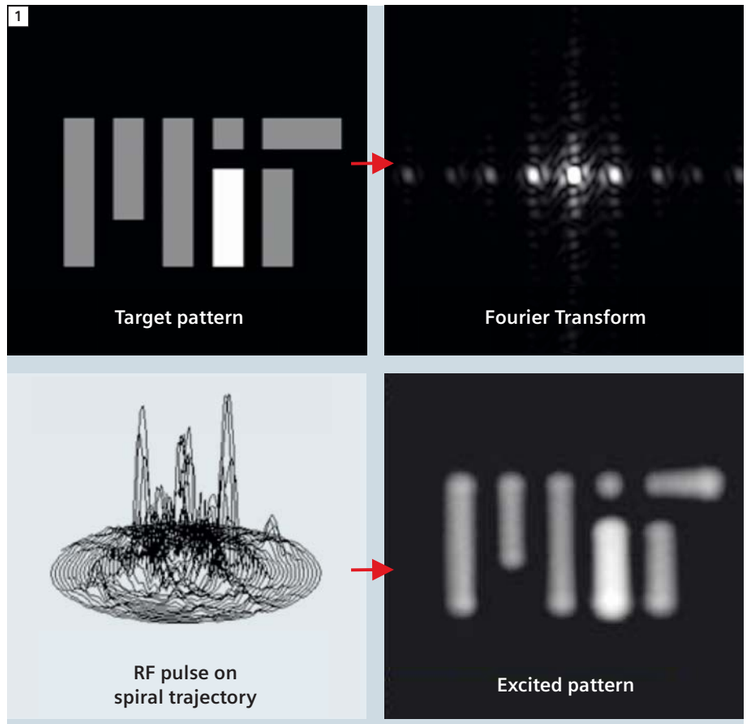

1 The design of a spatially tailored excitation starts with a choice of a spatial target pattern (in this case the MIT logo), and a gradient trajectory such as the spiral trajectory shown. The Fourier transform of the target pattern is used to modulate the amplitude and phase of the RF excitation waveform to achieve the desired distribution in excitation k-space. The RF waveform is played out during the gradient trajectory resulting in the desired excited magnetization pattern.

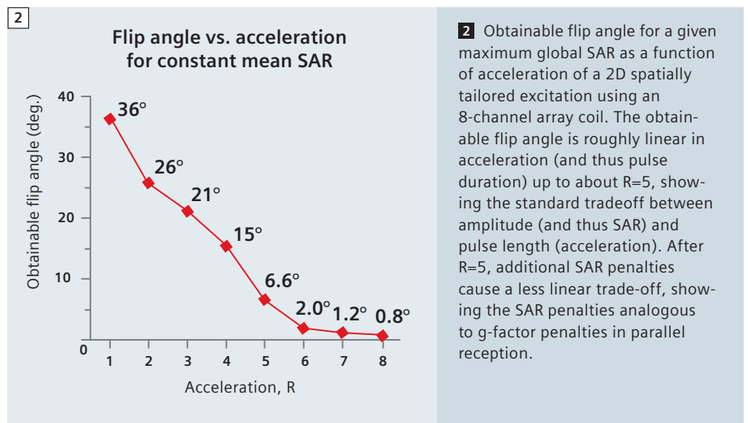

2 Obtainable flip angle for a given maximum global SAR as a function of acceleration of a 2D spatially tailored excitation using an 8-channel array coil. The obtainable flip angle is roughly linear in acceleration (and thus pulse duration) up to about R=5, showing the standard tradeoff between amplitude (and thus SAR) and pulse length (acceleration). After R=5, additional SAR penalties cause a less linear trade-off, showing the SAR penalties analogous to g-factor penalties in parallel reception.

"excitation k-space" trajectory to be undersampled, analogous to the reductions in encoding trajectory steps in parallel reception, but with some interesting contrasting properties. For instance, in accelerated parallel reception we are often limited by the image Signal-to-Noise Ratio (SNR) losses associated with the procedure. In parallel transmission, the RF waveforms take the position mathematically analogous to the final image in parallel reception and start with extraordinary high SNR since they are generated with robust digital-to-analog technology. Therefore, even with a modest 8-channel transmit array, we can reduce the duration of the pulse up to 6 fold without suffering from noise enhancement of the calculated RF pulse waveforms [2, 3]. Note that this level of acceleration would be difficult to achieve in parallel reception.

Instead, it is the SAR of the excitation that constitutes the limiting penalty in accelerating spatially tailored excitations with parallel transmission, with a secondary limitation arising from artifacts in the transmitted pattern due to imperfect knowledge of the array coil excitation profiles. The dramatic increase in SAR with acceleration can be understood intuitively. First, as the pulse length is reduced, the amplitude must be increased accordingly to achieve a given pulse area (flip angle). Increases in pulse amplitudes are expensive in SAR since the SAR increases with the square of the applied RF voltage. As a square pulse is shortened, the pulse amplitude must be increased linearly to maintain a given flip angle (pulse area). The instantaneous SAR thus increases inversely with the square of the duration, and the SAR associated with the use of this pulse within a fixed TR pulse sequence also increases linearly. Figure 2 demonstrates this effect for an eight-channel loop array at 7T as a nearly linear decrease in obtainable flip angle for a given global SAR value as a spatially tailored 2D excitation is accelerated by factor R via undersampling of its excitation k-space trajectory.

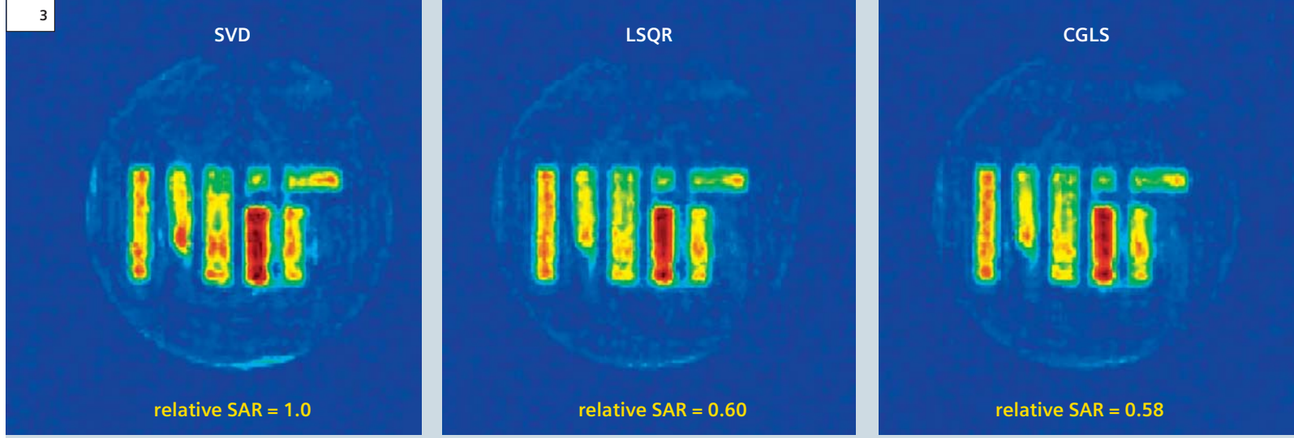

3 Accelerated spiral trajectory pulses with R=4 acceleration with approximately equal RMSE compared to the target pattern ("MIT" logo), but with the least-squares optimization performed with either the SVD, LSQR or CGLS method. In this case the global SAR was considerably lower for the LSQR or CGLS method compared to SVD. During the original work, we did not analyze the local SAR pattern, but now hypothesize that the local SAR pattern will be even more different among the three solutions.

Second, the impressive spatial definition of pTx excitation patterns obtained by these pulses come at a cost in SAR. The spatial pattern is achieved by temporally modulating the RF pulse in the presence of time-varying gradient waveforms, causing phase shifts in the excited magnetization that superimpose over time to achieve the desired pattern. Unfortunately, temporally modulating a pulse in amplitude or phase tends to create instances of higher peak power (as well temporal nulls in the pulse voltage) as the RF pulse deposits the requisite energy along the traversed excitation trajectory. Again the fact that instantaneous SAR is proportional to the square of the pulse waveform enhances the problem. Due to the nonlinear relationship between pulse amplitude and instantaneous SAR, the nulls do not counterbalance the increased peak values when the SAR is integrated over the pulse duration. This leads to increased SAR whenever a pulse is temporally modulated.

When the spatially tailored excitation strategy is generalized to multiple RF excitation channels, the excitation pattern is not simply the Fourier transform of the excitation k-space, but is determined from a linear model of the undersampled Fourier encoding and the spatial profiles of the transmit coils. This over-determined linear model is inverted to yield the needed RF waveforms. The optimization process used to invert the over-determined linear problem also gives rise to procedures for managing SAR. The simplest cost function for the optimization includes only a cost for the difference between actual excitation pattern and the original target. It is also straight forward to include a cost for the average pulse amplitude, thus acknowledging the cost of increased global SAR in the optimization. An obvious choice would be to also penalize local SAR by including the peak local SAR value in the cost function. Methods for rendering this latter approach computationally tractable are discussed below.

Aside from direct regularization procedures for global and local SAR such as the cost function modifications mentioned above, the pulse optimization offers multiple other possibilities for controlling local and global SAR. The next sections illustrate some of the approaches being pursued.

One-pulse design problem; many solutions

The first insight into controlling local and global SAR comes from the observation that the linear optimization problem generates many possible pulses with spatially similar transverse magnetization patterns, but which differ in other properties. Figure 3 illustrates one aspect of this finding by showing magnetization patterns obtained from 2D spiral-based pTx excitation patterns accelerated by R=4 for an 8 channel loop array at 7T. The optimization problem was identically posed, attempting to spatially match a target pattern (flip angle distribution in the shape of the MIT logo) with an additional term in the cost function penalizing the root-mean-squared (RMS) waveform average (proportional to global SAR). While it was expected that the three numerical approaches might obtain different degrees of accuracy, or have different computation burdens, the methods, in fact, produced very similar spatial solutions but with strikingly different global SAR. The SAR reduction amounted to 40% for the Least Squares QR decomposition (LSQR) and Conjugate Gradient Least Squares (CGLS) methods compared to the Singular Value Decomposition (SVD) method even though all of these methods attempted to penalize global SAR in the same way [4]. The fact that the solution space for the flip angle has many similar solutions but with a wide range of different power characteristics suggests that we can pick and chose from nearly equal spatial fidelities in order to improve other aspects of the excitation.

Not for distribution in the US.

Not for distribution in the US.

4

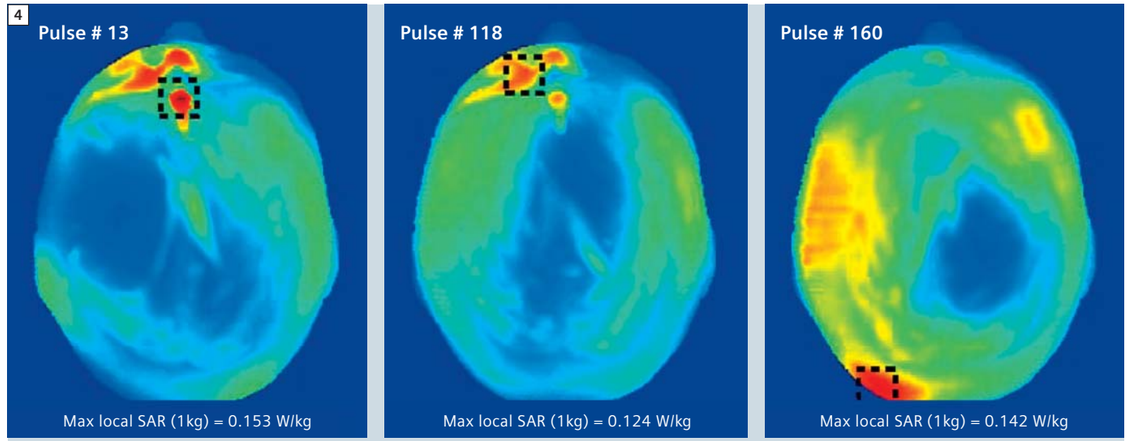

4 Maximum intensity projection of local SAR maps for 3 pulses from a set of 162 designed to produce a uniform flip angle distribution in an axial slice through the head at 7T. Maps are 1g SAR averages obtained from a tissue head model and FDTD simulation of the electric fields of the pulse. Although the pulses achieved nearly identical excitation patterns, the local SAR pattern is very different and would not coherently average with time if the acquisition could cycle through such pulses. *(Figure courtesy of Adam Zelinski.)*

SAR on the run...

A related strategy that expands on this core idea is to generate a family of solutions having similar spatial patterns but differing in the pattern of local SAR. When this set of pulses is used, for example, each pulse for a different imaging slice or even for each phase encode step, the local SAR hotspot will jump around spatially and not coherently time-average into a single long-term hotspot, thus spatially distributing the local SAR load [5-8]. Since the safety concern is local temperature increases which build up over minutes, this spatial-temporal averaging forms a meaningful solution and a viable approach to SAR management in pTx. Even if only two hotspot locations are possible, alternating between the two can lead to a 50% reduction in local SAR. An additional way to potentially force yet different local SAR patterns is to employ slightly different gradient trajectories for each pulse [8]. For example, a slice selective spokes excitation could be generated from any one of hundreds of trajectories. Combing through these solutions produces dozens of candidates within a given spatial fidelity and with different local SAR patterns. An even more sophisticated formalism computes the average SAR pattern from the collection of pulses and optimizes the individual pulses based on this time-averaged pattern [8]. Figure 4 shows the local SAR map for 3 pulses from a set of 162 calculated to mitigate B1+ inhomogeneities in the brain at 7T. The average spatial similarity of the SAR maps for a given pair of pulses was 87%, as computed from the spatial correlation of their SAR maps.

No place to hide...

In addition to forcing the local SAR hotspot to jump around in space, we pursue the regularization of local SAR in the pTx pulse design. Namely, we seek to penalize a potential pulse design during optimization by including its local SAR value into the cost function. The most straightforward way of doing this is to perform an exhaustive search of each pulse's local SAR during the iterative pulse design process. Unfortunately, computing and searching for the local SAR maximum based on the E field maps of an electromagnetic simulation is very computationally demanding, even on a relatively course grid. So while it is desirable to incorporate an exhaustive search over all spatial locations into pTx pulse design, it is currently not computationally feasible. A compromise has been proposed where the pulse is calculated without local SAR in the cost function, note the location of the local SAR hotspot and then redo the design with a penalty for local SAR at that one location [9]. This strategy, however, is likely to simply force the local SAR peak to pop up at a different spatial location. What is needed is a comprehensive regularization which gives the local SAR no place to hide.
Towards this end, Gebhardt and colleagues at Siemens Healthcare and at the University of Erlangen-Nuernberg have noted that the E field data for a coil array is "compressible" in a sense analogous to how a compressed image can provide a nearly faithful image representation at a fraction of the disk space of the original bitmap. Using a fraction of the hundreds of thousands of phase and amplitude representations that would be needed to represent all of the possible excitation combinations of an 8-channel array, the local SAR can be reasonably predicted by a subset of 36 "virtual observation points" [10]. While this subset alone does not promise a fully accurate depiction of local SAR and would not be a replacement for actually checking the local SAR maximum of a pulse, it offers a computational approximation with dramatically reduced computational burden that can be used to penalize local SAR during pulse design while covering nearly all "hiding places." After pulse design, the accurate SAR limits of the pulse would be traditionally calculated. Figure 6 shows the application of the virtual observation compression to regularization of the local SAR [11]. The graph shows the tradeoff between local SAR (y axis) and excitation error compared to the target pattern (x axis) as the relative weight of these two penalties is varied via the regularization parameter. Penalizing the local SAR in this way resulted in a 38% decrease in local SAR for this 8-channel array, spoke design slice-selective pulse for B1+ mitigation in the head at 7T.

5

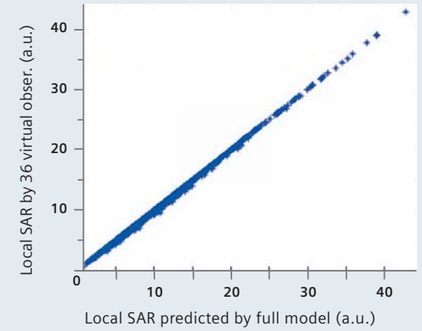

5 Comparison of the local SAR from 1000 randomly chosen transmit combinations evaluated with a full local SAR evaluation (x axis) vs evaluation through 36 virtual observation points (y axis). While the agreement between the two methods is not perfect, the vastly simpler 36 virtual observations reproduce the local SAR with good accuracy. *(Figure courtesy of M. Gebhardt, Siemens Healthcare.)*

6

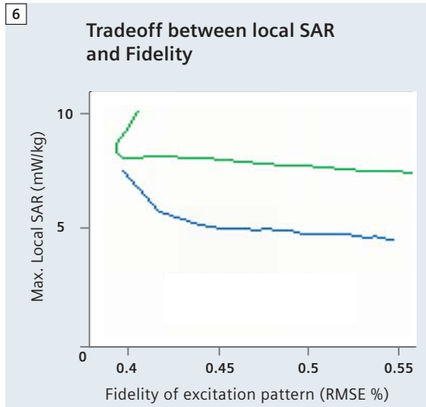

6 Trade-off between excitation error (x axis) and maximum local SAR as the regularization parameter λ is varied. Here the local SAR of the pulse is calculated from a set of 40 virtual observation points. A 38% decrease in local SAR is possible with this method.

Exploiting the choice of excitation coil mode

Since the above discussion centers on exploiting the spatial degrees of freedom in the pulse design process, it is worth considering hardware adaptations which can potentially further extend the number of spatial degrees of freedom. One obvious possibility is to increase the number of transmit channels. Some early exploration of this pathway has suggested significant SAR reduction might be possible with more highly parallel transmit arrays [12]. In this work Lattanzi and colleagues simulated increasing numbers (1, 8, 12, and 20) of circular transmit elements tiling a 30 cm diameter sphere at 7T. They compared the SAR values needed for producing a uniform excitation using RF shimming or a 2D pTx spatially tailored excitation pulse. As seen in practice [2], the pTx pulse was able to achieve a high degree of flip angle uniformity in human head at 7T even with

Not for distribution in the US.

Not for distribution in the US.

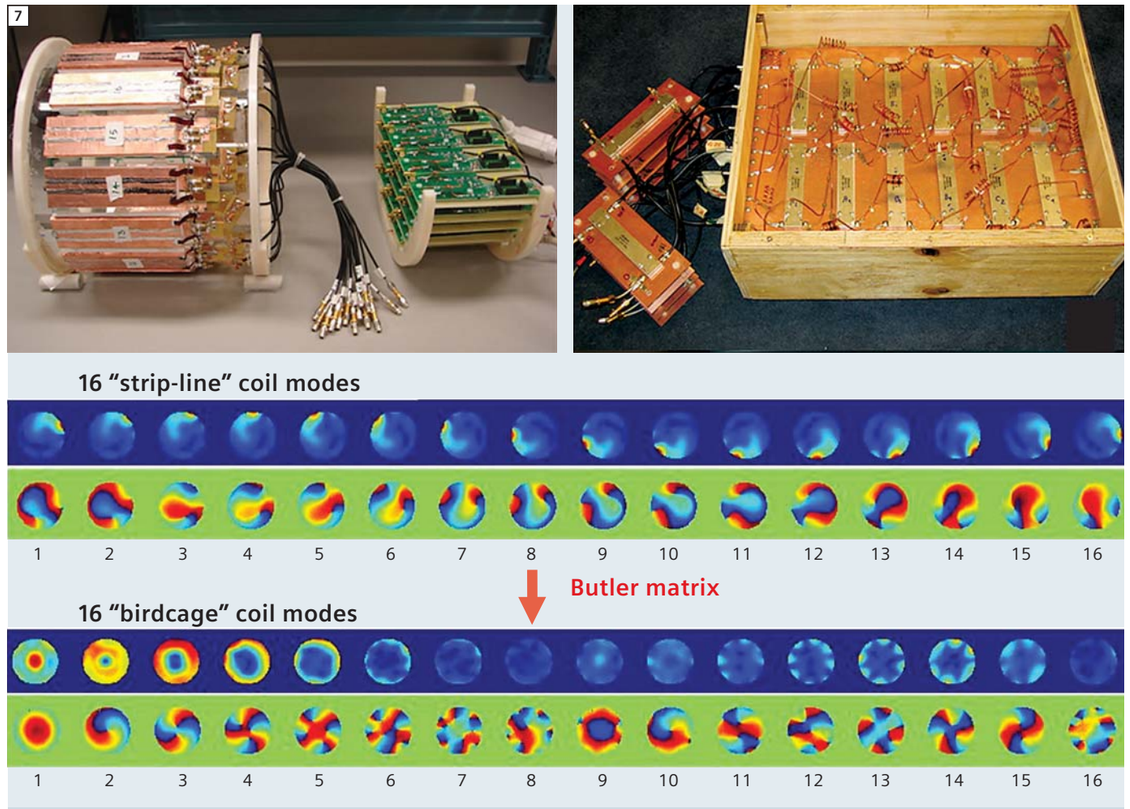

7 A 16-channel 7T strip-line array for the head (upper left) and a 16 x 8 Butler matrix (upper right). Below are the magnitude and phase B1 maps of each of the 16-channels for both the “strip-line” basis set, and the “birdcage” basis set. While excitation ability is roughly equally divided among the strip-line modes, it is concentrated in a few valuable modes in the birdcage basis set. We can choose which 8 modes to drive based on their performance. *(Figure courtesy of Vijay Alagappan, MGH.)*

the 8 coil array, while the RF shimming approach had difficulty even with 20 array elements. Although the additional elements were not needed from a spatial excitation fidelity point of view, they were helpful in reducing global SAR. Global SAR was seen to reduce from 7.9, to 5.5, to 3.3 as the element count increased from 8, to 12, to 20 array elements. Even more interesting, Lattanzi and colleagues calculated the “ultimate intrinsic SAR” consistent with array fields derived from conductor distributions outside the body and satisfying Maxwell’s equations. Constructed in analogy to previous work calculating the ultimate SNR for array distributions, this represents the minimum global SAR possible with a theoretically perfectly optimized array (of however many elements needed). The ultimate intrinsic SAR was an additional 3 fold lower than that obtained with the 20-channel array, suggesting that if additional transmit channels can be engineered in an appropriate and cost effective way, there is potential to utilize element counts well above 20 for reduced SAR in pTx.

By constructing an array with more coil elements than channels to drive them, we can potentially provide the benefit of a higher element count transmit array without actually having to increase the number of RF transmit channels. This is a relatively cost-effective approach since the transmit channels with their power amplifiers and power monitoring equipment are generally more expensive than the array elements themselves. While not increasing the number of transmit elements, this strategy still increases the available degrees of freedom by providing options in how we connect transmit channels to coils. It turns out that these are relatively uninteresting choices for conventional arrays, with transmit elements equally spaced around a cylinder, but it becomes more interesting when the spatial patterns of each array element are not just rotated version of their neighbors. If we think of the spatial distributions of the individual array elements as vectors, then the maximum degrees of freedom derived from this strategy occurs when these vectors are orthogonal. Thus we seek to transform our ‘boring” array of elements around a cylinder into orthogonal modes by finding a suitable linear combination. For loop arrays distributed around a cylinder, an effective linear combination to achieve this goal is the discrete Fourier transform and the resulting basis set is known as the “modes” of the birdcage coil. Similar optimizations in phased array radar have even provided us with a simple hardware realization of this transformation; the Butler matrix [13], which is a generalization of a quadrature hybrid. Figure 7 shows the transformation of the spatial patterns of a 16-element strip-line array into the 16 birdcage modes via the Butler matrix. Since the Butler matrix achieves these modes through simple linear combinations, at first blush it would appear that this “basis set” of excitation patterns would be no better or worse for accelerating spatially tailored excitation than simply driving the strip-line array directly. The superiority of the Butler matrix driven array becomes apparent when only a subset of the array modes is chosen for excitation. The truncation captures a majority of the transmit efficiency and acceleration capabilities in a valuable subset of the channels (and ignoring the less valuable channels). We explored this “array compression” principle by driving a 16-channel strip-line array for 7T head transmit with a 16 x16 Butler matrix connected to the 8-channel transmit system, and demonstrated the theoretically predicted tradeoffs. The excitation configuration that integrates a Butler matrix in this manner allowed us to pick and choose among the modes of a 16-channel array and drive only the best subset of the 16 available modes with our 8 transmit channels. The choice of the optimum 8 birdcage modes compared to 8 strip-line elements allowed a flip-angle inhomogeneity mitigating excitation to achieve a 43% more uniform excitation and 17% lower peak pulse power in a water phantom at 7T [14, 15]. Exploiting these degrees of freedom afforded by choosing among the unequal birdcage modes even further, Zelinski demonstrated that both excitation pattern fidelity and SAR can be improved by choosing the mode set based on the desired excitation pattern [16].

Verifying and monitoring local SAR

As demonstrated in the examples above, the pTx pulse design process has unprecedented ability to impact both global and local SAR. This suggests that global and local SAR need to be carefully checked for each new RF pulse design to insure safety and regulatory compliance. In the most ambitious applications, the pulse design is envisioned to be tailored to the needs of the patient on the table, e.g. providing a volume selective excitation including only the heart, or a curved saturation band following the spine. In this case, in addition to calculating the pulse during the examination, the expected global and local SAR must be checked against regulatory limits. Since the scanner can only monitor total power absorbed by the coil/body, calculations using the pulse shape and modeled E and B fields expected in the body are the only current method available to ensure that local SAR limits are not exceeded before global SAR limits. The scanner can measure the power to each channel, but not the local superposition of E fields in the conductive tissue which gives rise to SAR. This global and local SAR simulation must be performed for every pTx pulse created since a unique spatial-temporal combination of the transmit array elements are used. This is in contrast to conventional single-channel systems where SAR need only be checked once and scaled appropriately based on the transmit power and pulse duration. Therefore, the strategy for ensuring global and local SAR compliance in a parallel transmit system is a generalization of the single transmit case. A full workflow for pTx imaging requires integrated transmit field mapping followed by RF pulse design. The SAR distribution must then be calculated for the pulse based on pre-calculated B_1 and E_1 fields in the appropriate body and coil model. Once the local maximum SAR is found, the local-to-global SAR ratio is examined and the global power limit derated so that the scanner will shut down if the real-time measure of global power to each channel indicates that either the global or local SAR limit exceeded.

An important additional safety check is to monitor in real-time what is actually being transmited by each channel using either field sensing probes or directional couplers on each transmit channel [17]. Then if a single transmit channel fails, the scan can be stopped. This is important since a given transmit channel can create an E_1 field which opposes that of the other channels. In this case, transmit power to that channel reduces local SAR. Alternatively, disruption of a single channel can cause an unpredicted increase in local SAR.

Figure 8 shows the three sections of the workflow tools designed for preliminary pTx studies [18]. The top tool generates the B_1 fields from the data provided by the mapping sequence; a step which ultimately will be performed by the image reconstruction system in an integrated prescan step. The middle panel shows the RF pulse design tool, which at this stage is intended for development use. The

Not for distribution in the US.

Not for distribution in the US.

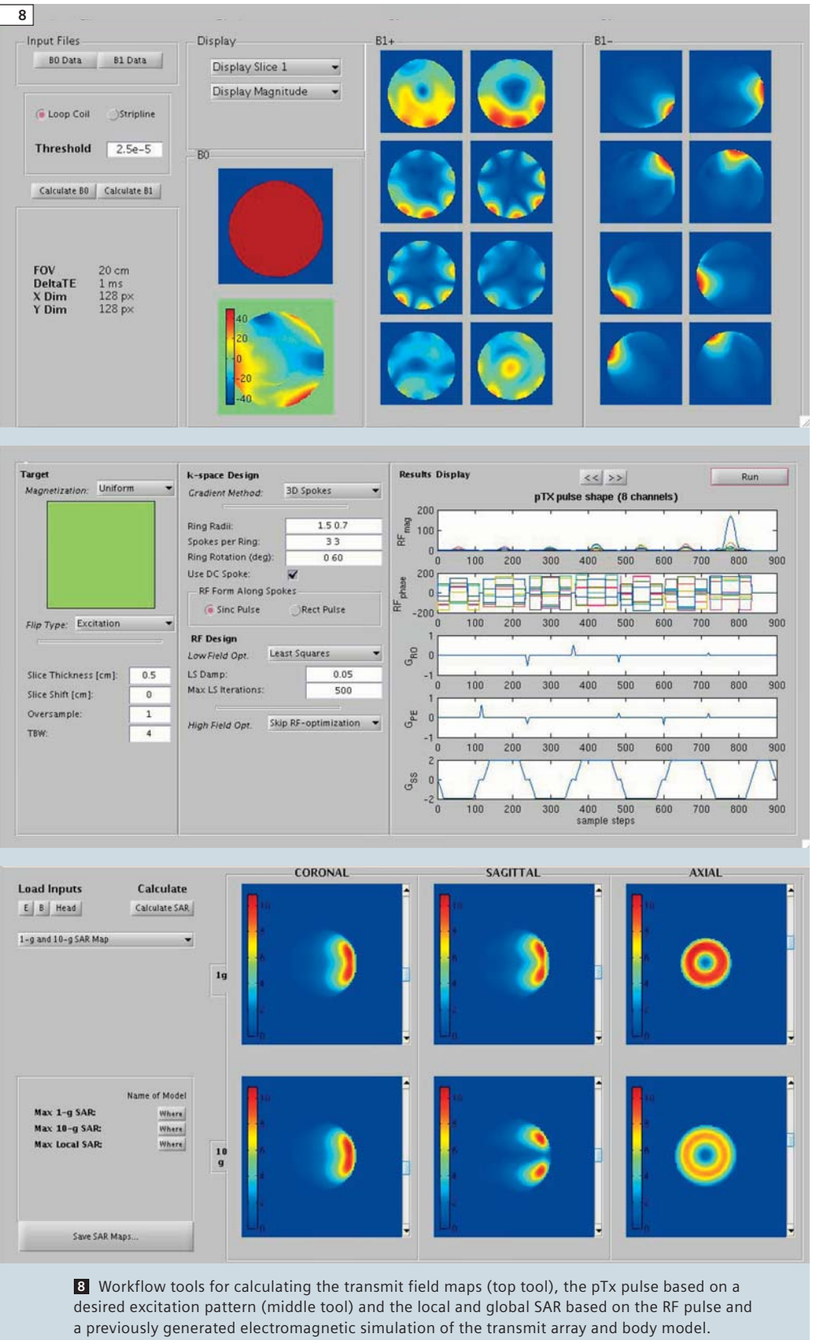

8 Workflow tools for calculating the transmit field maps (top tool), the pTx pulse based on a desired excitation pattern (middle tool) and the local and global SAR based on the RF pulse and a previously generated electromagnetic simulation of the transmit array and body model.

bottom panel shows the SAR maps generated based on the pTx pulse created in the pulse design tool using a previously calculated electromagnetic simulation of the array coil and body model. The SAR-check tool calculates the global power deratings needed in each channel to ensure that both global and local SAR are below safety limits. This information is incorporated into the header of the RF pulse file which is read by the pulse sequence. After checking that the pulse was SAR-checked and that the coil model used matches the coil on the scanner, the pulse sequence transfers the pulse waveforms to the image reconstruction computer where they are compared to the forward and reflected power from the directional couplers on each transmit channel. A disagreement between the measured and expected waveforms on any channel generates a fault which halts the scan.

Conclusions

Theoretical work on parallel RF transmission and recent experimental validations on 8-channel prototype systems at 3T and 7T indicate that parallel excitation has the potential to overcome critical obstacles to robust and routine human scanning at high field strength and enable new applications based on spatially selective excitations. Furthermore, the flexible exploitation of the degrees of freedom in the pulse design problem provides the potential to significantly decrease SAR. While most work has been concentrated on head-sized transmitters, the methods are rapidly translating to body transmit coils at 3T where clinical need is the highest and new generations of scanners offer a system architecture which is pTx-ready. Of course, intriguing research questions remain open in several areas such as the development of rapid and robust RF pulse designs that extend the current low-flip angle domain to arbitrary excitation angle, such as spin echoes, saturation, and inversions pulses. However, with continued development in these areas, progress is likely to accelerate, ultimately supporting fast, subject- and application-tailored RF pulse designs to extend MR excitation from the simple slice-select to the more generally tailored anatomy- or application-specific RF excitation pattern.

Acknowledgements

The authors would like to acknowledge the many researchers, students, and post-docs at Siemens, MGH and MIT whose work is summarized here. We especially acknowledge Kawin Setsompop, Vijay Alagappan, and Adam Zelinski whose thesis work was reviewed here. We also thank Ulrich Fontius and Andreas Potthast for their work setting up the 8-channel 3T and 7T systems and Franz Hebrank and Franz Schmitt for their leadership role in the collaboration and Michael Hamm, Josef Pfeuffer, Axel vom Endt, Mattias Gebhardt and Hans-Peter Fautz for their on-going support.
We acknowledge grant support from the NIH (P41RR14075, R01EB007942, and R01EB006847) and a research agreement and research support from Siemens Healthcare and the Siemens-MIT Alliance.

Contact
Lawrence L. Wald
Associate Professor of Radiology
Athinoula A. Martinos Center for Biomedical Imaging
Department of Radiology
Massachusetts General Hospital
Harvard-MIT Division of Health Sciences and Technology
wald@nmr.mgh.harvard.edu

Elfar Adalsteinsson
Associate Professor
Department of Electrical Engineering and Computer Science
Harvard-MIT Division of Health Sciences and Technology
Massachusetts Institute of Technology
elfar@mit.edu

References

1 Pauly, J., D. Nishimura, and A. Macovski, *A k-space analysis of small-tip angle excitation.* J Magn Reson, 1989. 81: p. 43–56.
2 Setsompop, K., et al., *Slice-selective RF pulses for in vivo B1+ inhomogeneity mitigation at 7 tesla using parallel RF excitation with a 16-element coil.* Magn Reson Med, 2008. 60(6): p. 1422–32.
3 Setsompop, K., et al., *Parallel RF transmission with eight channels at 3 Tesla.* Magn Reson Med, 2006. 56(5): p. 1163–71.
4 Zelinski, A.C., et al., *Comparison of Three Algorithms for Solving Linearized Systems of Parallel Excitation RF Waveform Design Equations: Experiments on an Eight-Channel System at 3 Tesla.* Concepts in Magnetic Resonance Part B (Magnetic Resonance Engineering), 2007. 31B(3): p. 176–190.
5 Adalsteinsson, A., et al., *Method For Reducing Maximum Local Specific Absorption Rate In Magnetic Resonance Imaging,* United States of America Serial No. 12/580076, Filed October 15, 2009.
6 Bornert, P., J. Weller, and I. Graesslin. *SAR Reduction in Parallel Transmission by k-Space Dependent RF Pulse Selection. in Proceedings of the ISMRM.* 2009. Honolulu Hawaii: p. 2600.
7 Graesslin, I., et al. *SAR Hotspot Reduction by Temporal Averaging in Parallel Transmission. in Proceedings of the ISMRM.* 2009: p. 176.
8 Zeliniski, A.C., *Improvements in Magnetic Resonance Imaging Excitation Pulse Design, in Electrical Engineering and Computer Science.* PhD Thesis, 2008, Massachusetts Institute of Technology: Cambridge MA. http://hdl.handle.net/1721.1/45862
9 Graesslin, I. *A Minimum SAR RF Pulse Design Approach for Parallel Tx with Local Hot Spot Suppression and Exact Fidelity Constraint. in Proceedings of the ISMRM.* 2008. Toronto Canada: p. 621.
10 Gebhardt, M., et al. *Evaluation of maximum local SAR for parallel transmission (pTx) pulses based on pre-calculated field data using a selected subset of "Virtual Observation Points". in ISMRM.* 2010.
11 Lee, J., et al. *Parallel Transmit RF Design with Local SAR Constraints. in Proceedings of the ISMRM.* 2010. Stockholm Sweden.
12 Lattanzi, R., et al., *Electrodynamic constraints on homogeneity and radiofrequency power deposition in multiple coil excitations.* Magn Reson Med, 2009. 61(2): p. 315–34.
13 Butler, J. and R. Lowe, *Beamforming matrix simplifies design of electronically scanned antennas.* Electron. Design, 1961. 9: p. 170–173.
14 Alagappan, V., et al. *A Simplified 16-channel Butler Matrix for Parallel Excitation with the Birdcage Modes at 7T. in International Society for Magnetic Resonance in Medicine.* 2008. Toronto, Canada: p. 144.
15 Alagappan, V., et al. *Mode Compression of Transmit and Receive Arrays for Parallel Imaging at 7T. in International Society for Magnetic Resonance in Medicine.* 2008. Toronto, Canada: p. 619.
16 Zelinski, A., et al. *Sparsity-Enforced Coil Array Mode Compression for Parallel Transmission. in International Society for Magnetic Resonance in Medicine.* 2008. Toronto, Canada: p. 1302.
17 Gagoski, B.A., et al. *Real time RF monitoring in a 7T parallel transmit system. in Proceedings of the ISMRM.* 2010. Stockholm Sweden.
18 Makhoul, K., et al. *SAR Monitoring and Pulse Design Workflow in Parallel Transmission at 7 Tesla. in Proceedings of the ISMRM.* 2010. Stockholm Sweden.

Not for distribution in the US.

Not for distribution in the US.

Time-of-Flight MRA at 7 Tesla

Michael Bock[1]; Armin Nagel[1]; Sebastian Schmitter[1,2]; Sören Johst[1]; Lars Gerigk[3]; Armin Biller[3,4]; Angelika Milker-Zabel[5]; Lydia Schuster[3]; Marco Essig[3]; Heinz-Peter Schlemmer[3]; Wolfhard Semmler[1]

[1]Dept. of Medical Physics in Radiology, German Cancer Research Center (DKFZ), Heidelberg, Germany
[2]Center for Magnetic Resonance Research (CMRR), University of Minnesota, USA
[3]Dept. of Radiology, German Cancer Research Center (DKFZ), Heidelberg, Germany
[4]Dept. of Diagnostic and Interventional Radiology, University Hospital Heidelberg, Germany
[5]Dept. of Radiotherapy, University Hospital Heidelberg, Germany

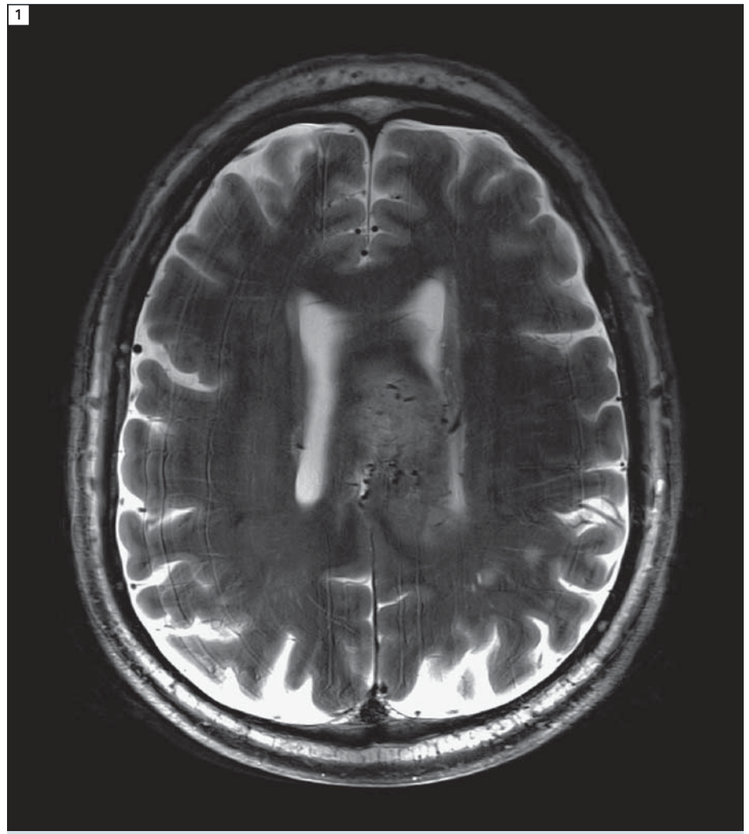

1 T2w TSE image with 300 µm in-plane resolution of a 70-year-old patient with a glioblastoma. The central lesion is visualized with excellent detail, in particular the internal venous vascular network.

Introduction

Over the recent 10 years more than 20 whole-body high field MR systems with field strengths exceeding 4 Tesla have been installed worldwide. The majority of these systems operate at a B_0 of 7 Tesla; however, already four 9.4 Tesla systems are in operation, and an 11.7 Tesla installation in Paris is expected to be finished soon.
The increased signal and the specific new contrasts available at higher magnetic field strengths have been used in various applications. The higher signal strength has been utilized to acquire high-resolution morphologic MR images with 200 µm in-plane voxel size. The enhanced susceptibility difference between oxygenated and de-oxygenated blood, which increases the BOLD contrast nearly linearly with field strength, has been exploited in neuro-functional MRI studies. The prolonged longitudinal relaxation time of blood has been used in arterial spin labeling perfusion studies to visualize the tagged blood for a longer time during the passage through the tissue. Finally, high field MR systems have allowed acquiring spectroscopic data sets with a better spectral differentiation of the individual metabolites.

Time-of-Flight MR Angiography (TOF-MRA)

One particular application that has been shown to profit from higher field strengths is time-of-flight (TOF) MR angiography [5, 16, 10, 7]. In TOF-MRA use is made of the signal difference between the unsaturated blood flowing into an imaging slab and the partially or fully saturated signal of the static tissue surrounding the blood vessels. The 3D TOF-MRA data sets show the vessels against a dark background, and for data post-processing and visualization typically maximum intensity projections (MIP) are calculated. TOF-MRA is preferably used in the delineation of the arterial intracranial vessels, because the direction of the flow from the arteries in the neck into the skull is clearly defined. Furthermore, in the brain long image acquisition times of 5 to 10 min are possible due to the lack of patient motion.
To acquire the TOF-MRA data sets 3D spoiled gradient echo (FLASH) pulse sequences are applied with flow compensation in all three directions to minimize flow-related signal voids in the vessels. In TOF-MRA not a single thick 3D imaging slab is used as in morphologic 3D imaging, but multiple overlapping thin slabs (MOTSA) are sequentially acquired to reduce the progressive saturation that the blood experiences during its passage through the imaging slab. To further reduce this saturation effect, the flip angle is often increased over the slab (Tilted Optimized Nonsaturating Excitation, TONE) which leads to a nearly constant signal for those blood spins that traverse the slab at a predefined velocity. Furthermore, magnetization transfer contrast (MTC) pulses are applied to selectively saturate the static tissue and thus to increase the vessel-to-background contrast.
Theoretically, TOF-MRA profits twofold from higher field strengths. First, the increased MR signal allows reducing the voxel size so that smaller vessels can be delineated. Unfortunately, the SNR increase is scaling only linearly with field strength, whereas the increase in spatial resolution – if isotropic – reduces the signal by the third power of the linear voxel dimensions (Δx). Thus, to maintain the SNR, with an increase of the field strength by a factor of 2.3 (e.g. from 3T to 7T) Δx can theoretically only be reduced by a factor of $\sqrt[3]{2.3}$=1.3. Fortunately, this argument is only valid if the signal within the voxel is homogeneously distributed – in TOF-MRA, small blood vessels can occupy only a fraction of the voxel volume (partial volume effect), and thus a reduction of Δx does not necessarily reduce the amount of signal-emitting spins from blood. In practice, the linear voxel dimensions are therefore often reduced further than the theoretical limits given above.
A second advantage of higher field

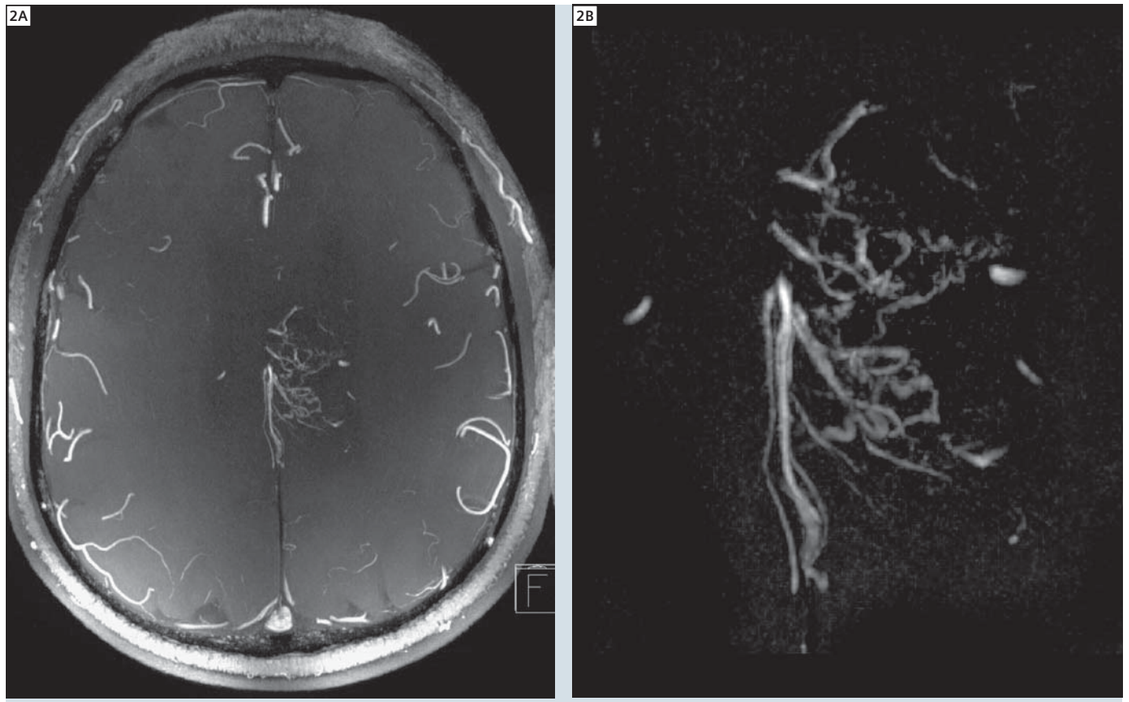

2 Targeted MIP image of a 3D TOF-MRA data set from the same patient as in Fig 1. The irregular tumor-supplying vessels are clearly visualized in the high-resolution MRA data.

Not for distribution in the US.

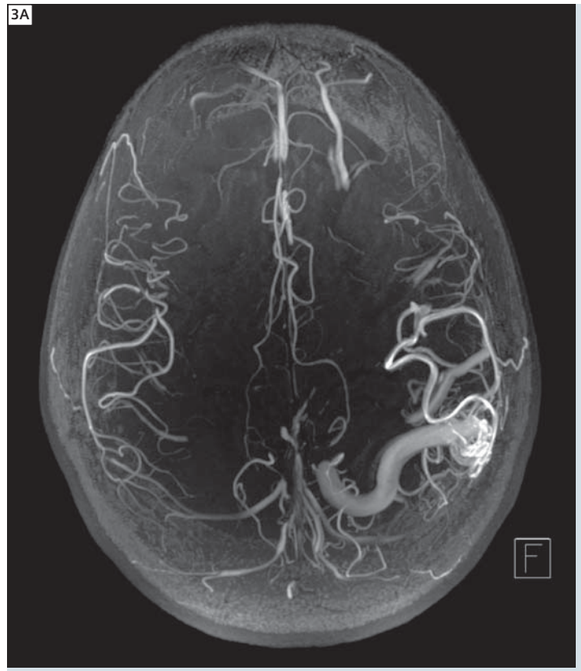

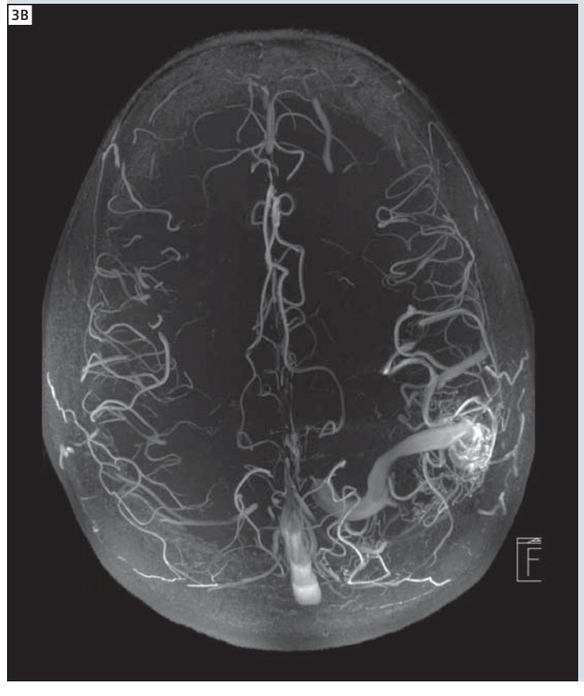

3 Comparison of a 3D TOF-MRA of a 33-year-old AVM patient acquired at 3T and at 7T. In the 3T data the arterial feeders of the AVM appear with a stronger signal, but they are also clearly seen at 7T. Smaller vessels in the AVM nidus are better delineated at 7T demonstrating the complexity of the vascular network. Note that at 7T no venous suppression was applied due to SAR constraints and, thus, the sagittal sinus remains visible.

strengths is the increase of the longitudinal relaxation time T1 with B_0. For the same imaging parameters, longer T1 values lead to a lower FLASH steady state signal of static tissue, and tissue background suppression is becoming more effective. At 3 Tesla, the T1 of white brain matter is 840 ms [17], which increases to 1130 ms at 7 Tesla. For typical TOF-MRA imaging parameters of TR = 15 ms and $\alpha = 20°$ the FLASH signal of white brain matter is then reduced by 22%. At 7 Tesla the background signal constitutes only 18% of the blood signal, so that it often becomes indistinguishable from noise. Note, that this estimate is only valid near the entry of the vessel into the imaging slab where the blood signal has not experienced any RF excitations. The longer the blood remains in the slab the more it gets saturated. Since the blood T1 is also prolonged at higher field strengths this saturation significantly reduces the contrast-to-noise ratio along the path of the blood vessel [3].

Challenges of TOF-MRA at high magnetic fields

The implementation of TOF-MRA protocols at high magnetic fields is challenging due to a number of different problems. At tissue boundaries the static gradients caused by the susceptibility differences have to be compensated by the imaging gradients to avoid local image distortions. In TOF-MRA of the brain this effect is noticeable near the nasal cavities where tissue-air interfaces are present, but it is less pronounced in the brain itself, which has a relatively homogeneous susceptibility.
A more severe limitation is given by the increased energy deposition of the RF system – to achieve the same flip angle as at 3 Tesla the amount of RF energy at 7 Tesla needs to be increased by a factor of $(7/3)^2 = 5.3$. Thus, energy-intensive RF pulses such as MTC pulses cannot be applied due to regulatory constraints (i.e., specific absorption rate or SAR limits). Since background suppression is already very effective at higher fields, the omission of the MTC pulses is no fundamental problem. Another sort of RF pulse, however, is also difficult to integrate due to the SAR limitations: parallel saturation slab pulses, which suppress the signal from venous blood to avoid venous signal overlay in the MIP reconstructions.
Fortunately, there are several options to integrate saturation pulses into TOF-MRA sequences that lead only to a limited increase of the time-averaged SAR. The saturation pulses can be applied less often than the normal excitation pulses – if e.g. the saturation pulse is inserted only after every 10th k-space line, this significantly reduces the total SAR of the pulse sequence. One drawback of this implementation is the reduced saturation efficiency which can lead to non-vanishing signal in veins with a moderate to high blood flow velocity.
Another method to reduce the RF energy of a pulse is given by the variable rate selective excitation (VERSE) technique [2]: here, use is made of the fact that only a certain fraction of the pulse (typically, the so-called main lobe) is contributing most to the SAR of the RF pulse. By selectively reducing the RF amplitude in combination with the gradient amplitude the duration of the RF pulse is only moderately increased, but a substantial reduction in RF power is achieved. In principle, VERSE can be used with every slice-selective RF pulse, and so a SAR reduction can be achieved both for the normal slab-selective excitation pulse as well as for the 90° saturation pulses [6]. VERSE requires a very good synchronization of the gradient activity with the RF pulse modulation, it increases the sound pressure levels [13] and it makes the RF pulse more susceptible to off-resonance effects due to the lower gradient amplitudes [12]. Thus, in practice a compromise between SAR reduction, off-resonance susceptibility and gradient noise needs to be found.

Clinical applications of TOF-MRA at 7 Tesla

In the following two clinical applications of TOF-MRA of the brain are presented, that profit especially from the increased spatial resolution provided by the higher field strength: imaging of tumor blood vessels and of arterio-venous malformations.

Tumor vasculature

The growth of highly malignant brain tumors is facilitated by the ability to induce neoangiogenesis to maintain the supply with nutrients. This is mainly achieved by expression of several growth factors, the most important being vascular endothelial growth factor (VEGF) [8]. Neoangiogenesis leads to a higher microvascular density inside the tumor. Modern therapies target the factor mediated signaling cascade to inhibit neoangiogenesis. One of the most recent agents is Bevacixumab (Avastin), a monoclonal antibody against VEGF [15]. Alternatively, radiotherapy and radiosurgery target the neovasculature of the tumor.
High-grade brain tumors often show a diffuse network of blood vessels, which are less organized [1], more tortuous and of more irregular diameter than normal brain vessels. During tumor growth, the vascular pattern changes from regularly shaped vessels as found in normal tissue to more dilate and higher caliber vessels as well as glomeruloid vessels in glioblastoma [1]. This reorganization leads to a decrease in microvascular density, i.e. the number of vessel cross sections in a given area, but an increase in the mean area occupied by vessels. As the size of the induced microvessels is usually below the detection limit of MRI at 1.5 or 3T, perfusion MRI markers like relative cerebral blood volume (rCBV) or relative cerebral blood flow (rCBF) have been investigated. Whereas a differentiation of lower and higher grade tumors according to their rCBV and rCBF levels is usually possible in large patient groups, due to the limited reproducibility of perfusion MRI it is difficult to use them for follow-up examinations in clinical routine. In addition, VEGF also increases vascular permeability, leading to an extravasation of contrast agent into the tissue, which is not accounted for in most perfusion models. With conventional MRI at 1.5T or 3T the small 100 µm to 300 µm vasculature is not directly visible due to limitations in both spatial resolution and SNR. At 7 Tesla TOF-MRA can be applied with a spatial resolution of 300 µm and better. In combination with an excellent background suppression of the signal from static tissue this higher resolution is capable of visualizing the neovasculature of malignant brain tumors. In Figure 1, a T2w 7 Tesla image of a 70-year-old patient with an astrocytoma WHO grade IV (glioblastoma) is shown. The lesion is visualized with very good contrast in both T1 and T2-weighted images, and the heterogeneous interior is clearly resolved in susceptibility-weighted images that particularly highlight the venous vasculature [4].
In the TOF-MRA data of the same patient the arterial vasculature is highlighted (Fig. 2), and the highly anomalous vessels are seen - this vascular network can clearly be identified as neo-vasculature because of its irregular shape and surplus vessels not found in normal brain parenchyma. The following imaging parameters were used: TR 15 ms, TE 4.8 ms, flip angle 19°, TONE setting 70%, parallel imaging GRAPPA 2x, bandwidth 165 Hz/pixel, matrix 516 x 704, FOV 14 x 200 mm², 4 slabs, partition thickness 410 µm, TA 4x 2:34 min. At a lower field strength this vessel network could not be visualized. Thus, there is first evidence that therapies targeting neo-angiogenesis might be better assessed with high-resolution TOF-MRA providing comparable results than the different perfusion imaging techniques.

Arteriovenous malformations (AVM)

Arteriovenous malformations are congenital vascular lesions that arise during the embryonic stage from capillary dismorphogenesis. As a consequence, AVMs manifest as one or more arteries that feed a nidus of abnormal vessels instead of the normal capillary bed, and

Not for distribution in the US.

which are then drained by one or more veins. AVMs are the cause of 1–2% of all strokes, and have a 2–3% risk of hemorrhage [9]. TOF-MRA can provide an overview of the architecture of the AVM, and it helps to identify abnormally dilated feeding and draining vessels. At present, X-ray digital subtraction angiography is still considered the gold standard for AVM imaging due to the higher spatial resolution that allows identifying very small feeding vessels.

With TOF MRA at 7 Tesla the feeding arteries, the nidus and the draining veins are excellently visualized (Fig. 3). Compared to TOF-MRA data acquired at 3T, at first glance no significant difference between the 3T and the 7T data is visible. However, the more detailed visualization of the small sub-millimeter vasculature of the nidus at 7 Tesla becomes apparent. If not operable, AVMs are treated either by embolisation to occlude the feeding arteries, or with radiation therapy to initiate an endothelial reaction which will gradually reduce the free vessel lumen and thus increase the vascular resistance. With the high spatial resolution provided with TOF-MRA, which is delineating the free vessel lumen, the slow lumen reduction of the feeding arteries might be visualized directly, so that treatment-related changes in the angioarchitecture can be identified at an earlier stage.

A quantitative comparison between the 3T and the 7T data is difficult, because different RF coils were used for data acquisition. At 3T, the MAGNETOM Tim Trio system's 32-channel receive-only head coil was used, whereas at 7T a 24-channel transmit receive coil was applied. Due to the intrinsic transmit inhomogeneity at 7 Tesla, a spatially varying contrast is seen in the 7T TOF data, because the flip angle decreases from the center of the coil (where flip angle calibration was performed) to the periphery.

Conclusion

Time-of-flight MRA benefits from the increased SNR and the different contrasts available at higher field strengths. The increase in spatial resolution is particularly beneficial for the assessment of intracranial lesions such as AVMs and high-grade gliomas.

References

1 Bulnes S, Bilbao J, Lafuente JV. *Microvascular adaptive changes in experimental endogenous brain gliomas.* Histol Histopathol 24 (6): 693–706, 2009.

2 Conolly S, Nishimura DG, Macovski A, Glover G. *Variable-rate selective excitation.* J Magn Reson 78:440–458, 1988.

3 Eissa A, Wilman A. *3D TOF MRA of the intracranial arteries: effects of increasing magnetic field to 4.7T.* Proc. Intl. Soc. Mag. Reson. Med. Vol. 14, pp. 1945, 2006.

4 Gerigk L, Nagel A, Biller A, Dinkel J, Schuster L, Hauser T, Puderbach M, Essig M, Delorme S, Bock M. *Assessment of Vascularity in Malignant Glioma: Development of an Imaging Protocol at 7 T.* Proc. Intl. Soc. Mag. Reson. Med. Vol 18, pp. 4424, 2010

5 Heverhagen JT, Duraj J, Schmalbrock P, Thompson MR, Chakeres D, Knopp MV. *Ultrahigh Field (>7T) Time-of-Flight and Phase Contrast Magnetic Resonance Angiography of the Intracerebral Arteries.* Proc. Intl. Soc. Mag. Reson. Med. Vol. 14, pp. 814, 2006.

6 Johst S, Schmitter S, Bock M. *Towards True Arterial Intracranial TOF-MRA at 7T: Protocol Optimization Using VERSE Pulses.* Proc. Intl. Soc. Mag. Reson. Med. Vol 18, pp. 2252, 2010.

7 Kang CK, Hong SM, Han JY, Kim KN, Kim SH, Kim YB, Cho ZH. *Evaluation of MR angiography at 7.0 Tesla MRI using birdcage radio frequency coils with end caps.* Magn Reson Med 60 (2): 330–8, 2008.

8 Kapoor GS, Gocke TA, Chawla S, Whitmore RG, Nabavizadeh A, Krejza J, Lopinto J, Plaum J, Maloney-Wilensky E, Poptani H, Melhem ER, Judy KD, O'Rourke DM. *Magnetic resonance perfusion-weighted imaging defines angiogenic subtypes of oligodendroglioma according to 1p19q and EGFR status.* J Neurooncol 92 (3): 373–86, 2009.

9 Ko H, Johnston S, Young W, Singh V, Klatsky A. *Distinguishing intracerebral hemorrhages caused by arteriovenous malformations.* Cerebrovascular Disease 15: 206–209, 2003.

10 Maderwald S, Ladd SC, Gizewski ER, Kraff O, Theysohn JM, Wicklow K, Moenninghoff C, Wanke I, Ladd ME, Quick HH. *To TOF or not to TOF: strategies for non-contrast-enhanced intracranial MRA at 7 T.* MAGMA 21 (1–2): 159–67, 2008.

11 Narayana A, Kelly P, Golfinos J, Parker E, Johnson G, Knopp E, Zagzag D, Fischer I, Raza S, Medabalmi P, Eagan P, Gruber ML. *Antiangiogenic therapy using bevacizumab in recurrent high-grade glioma: impact on local control and patient survival.* J Neurosurg 110 (1): 173–80, 2009.

12 Schmitter S, Johst S, Bock M, Ugurbil K, van de Moortele PF. *Implementing VERSE for Time of Flight RF pulses at 7Tesla: Methodological Considerations.* Proc. Intl. Soc. Mag. Reson. Med. Vol 18, pp. 4424, 2010.

13 Schmitter S, Mueller M, Semmler W, Bock M. *A VERSE algorithm with additional acoustic noise constraints.* Proc. Intl. Soc. Mag. Reson. Med. Vol 17, pp. 179, 2009.

14 Suzuki M, Matsui O, Kobayashi K, Ueda F, Saitoh C, Katagiri A, Sanada J, Tawara M, Terayama N, Kawashima H, Kida S, Yamashita J. *Contrast-enhanced MRA for investigation of cerebral arteriovenous malformations.* Neuroradiology 45 (4): 231–5, 2003.

15 Verhoeff JJ, van Tellingen O, Claes A, Stalpers LJ, van Linde ME, Richel DJ, Leenders WP, van Furth WR. *Concerns about anti-angiogenic treatment in patients with glioblastoma multiforme.* BMC Cancer 9: 444, 2009.

16 von Morze C, Xu D, Purcell DD, Hess CP, Mukherjee P, Saloner D, Kelley DA, Vigneron DB. *Intracranial time-of-flight MR angiography at 7T with comparison to 3T.* J Magn Reson Imaging 26 (4): 900–4, 2007.

17 Wright PJ, Mougin OE, Totman JJ, Peters AM, Brookes MJ, Coxon R, Morris PE, Clemence M, Francis ST, Bowtell RW, Gowland PA. *Water proton T1 measurements in brain tissue at 7, 3, and 1.5 T using IR-EPI, IR-TSE, and MPRAGE: results and optimization.* MAGMA 21 (1–2): 121–30, 2008.

Contact
Michael Bock, PD Dr. rer. nat. Dipl. Phys.
German Cancer Research Center (DKFZ)
Dept. Medical Physics in Radiology
Im Neuenheimer Feld 280
69120 Heidelberg
Germany
Phone: ++49 6221 42-2528 or -3063
m.bock@dkfz.de

Listen to the 31 talks on 7T imaging that we have captured during the Ultra High Field User Meeting

Robert Turner
Max-Planck-Institute (Leipzig, Germany)
Grey Matter Structure by 7T

Larry Wald
MGH (Boston, USA)
Physics of ultra high field

Kamil Ugurbil
CMRR, Univ. of Minnesota (Minneapolis, USA)
How to conquer 7T and higher

Zang-Hee Cho
NRI, Gachon Medical School (Incheon, Korea)
7T Applications

Oliver Speck
IfN, Univ. Magdeburg (Magdeburg, Germany)
EPI & fMRI at 7T

Christopher Wiggins
CEA (Saclay, France)
Diffusion Imaging at 7T

John Thomas Vaughan
CMRR, Univ. of Minesota (Minneapolis, USA)
Body Imaging at 7T

Jeanette Schulz-Menger
Max Delbrueck Center (Berlin, Germany)
Cardiac Imaging at 7T

Rolf Gruetter
EPFL (Lausanne, Switzerland)
Spectroscopy and imaging on a 7T/680 scanner

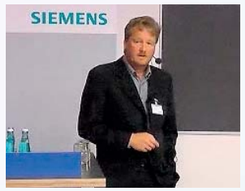

Elfar Adalsteinsson
MIT (Boston, USA)
Basics & challenges in accelerated pTx

Visit us at **www.siemens.com/magnetom-world**
Go to **International Version > Education > e-trainings & Presentations**

syngo TimCT – MR Angiography in Clinical Routine

K. Lederle; S. Haneder; U. Attenberger; G. Weisser;
S. O. Schoenberg; H. J. Michaely

*Institute of Clinical Radiology and Nuclear Medicine,
University Medical Center Mannheim, Mannheim, Germany*

The University Medical Center Mannheim currently operates five MR units (2x 3T equipped with latest Tim technology and with at least [10x32] channel configuration. 1x 1.5T non-Tim system and 2x 1.5T with [76x32]channel configuration. All scanners equipped with Tim technology are equipped with the *syngo* TimCT-Oncology and *syngo* TimCT-MRA suites.

Background

Due to a very close cooperation with the departments of vascular surgery and angiology, 8–10 patients with suspected or proven peripheral arterial obstructive vascular disease (PAOD) are examined per week. Because of its non-invasiveness and the good depiction of smallest vessels even with heavy calcification, MR Angiography (MRA) of the lower extremity is considered the most appropriate diagnostic imaging technique for PAOD (Fig. 1). Recent data on the accuracy of 3T MRA of the peripheral arteries in patients with PAOD showed a sensitivity of MRA of 95.3% and a specificity of 98.5% when compared to conventional, invasive DSA [1]. A major disadvantage of conventional large field-of-view (FOV) imaging, such as bolus-chase stepping table MRA, is the complexity of the exam. Three different FOVs have to be planned and examined step-by-step. Thus, images are not acquired as one complete set of data but in several steps. This is error-prone on the one hand and time-consuming on the other hand, in terms of setting up the exam and of actually performing the exam. Afterwards, the images are composed for reading and for demonstration in clinical case conferences. However, the image quality in the overlapping sections of the composed images at the end of the individual FOVs is more likely to be artifact-ridden so that, in the worst case, erroneous interpretation can occur. If MRA images are not composed and are presented as single FOV series, the images are much harder to comprehend for the referring clinical colleagues.

syngo TimCT-MRA advantages

The *syngo* TimCT-MRA application overcomes these problems by offering a continuous table movement during acquisition of a three-dimensional MRA data set with a continuous z-axis FOV of up to 1200 mm. The single steps of conventional MRA are limited to a FOV

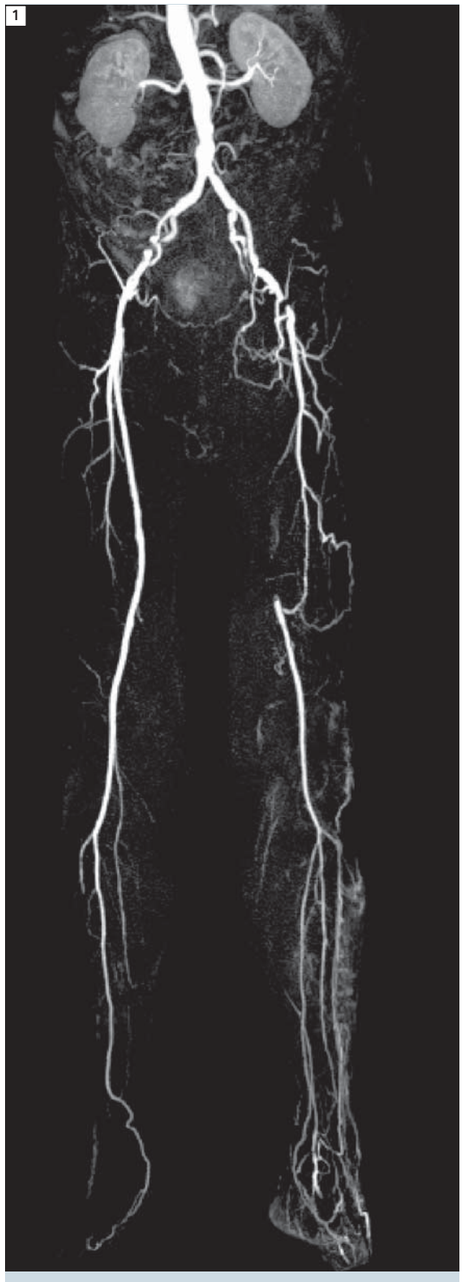

1 Thick slab MIP of a patient with PAOD III-IV showing multiple stenoses in the pelvis, an obliteration of the superficial femoral artery, collateralization by the PFA and extensive soft tissue contrast enhancement due to ischemic inflammation on the left side.

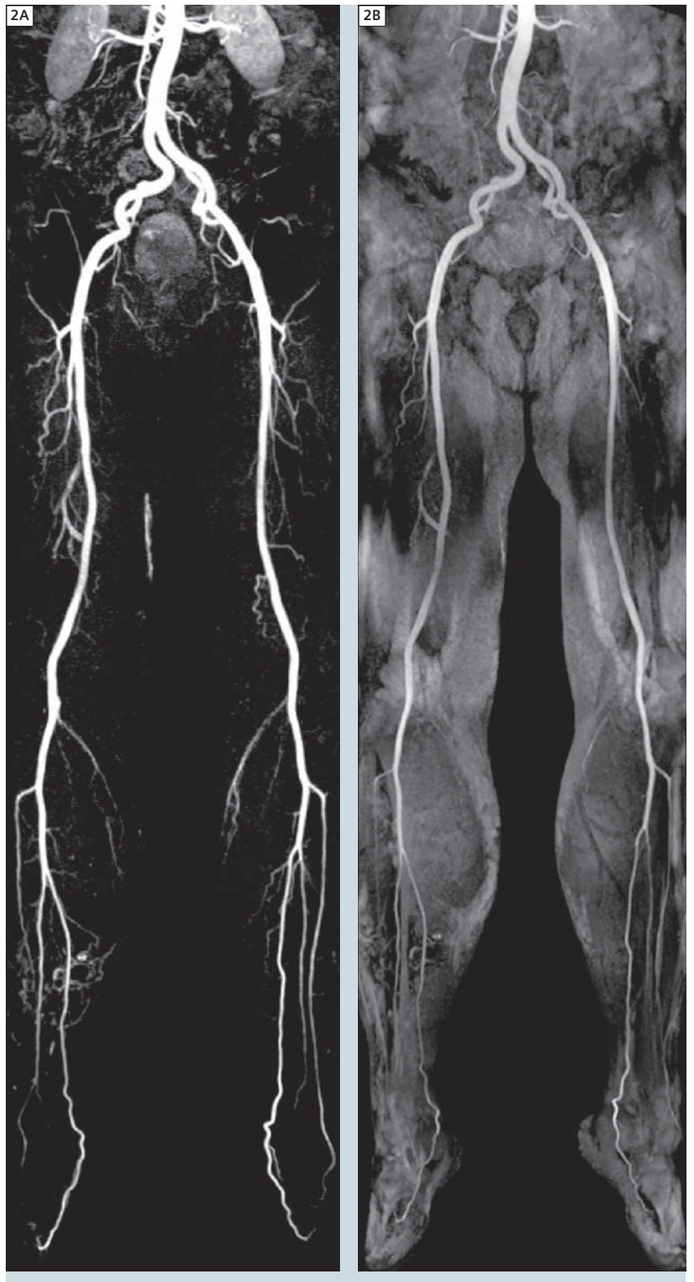

2 Thick slab coronary view of the vessels of the lower extremity in a patient with PAOD II with and without subtraction.

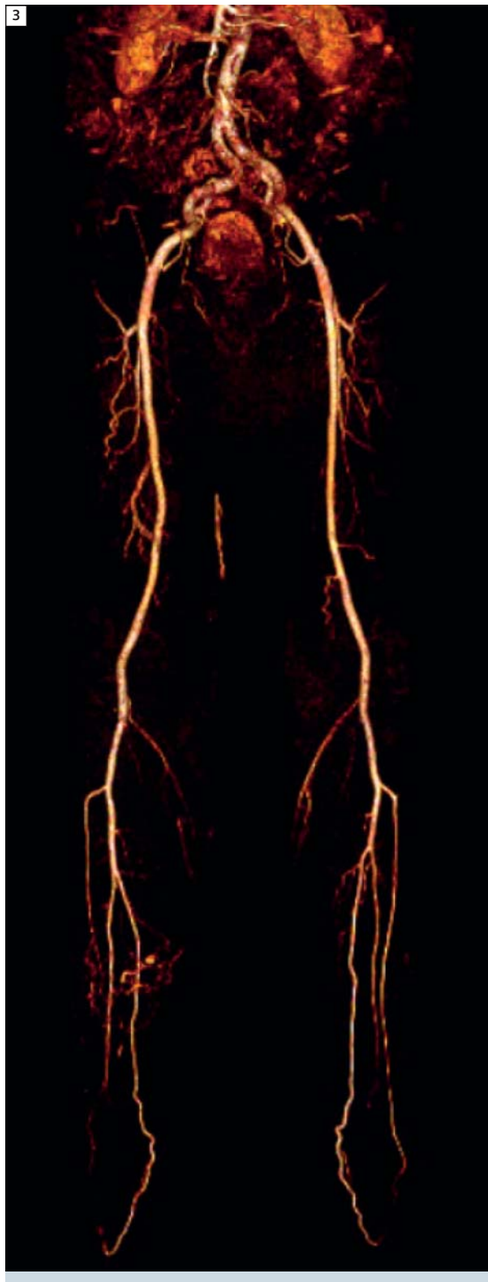

3 3D reformation of an MR-angiography of the same patient as in figure 2. The high signal-to-noise ratio (SNR) allows for superb depiction of the vessels.

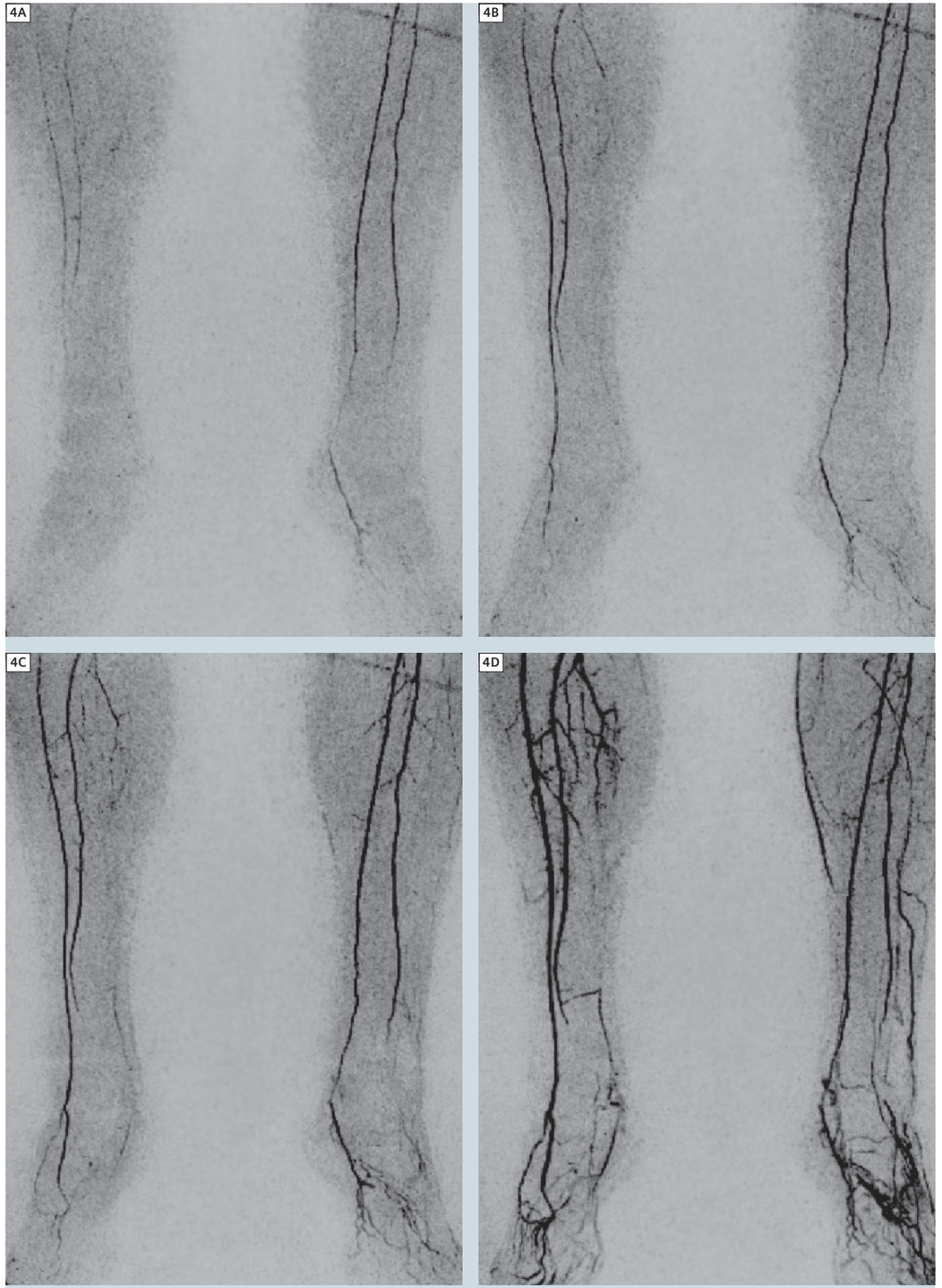

4 Dynamic imaging of the calf vessels (1.1 x 1.1 x 1.1 mm³, 5 s temporal resolution) with low dose *syngo* TWIST-Angiography in a patient with PAOD III showing obliterations of the posterior tibial artery on the right and of the distal anterior tibial artery on the left side.

of 400 to 500 mm depending on the equipment used, which have to be composed manually after the exam. Beyond the easy visualization, TimCT MRA is beneficial in two other ways. Firstly, due to the ease of planning of the exam without angulation of different slabs and without the need to optimize the overlapping segments. Secondly, whilst the conventional step-by-step approach requires two periods of dead-time (for the table to move without acquiring images and for the contrast agent bolus to travel further through the body), by contrast *syngo* TimCT is very time-effective since it eliminates these dead-times. The more effective use of the contrast agent enables a reduction in the dose of contrast agent of 20–40%.

syngo TWIST dynamic information

Characteristically, up to 50% of patients with PAOD III-IV show venous overlay in the calves due to inflammatory hyperemia and side-different flow [1]. Therefore, our protocol is supplemented by an additional dynamic TWIST angiography of the critical calf station after the TimCT-MRA. The *syngo* TWIST-MRA allows dynamic depiction of the small run-off vessels and collateral vessels. Due to the dynamic nature of the TWIST MRA purely arterial images of the calf vessels can be acquired even in patients with severe inflammation or those with side-different flow.

TimCT-MRA and TWIST in clinical routine

The protocol is very simple and – at our institution – includes a *syngo* TimCT localizer, a vessel scout, the T1w FLASH angiography sequence before and after contrast administration (TR 2.42 ms, TE 1.02 ms, spatial resolution 1.2 x 1.2 x 1.2 mm²) and the TWIST-angiography of the lower legs (TR 2.75 ms, TE 1.02 ms, spatial resolution 1.1 x 1.1 x 1.1 mm) 1–2 minutes after the TimCT-MRA. The examination is performed with a sub-single dose of contrast media (Gadobutrol) for the TimCT-MRA, and with a second administration of a reduced dose of contrast media for the dynamic TWIST-angiography. In order to increase the injected volume and to save on contrast media, at our institution Gadobutrol is diluted with saline 1:1. The dosage of contrast media does not exceed that of a traditional single-dose multi-step MRA.

The images acquired in patients with the *syngo* TimCT-MRA technique show consistently good image quality (Figs. 2 and 3). In a feasibility study on the image quality of low-dose TimCT-MRA, 393 out of 397 vessel segments showed diagnostic image quality and 213 vessel segments were scored with excellent image quality. Non-assessable segments were only encountered in 4 out of 397 vessel segments (1%). A slight venous overlay occurred in 27% in the lower leg station, not interfering with diagnostic reading, whereas no venous overlay occurred in the pelvis or the thighs [2, 3]. Additional relevant information was found in 64% of the patients with the *syngo* TWIST-MRA, such as collateral vessels not detectable in the TimCT-MRA due to venous overlay or tissue contrast media enhancement (Fig. 4) [2]. Although the spatial resolution of the *syngo* TimCT MRA suite (1.2 mm isotropic at 3T with software version *syngo* MR B15) is currently inferior to the conventional DSA exams (0.3 mm in-plane) and slightly inferior to CT angiography, evaluation of pathologies is nearly equivalent in our experience. A further improvement is the introduction of a higher spatial resolution in the calf station which is available with the latest software version *syngo* MR B17 allowing 0.7 mm isotropic resolution in the calves.

Conclusion

Overall, the *syngo* TimCT MRA suite is a huge improvement in imaging the lower extremities in a clinical setting as it combines an easy, fast and robust workflow with good clinical results and is applicable to a broad range of patients.

References

1 Berg F, Bangard C, Bovenschulte H, Hellmich M, Nijenhuis M, Lackner K, Gossmann A: Feasibility of Peripheral Contrast-Enhanced Magnetic Resonance Angiography at 3.0 Tesla With a Hybrid Technique. Comparison With Digital Subtraction Angiography, Invest Radiol. 2008;43: 642–649

2 Voth M, Haneder S, Huck K, Gutfleisch A, Schoenberg SO, Michaely HJ: Peripheral Magnetic Resonance Angiography With Continuous Table Movement in Combination With High Spatial and Temporal Resolution Time-Resolved MRA With a Total Single Dose (0.1 mmol/kg) of Gadobutrol at 3.0T, Invest Radiol 2009;44: 627–633

3 Kramer K, Zenge M, Schmitt P, Glaser C, Reiser MF, Herrmann KA: Peripheral Magnetic Resonance Angiography (MRA) With Continuous Table Movement at 3.0 T. Initial Experience Compared With Step-by-Step MRA. Invest Radiol 2008;43: 627–634

Contact
Henrik J. Michaely, M. D.
Associate Professor of Radiology
Section Chief Abdominal and Vascular MRI
Institute of Clinical Radiology and Nuclear Medicine
University Medical Center Mannheim
Theodor-Kutzer-Ufer 1–3
68167 Mannheim
Germany
henrik.michaely@umm.de

Case Report: Complex Tear of the Anterosuperior Labrum

Michael Recht, M.D.

New York University Langone Medical Center, New York, USA

Patient history

The patient is a 29-year-old medical student who has a history of bilateral hip pain which is significantly affecting her activity level. She underwent MR arthrography of the left hip on a 1.5 T scanner. There were findings suggestive of labral tear (Figs. 1 and 2) but the pathology was not optimally visualized. In addition it was difficult to be certain of the integrity of the articular cartilage. Therefore a repeat examination was performed on the 3T MAGNETOM Verio (software version *syngo* MR B17) using the 4-channel small flex coil. The patient was injected with intravenous gadolinium and dGEMRIC images were acquired to improve further assessment of the articular cartilage. Sequences included axial fat suppressed proton density, coronal proton density, coronal fat suppressed proton density, sagittal fat suppressed proton density, radial proton density, and VIBE for T1 mapping.
A detailed description of the imaging protocol we use at our department in such a clinical setting is provided in table 1.

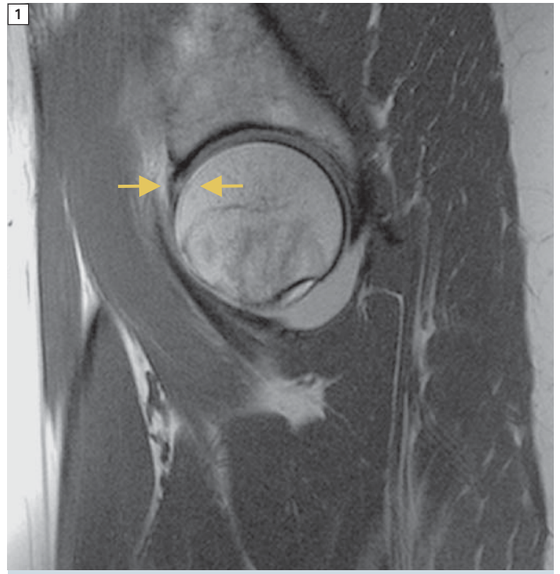

1 Sagittal T1-weighted image post intraarticular gadolinium injection on a 1.5T non Tim MAGNETOM Symphony. There is signal abnormality in the anteriosuperior labrum suggestive of a labral tear. No gross defects are visualized in the adjacent articular cartilage but there is suboptimal delineation of the articular cartilage on the image.

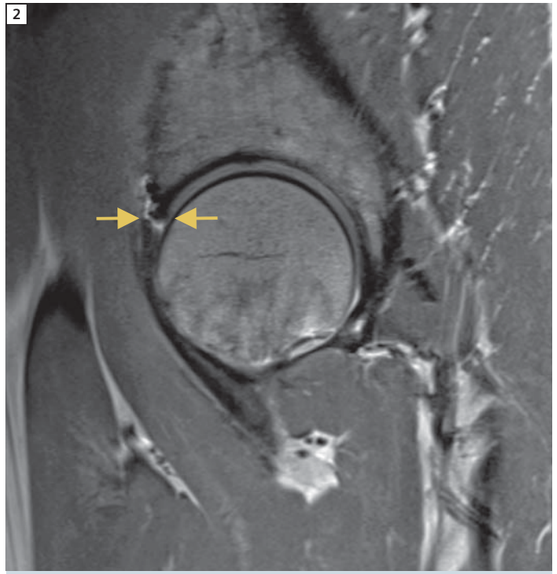

2 Corresponding sagittal Proton density MRI demonstrating abnormal signal in the labrum extending to the surface of the labrum consistent with a labral tear.

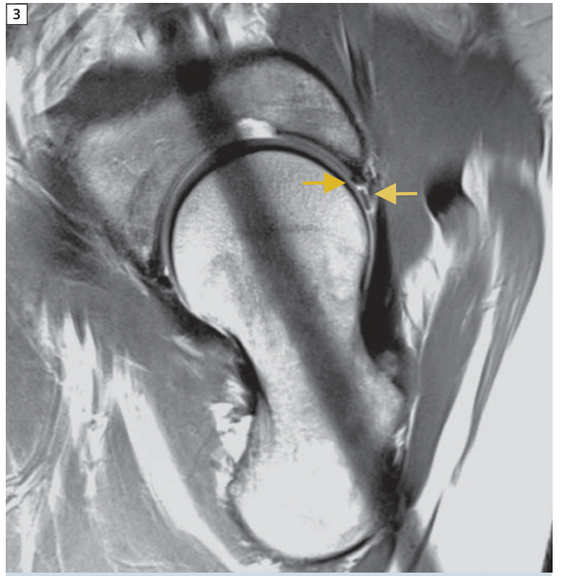

3 Radial Proton Density MRI at 3T demonstrating a complex labral tear with both a radial and longitudinal component. The adjacent articular cartilage appears normal.

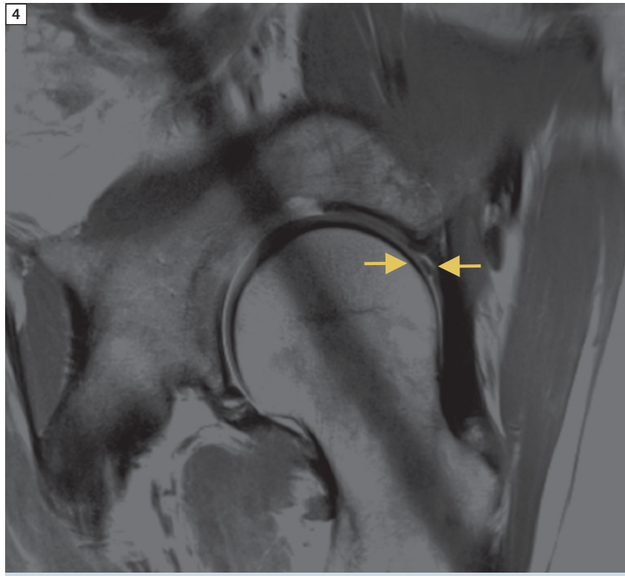

4 The longitudinal component of the tear is well visualized on this radial image (3T MR scan).

Table 1: Sequence details of the used imaging protocol at 3T with the 4-channel small flex coil.

Sequence:	cor T1 loc	ax T1 loc	cor pd fs	sag pd fs	ax t1	pd radial	cor T1	sag T1
Type:	tse	tse	tse	tse	gre	tse	vibe	vibe
Scantime [mm:ss]:	1,35	0,49	6,07	4,32	2,56	4,32	3,38	3,40
Res [mm³]:	1.0 x 0.6 x 3.0	1.0 x 0.6 x 3.0	0.5 x 0.5 x 3.0	0.5 x 0.5 x 3.0	0.5 x 0.5 x 2.0	0.4 x 0.4 x 3.5	0.6 x 0.6 x 4.0	0.6 x 0.6 x 4.0
TR [ms]:	300	300	2750	2080	170	3110	20	20
TE [ms]:	10	10	26	23	6.15	25	3.54	3.54
FOV[mm]:	160	160	150	150	120	160	160	160
Slices	5	5	24	24	11	8	32	32
Gap	25%	25%	10%	10%	10%	25%	20%	20%
Average	2	2	1	1	2	1	1	1
Concatena-tions	2	2	1	1	1	1	1	1
Flip Angle	150	150	131	131	90	150	first angle 5 second angle 30	first angle 5 second angle 30
Slice Thickness	3	3	3	3	2	3.5	4	4
Bandwidth	250	250	180	180	240	211	130	130
Turbo Factor	4	4	4	4	n/a	10	n/a	n/a
Echo Train	77	39	132	128	n/a	86	n/a	n/a

Imaging findings

There is a complex tear of the anterosuperior labrum best visualized on the radial images. There are both radial and longitudinal components of the tear. The additional dGEMRIC images (not shown) confirmed that the articular cartilage is within normal limits in this case.

Discussion

Although the labral pathology was identified on the original MR arthrography on the 1.5T system, it was much more conspicuous on the optimized 3T exam using a multichannel coil. This optimized MR scan including dGEMRIC images allowed for a confident diagnosis of normal adjacent articular cartilage, a key factor in determining the patient's operative treatment.

Contact
Michael Recht, M. D.
Louis Marx Professor and Chairman
Department of Radiology
New York University
Langone Medical Center
550 First Ave.
New York, NY 10016
USA
Michael.Recht@nyumc.org

Musculoskeletal Advisory Board Provides Protocols for 1.5 and 3T MAGNETOM systems

We have launched the MSK Advisory Board website, providing proven MSK protocols (.edx files) for download. To support Technologists there are also coil positioning videos and tips & tricks.

Board members are:

- Christian Glaser, LMU Grosshadern, Germany
- Jürg Hodler, Balgrist University Hospital, Switzerland
- Young-Jo Kim, Harvard Medical School, Children's Hospital Boston, USA
- Tallal Charles Mamisch, Bern University, Switzerland
- Michael Recht, New York University, USA
- Siegfried Trattnig, AKH Wien, Austria
- Lawrence M. White, University of Toronto, Canada

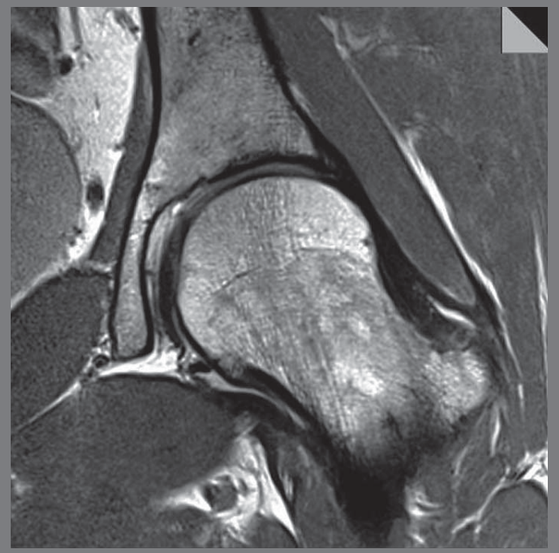

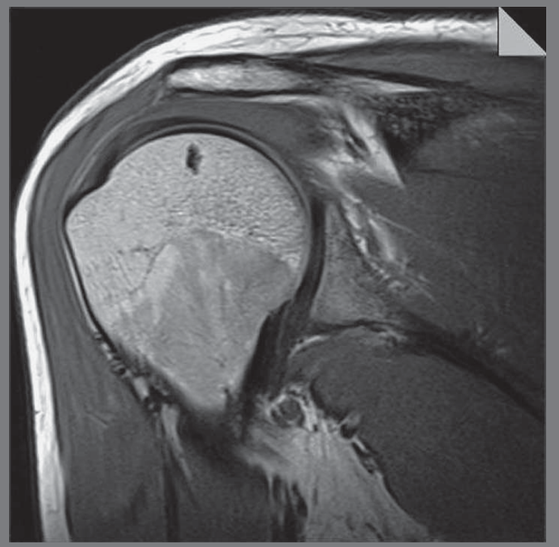

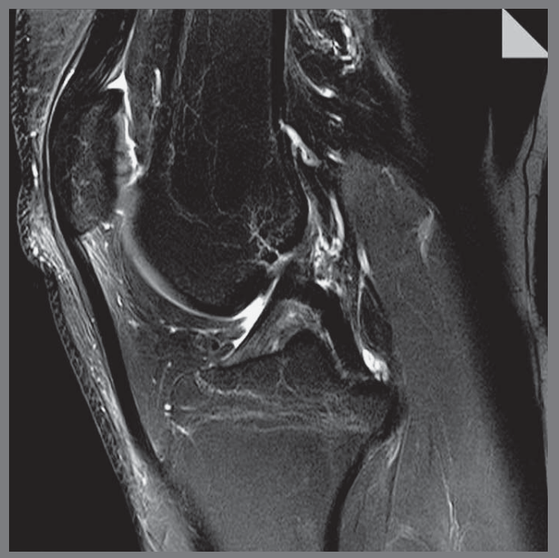

Visit us at

www.siemens.com/magnetom-world

Case Reports: Musculoskeletal MRI in Sports Medicine

Heinz-Peter Schlemmer[1,3]; Tina Holder[1]; T. Nägele[1,2]; Claus D. Claussen[1,2]

[1]Radiologie SpOrt Stuttgart, Germany
[2]University Hospital of Tuebingen, Germany
[3]German Cancer Research Center, Heidelberg, Germany

Background

In contrast to its role in oncology, for example, MR imaging in sports medicine deals primarily with healthy and young individuals. This imaging technique is an invaluable tool in sports medicine, not only because of its excellent soft tissue contrast but also because of its non-invasive and non-ionizing nature. While imaging in recreational sports is mainly limited to an evaluation of the effects of severe traumatic events, such as a skiing accident, the role of musculoskeletal MRI in case of competitive sports is much more extensive. For example, following an injury, MRI is also used to assist in the detailed evaluation of the degree of performance impairment of the athlete – with direct impact on treatment / training actions taken for effective fast and full recovery. This implies that time-to-diagnosis and the easy access and availability of MRI scan time (also for follow-up exams) is important for these athletes. One should also take into account that the pattern and severity of injuries can differ between recreational and competitive sports. This has a direct impact on the indication to MRI and the required knowledge of technologists and radiologists. But also non-traumatic pain and limitation of mobility, and as a consequence insufficient training and competitive performances, of athletes can have various causes and are one of the main indications for MRI. Because of the importance of the results of such MR exams to the athlete, the interdisciplinary approach is one of the key elements for optimal and responsible treatment and support. Consequently, all cases shown in this article were examined at and treated by an association of different facilities including the Department of Sports Medicine at Tuebingen University and the Olympic Training Center Stuttgart.

In this article, we present a selection of cases. Whilst not being a representative selection, they do reflect very well the variety and range of musculoskeletal imaging in sports medicine: in cases 1 and 2, MRI was used to support the clinical diagnoses of ligamental tear / rupture. Cases 3 through 5 show typical patterns of muscular tears and haematoma after trauma. In these patients, MRI was used to evaluate the involvement and extension of the different muscles to evaluate and quantify the degree of performance impairment and to provide information for further rehabilitation training. And finally, in cases 6 and 7, the images of two young athletes with pain at training but without corresponding trauma are shown.

All MRI exams shown in this article were performed at 1.5 Tesla (MAGNETOM Avanto).

Case 1

22-year-old male soccer player with severe knee pain after traumatic knee injury.

An extensive effusion is obvious. Already suspected by clinical signs, oedema and tear of the anterior cruciate ligament supports the diagnosis of a complete rupture of the ligament (arrowhead in Fig. 1A). In addition, a horizontally shaped oedema within the dorsal medial meniscus supports the suspicion of a horizontal (smaller) meniscal tear (arrow in Fig. 1B).

Images were acquired with the dedicated CP extremity coil. Sequence parameters for the shown images were:

- Sagittal PDw TSE with spectral fat suppression: TR / TE = 3754 / 37 ms, SL 1.5 mm, FOV 140 x 140 mm, Matrix 269 x 384 px
- Coronal PDw TSE with spectral fat suppression: TR / TE = 3754 / 37 ms, SL 1.5 mm, FOV 140 x 140 mm, Matrix 269 x 384 px

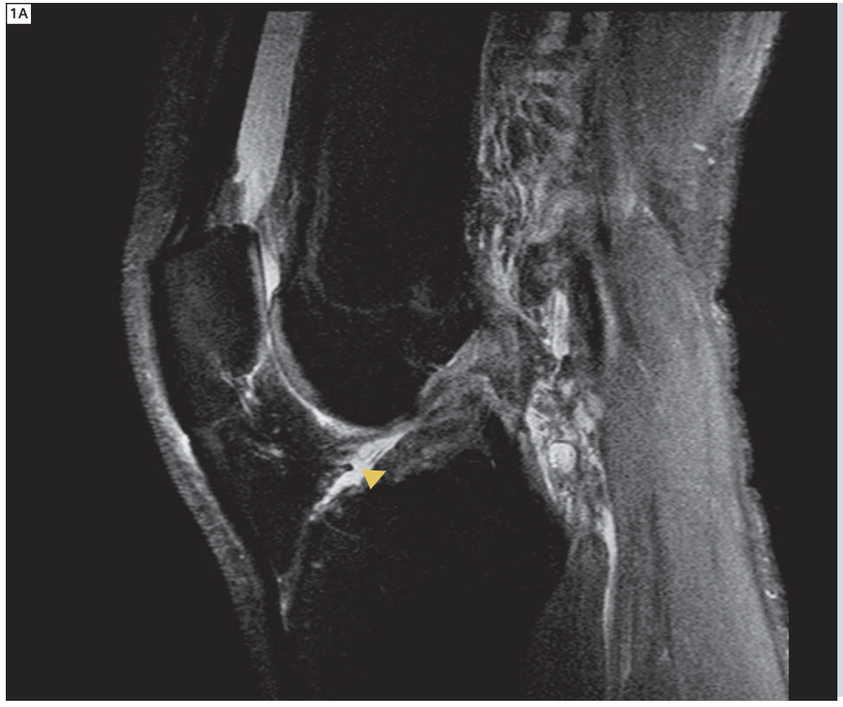

1A Sagittal PDw STIR.

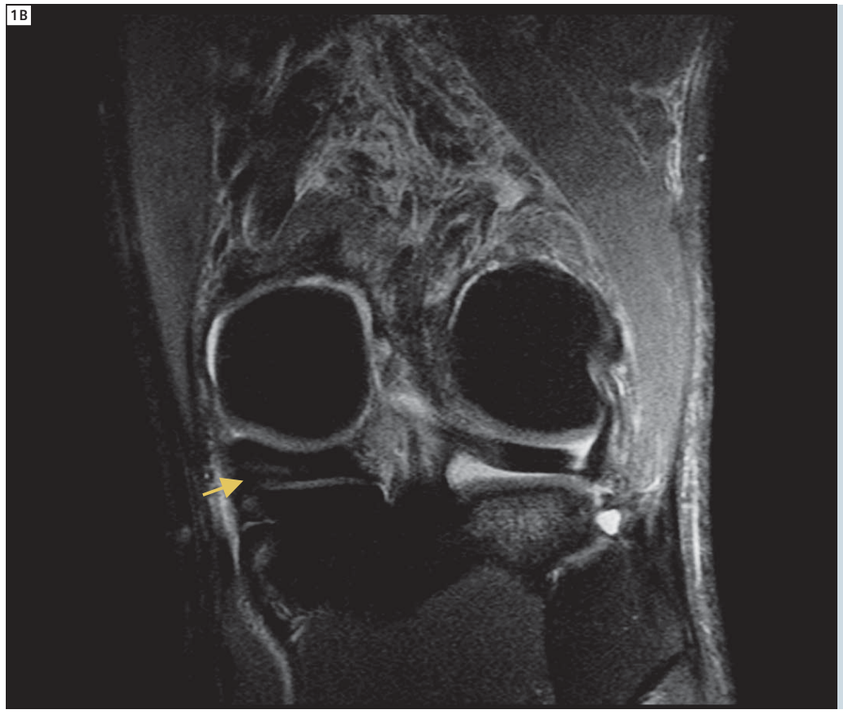

1B Coronal PDw STIR

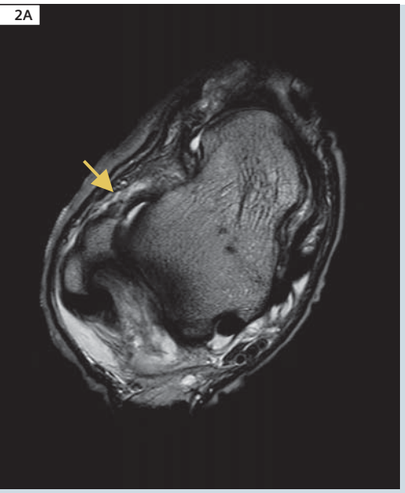

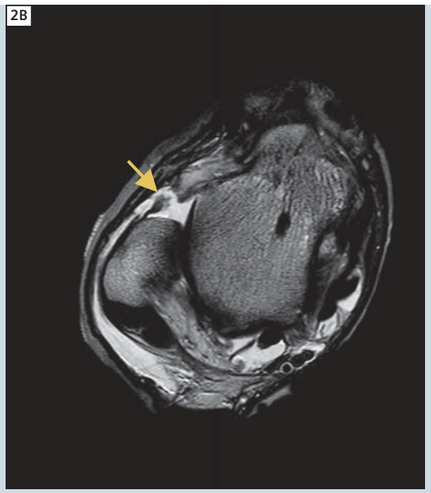

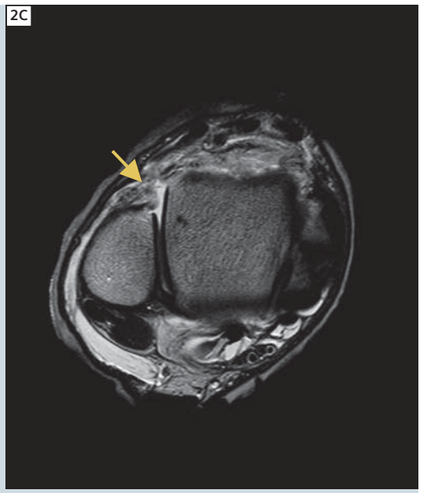

2A–C 1st trauma: transversal T2w TSE.

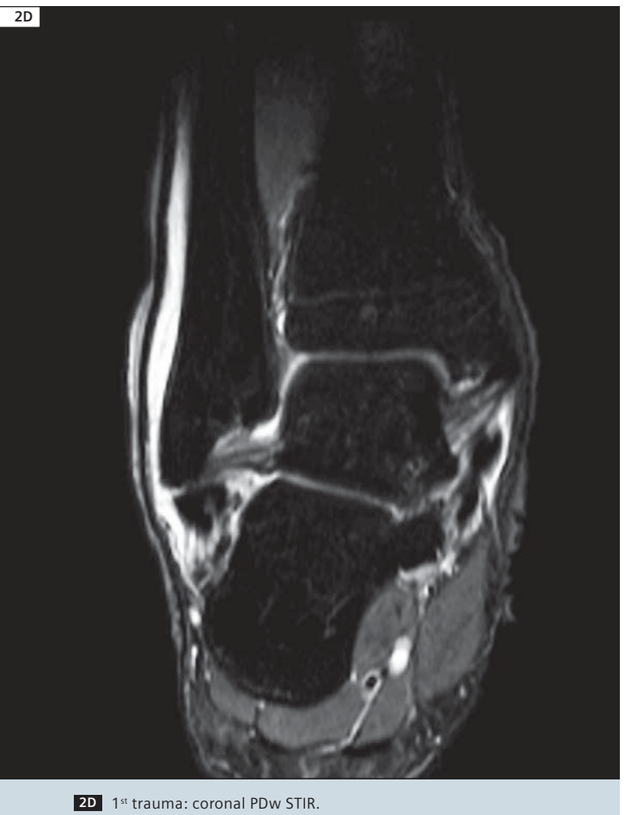

2D 1st trauma: coronal PDw STIR.

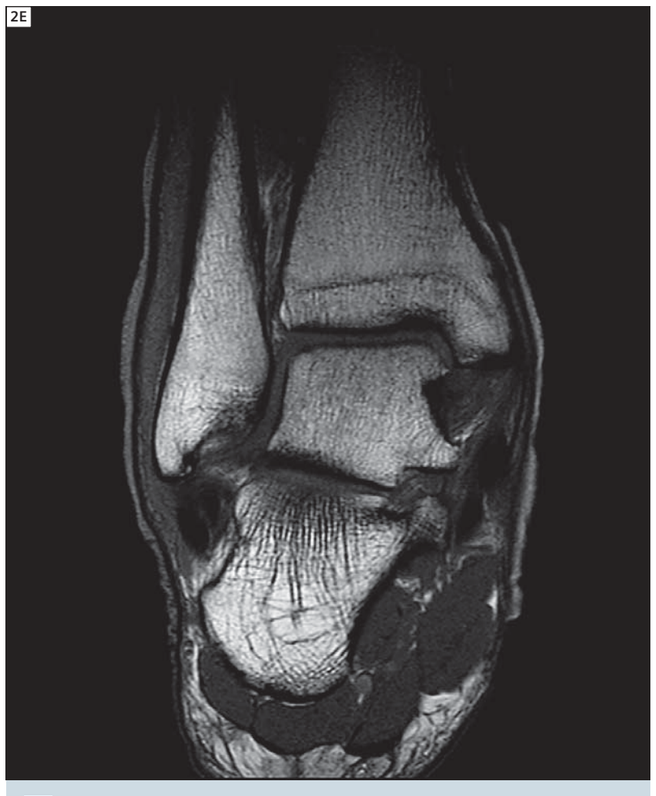

2E 1st trauma: coronal T1w TSE.

Case 2

23-year-old male soccer player after traumatic ankle injury.
MRI demonstrates a complete rupture of the anterior fibulotalar ligament (arrow in Figs. 2A–C). In addition, a partial rupture of the anterior syndesmosis ligament is present and an extensive oedema and haemorrhage of the surrounding soft tissue can also be observed (Figs. 2D and E). 7 months after the initial traumatic event, another trauma of similar type occurred. Follow-up MRI showed a thickened but now continuous fibulotalar ligament and ventral syndesmosis (arrowheads in Figs. 2D–F); no re-rupture was found.
Images were acquired with the 4-channel flex coil. Sequence parameters for the shown images were:

- Transversal T2w TSE: TR / TE = 5259 / 85 ms, SL 3 mm, FOV 140 x 140 mm, Matrix 269 x 448 px
- Coronal PDw STIR: TR / TE / TI = 6500 / 29 / 160 ms, SL 3 mm, FOV 160 x 160 mm, Matrix 169 x 256 px
- Coronal T1w TSE: TR / TE = 537 / 9.5 ms, SL 3 mm, FOV 111 x 160 mm, Matrix 250 x 448 px, TA
- Follow-up MRI transversal T2w TSE: TR / TE = 4110 / 105 ms, SL 3 mm, FOV 110 x 110 mm, Matrix 512 x 512 px

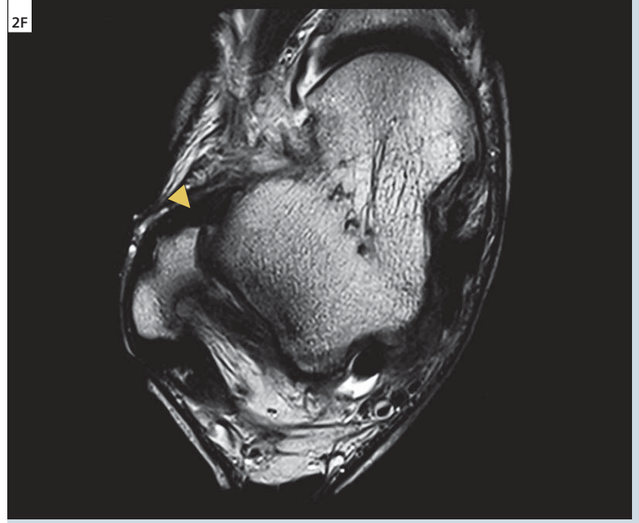

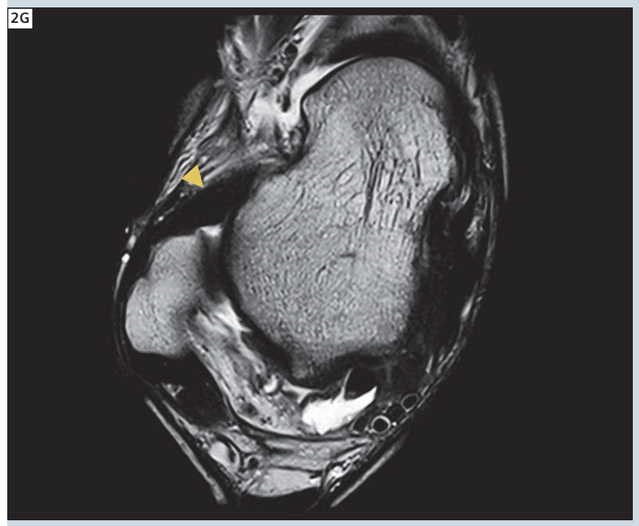

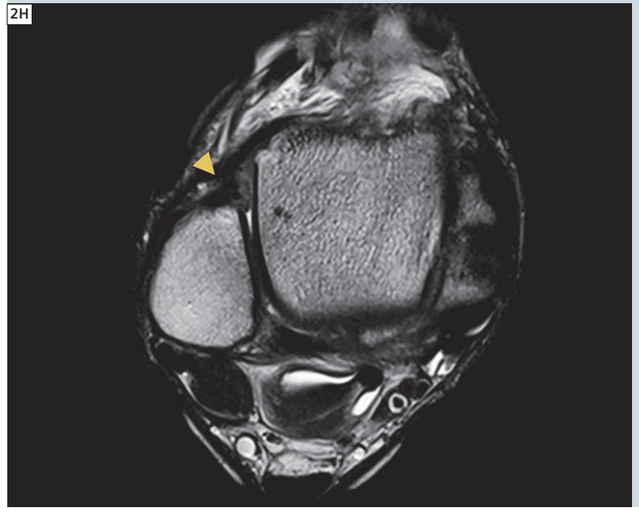

2F–H 2nd trauma: transversal T2w TSE.

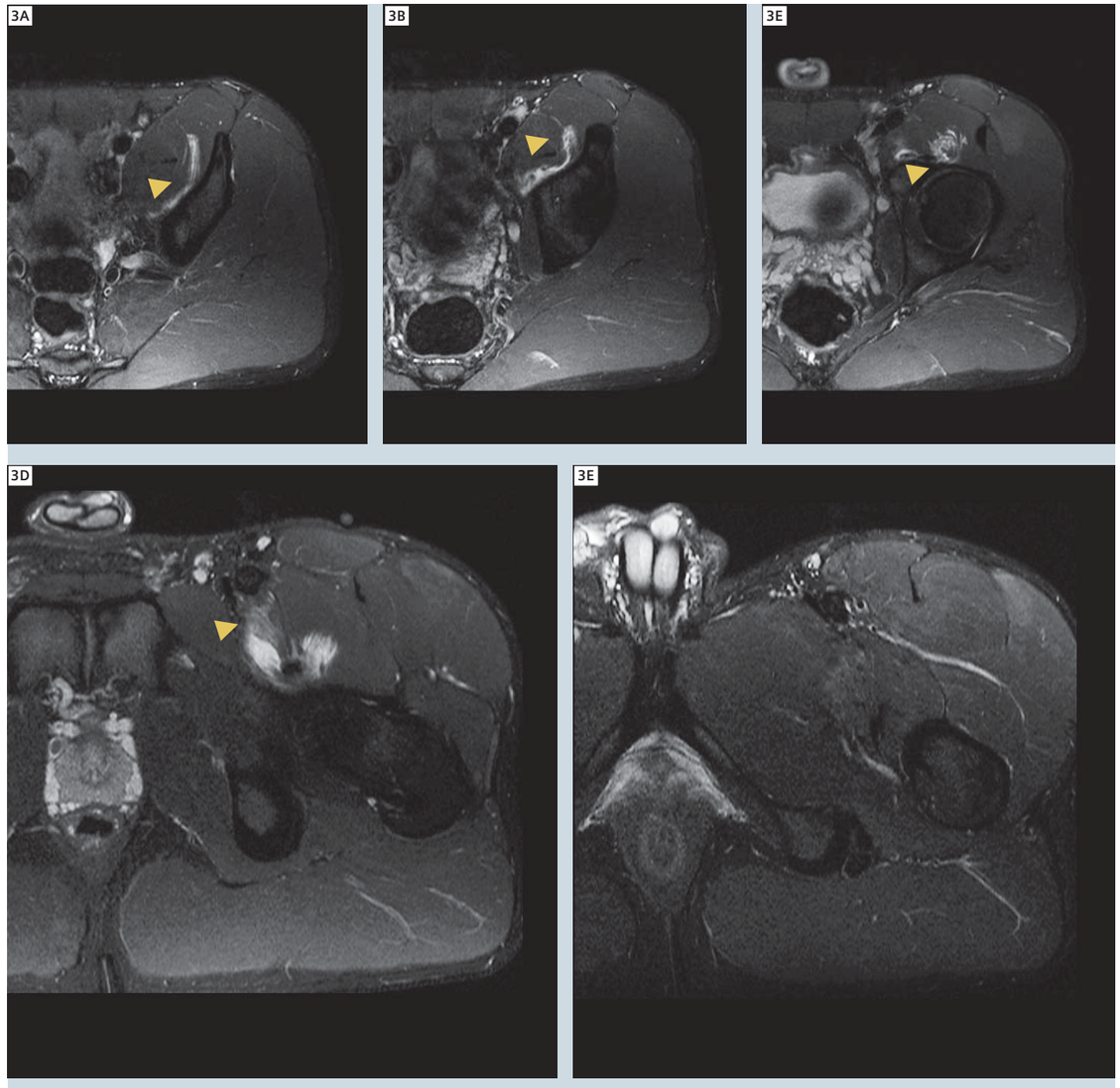

3A–E Transversal PDw STIR.

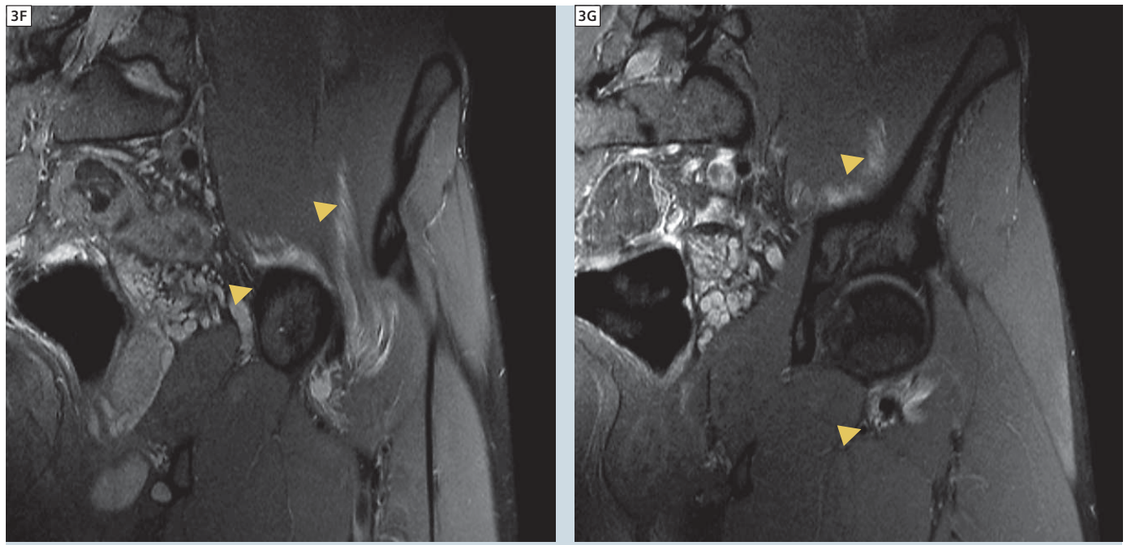

3F–G Oblique coronal PDw STIR.

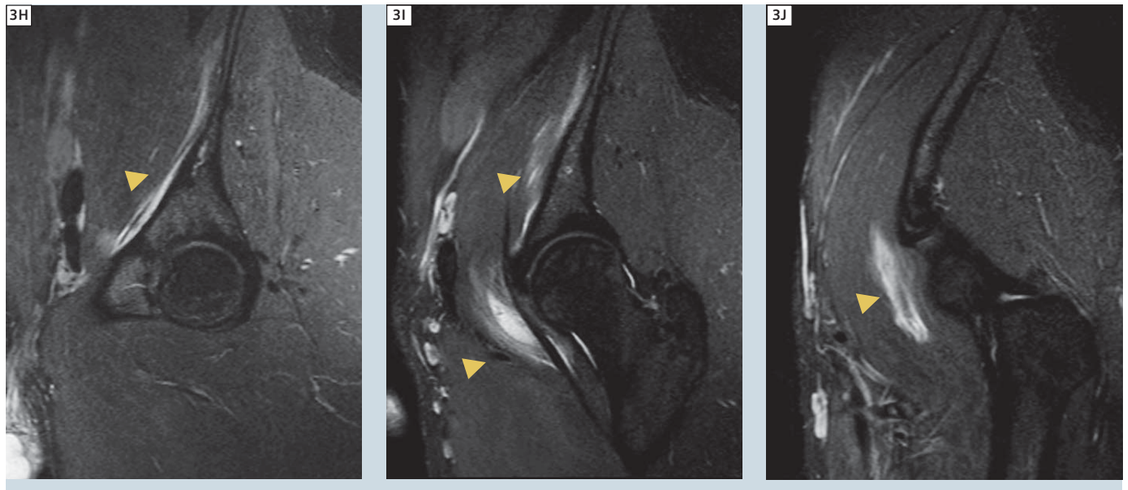

3H–J Oblique sagittal PDw STIR.

Case 3

22-year-old male soccer player after trauma of the left upper leg.
Tear of the fascia of the left iliac muscle at the ventral border of the acetabulum and less prominent tear of the iliac muscle itself (arrowheads in Fig. 3).
Images were acquired with the Spine and Body Matrix coil. Sequence parameters for the shown images were:

- Transversal PDw STIR: TR / TE / TI = 5390 / 29 / 160 ms, SL 4 mm, FOV 220 x 200 mm, Matrix 224 x 320 px
- Oblique coronal PDw TSE with spectral fat saturation: TR / TE = 4340 / 13 ms, SL 3 mm, FOV 250 x 250 mm, Matrix 240 x 320 px, TA
- Obliques sagittal PDw STIR: TR / TE / TI = 7540 / 29 / 160 ms, SL 4 mm, FOV 189 x 270 mm, Matrix 157 x 320 px

→ Visit **www.siemens.com/magnetom-world** to check out the protocols of the MSK Advisory Board.

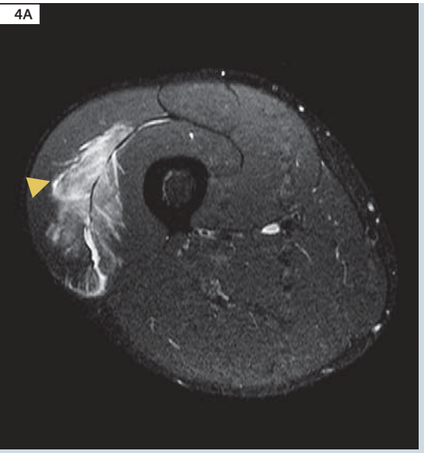

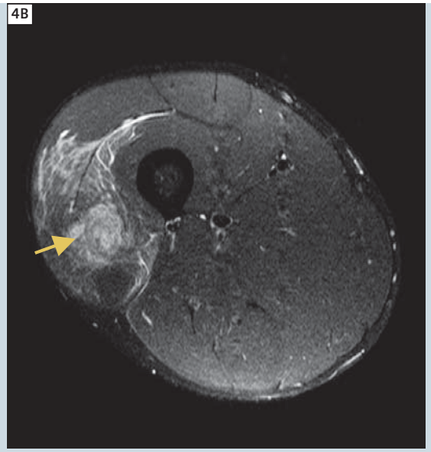

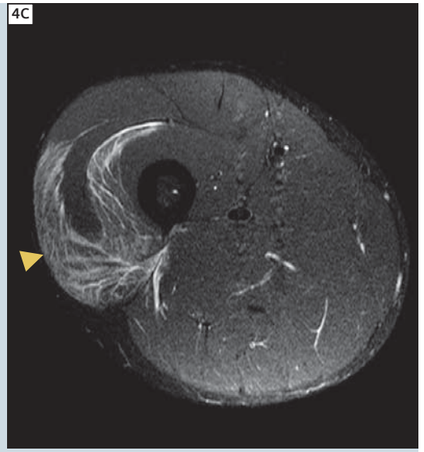

4A–C Transversal PDw STIR.

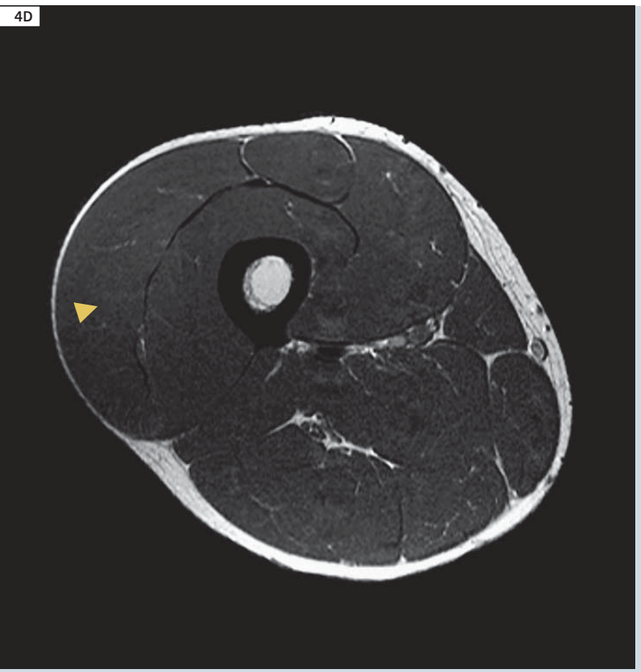

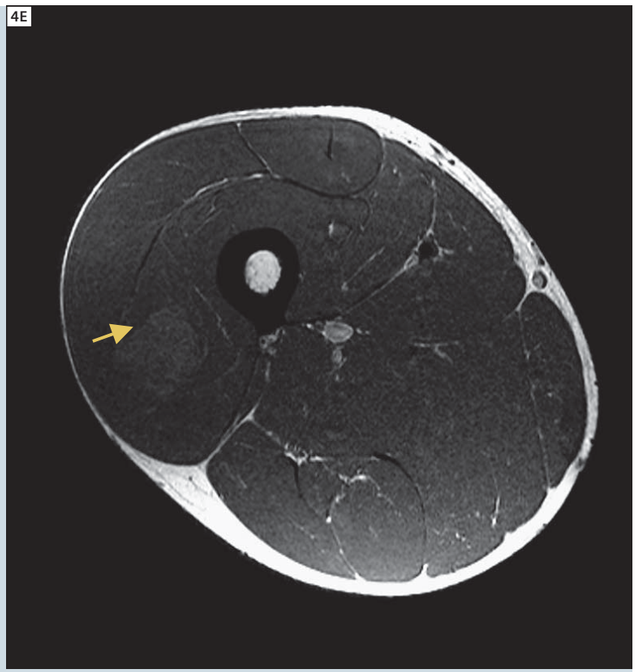

4D–E Transversal T1w TSE.

Case 4

24-year-old male soccer player after direct trauma (pound on right upper leg). On T2w images, a space occupying lesion within the lateral vastus muscle (arrow) and slight increased signal intensities on T1w images was seen, representing an extensive haematoma. Also a surrounding haemorrhage (arrowheads) was obvious. There were no clear signs of a tear in the muscles. The femur showed neither a fracture nor abnormalities of the signal intensities of the bone marrow.
Images were acquired using the Spine and Body Matrix coil. Sequence parameters for the shown images were:

- Transversal PDw STIR: TR / TE / TI = 8073 / 29 / 160 ms, SL 4 mm, FOV 220 x 220 mm, Matrix 224 x 320 px
- Transversal T1w TSE: TR / TE = 580 / 13 ms, SL 4 mm, FOV 200 x 200 mm, Matrix 256 x 320 px
- Sagittal PDw STIR: TR / TE / TI = 4580 / 29 / 160 ms, SL 4 mm, FOV 280 x 400 mm, Matrix 157 x 320 px
- Coronal T2w TSE: TR / TE = 7130 / 86 ms, SL 4 mm, FOV 281 x 399 mm, Matrix 216 x 384 px

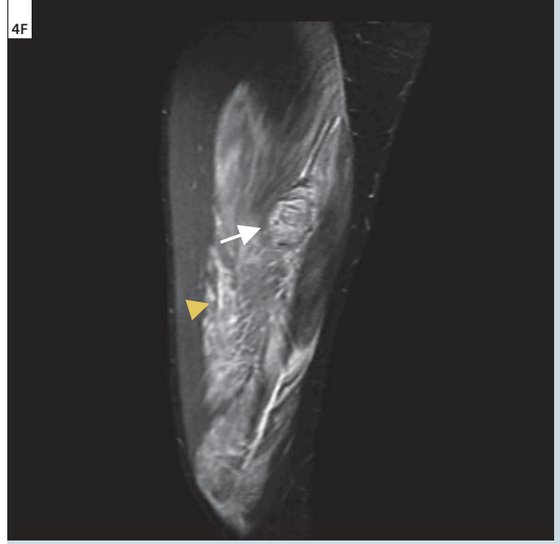

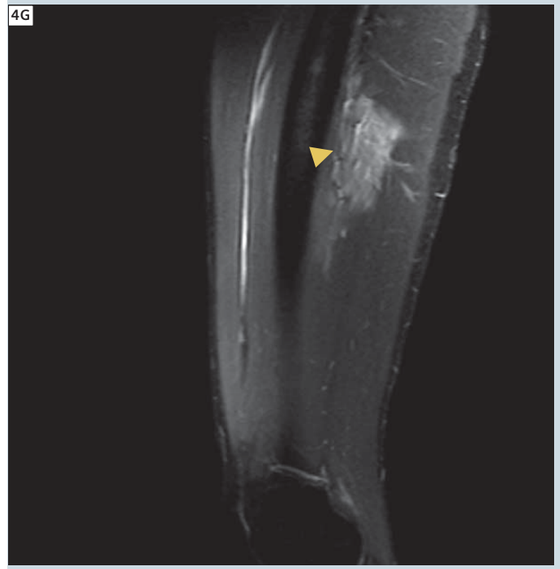

4F–G Sagittal PDw STIR.

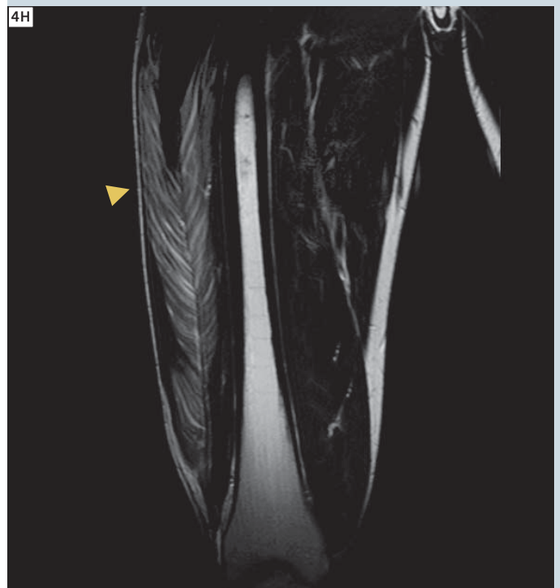

4H Coronal T2w TSE.

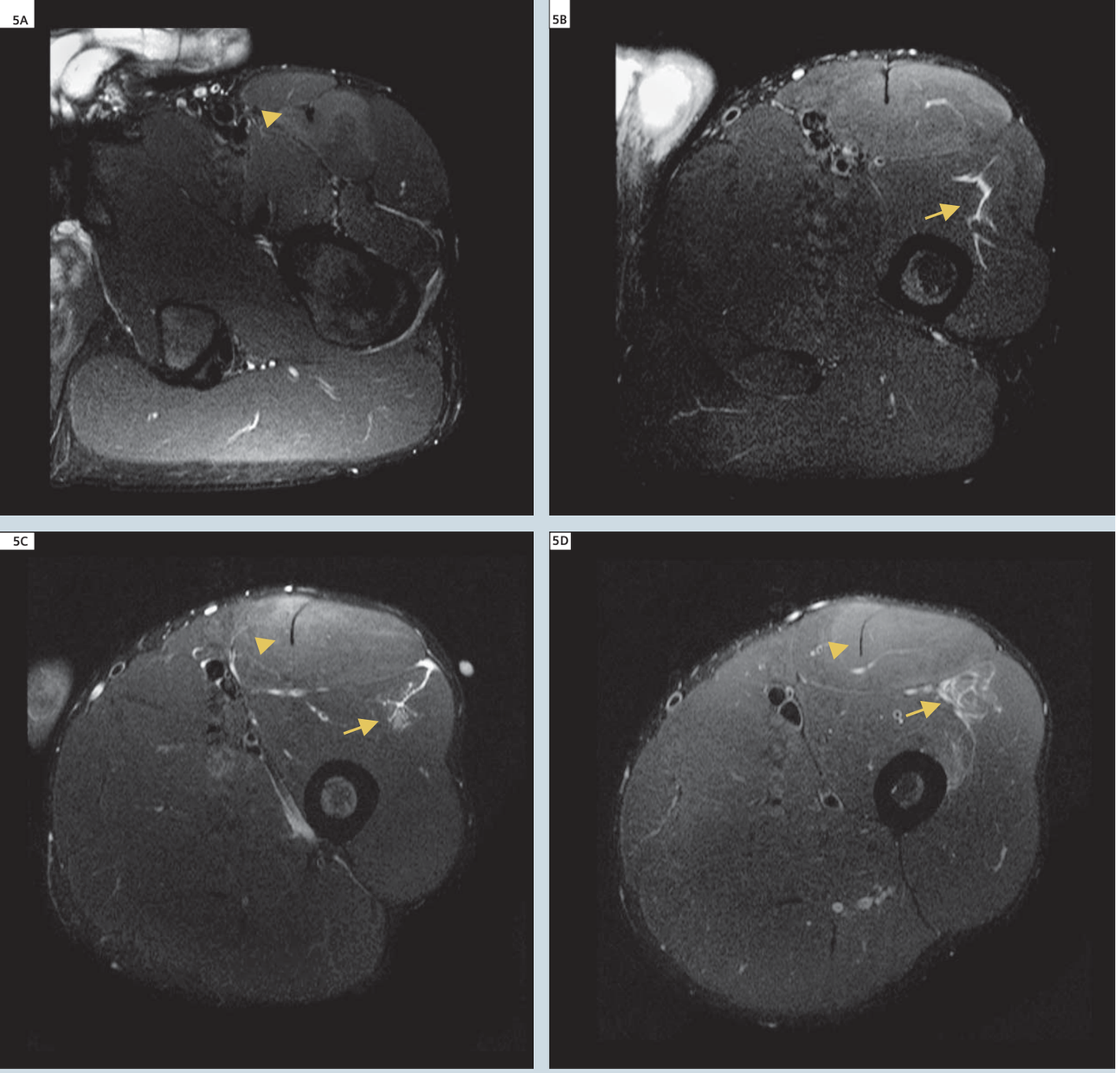

5A–D Transversal PDw STIR.

Case 5

24-year-old male soccer player after trauma.
In contrast to case 4, an approximate 15 mm long acute tear of the lateral vastus muscle (arrow) was seen in this patient but there were no signs of a dehiscence of the muscles. Slight increase of the signal intensities on PDw images within the vastus intermedius and rectus femoris muscles were rated as a strain.
The patient was positioned feet first and the images were acquired with the Spine and Body Matrix coil. Sequence parameters for the shown images were:

- Transversal PDw STIR: TR / TE / TI = 5390 / 29 / 160 ms, SL 4 mm, FOV 220 x 220 mm, Matrix 224 x 320 px

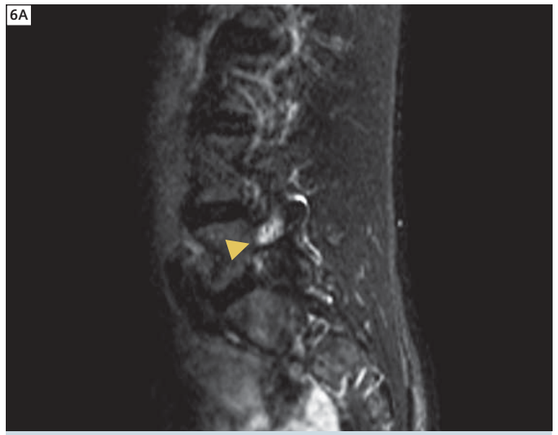

6A Sagittal T2w STIR.

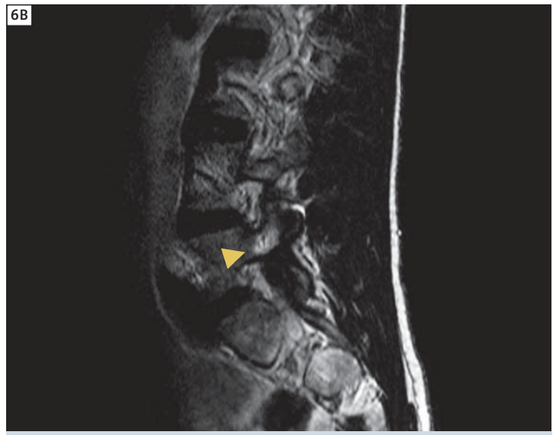

6B Sagittal T2w TSE.

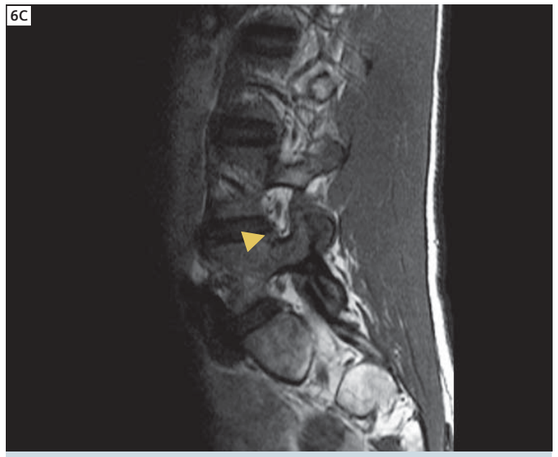

6C Sagittal T1w TSE.

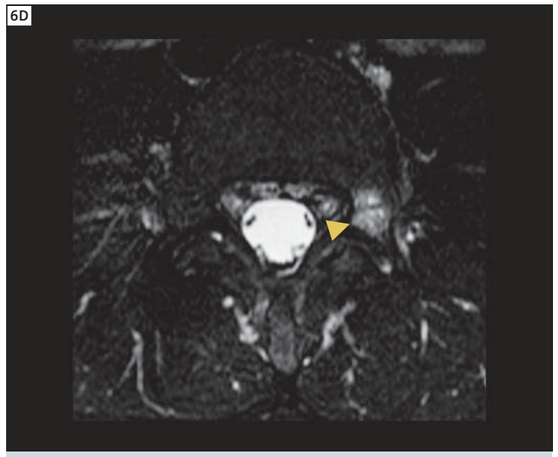

6D Oblique transversal T2w STIR.

Case 6

16-year-old female high-jumper with consistent pain during training sessions and while making sudden jerky movements.
High signal intensity within the bone marrow of the left pedicel of the 5th vertebra could be seen. Within this oedema, a continuous hypointense line was crossing the pedicel. This finding was rated as a 1st degree spondylolysis without signs of listhesis or cleft.
Images were acquired using the spine coil. Sequence parameters for the shown images were:

- Oblique transversal T2w TSE with spectral fat saturation: TR / TE = 3800 / 105 ms, SL 3 mm, FOV 180 x 180 mm, Matrix 192 x 256 px
- Sagittal T2w STIR: TR / TE / TI = 7300 / 63 / 150 ms, SL 3 mm, FOV 300 x 300 mm, Matrix 195 x 256 px
- Sagittal T1w TSE: TR / TE = 621 / 12 ms, SL 3 mm, FOV 280 x 280 mm, Matrix 269 x 384 px
- Sagittal T2w TSE: TR / TE = 8660 / 120 ms, SL 3 mm, FOV 280 x 280 mm, Matrix 269 x 384 px

Case 7

13-year-old female soccer player with pain within the right forefoot but without adequate corresponding trauma. Caudal of the epiphyseal line of the second metatarsal bone, an oedema of the bone marrow and very apical loss of shape of the bone and compression of bone trabeculae. The epihyseal line is of regular shape. The caudal head of the metacarbal bone is also surrounded by oedema and an effusion of the joint was present, too. These findings were concordant with an osteonecrosis in the stadium of vitrification (Morbus Köhler-Freiberg / Morbus Köhler II).
Images were acquired with the 4-channel flex coil. Sequence parameters for the shown images were:

- Coronal T2w STIR: TR / TE / TI = 4180 / 70 / 140 ms, SL 2 mm, FOV 140 x 140 mm, Matrix 460 x 512 px
- Coronal T1w TSE: TR / TE = 684 / 13 ms, SL 2 mm, FOV 140 x 140 mm, Matrix 256 x 512 px
- Sagittal T2w STIR: TR / TE / TI = 3700 / 70 / 140 ms, SL 2 mm, FOV 140 x 140 mm, Matrix 460 x 512 px
- Transversal T2w TSE: TR / TE = 3880 / 103 ms, SL 3 mm, FOV 89 x 130 mm, Matrix 352 x 512 px

Contact
Prof. Heinz-Peter Schlemmer, M.D; Ph.D.
Radiologie SpOrt Stuttgart
Fritz-Walter-Weg 19
D-70372 Stuttgart
Germany
h.schlemmer@Dkfz-Heidelberg.de
www.radiologie-neckarpark.de
www.sport-medizin.eu

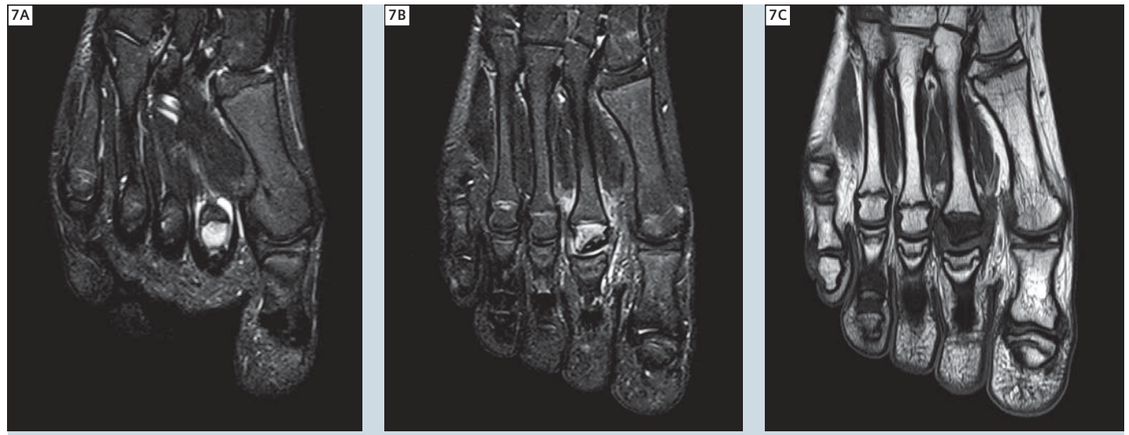

7A–C **A** and **B:** Coronal T2w STIR. **C:** Coronal T1w TSE.

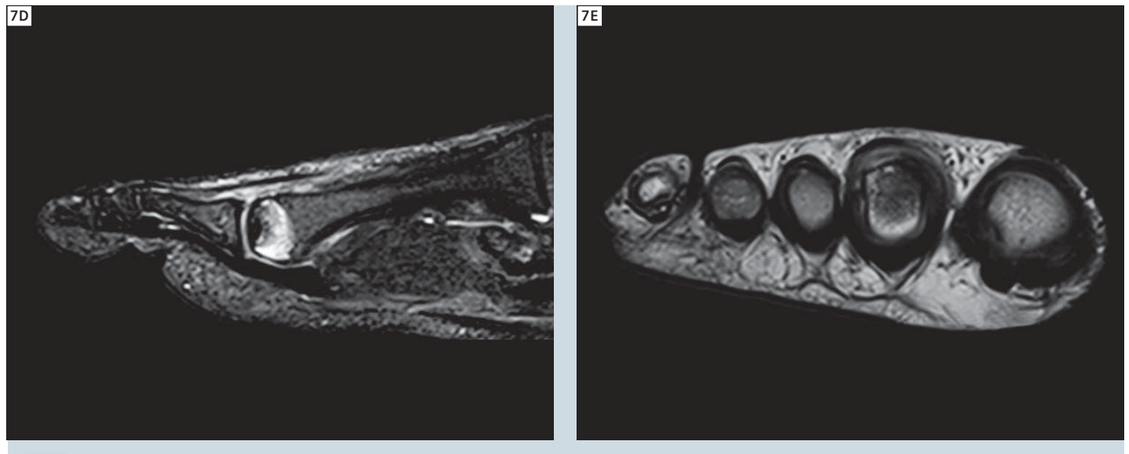

7D–E **D:** Sagittal T2w STIR. **E:** Transversal T2w TSE.

Case Report:
Fast Joint Imaging at 1.5 Tesla with a Combination of the Quadrature Knee and Body Matrix Coil in Case of Severe Knee Pain of an Obese Patient

Marietta Garmer M.D., Serban Mateiescu

Grönemeyer Institute of Microtherapy, Bochum, Germany

Introduction

Examinations of the knees of obese patients are challenging; most dedicated knee coils are optimized to offer a comfortable positioning and optimal coil load as well as signal contribution for a wide range of patients. However, even under such prerequisites, some patients do require special coil setups and cannot be examined with a conventional closed knee coil. This is not only true for obese patients; it may also apply also under other clinical conditions such as casted or stiffed joints and can result in an insufficient image quality (e.g. caused by inadequate signal contribution of the coil). But an uncomfortable patient positioning can also compromise the outcome of such an MR exam. Fortunately, imaging of a joint under such conditions is a rare request in the daily clinical routine. But if required it represents a clear challenge for the technologist. In addition to the simple technical challenges of such an examination, the patient is very often in pain and the compliance strongly depends on comfortable positioning – which may be difficult to achieve. Additionally, because of the pain, image acquisition must be fast and of sufficient quality to avoid re-examination. In the presented case we demonstrate how a flexible coil setup provided by the Tim coil technology in combination with open-bore MR technology can assist in the diagnoses of knee pain in obese patients.

Patient history

An obese 60-year-old female patient (150 kg, 175 cm, BMI = 49) consulted our institution because of progressive knee pain over the previous two weeks. The pain persisted under stress as well as in rest. Walking was only possible with assistance.
The patient could not remember any traumatic accident. The clinical examination showed neither findings of crepitation of the patella nor medial pressure pain. Patient anamneses revealed known osteoarthritis; an artificial hip joint had been implanted in 2005 because of hip osteoarthritis. MRI was performed to evaluate known osteoarthritis.

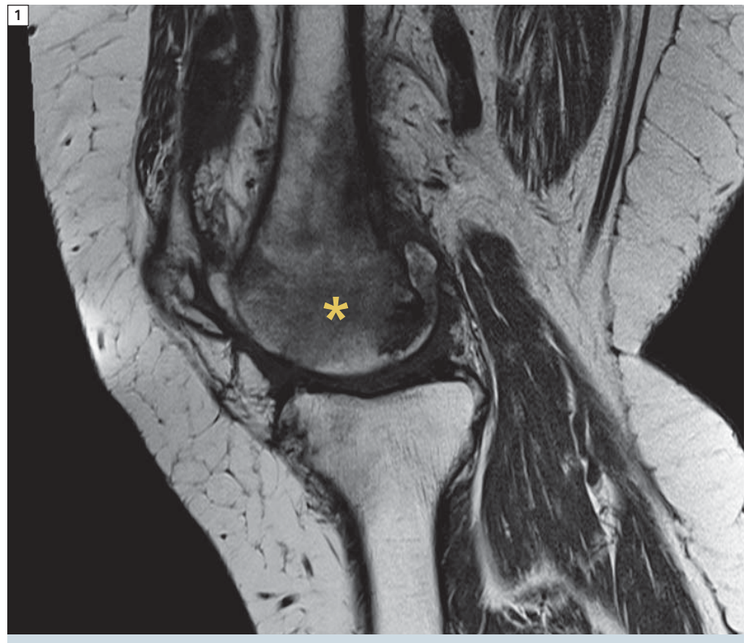

1 Sagittal T1w SE.

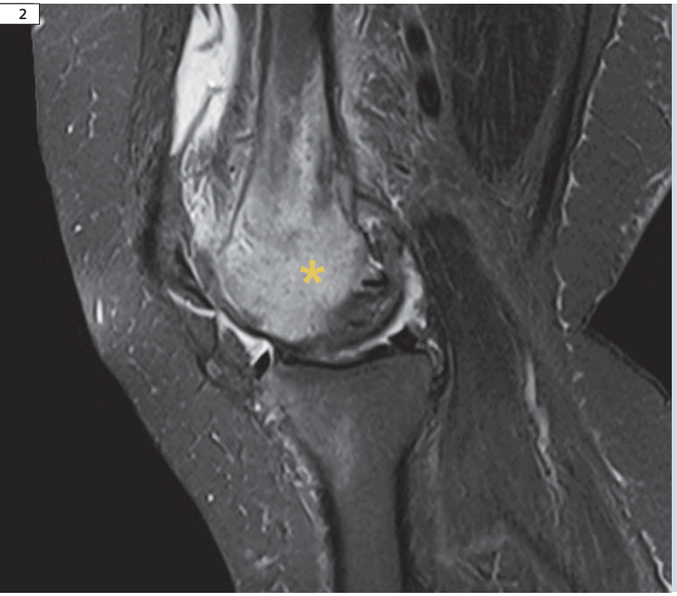

2 Sagittal T2w STIR.

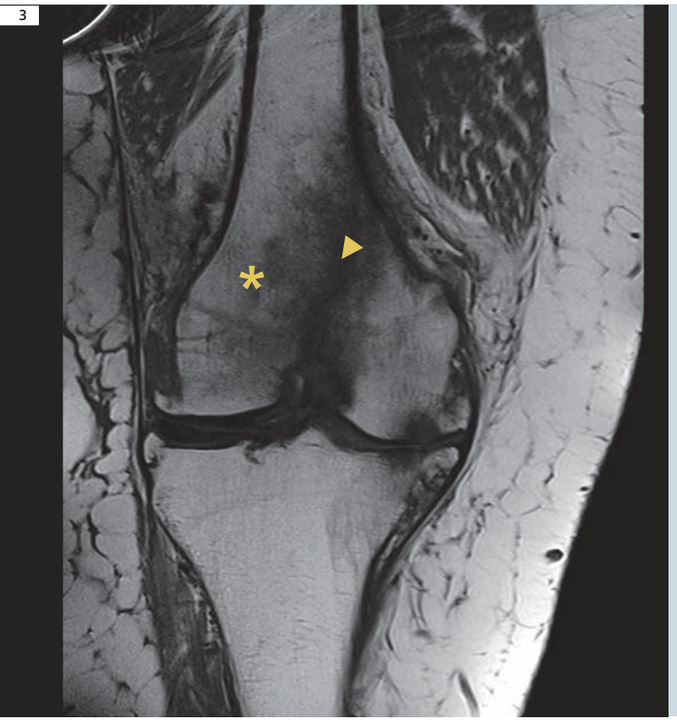

3 Coronal T1w SE.

MR examination

All shown images were acquired with an open-bore 1.5 Tesla system (MAGNETOM Espree; software version *syngo* MR B15).
The patient was positioned feet first in supine position.
The affected knee was positioned inside the lower part of the quadrature knee coil. Because of the large size of the knee (68 cm circumference) the extremity coil could not be closed. Therefore the examination required a different imaging strategy; to achieve an optimal illumination of the knee, one Body Matrix coil was used and replaced the upper part of the knee coil. The other knee was covered by an electrical shielding to avoid back folding.

The imaging protocol included:

- Sagittal T1w SE: TR 544 ms, TE 18 ms, slice thickness 4 mm, FOV 196 x 220 mm , Matrix 260 x 512, phase-encoding head – feet , TA 3:31 min (Fig. 1)
- Sagittal T2w STIR: TR 4850 ms, TE 40 ms, TI 130 ms, slice thickness 4 mm, FOV 196 x 220 mm , Matrix 392 x 512i, phase-encoding head – feet, TA 3:00 min (Fig. 2)
- Coronal T1w SE: TR 544 ms, TE 18 ms, slice thickness 4 mm, FOV 230 x 230 mm, Matrix 292 x 512, phase-encoding right – left, TA 3:20 min (Fig. 3)
- Coronal T2w STIR: TR 4650 ms, TE 39 ms, TI 150 ms, slice thickness 4 mm, FOV 230 x 230 mm, Matrix 384 x 512i, phase-encoding right – left, TA 3:20 min (Fig. 4)
- Transversal T1w SE: TR 544 ms, TE 18 ms, slice thickness 6,5 mm, FOV = 230 x 230 mm, Matrix 292 x 512, phase-encoding right – left, TA 3:01 min (Fig. 5)
- Sagittal PDw FS: TR 1610 ms, TE 36 ms, PAT2, slice thickness 4 mm, FOV 240 x 240 mm, Matrix 320 x 320, phase-encoding head-feet, TA 1:48 min (not shown)
- Transversal T2*w MEDIC: TR 1130 ms, TE 33 ms, slice thickness 6,5 mm, FOV 230 x 230 mm, Matrix 256 x 512, phase-encoding right-left, TA 4:18 min (not shown)

The resulting total imaging time was less than 25 minutes.

Imaging findings and diagnosis

A bone marrow edema (asterisk in figures 1–5) of the femur and signs of knee osteoarthritis were found as well as an effusion in the suprapatellar bursa (Figs. 1, 2). A hypointense linear band (arrowhead in figures 3–5) on both T1-weighted images (Figs. 3, 5) and STIR sequence (Fig. 4) was observed, representing a fracture cleft. Edema and partial loosening of the anterior cruciate ligament was present, too. In conclusion, a clinically not suspected non-traumatic stress fracture of the distal femur was diagnosed although, based on the image findings, a partial rupture of the anterior cruciate ligament could not be excluded. In addition, severe osteoarthritis with defects of the articular cartilage, medial meniscopathy and arthrosis of the femoropatellar joint were also diagnosed.

Contact
Marietta Garmer, M.D.
Grönemeyer Institute of Microtherapy
Universitätsstr. 142
D-44799 Bochum
Germany
garmer@microtherapy.de
Phone: +49-234-9780312

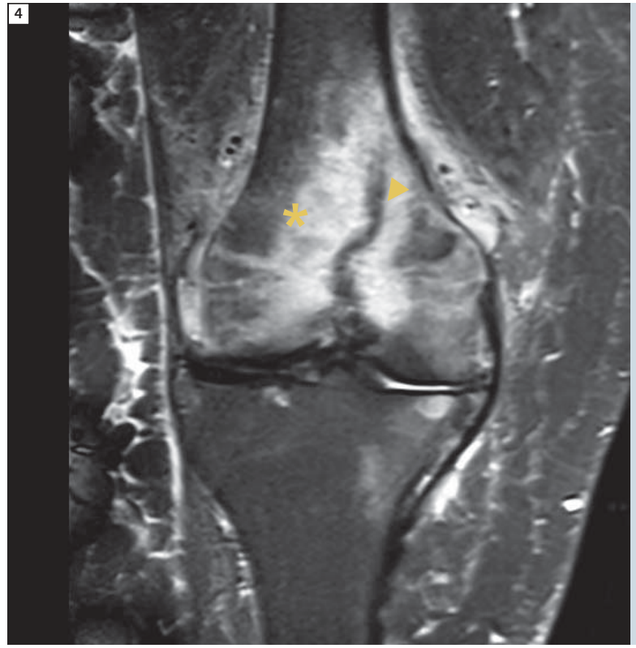

4 Coronal T2w STIR.

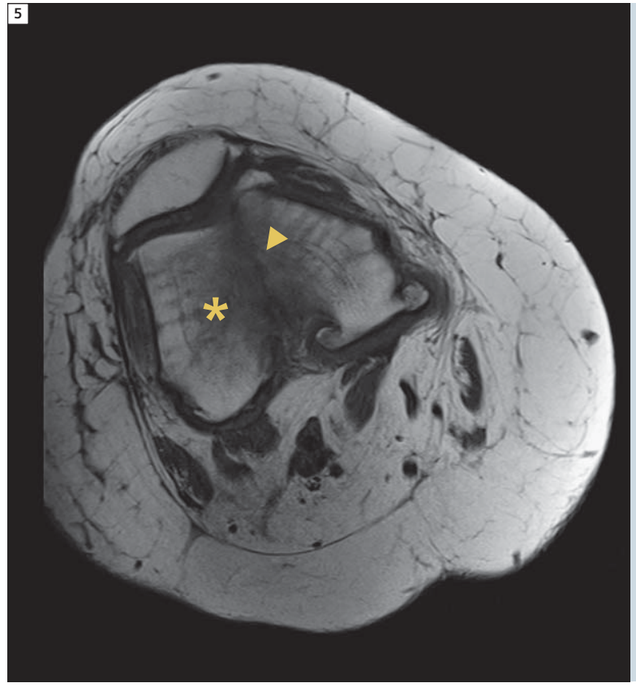

5 Transversal T1w SE.

Case Report:
Traumatic Lesion of the Left Brachial Plexus

Markus Lentschig, M.D.

MR and PET/CT Imaging Center Bremen Mitte, Bremen, Germany

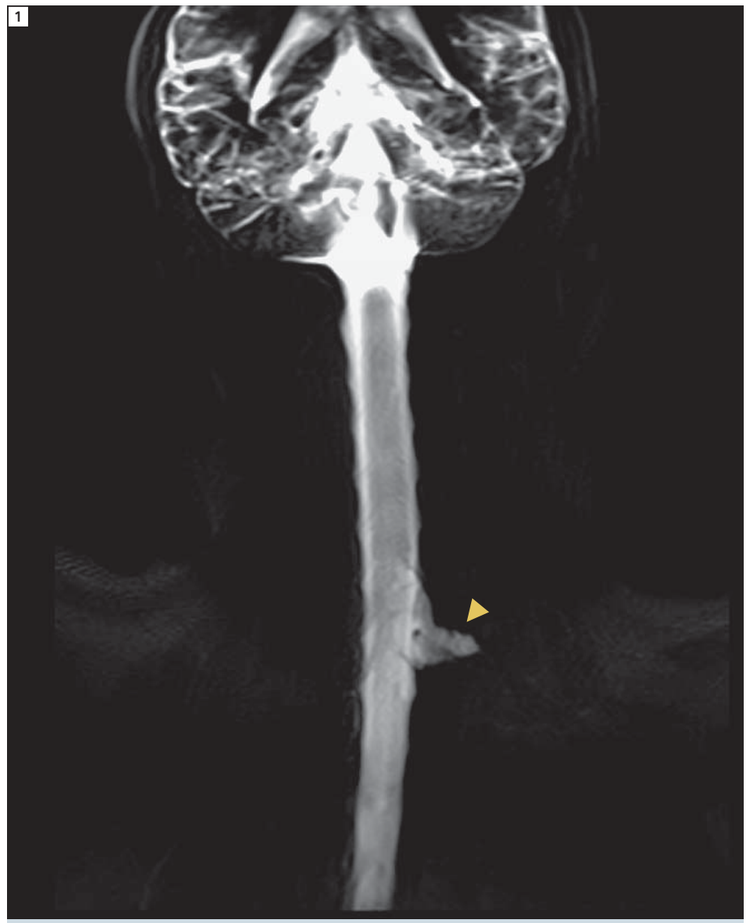

1 MR myelogram.

Patient history

An 18-year-old patient was referred to our institution for evaluation of the integrity of the left brachial plexus 4 weeks after a severe traumatic event. The presented symptoms at the time-point of MR imaging suggested an involvement of the medial and inferior left brachial plexus.

Sequence details

All images were acquired on our 1.5 Tesla MAGNETOM Espree with a combination of the dorsal elements of the head/neck and the spine matrix coils. The imaging protocol comprised a coronal single shot HASTE myelogram, sagittal T1w and T2w TSE, coronal T1w TSE and T2w TIRM, transversal fat saturated T2w TSE and MEDIC and finally 3D T2w TSE (*syngo* SPACE) in coronal orientation. No contrast media was applied in this patient.

Coronal HASTE Myelogram: TR / TE 4500 / 755 ms; FOV 350 x 350 mm; matrix 307 x 384; SL 60 mm; PAT 2; no averages; TA 1.8 s.

Sagittal T2w TSE: TR / TE 4274 / 113 ms; FOV 300 x 300 mm; matrix 314 x 448; SL 3 mm; no iPAT; averages 2; TA 4:13 min.

Sagittal T1w TSE (not shown): TR / TE 689 / 11 ms; FOV 241 x 300 mm; matrix 270 x 448; SL 3 mm; no iPAT; averages 3; TA 3:06 min.

Transversal T1w TSE wit spectral fat saturation (not shown): TR / TE 3740 / 93 ms; FOV 303 x 380 mm; matrix 204 x 512; SL 4 mm; no iPAT; averages 2; TA 3:56 min.

Coronal T1w TSE: TR / TE 639 / 20 ms; FOV 309 x 380 mm; matrix 250 x 512; SL 4 mm; no iPAT; no averages; TA 5:20 min.

Coronal T2w TIRM: TR / TE / TI 5940 / 36 / 160 ms; FOV 285 x 380 mm; matrix 192 x 512; SL 4 mm; no iPAT; no averages; TA 5:22 min.

Coronal 3D T2w TSE (*syngo* SPACE): TR / TE 1500 / 173 ms; FOV 280 x 280 mm; matrix 323 x 320; SL 1 mm; PAT 3; no averages; TA 3:56 min.

Imaging findings

A large cystic lesion at the level of the 1st thoracic and 8th cervical nerve root is obvious on the HASTE myelogram (arrowhead in Fig. 1). Accordingly a displacement of the dural border and widening of the subdural space is also obvious (compare transversal T2w MEDIC images in figures 2A, B). A displacement of the spinal dural mater (Fig. 2) can be found on transversal and sagittal T2w images. Edema of the left

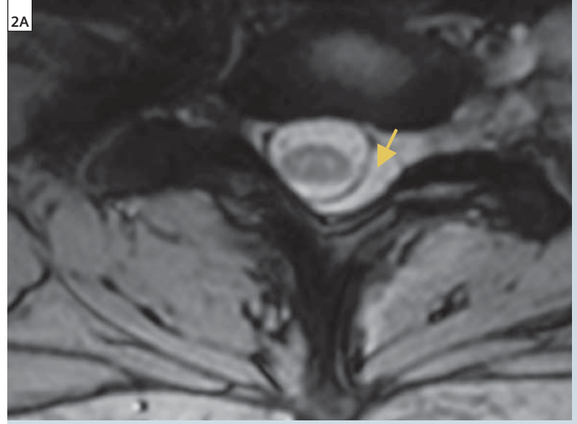

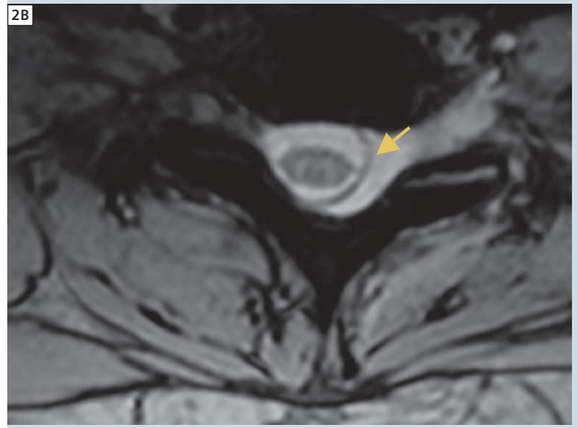

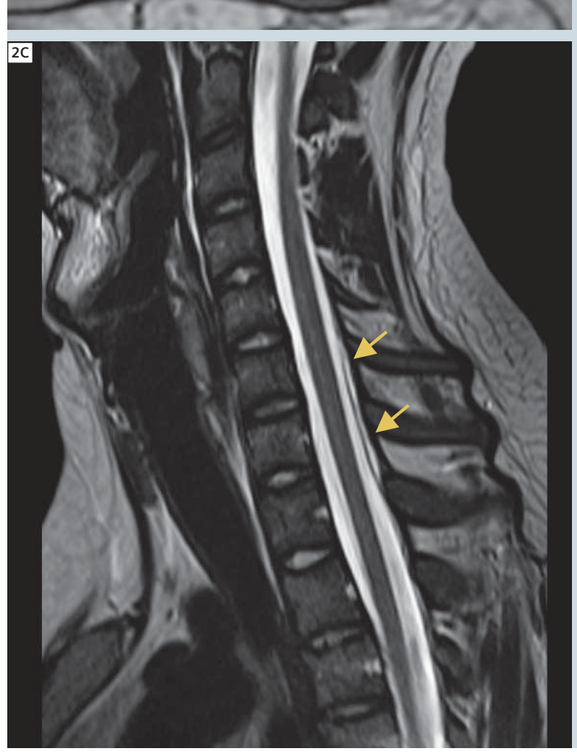

2 A and B transversal MEDIC, C sagittal T2w TSE.

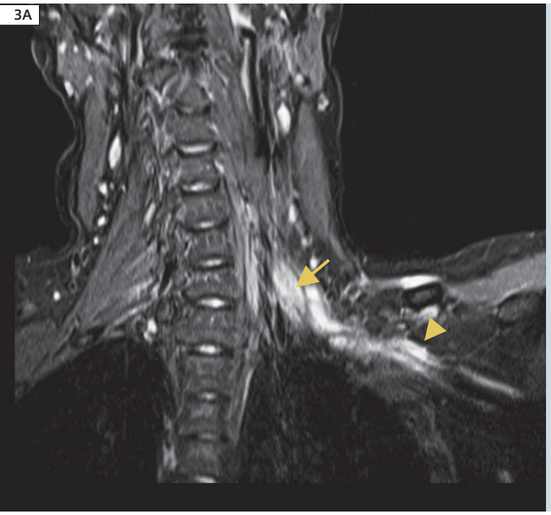

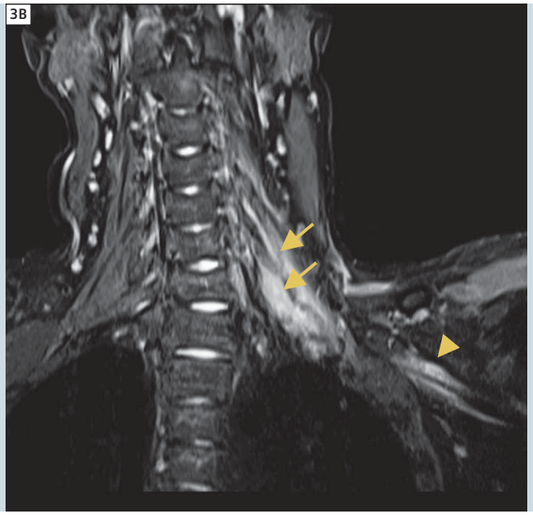

3 Coronal TIRM.

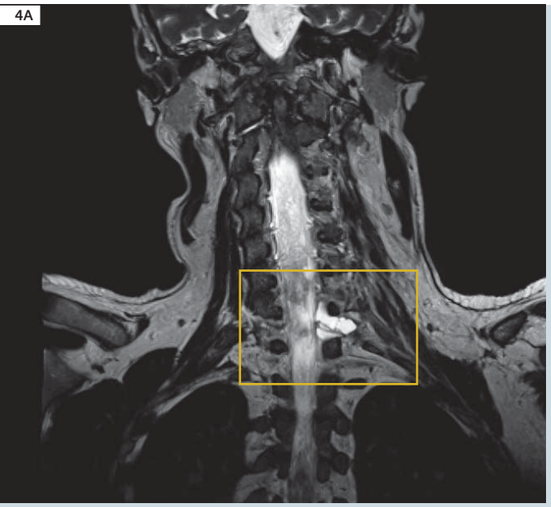

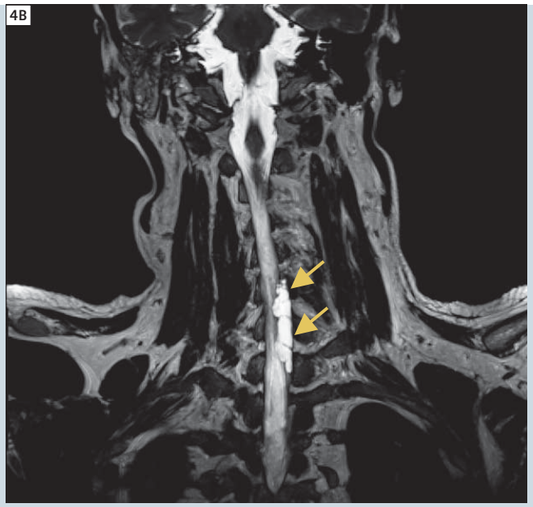

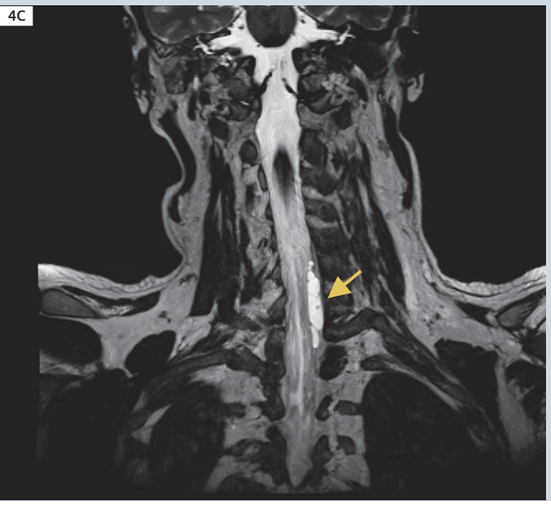

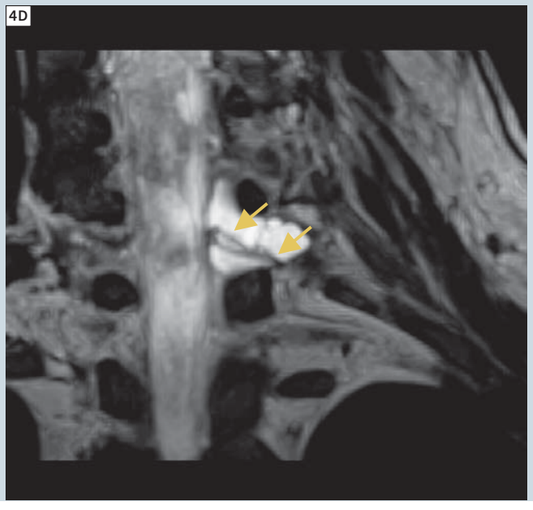

4 A, B, C coronal 3 mm thin-slice MPR based on a 3D T2w TSE scan (*syngo* SPACE).

D: magnified detail of Fig. 3A.

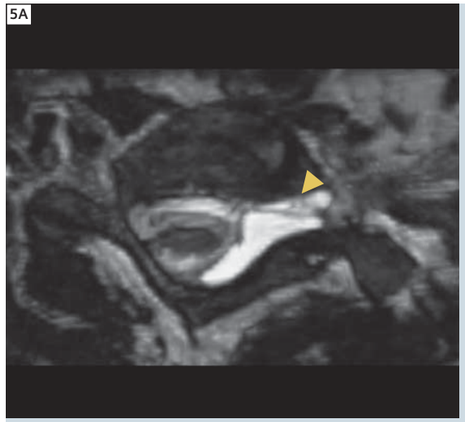

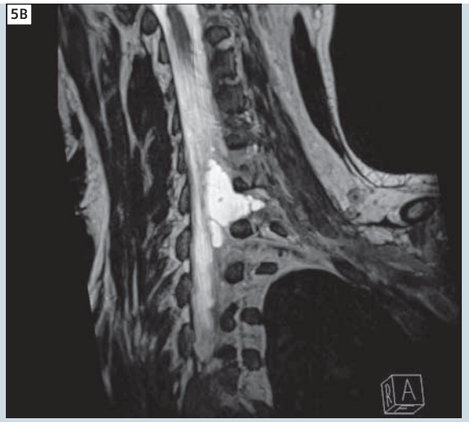

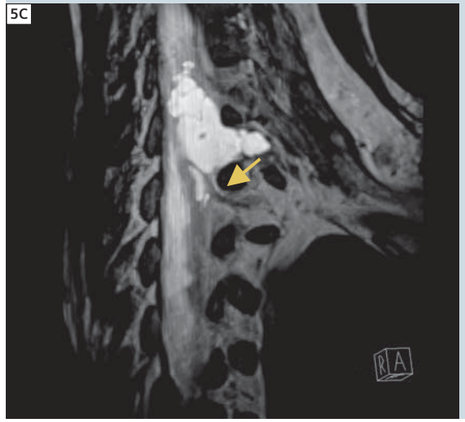

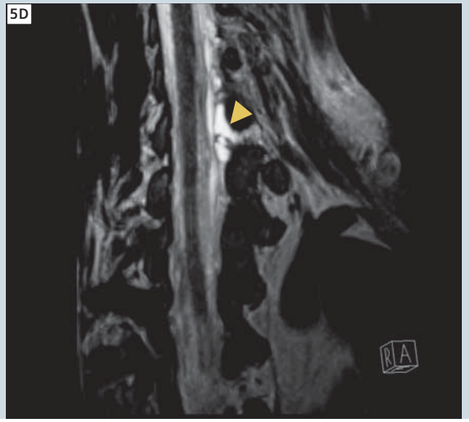

5 Oblique transversal **(A)** and coronal **(B–D)** 3 mm thin-slice MPR based on a 3D T2w TSE scan (*syngo* SPACE) for detailed visualisation of the nerve roots.

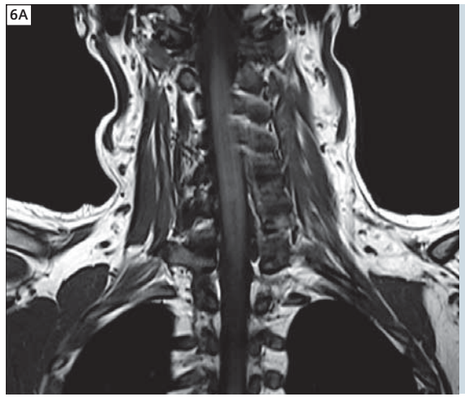

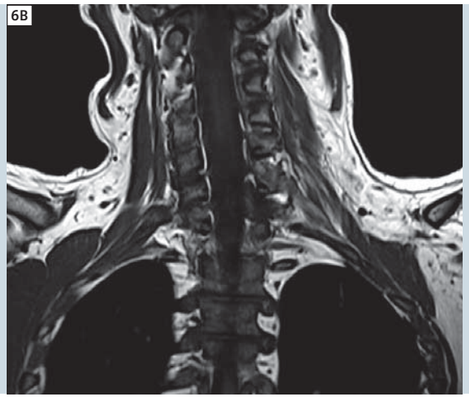

6 Coronal T1w TSE.

cervical muscles (arrows Figs. 3A, B) and of the inferior and medial trunc of the brachial nerve plexus (arrowhead Fig. 3) is clearly delineated on the coronal T2w TIRM images. Best visualized in the 3D T2w TSE (Figs. 4, 5), a nearly complete rupture of the 8th cervical nerve root is the obvious diagnosis, together with an affection and at least partial rupture of the 1st thoracic and 7th cervical nerve root. There is a regular alignment of the vertebra bodies and no evidence of a fracture. There are regular signal intensities of the myelon on the T1w and T2w images; there is no larger hemorrhage within either the myelon or the nerval plexus.

Contact
Markus G. Lentschig, M.D.
MR and PET/CT Imaging Center Bremen Mitte
Sankt-Juergen-Str. 1
28177 Bremen
Germany
www.mr-bremen.de

Tips for T2-weighted TSE Shoulder Imaging with Spectral Fat Saturation

Wei Jun Zhang[1]; Hans-Peter Hollenbach[2]

[1]*Siemens Mindit Magnetic Resonance Ltd., Shenzhen, China*
[2]*Siemens Healthcare, Erlangen, Germany*

Robust fat saturation can be achieved by different approaches including the application of inversion recovery sequences or advanced fat suppression pulses such as SPAIR. However, in some cases, such as the musculoskeletal imaging of the shoulders, the combination of a T2-weighted turbo spin echo (TSE) sequence with a conventional spectral fat saturation pulse is needed.
When imaging obese or very tall patients, the shoulder has to be positioned off-center in many MR exams and therefore several factors will affect image quality with spectral fat saturation:
B_0-inhomogeneity – if present – will cause a frequency shift, off-setting the frequency that has been implemented for spectral fat saturation relative to the fat peak. Consequently, fat will not be sufficiently suppressed. Secondly, the eddy current effect can be more serious at a very off-center position. And finally, distortions introduced by B0-inhomogeneity and non-linearity of the gradients at the edge of the maximum field-of-view can cause crosstalk effects.
The following hints on patient positioning and sequence set-up will help you to achieve high quality spectral fat saturation:

1. Try to position the shoulder as close to the magnet center as possible. (For further information on patient positioning, including a video and application hints, please visit the MSK Advisory Board on www.siemens.com/magnetom-world).
2. Try to reduce the eddy current effect by applying a lower bandwidth, changing the phase-encoding direction and using a lower sampling density. Keep in mind that the sampling density can also be influenced by the turbo factor for TSE sequences. With a fixed TR and number of slices, reducing the turbo factor will allow you to set a lower sampling rate.
3. Try to reduce the crosstalk effect by increasing the number of concatenation e.g. 2 instead of 1.

Imaging and sequence details

The shown images were acquired using a 1.5 Tesla MAGNETOM Symphony. Only one parameter was changed for best comparison. Sequence parameters for the shown T2-weighted TSE sequence were: TR / TE 3690 / 71 ms, slice thickness 3 mm, matrix 436 x 512 (interpolated), FOV 160 x 160; no averaging, no restore pulse used. In figure 1, the bandwidth was set to 120 Hz/px. Areas with insufficient spectral fat suppression are marked by an arrow in figures 1 and 2A).
In figure 1A the shoulder was placed at the very edge of the maximum field-of-view. Just by moving the region-of-interest a bit more to the isocenter of the magnet, a clear improvement in the quality of the spectral fat suppression can be achieved (Fig. 1B). In an open-bore magnet this is no problem, but even in a tighter bore, the shoulder can be moved away from the edge of the maximum field-of-view by slightly angulating the patient's position. In figure 2A the bandwidth was set to 90 Hz/px. By reducing the sampling rate to 50 Hz/px, eddy current effects are reduced and resulting in improved fat saturation.

Contact
Hans-Peter Hollenbach
Siemens AG
H IM MR PLM AW Orthopedics
Karl-Schall-Str. 6
91052 Erlangen
Germany
hans-peter.hollenbach@siemens.com

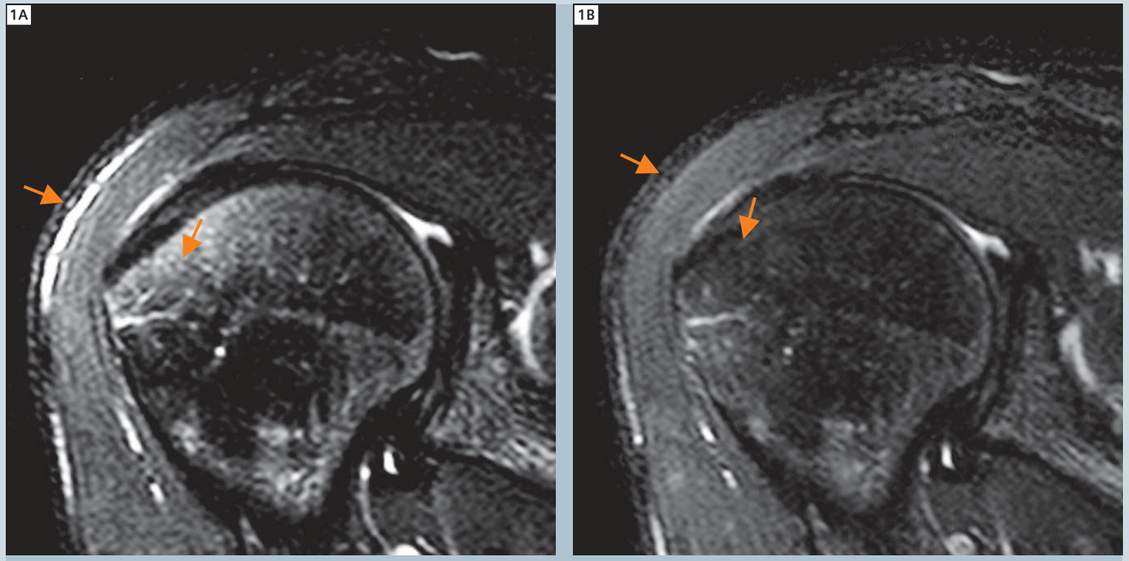

1 Improving the quality of fat saturation by moving the region of interest towards the isocenter.

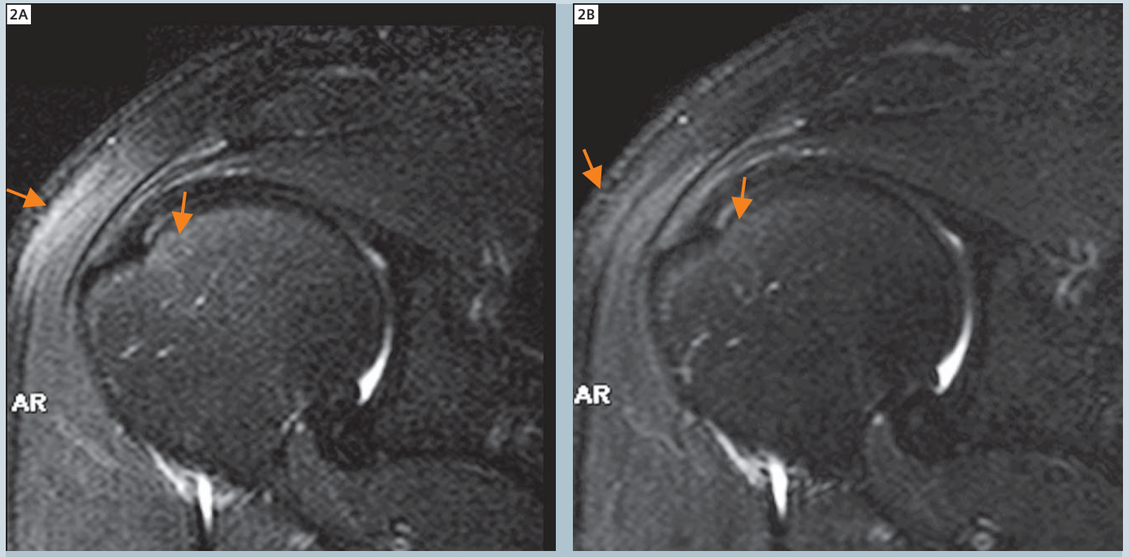

2 Reducing eddy current effects by decreasing the sampling rate.

Not for distribution in the US.

Workflow Optimized Reporting of Multi-Region MR Exams with a Novel Image Reading Software – Experiences with a Prototype

Christian Müller-Horvath[1]; Christian Plathow[1]; Burkhard Ludescher[1]; Matthias Philipp Lichy[1,2]; Valer Canda[2]; Christoph Zindel[2]; Claus D. Claussen[1], Heinz-Peter Schlemmer[1,3]

[1]*University of Tübingen, Department of Diagnostic and Interventional Radiology, Tübingen, Germany*
[2]*Siemens Healthcare, Erlangen, Germany*
[3]*German Cancer Research Center, Heidelberg, Germany*

Introduction and background

Accurate evaluation of systemic malignancies for optimized and individualized therapy regime involves a reliable TNM classification of all relevant body regions. Within the last decade, whole-body / multi-region cross-sectional imaging became an invaluable clinical tool and the available technologies for this purpose are not limited to CT and PET/CT alone; with the introduction of the Tim technology, there is no doubt that MRI – with its superior soft tissue contrast – also plays an important role in multi-region imaging. While not only true for oncologic whole-body imaging, it is especially clear for these types of MR exams that MRI faces the problem that in clinical routine the almost unlimited numbers of images generated (at our institution the radiologist has to read 1,000 to 1,500 images per patient for a standard whole-body MRI) with their different contrasts and information content are one of the major threats for the reporting radiologist and referring physician. This problem is aggravated when it comes to exact documentation of tumor load, presence of further suspicious lesions and other relevant findings and their presentation at, for example, interdisciplinary conferences. But even relatively simple tasks during the reading process, like the generation of cross-references between the different image contrasts / image series and the anatomic sorting of the images, are a daily challenge for radiologists and have a clear impact on the required time for reading and on the accuracy of the final report.

Purpose

The aim of the presented work was therefore to create and evaluate a new software tool to assist and automate the process of reading whole-body / multi-region data sets.

The prototype

In close cooperation between the Department of Diagnostic and Interventional Radiology of the University of Tübingen, Germany, and Siemens Healthcare a novel prototype for workflow optimized reading of multi-region MRI data was developed. This software was based on the research and developer platform MeVislab (MeVis, Center for Medical Imaging Computing, Bremen, Germany). In contrast to a conventional reading software, the user interface of the prototype included

- an anatomical navigator (series are sorted in an automated processing step according to their anatomical coverage)
- a workflow navigator (series are sorted and presented according to their logical assignment e.g. scanning for brain or bone metastases)
- a findings navigator (marked findings are stored in an interactive list).

These three elements can be easily identified on the screenshot of the user interface provided in figure 1. The measurement tools implemented in this prototype focus on oncologic reading (e.g. 3D MPR, distance line etc.). In contrast to image interpretation with a traditional reading software, the acquired images are directly transferred from the PACS archive to the prototype system and the images are then prepared by automated pre-processing steps by the software. For this prototype this step includes the preparation / calculation of 3D data sets, image / series sorting and generation of a multi-image TIFF file including preview image stamps. The premise behind this automated pre-processing step is that the radiologist profits both during start-up as well as during the whole reading process. The radiologist can start immediately with its real work and has immediate access to all relevant data for precise and accurate interpretation of MRI; image sorting, loading and layout adaption during reading are eliminated ideally in this scenario. Despite the clear time advantage (mainly introduced by the elimination of manually loading and image sorting steps), the main differences / advantages of such a prepared reading workflow compared to a traditional reading procedure are as follows:

1. **Reading:** at the same time as a suspicious lesion is marked by the radiologist, all available images with the same location (but different contrasts and orientations) can be displayed via cross reference.
2. **Finding documentation:** all findings are listed in a dedicated template; cross-linking with dedicated text, finding tables and reference images are available at any time and can be shared between different users.
3. **Reproducibility of findings:** as a consequence of the above two advantages, all lesions marked in a previous reading can be easily displayed and all images are displayed for follow-up exams and also for conferences; this eliminates the need to locate once again all findings based on a written report.

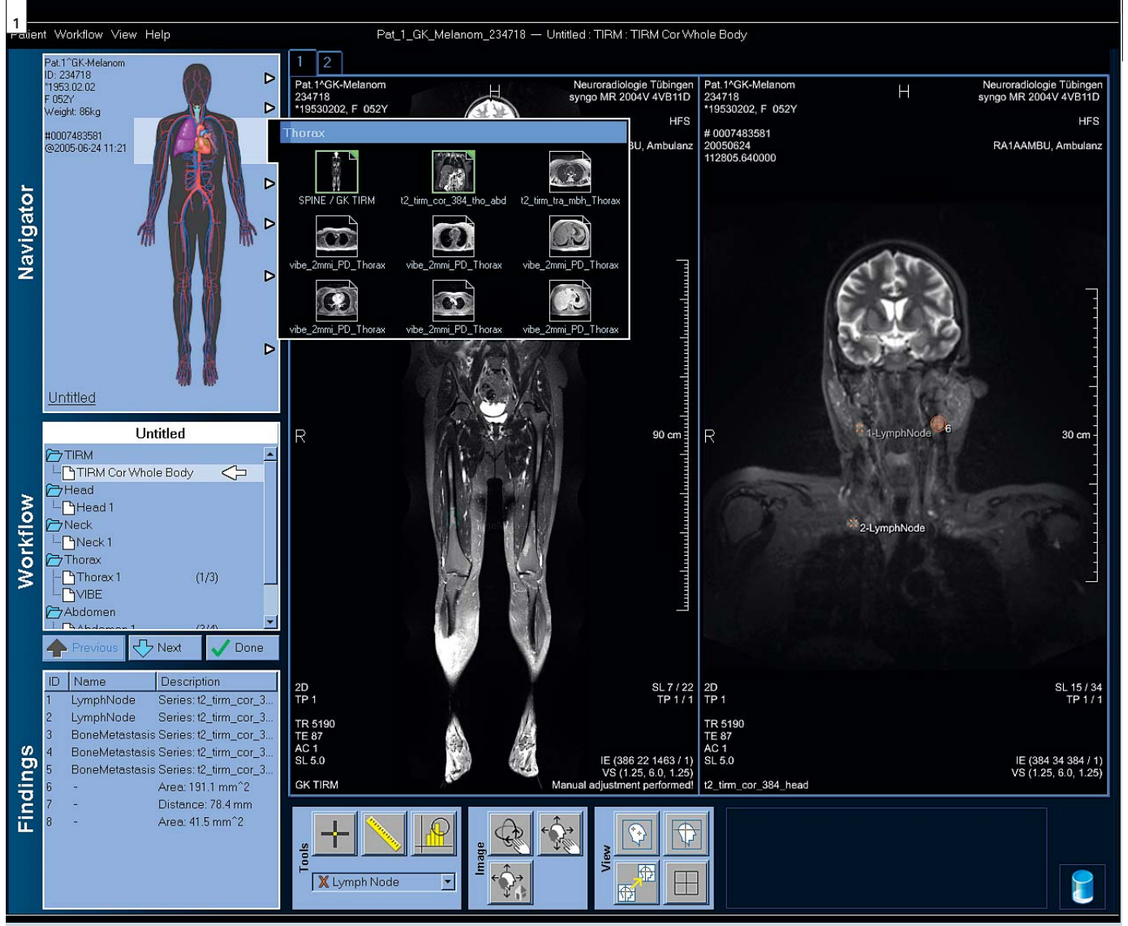

1 A screenshot of the prototype is shown. In contrast to a conventional image reading software user interface, there are three unique sections labelled "Navigator", "Workflow" and "Findings". A whole-body MR exam is loaded and all images defined within a dedicated workflow task are displayed (here: coronal TIRM images). All images are also sorted according to their anatomical relationship ("Navigator" section). Marked findings are listed in the "Findings" section and can easily be retrieved by a single click action. At the bottom, some basic reading tool icons are shown.

Materials and methods

To evaluate the clinical potential of this prototype, a multi-reader study was conducted. Thirteen whole-body datasets of patients with advanced malignant melanoma were evaluated by three radiologists: 3 / 13 were female (mean age 65 +/- 14 years), 10 / 13 male (mean age 56 +/- 9 years). All patients were also examined with an 18F FDG PET/CT whole-body scan as reference scan (metastases of malignant melanoma are characterized by high glucose uptake). In all patients, a stage IV was present; this tumor stage is characterized by ubiquitary multiple metastases without preferences to an organ system and therefore rises a big

Not for distribution in the US.

2A

2A Screenshot of a whole-body reading with a prototype of the newly developed reading software platform (*syngo*.via) is shown in this figure, which is also evaluated at our institution. Most important principles of the prototype tested in this article are preserved and can easily be recognized: the former "Workflow" section is shown on the left hand side. In the upper section, by simply clicking on the desired area of interest, all images are loaded in a predefined layout (here for screening the head and neck section). Findings are listed in the lower row ("Findings Navigator"). Additional images which cannot be assigned to either a dedicated anatomical region or to a workflow are allocated to the "MR Remaining images" task. Different colour layouts and icons enable the radiologist to easily grasp matters such as uncompleted tasks or the presence of unassigned images. At the bottom, a set of tools for changing the screen layout and modifying display options e.g. synchronisation between different image series are available. The full range of reading tools including post-processing tools e.g. image fusion can be easily accessed from any image via corner menus (not shown in this screenshot).

challenge to any cross-section imaging modality in the accurate evaluation of tumor load.

Quantitative measurements for evaluation of the prototype included the required time for loading and opening of an exam, time required for reporting including the comparison of reference series. Documentation was separated also for different body regions (head, neck, thorax, abdomen, pelvis). Also the time required for retrieving a defined lesion was documented. For qualitative evaluation of this prototype, the level of comfort for loading of images, help provided for retrieving a lesion and usability was rated on a 5-point scale (from 0 = poor to 4 = excellent).

All data sets were read by 3 radiologists independently and blinded to any patient data with different levels of clinical experiences (two readers with high experience in all cross section modalities including PET/CT, one with less than six months experience with MR whole-body exams). Statistical analysis included Student-t-tests and calculation of kappa-values for inter-observer variability.

A short comparison between the hardware used for the two evaluated programs is given in table 1.

Results

For one MR exam, an average of 1141 images were read by each reader.

The average loading time was 39.7 (+/- 5.5) seconds with the conventional reading software and with the prototype 6.5 (+/- 1.4) seconds ($p < 0.01$).

To display the different regions, the achieved time reductions by the prototype for readers 1 / 2 / 3 were as follows:

Not for distribution in the US.

2B

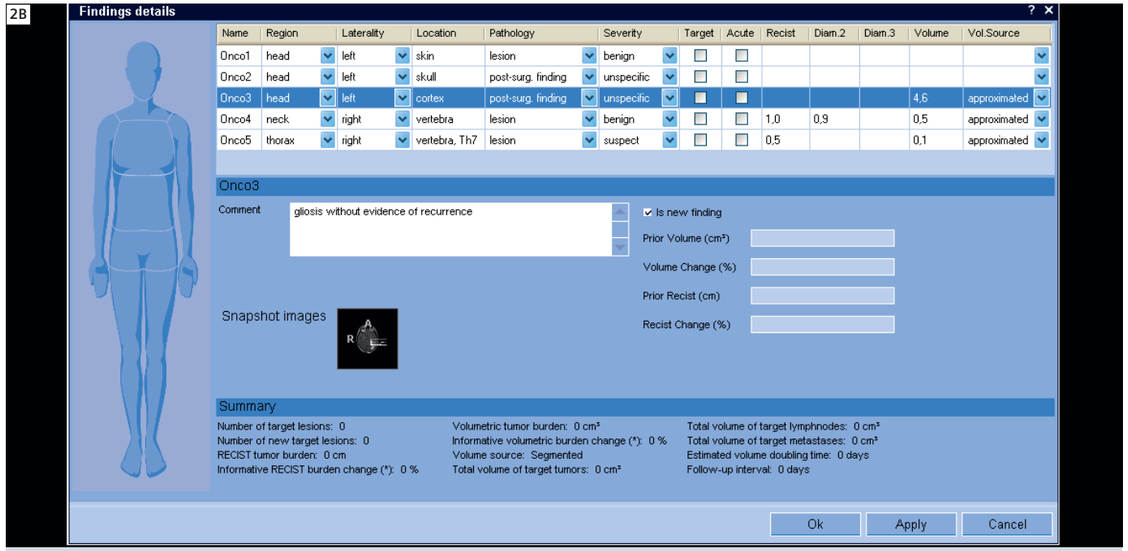

2B In a next step, the new software platform provides a fast and precise definition of all image findings via drop-down menus and input boxes. If a malignancy is present and the data assigned, all relevant information for the referring physician is summarized in the lower section. For an oncology study as performed in this example, this also includes the tumor burden according to RECIST criteria.

2C

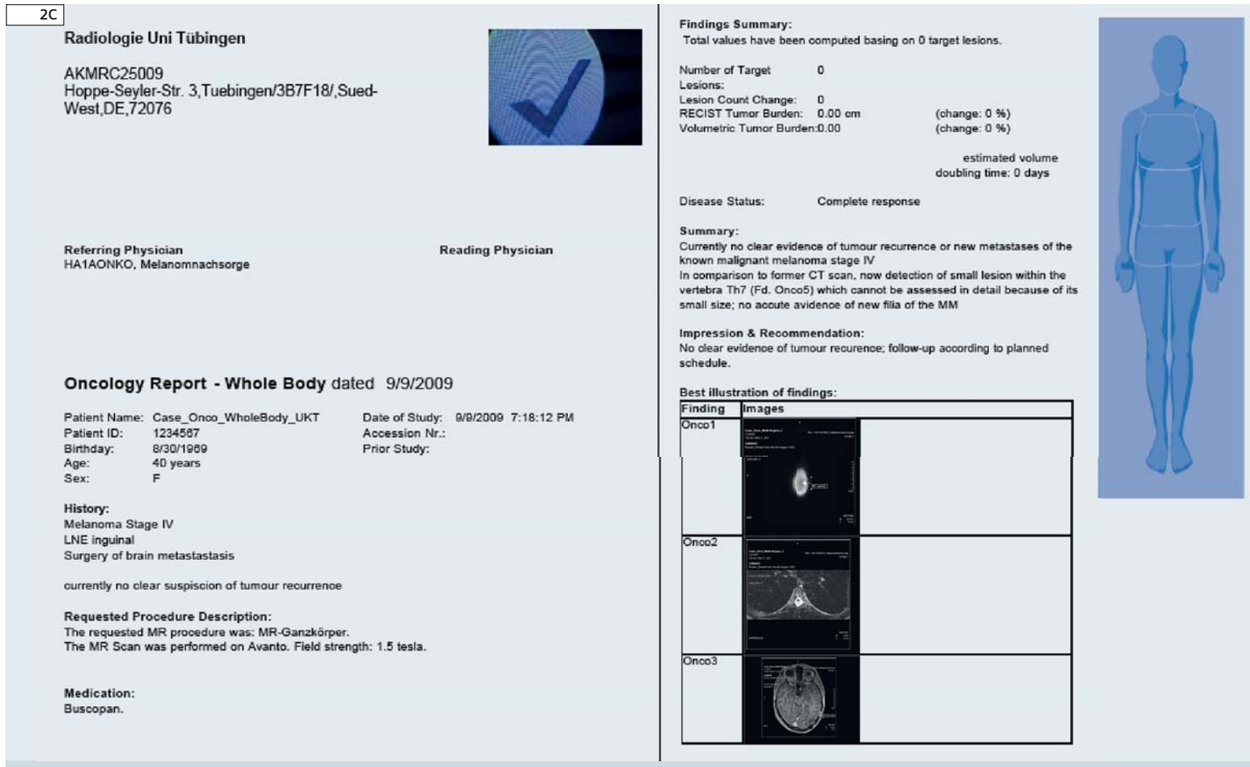

2C The results can also be transferred into a standardized report form which can also include images for a better visualization of the findings for the referring physician and the patient. This screenshot shows an example of how such a report can look.

Not for distribution in the US.

3

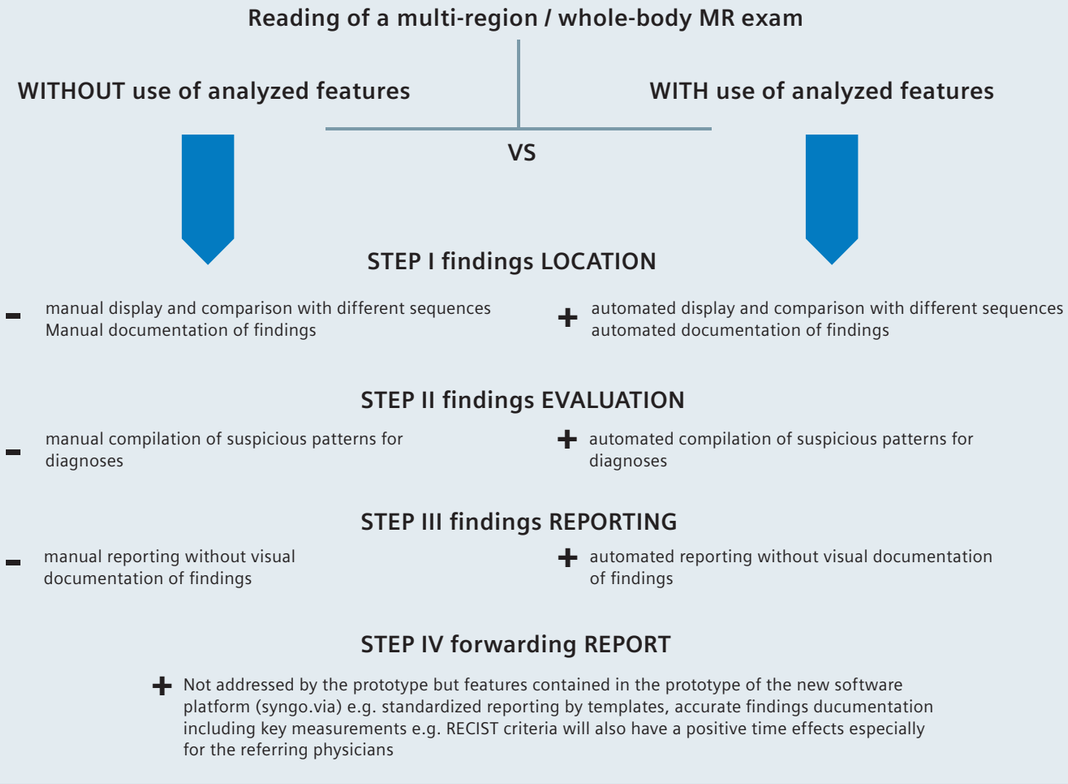

3 Short overview of the reading process with and without a workflow-oriented reading software with special focus on time-consuming process steps. Negative influences on an effective image reading are marked by a "minus" sign, positive effects which result in a clear reduction of the total image reading time are marked with a "plus" sign.

head region 36 / 50 / 54%,
thorax region 59 / 56 / 62%,
abdominal region 62 / 63 / 48%,
pelvic region 73 / 64 / 55%.
To retrieve a previously described finding, an average of 148 (+/- 95) seconds were required with the standard reading software whereas this finding was displayed after 2.5 (+/- 0.5) with the prototype (up to 98% time saved).
In total, 629 lesions were classified as potentially malignant by the three readers (301 with the conventional reading software, 328 with the prototype).
Based on reference exams, the same number of metastases was detected with both systems and there was no statistically significant difference between the three readers ($p < 0.01$, $k > 0.9$).

Discussion

One of the main problems in the integration of multi-region / whole-body MR exams in our clinical routine is founded on the immense amount of data which has to be handled during the reading process. While the implementation of PACS systems within a department allows a wide and fast contribution of images throughout the institution and beyond, the implemented software for displaying the images and also for post-processing has not disburdened the radiologist significantly. In reality, without any real assistance e.g. for image sorting, optimal layouts, no standardized reports etc. provided by these systems, the radiologist has to spend a lot of effort in these operative / administrative tasks and as a consequence negative effects on the time efficiency of the reading process as well as his attention for his real task – providing best care to the patient by accurate and error-free reporting – are likely. A potential approach for improving the efficiency of reading large MRI data sets is shown with the evaluated prototype. Previous studies by different working groups already pointed out that the implementation of an automated working lists and

changes within the workflow chain can result in significant time gains [Gale et al., Siegel et al.]. As an example, Gale et al. could reduce the required time for reading by an "autoread-function" by 38%; by automated importing and sorting of the next exam Siegel et al. could reduce the time between the reading of exams by approximately 10%.
Cross-section exams with large image data are not read immediately in clinical routine (although a few exceptions do exist, such as computed tomography as part of the emergency room procedure) and before starting the reading process, these images are transferred to a PACS archive. With our prototype, the pre-processing step required 2 to 3 minutes for preparing a whole-body MR exam; compared to the required time in a conventional reading process including archiving the images as well as request and delivery of the whole exam to the reading workstation. This one-time step did not have a negative effect on the reading process. It should also be emphasized that the required time for such a preparation step will clearly be reduced since firstly the available computing power is increasing dramatically each year and secondly the status of the software reported in this article is prototype status. This study clearly demonstrated that a workflow-optimized automated reading software has a clear time benefit compared to conventional ones. Obviously the radiologist's experience has an effect on the speed and accuracy of the reading process. Nevertheless, even for the highly experienced readers in this study, the time benefit as well as the gain in comfort was obvious; this is especially true for retrieving a predefined lesion. In conclusion it can be stated that with the demonstrated new software a significant time saving when working with whole-body data sets can be realized without any compromise with regard to diagnostic confidence and with a significant advantage in terms of convenience. As a result, the problem of evaluating examinations with thousands of images can be approached systematically.
The tested prototype was implemented to demonstrate the key elements of a new workflow-oriented reading software. After proving the advantages of such a technology, the next step would be the integration of such a new approach in image reading within a framework for a real multi-modality reading platform. The requirements for such a software also include further advancements in handling advanced image data and reading tools such as image fusion for reading, for example, PET/CT data. In addition, techniques for linking the image acquisition and reading without any time delays are also required to meet the demands for image interpretation on the fly, a prerequisite for efficient reading in emergency scenarios. We are currently testing a prototype of a new image reading software platform and within this platform, the evaluated workflow-features in our prototype are now available for all image modalities; we believe that this represents a great step forward in workflow-oriented image reading technology. The radiologist is supported actively in its reading task in an intuitive as well as efficient way and is not hampered by predetermined steps required by most of currently available reading platforms.

References
1 Gale DR, Gale ME, Schwartz RK, Muse VV, Walker RE. An automated PACS workstation interface: a timesaving enhancement. AJR Am J Roentgenol. 2000 Jan;174(1):33-6.
2 Siegel E, Reiner B. Work flow redesign: the key to success when using PACS. AJR Am J Roentgenol. 2002 Mar;178(3):563-6.

Contact
Prof. Heinz-Peter Schlemmer
Department of Radiology
German Cancer Research Center (DKFZ)
Im Neuenheimer Feld 280
69120 Heidelberg
Germany
h.schlemmer@dkfz.de

Table 1: For the evaluation of the prototype, a standard PC equipped with two 19" TFT displays was used. For reference, a standard reading workstation was used. Both systems were installed within the same subnetwork. The technical specifications were as follows:

	Prototype	reference reading system (MV 1000)
OS	Microsoft Windows XP	Microsoft Windows 2000
CPU	2x 1.7 GHz Intel Xeon	2x 2.8 GHz Intel Xeon
RAM	1 GB	3 GB
GPU	NVIDIA Quadro4 750 XGL	Matrox Millenium 450
Harddisk controller	Ultra ATA system	SCSI system
Network controller	Intel Pro/100 S	Intel Pro/1000 MT

Siemens Healthcare – Customer Magazines

Our customer magazine family offers the latest information and background for every healthcare field. From the hospital director to the radiological assistant – here, you can quickly find information relevant to your needs.

Medical Solutions
Innovation and trends in healthcare. The magazine, published three times a year, is designed especially for members of the hospital management, administration personnel, and heads of medical departments.

News
Our latest topics such as product news, reference stories, reports, and general interest topics are always available at www.siemens.com/healthcare-news

AXIOM Innovations
Everything from the worlds of interventional radiology, cardiology, fluoroscopy, and radiography. This semiannual magazine is primarily designed for physicians, physicists, researchers, and medical technical personnel.

MAGNETOM Flash
Everything from the world of magnetic resonance imaging. The magazine presents case reports, technology, product news, and how-to's. It is primarily designed for physicians, physicists, and medical technical personnel.

SOMATOM Sessions
Everything from the world of computed tomography. With its innovations, clinical applications, and visions, this semiannual magazine is primarily designed for physicians, physicists, researchers, and medical technical personnel.

Perspectives
Everything from the world of clinical diagnostics. This semi-annual publication provides clinical labs with diagnostic trends, technical innovations, and case studies. It is primarily designed for laboratorians, clinicians and medical technical personnel.

For current and older issues and to order the magazines, please visit **www.siemens.com/healthcare-magazine**

Over already?

... I was just getting comfortable!

Experience the new 3T MAGNETOM Verio MRI — now available at ABC Imaging Center

Comfort: **A more relaxing experience**
An extra-large opening means it can comfortably accommodate patients of different shapes and sizes and can help reduce anxiety and claustrophobia.

Speed: **A quicker exam**
Exclusive Tim™ (Total imaging matrix) technology helps make exams faster.

Confidence: **Detailed images for your doctor**
Extraordinary images with exceptional details — your doctors will have the information they need to help make a more confident diagnosis.

Rest easy!

Now available at ABC Imaging Center
(000) 000-0000

Market your MAGNETOM system

All the tools necessary to market your facility to patients and referring physicians are waiting for you in the **Your MAGNETOM** section on **www.siemens.com/magnetom-world**

Here you will find everything you need from patient pamphlets to advertisements, to trailers and press releases, postcards, posters, event checklists, high-resolution images and much more – ready for immediate use.

MAGNETOM Flash – Imprint

© 2010 by Siemens AG, Berlin and Munich, All Rights Reserved

Publisher:
Siemens AG
Medical Solutions
Business Unit Magnetic Resonance,
Karl-Schall-Straße 6, D-91052 Erlangen, Germany

Editor-in-Chief: Dr. Matthias Lichy, M.D. (matthias.lichy@siemens.com)

Associate Editor: Antje Hellwich (antje.hellwich@siemens.com)

Editorial Board: Dagmar Thomsik-Schröpfer, Ph.D.; Okan Ekinci, M.D.; Ignacio Vallines, Ph.D.; Wellesley Were; Milind Dhamankar, M.D.; Michelle Kessler; Gary McNeal; Sunil Kumar, M.D.

Production: Norbert Moser, Siemens AG, Medical Solutions

Layout: independent Medien-Design Widenmayerstrasse 16, D-80538 Munich

Printers: Farbendruck Hofmann, Gewerbestraße 5, D-90579 Langenzenn, Printed in Germany

MAGNETOM Flash is also available on the internet:
www.siemens.com/magnetom-world

Note in accordance with § 33 Para.1 of the German Federal Data Protection Law: Despatch is made using an address file which is maintained with the aid of an automated data processing system.
MAGNETOM Flash with a total circulation of 20,000 copies is sent free of charge to Siemens MR customers, qualified physicians, technologists, physicists and radiology departments throughout the world. It includes reports in the English language on magnetic resonance: diagnostic and therapeutic methods and their application as well as results and experience gained with corresponding systems and solutions. It introduces from case to case new principles and procedures and discusses their clinical potential.
The statements and views of the authors in the individual contributions do not necessarily reflect the opinion of the publisher.
The information presented in these articles and case reports is for illustration only and is not intended to be relied upon by the reader for instruction as to the practice of medicine. Any health care practitioner reading this information is reminded that they must use their own learning, training and expertise in dealing with their individual patients. This material does not substitute for that duty and is not intended by Siemens Medical Solutions to be used for any purpose in that regard. The drugs and doses mentioned herein are consistent with the approval labeling for uses and/or indications of the drug. The treating physician bears the sole responsibility for the diagnosis and treatment of patients, including drugs and doses prescribed in connection with such use. The Operating Instructions must always be strictly followed when operating the MR system. The sources for the technical data are the corresponding data sheets. Results may vary.
Partial reproduction in printed form of individual contributions is permitted, provided the customary bibliographical data such as author's name and title of the contribution as well as year, issue number and pages of MAGNETOM Flash are named, but the editors request that two copies be sent to them. The written consent of the authors and publisher is required for the complete reprinting of an article.
We welcome your questions and comments about the editorial content of MAGNETOM Flash. Please contact us at magnetomworld.med@siemens.com. Manuscripts as well as suggestions, proposals and information are always welcome; they are carefully examined and submitted to the editorial board for attention. MAGNETOM Flash is not responsible for loss, damage, or any other injury to unsolicited manuscripts or other materials. We reserve the right to edit for clarity, accuracy, and space. Include your name, address, and phone number and send to the editors, address above.

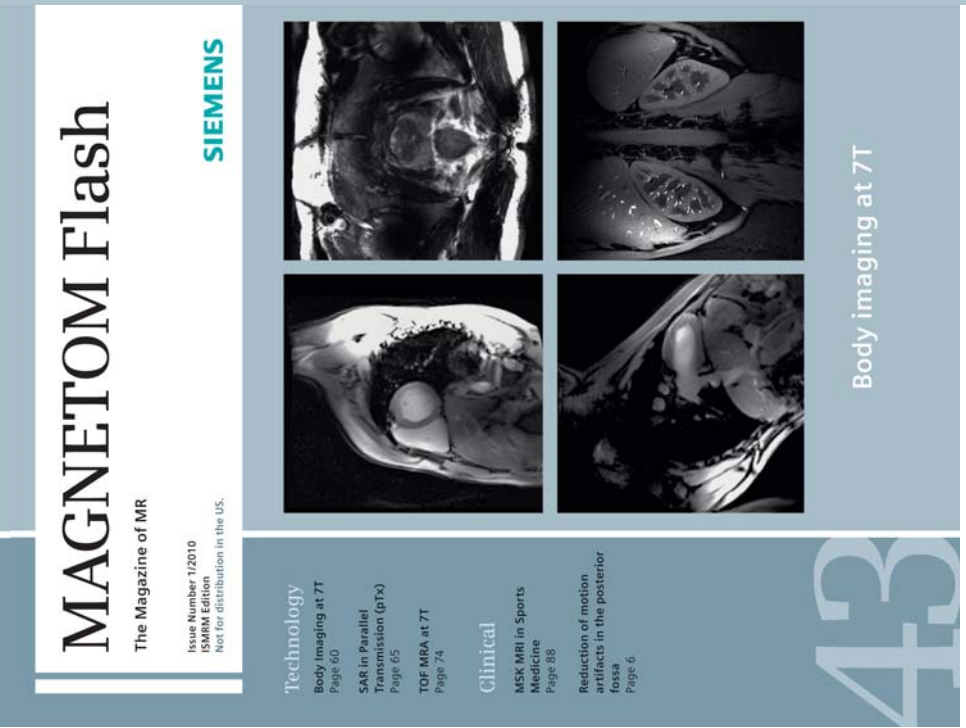

Subscription

Please enter your business address

Institution

Department

Function

Title

Name

Street

Postal Code

City

State

Country

MR system used

Please include me in your mailing list for the following Siemens Healthcare customer magazine(s):

- ☐ Medical Solutions
- ☐ MAGNETOM Flash
- ☐ SOMATOM Sessions
- ☐ AXIOM Innovations

Stay up to date with the latest information Register for:

- ☐ the monthly e-Newsletter

E-mail

- ☐ Yes, I consent to the above information being used for future contact regarding product updates and other important news from Siemens.
- ☐ unsubscribe from info service

Please print clearly!

→ Visit www.siemens.com/magnetom-world for case reports, clinical methods, application tips, talks and much more clinical information.

SUBSCRIBE NOW!

– and get your free copy of future MAGNETOM Flash! Interesting information from the world of magnetic resonance – gratis to your desk. Send us this postcard, or subscribe online at www.siemens.com/MAGNETOM-World

Siemens AG
Medical Solutions
Magnetic Resonance
Antje Hellwich - Marketing
P.O. Box 32 60
D-91050 Erlangen
Germany

MAGNETOM Flash

Global Siemens Headquarters

Siemens AG
Wittelsbacherplatz 2
80333 Muenchen
Germany

Global Siemens Healthcare Headquarters

Siemens AG
Healthcare Sector
Henkestr. 127
91052 Erlangen
Germany
Phone: +49 9131 84-0
www.siemens.com/healthcare

www.siemens.com/healthcare-magazine

Order No. A91MR-1000-71C-7600 | Printed in Germany | CC MR 01000 ZS 041015. | © 04.10, Siemens AG

On account of certain regional limitations of sales rights and service availability, we cannot guarantee that all products included in this brochure are available through the Siemens sales organization worldwide. Availability and packaging may vary by country and is subject to change without prior notice. Some/All of the features and products described herein may not be available in the United States.

The information in this document contains general technical descriptions of specifications and options as well as standard and optional features which do not always have to be present in individual cases.

Siemens reserves the right to modify the design, packaging, specifications and options described herein without prior notice.
Please contact your local Siemens sales representative for the most current information.

Note: Any technical data contained in this document may vary within defined tolerances. Original images always lose a certain amount of detail when reproduced.

Global Business Unit

Siemens AG
Medical Solutions
Magnetic Resonance
Henkestr. 127
DE-91052 Erlangen
Germany
Phone: +49 9131 84-0
www.siemens.com/healthcare

Local Contact Information

In Asia
Siemens Pte Ltd
The Siemens Center
60 MacPherson Road
Singapore 348615
Phone: +65 6490-8096

In Canada
Siemens Canada Limited
Medical Solutions
2185 Derry Road West
Mississauga ON L5N 7A6
Canada
Phone: +1 905 819-5800

Europe/Africa/Middle East
Siemens AG
Medical Solutions
Henkestr. 127
91052 Erlangen
Germany
Phone: +49 9131 84-0

Latin America
Siemens S.A.
Medical Solutions
Avenida de Pte. Julio A. Roca No 516,
Piso 7
C1067ABN Buenos Aires
Argentina
Phone: +54 11 4340-8400

USA:
Siemens Medical Solutions U.S.A., Inc.
51 Valley Stream Parkway
Malvern, PA 19355-1406
USA
Phone: +1-888-826-9702